Spring 2013

Flow structure in the wake of a low-aspect-ratio wall-mounted bluff body

Seyed Mohammad Hajimirzaie
University of Iowa

FLOW STRUCTURE IN THE WAKE OF A LOW-ASPECT-RATIO WALL-MOUNTED BLUFF BODY

by

Seyed Mohammad Hajimirzaie

An Abstract

Of a thesis submitted in partial fulfillment of the
requirements for the Doctor of Philosophy degree
in Civil and Environmental Engineering
in the Graduate College of
The University of Iowa

May 2013

Thesis Supervisors: Professor Larry Weber
Assistant Professor James Buchholz

ABSTRACT

The effects of shape and relative submergence (the ratio of flow depth to obstacle height, d/H) were investigated on the wakes around four different low-aspect-ratio wall-mounted obstacles semi-ellipsoids with the major axes of the base ellipses aligned in the streamwise and transverse directions, two cylinders with aspect ratios matching the ellipsoids. The wake structure of a fully submerged, spherical obstacle was also investigated in the same flow conditions to provide insight into the flow-obstacle interaction with implication to sediment transport. A low-aspect-ratio semi-ellipsoid was chosen as broadly representative of a freshwater mussel projecting from a river bed, and a sphere was employed as representative of a boulder. Two cylinders were used due to their similarity to geometries investigated in other studies. Digital Particle Image Velocimetry and thermal anemometry were used to interrogate the flow. For ellipsoids and cylinders, streamwise features observed in the mean wake included counter-rotating distributions of vorticity inducing downwash (tip structures), upwash (base structures), and horseshoe vortices. In particular, the relatively subtle change in geometry produced by the rotation of the ellipsoid from the streamwise to the transverse orientation resulted in a striking modification of the mean streamwise vorticity distribution in the wake. Tip structures were dominant in the former case while base structures were dominant in the latter. A vortex skeleton model of the wake is proposed in which arch vortex structures are deformed by the competing mechanisms of Biot-Savart self induction and the external shear flow, making the ellipsoid wakes an archetypical model for understanding more complicated wakes. The wake of the sphere, is somewhat more complex than the ellipsoidal geometries. The knowledge from the wake of ellipsoids was employed for sphere wake structures in which two vertex pairs were found in the wake with the same sign as the horseshoe vortices. Streamwise features observed in the mean wake including tip, horseshoe

structures, and weak upwash. The shedding characteristics and dynamics of the wake were examined. Weak, approximately symmetric shedding was observed in the wakes of streamwise and transverse ellipsoids and sphere at $d/H > 3$ while cross-spectral measurements confirmed downstream and upstream tilting of arch structures shed by the transverse and streamwise ellipsoids, respectively. Much weaker peaks in the power spectrum were observed for low- and high-aspect-ratio cylinders. An inverse relationship was observed between the relative submergence and the strength of the base structures for the ellipsoids. While the dominant Strouhal number remained constant as the relative submergence was reduced to $d/H = 2.5$ for the ellipsoids, it increased abruptly at $d/H = 1$ and transitioned to an antisymmetric mode. For the sphere geometry at $d/H = 3.5$, a weak dominant frequency was observed close to obstacle junction. The bed shear stress distribution was estimated around the sphere for comparison with past and future studies on sediment transport in open channel flow, demonstrating high values beneath the lobes structures. These results demonstrate a means by which to achieve significant modifications to flow structure and transport mechanisms in the flow.

Abstract Approved: _____
Thesis Supervisor

_____
Title and Department

_____
Date

_____
Thesis Supervisor

_____
Title and Department

_____
Date

FLOW STRUCTURE IN THE WAKE OF A LOW-ASPECT-RATIO WALL-MOUNTED BLUFF BODY

by

Seyed Mohammad Hajimirzaie

A thesis submitted in partial fulfillment of the
requirements for the Doctor of Philosophy degree
in Civil and Environmental Engineering
in the Graduate College of
The University of Iowa

May 2013

Thesis Supervisor: Professor Larry Weber
Assistant Professor James Buchholz

Graduate College
The University of Iowa
Iowa City, Iowa

CERTIFICATE OF APPROVAL

PH.D. THESIS

This is to certify that the Ph.D. thesis of

Seyed Mohammad Hajimirzaie

has been approved by the Examining Committee for the thesis requirement for the Doctor of Philosophy degree in Civil and Environmental Engineering at the May 2013 graduation.

Thesis Committee: _____
Larry Weber, Thesis Supervisor

_____
James Buchholz, Thesis Supervisor

_____
George Constantinescu

_____
Ching-Long Lin

_____
Thanos Papanicolaou

To my family and my lovely wife who has been my strength through hard times

ACKNOWLEDGEMENTS

I must extend my deepest gratitude to Professor James Buchholz for his time, effort, enduring patience, and guidance in opening my eyes to the wonderful world of vortex structures and shaping my understanding of turbulent vortex shedding flows outlined in this thesis. His direction and keen insights have been essential for the work that follows. I would like to express my sincere gratitude to Professor Larry Weber, for his continuous support of my Ph.D study and research. Without fail, he has encouraged me when I needed assurance and given me self-confidence when I was overwhelmed.

Thanks also to Professor Thanos Papanicolaou for his encouragements and his words of wisdom during tough times. My gratitude also goes to Professors George Constantinescu and Ching-Long Lin for agreeing to serve on my Thesis Committee and providing valuable insight into this thesis. To all of you, I am very grateful.

I would also like to thank my colleagues James Akkala, Juan Correa, Azar EslamPanah, Hamid Fahimrezaie, Alireza Firoozfar, Mohammad S. Miri, Hamid S. Hosseini, Achilleas Tsakiris, and Craig Wojick at the University of Iowa who have worked with me on the extensive measurement campaign and analysis of the large-scale turbulent structures in finite body flows presented in my thesis. The data collected is considerable; and the progress in understanding these flows would not have been possible without the diligence of these hardworking friends. I would also like to extend my appreciation to the IIHR mechanical shop staff.

I want to especially thank my wife for her ever-lasting love and support throughout this process. Finally, I would not be the man I am today without my parents' unconditional love and continued encouragements. I am forever thankful to them.

This work was sponsored by the National Science Foundation under award number CBET-1033732.

TABLE OF CONTENTS

LIST OF TABLES v

LIST OF FIGURES vi

CHAPTER

1 INTRODUCTION 1

1.1 Motivation 1
1.2 Thesis Objectives and Overview 4

2 LITERATURE REVIEW 7

2.1 Flow Structure in the Wake of a Wall-Mounted Bluff Body 7
2.2 Mean Flow Structure 7
2.2.1 Horseshoe Vortices 10
2.2.2 Tip Vortices 12
2.2.3 Base Vortices 14
2.3 Effects of Obstacle Shape 18
2.4 Flow Characteristics around a Wall-Mounted Spherical Obstacle 24
2.5 Effects of Boundary Layer Thickness 37
2.6 Effect of Relative Submergence 40
2.7 Shedding Characteristics 45
2.8 Summary 49

3 EXPERIMENTAL FACILITY AND TECHNIQUES 55

3.1 Water Channel Facility and Flow Quality 55
3.1.1 High Free-Stream Turbulence Flow 56
3.1.2 Low Free-Stream Turbulence Flow 58
3.1.3 Measurement Conditions 58
3.2 Obstacle Geometries and Experimental Setup 60
3.3 Flow Measurement Techniques 64
3.3.1 Digital Particle Image Velocimetry (DPIV) 64
3.3.2 Hot-Film Anemometry 70

4 FLOW CHARACTERISTICS AROUND A WALL-MOUNTED SEMI-ELLIPSOID 74

4.1 High Free-Stream Turbulence Flow 74
4.1.1 Boundary Layer Characteristics 74
4.1.2 Flow Patterns in the Streamwise Symmetry Plane 75
4.1.3 Streamwise Vorticity Distributions 79

4.1.4 The Role of Relative Submergence 87
4.2 Low Free-Stream Turbulence Flow 94
4.2.1 Boundary Layer Characteristics 96
4.2.2 Flow Patterns in the Streamwise Symmetry Plane 97
4.2.3 Streamwise Vorticity Distributions 98
4.2.4 Proposed Model for Ellipsoid Wakes and Its Application to Cylinder Wakes 101
4.2.5 Spectra and correlation analysis in the wake 108
4.2.6 Model for Ellipsoid Wakes 114
4.2.7 Relative Submergence Revisited 116

5 FLOW CHARACTERISTICS AROUND A WALL-MOUNTED SPHERE 127

5.1 Flow Patterns in the Streamwise Symmetry Plane 127
5.2 Streamwise Vorticity Distributions 134
5.3 Shedding Characteristics 139
5.4 Proposed Model for the Sphere Wake 141
5.5 Shear Stress Distribution 145

6 CONCLUSIONS AND FUTURE WORK 163

6.1 Conclusions 163
6.2 Future Work 167

APPENDIX A UNCERTAINTY ANALYSIS-DPIV 170

A.1 Transverse Plane 170
A.2 Symmetry Plane 173

APPENDIX B UNCERTAINTY ANALYSIS-THERMAL ANEMOMETRY 174

B.1 Strouhal Number 174

REFERENCES 175

LIST OF TABLES

Table

2.1 Summary of previous experiments have been conducted on the wake of obstacles. 52

4.1 Mean dimensionless reattachment lengths on the symmetry plane measured from the obstacle center line, and nondimensionalized by obstacle height (which remains constant for all obstacles) and obstacle diameter . 77

4.2 Circulation of base vortex in different relative submergence in Figure 4.14. 90

4.3 Average dimensionless circulations of structures identified for streamwise and transverse ellipsoid at $x/H = 1.5$ in two different turbulence intensity, and the left/right deviation. 99

5.1 Bed shear stress, τ_0, in z/D =0.035 at $x/D = 0.5$ to 3 and $y = 0$ 162

LIST OF FIGURES

Figure

1.1 Freshwater mussel on the river bed (internetstones.com) 3

1.2 Steep mountain stream (Rocky Mountain river, Photo by: Rolf Hicker) . 4

1.3 Effect of relative submergence (RS) on depositional pattern: (top) LRS-Low Relative Submergence-where particles deposit at the upstream face of the clast, (bottom) HRS-High Relative Submergence-where particles deposit at the wake of the clast (Papanicolaou and Kramer, 2005) 5

2.1 Flow around a finite circular cylinder (3D view and plan view) (a) $AR > criticalAR$, (b) $AR \leq criticalAR$ (from Kawamura et al. (1984)). . . . 8

2.2 Three-dimensional vortex topology surrounding an obstacle ($AR = 1$) at high relative submergence (from Pattenden et al. (2005)). 9

2.3 Three-dimensional vortex topology surrounding an obstacle ($AR = 2$) at high relative submergence (from Frederich et al. (2008)). 10

2.4 Time-mean velocity vectors in the plane of symmetry in front of a Rood wing at $Re = 6700$. Histogram of x-component velocity fluctuations at $x/T = 0.204$, $y/T = 0.0046$ inset. Bimodal flow zone for U velocity component enclosed by solid line (from Devenport and Simpson (1987b)). 12

2.5 Topological flow pattern over the free end surface, the overall vortical structure over the free end surface is comprised of the tornado-like vortices evolving from the two spiral nodes and the side tip vortices. The adjacent vortices are counter-rotating each other. The arrows (A) and (A') point out the down-wash flows (from Roh and Park (2003)). . . 13

2.6 Arch vortex in the wake flow around cylinder AR=1.25 to 10 (from Tanaka and Murata (1999)). 14

2.7 Non-dimensional, time-averaged, streamwise vorticity field in the wake of different aspect ratio cylinders in $x/D = 6$. a $AR = 9$. b $AR = 7$. c $AR = 5$. d $AR = 3$: no base vortices in low-aspect-ratio-cylinder. Vorticity contour increment 0.05, minimum vorticity contour ±0.05, solid lines represent positive (CCW) vorticity, dashed lines represent negative (CW) vorticity (from Sumner et al. (2004)). 15

2.8 Schematic illustration of the dominant sense of vortex in the wake of obstacles at $Re_D = O(100)$ (from Mason and Morton (1987)). 16

2.9 Model of the flow structure around a wall-mounted finite-length square cylinder: (a) symmetrically arranged two spanwise vortex roll, (b) staggered arranged spanwise vortex roll (from Wang and Zhou (2009)). . . . 17

2.10 Circular cylinder of $AR = 6$: Streamlines and velocity vectors in the lower part of the near wake (left) and near wake visualized with vortex cores and streamlines and velocity vectors in plane $y = 0$ (right). The velocity vectors are not to scale for clarity (from Krajnović (2011)). 18

2.11 Distribution of vorticity in the flow regime associated with a hemisphere 20

2.12 LDV measurements at one transverse plane in the wake of bump (from Byun and Simpson (2006)). 21

2.13 Illustration of flow structures on lee side of bump 22

2.14 The position of an arch vortex behind the hill 22

2.15 Mean velocity field around a low-aspect-ratio pyramid 23

2.16 Surface-flow patterns on the side faces for a low-aspect-ratio pyramid . 23

2.17 Vortex skeleton sketch for the flow around a low-aspect-ratio pyramid . 24

2.18 Proposed model for a wall-mounted sphere (Okamoto, 1980) 26

2.19 Horseshoe vortex behind the sphere observed by the tuft-grid method (Okamoto, 1980) 27

2.20 Flow visualization of the wall-mounted sphere ($\delta/D = 0.46$) using smoke-wire method: (a) $Re_D = 8.3 \times 10^4$, (b) $Re_D = 1 \times 10^4$ (Tsutsui, 2008). 28

2.21 Surface oil-flow patterns of the wall-mounted sphere ($\delta/D = 0.46$, $Re_D = 8.3 \times 10^4$ (Tsutsui, 2008) 29

2.22 Pressure distribution of the wall-mounted sphere and the plane ($\delta/D = 0.46$, $Re_D = 8.3 \times 10^4$ (Tsutsui, 2008) 30

2.23 Flow visualization of flow structure with laser illumination of Rhodamine dye injection technique around the smooth sphere at $Re_D = 5000$ (Ozgoren et al., 2012) 30

2.24 Proposed model for sphere supported by rod in the rear (Taneda, 1978) . 31

2.25 Perspective view of the experimental boulder section (top), and Plan view sketch of the ADV measurement locations (bottom). (Papanicolaou et al., 2012a) 32

2.26 Vertical profiles of u/u^* (left) and τ/u^{*2} (right) at different streamwise locations of sphere of $D = 40$ mm (Dey et al., 2011). 33

2.27 Comparison between the measured and simulated streamwise turbulent intensity profiles normalized with u^* from the boundary characteristics method for: (a) transect $0Dy$ (flume centerline), and (b) for transect $1Dy$ (from (Papanicolaou et al., 2012a). 34

2.28 Magnitude of the instantaneous vorticity vector (a) in a longitudinal plane, and (b) in a horizontal plane at half boulder height (Papanicolaou et al., 2012a). 35

2.29 Contours of the time-averaged streamwise vorticity together with vectors of the secondary flow around a boulder (sphere) with LES at locations: (a) $6Dx(x/dc = 6)$, and (b) $7Dx(x/dc = 7)$ where dc is boulder (clast) diameter (from (Papanicolaou et al., 2012a). 36

2.30 The enhanced upwash flow with growing boundary layer thickness . . . 38

2.31 Effect of boundary layer thickness on flow topology 39

2.32 Side view of time-averaged normalized vorticity contours upstream and downstream of the cylinder in $RS = 1$. The positive and negative contours are displayed with solid and dashed lines (Ozturk et al., 2008). 41

2.33 Mean flow around hemispherical fish habitat structures in shallow open channel flows 42

2.34 Plan view of the tests section for the: (a) d/d_{clast}= 3.5, (b) d/d_{clast}= 0.8, (from Papanicolaou and Kramer (2005)). 43

2.35 Spatial distributions are presented for experimental runs d/H=3.0, 2.5, and 2.0, and $x - y$ measurement planes $z^+ = 0.30$, 0.95, and 1.3: (a) Turbulent kinetic energy, k_e, in m^2/s^2, (b) Principal Reynolds shear stress $-\overline{u'w'}$ in N/m^2 (from Lacey and Rennie (2012). 53

2.36 Power spectral density function of pressure measurements for cylinder of $AR = 1$ 54

2.37 Spectral sequences for $TR = 7.5$ (top) and 3.73 (bottom). Curves are ordered vertically as indicated by the $z' = z/L$ values shown for each. The dashed line in follows the successive peaks which correspond to lower base frequency (Castro and Watson, 2004). 54

3.1 Mean velocity profile of boundary layer at high free stream turbulence flow on the plate at the location of the obstacle. z measured from the plate. 56

3.2 rms velocity profile at high free stream turbulence flow. z measured from the flume bed. 57

3.3 Longitudinal velocity auto-correlation function from PIV data 58

3.4 Plan view of head-box of the flume after overhaul 59

3.5 Mean velocity profile of boundary layer at low free stream turbulence flow on the plate at the location of the obstacle. z measured from the plate. 59

3.6 rms velocity profiles in the absence of the obstacle at low free stream turbulence. z measured from the plate. 60

3.7 Schematic of different level of relative submergence 60

3.8 Coordinate system definition and idealized mussel geometry. The streamwise configuration is shown. 62

3.9 Mussels location map 62

3.10 Photographs of a Threeridge (Amblema plicata) mussel shell collected from Pool 16 of the Upper Mississippi River near Fairport, IA. (a) side view (flow left to right), (b) upstream-looking view, (c) top view (flow top to bottom).) 63

3.11 Streamwise projections of obstacle cross sections 63

3.12 The boundary between separated and unseparated flow in the plane of the two nose shape parameters, axis ratio a/b and exponent n (Narasimha and Prasad, 1994). 64

3.13 Side view of PIV experimental setup. 65

3.14 Side view of thermal anemometry experimental setup. 65

3.15 Plan view of probe positions in thermal anemometry experiments. Dotted-line shows the access window cut into the upper plate to facilitate positioning of hot-film probes. 66

3.16 Locations of Reynolds shear stress measurement around the sphere. . . 66

3.17 Experimental DPIV measurement planes. 68

3.18 Intersection of $x-z$ and $y-z$ planes for Reynolds shear stress measurement around the sphere. Planes in figure are $x-z$ plane at y/D =-1 and $y-z$ plane at x/D =2 69

3.19 Cylindrical hot-film probe (TSI model 1210-20) 70

3.20 Two-point hot-film measurements 72

3.21 The orientation of the sensor in the flow 72

4.1 Mean streamlines upstream of the ellipsoids 76

4.2 Closer view of mean streamlines upstream of the transverse ellipsoid . . 76

4.3 Mean streamlines downstream of the obstacle in $d/H = 3.9$ 78

4.4 Isocontours of non-dimensional spanwise vorticity, ω_y^*, downstream of the obstacle in $d/H = 3.9$ 79

4.5 Isocontours of Reynolds shear stress, $-\overline{u'w'}/U^2$, downstream of the obstacle in $d/H = 3.9$ for: (a) streamwise ellipsoid, (b) transverse ellipsoid, (c) cylinder (AR=0.89) and (d) cylinder (AR=0.67) 80

4.6 Isocontours of non-dimensional turbulence intensities $(v'^2 + w'^2)/U^2$, downstream of the obstacle at $x/H = 1.5$ and d/H =3.9 for: (a) streamwise ellipsoid, (b) transverse ellipsoid, (c) cylinder (AR=0.89) and (d) cylinder (AR=0.67). 81

4.7 Isocontours of non-dimensional streamwise vorticity, ω_x^*, in the plane $x/H = 1$ at $d/H = 3.9$ for: (a) streamwise ellipsoid, (b) transverse ellipsoid, (c) cylinder (H/D=0.89), and (d) cylinder (H/D=0.67). Red shades indicate counter-clockwise rotation and blue shades indicate clockwise rotation. 82

4.8 Isocontours of non-dimensional streamwise vorticity, ω_x^*, in the plane $x/H = 1.5$ in $d/H = 3.9$ for: (a) Streamwise ellipsoid, (b) transverse ellipsoid, (c) cylinder (AR=0.89), and (d) cylinder (AR=0.67). Red shades indicate counter-clockwise rotation and blue shades indicate clockwise rotation. 83

4.9 Isocontours of non-dimensional streamwise vorticity, ω_x^*, in the plane $x/H = 2$ in $d/H = 3.9$ for: (a) Streamwise ellipsoid, (b) transverse ellipsoid, (c) cylinder (AR=0.89), and (d) cylinder (AR=0.67). Red shades indicate counter-clockwise rotation and blue shades indicate clockwise rotation. 84

4.10 Isocontours of non-dimensional streamwise vorticity, ω_x^*, in the plane $x/H = 3$ in $d/H = 3.9$ for: (a) cylinder (AR=0.67), (b) transverse ellipsoid. Red shades indicate counter-clockwise rotation and blue shades indicate clockwise rotation. 85

4.11 Isocontours of non-dimensional streamwise vorticity, ω_x^*, in the plane $x/H = 4$ in $d/H = 3.9$ for: (a) Cylinder (AR=0.67), (b) Transverse ellipsoid. Red shades indicate counter-clockwise rotation and blue shades indicate clockwise rotation. 85

4.12 Average dimensionless circulations of structures identified for ellipsoids in Fig. 4.7 to Fig. 4.9a and 4.9b, and the left/right deviation. 87

4.13 Average dimensionless circulations of structures identified for cylinders in Fig. 4.7 to Fig. 4.9c and 4.9d, and the left/right deviation. 88

4.14 Streamwise vorticity distribution, ω_x^*, with varying relative submergence for the transverse ellipsoid 89

4.15 Isocontours of non-dimensional streamwise vorticity distribution, ω_x^*, with varying relative submergence for the streamwise ellipsoid 90

4.16 Tip and base vortex strengths with varying relative submergence for streamwise and transverse ellipsoids. 91

4.17 Dye visualizations of the flow around the transverse ellipsoid at $Re_H = 5500$. (a) $d/H = 3.9$, (b) $d/H = 1$. 92

4.18 Mean streamlines in the wake of the streamwise and transverse ellipsoids at $d/H = 1$ 95

4.19 Isocontours of non-dimensional spanwise vorticity, ω_y^*, downstream of the obstacle in $d/H = 3.9$ at low free stream turbulence 97

4.20 Isocontours of Reynolds shear stress, $-\overline{u'w'}/U^2$, downstream of the obstacle in $d/H = 3.9$ for: (a) streamwise ellipsoid, (b) transverse ellipsoid low free stream turbulence 98

4.21 Isocontours of non-dimensional streamwise vorticity, ω_x^*, in the plane $x/H = 0.5$, 1, 1.5 (top to bottom) in $d/H = 3.9$ at low free stream turbulence intensity 0.3% for: (a) (c) (e) Streamwise ellipsoid, (b) (d) (f) transverse ellipsoid. Red shades indicate counter-clockwise rotation and blue shades indicate clockwise rotation. 100

4.22 Average dimensionless circulations of structures with FST=0.3% identified in Fig. 4.21 and the left/right deviation. 101

4.23 Isocontours of non-dimensional streamwise vorticity, ω_x^*, in the plane $x/H = 0.5$, 1, 1.5 (top to bottom) in $d/H = 3.9$ at low free stream turbulence intensity 0.3% for: (a) (c) (e) Cylinder (AR=0.89), (b) (d) (f) Cylinder (AR=0.67). Red shades indicate counter-clockwise rotation and blue shades indicate clockwise rotation. 102

4.24 Average dimensionless circulations of structures with FST=0.3% identified in Fig. 4.23 and the left/right deviation. 103

4.25 Proposed evolution of the arch structures for (a) the streamwise ellipsoid (self-induction dominated deformation) and b) the transverse ellipsoid (external shear dominated deformation). The arrows indicate the orientation of the vorticity vector. 106

4.26 Snapshots of dye visualizations of the transverse ellipsoid at $Re_H = 5500$ unveiling intermittent plunging of the shear layer by a time interval of 8 s. Inserted white arrows show plunge occurrence. 110

4.27 The power spectral density function, PSD, of the of the streamwise velocity component in $d/H = 3.9$ for transverse ellipsoid at $y/D = 1$: (a) $x/D = 1$, (b)$x/D = 2$ and (c) $x/D = 3$. Each spectrum is the average of 20 individual spectra. Spectra are off-set by constant factor for clarity. . . . 111

4.28 The power spectral density function Eu of the of the streamwise velocity component in $d/H = 3.9$ for streamwise ellipsoid at $y/D = 1$: (a) $x/D = 1$, (b)$x/D = 2$ and (c) $x/D = 3$. Each spectrum is the average of 20 individual spectra. Spectra are off-set by constant factor for clarity. . . . 111

4.29 The power spectral density function of the streamwise velocity component in $d/H = 3.9$ for cylindrs of AR=0.67 (left) and AR=0.89 (right) at $x/D = 1$ and $y/D = 1$. Each spectrum is the average of 20 individual spectra. Spectra are off-set by constant factor for clarity. 112

4.30 The power spectral density function of the streamwise velocity component in $d/H = 3.9$ for cylindrs of AR=0.67 in linear axis 113

4.31 Correlations of the fluctuating velocity for the transverse and streamwise ellipsoid 114

4.32 Spectral coherence $Coh_{u_1u_2}$ between streamwise fluctuating velocity u_1 and u_2 for (a) streamwise, and (b) transverse ellipsoid at $x = y = 1D$. u_1 was measured at $z/H = 0.2$ and u_2 was measured from $z/H = 0.4$ to 1 . . 116

4.33 The phase shift between u_1 and u_2 for transverse ellipsoid at $x = y = 1D$. u_1 was measured at $z/H = 0.2$ and u_2 was measured from $z/H = 0.4$ to 1. Results with u_2 at $z/H = 0.4$ have been illustrated as an example. . . . 117

4.34 Dependence of the phase angle $\phi_{u_1u_2}(fs)$ between streamwise fluctuating velocities u_1 and u_2 at $x/D = 1$ and $y/D = 1$ at varying spanwise locations, where u_1 was measured at $z/H = 0.2$ and u_2 was measured from $z/H = 0.4$ to 1. (a) Streamwise ellipsoid, (b) Transverse ellipsoid. . 118

4.35 Isocontours of non-dimensional streamwise vorticity, ω_x^*, in the plane $x/H = 0.56$ and 0.75 at $d/H = 1$ for: (a) streamwise ellipsoid, (b) transverse ellipsoid. Red shades indicate counter-clockwise rotation and blue shades indicate clockwise rotation. 119

4.37 Isocontours of non-dimensional streamwise vorticity, ω_x^*, in the plane $x/H = 1.5$ in $d/H = 1$ for: (a) Streamwise ellipsoid, (b) transverse ellipsoid.Red shades indicate counter-clockwise rotation and blue shades indicate clockwise rotation 120

4.38 IIsocontours of non-dimensional streamwise vorticity, ω_x^*, in the plane $x/H = 2$ in $d/H = 1$ for: (a) Streamwise ellipsoid, (b) transverse ellipsoid. Red shades indicate counter-clockwise rotation and blue shades indicate clockwise rotation. 121

4.41 The power spectral density function of the streamwise velocity component at $d/H = 1$ for: (a) streamwise ellipsoid, (b) transverse ellipsoid, (c) cylinder ($H/D = 0.67$), (d) cylinder ($H/D = 0.89$) at $x/D = 1$ and $y/D = 1$. Each spectrum is the average of 20 individual spectra. Spectra are off-set by constant factor for clarity. 124

4.42 Auto- and cross-correlation of fluctuating velocity on opposite side for transverse ellipsoid an $d/H = 1$ 125

4.43 Auto- and cross-correlation of fluctuating velocity for streamwise ellipsoid at d/H=1 126

5.1 Mean streamlines of the sphere: (a) upstream (b) downstream. 128

5.2 Time-averaged, streamwise velocity, u, profiles along the centerline at $y/D = 0$ 129

5.3 Isocontours of nondimensional spanwise vorticity, ω_y^*, downstream of the sphere. Red shades indicate clockwise rotation and blue shades indicate counter-clockwise rotation. 129

5.4 Isocontours of nondimensional spanwise vorticity, ω_y^*, upstream and downstream of the sphere using the laser under the flume. Red shades indicate clockwise rotation and blue shades indicate counter-clockwise rotation. 130

5.5 Isocontours of Reynolds shear stress, $-\overline{u'w'}/U^2$, downstream of the sphere. 132

5.6 Streamwised turbulence intensity profiles at $y/D = 0$ 133

5.7 Streamwised turbulence intensity profiles at $y/D = -1$ 133

5.8 Time-averaged, wall-normal velocity, w, profiles along the centerline at $y/D = 0$ 134

5.9 Isocontours of non-dimensional streamwise vorticity, ω_x^*, in the plane $x/D = 0$, 0.2, 0.4, 0.5, 0.6, 0.7, 0.8, and 1 (left to right and top to bottom) in $d/H = 3.5$. Red shades indicate counter-clockwise rotation and blue shades indicate clockwise rotation. 136

5.10 Isocontours of non-dimensional streamwise vorticity, ω_x^*, in the plane $x/D = 1.2$, 1.6, 2, and 2.5 (left to right and top to bottom) in $d/H = 3.5$. Red shades indicate counter-clockwise rotation and blue shades indicate clockwise rotation. 137

5.11 Average dimensionless circulations of structures identified for the sphere in Fig. 5.9c to Fig. 5.9f and the left/right deviation. 138

5.12 The power spectral density function of the of the streamwise velocity component in $d/H = 3.5$ for sphere at $y/D = 1$: (a) $x/D = 1$, (b) $x/D = 2$, and (c) $x/D = 3$. Each spectrum is the average of 20 individual spectra. Spectra are off-set by constant factor for clarity. 140

5.13 Cross-correlation of fluctuating velocity on opposite side for the sphere at $x/D = 1$ and $y/D = \pm 1$ and $z/H = 0.25$ to 1. 141

5.14 Existence of horseshoe lobes on the side of the sphere: (a) Horseshoe vortex behind the sphere observed by the tuft-grid method (Okamoto, 1980), (b) Isocontours of non-dimensional streamwise vorticity, ω_x^*, in the plane $x/D = 0.5$ in $d/H = 3.5$. Red shades indicate counter-clockwise rotation and blue shades indicate clockwise rotation 143

5.15 Mean streamwise velocity profile, u, upstream of the sphere at $y/D = 0$ and $x/D = -1.1$ to -0.4 143

5.16 Proposed evolution of the arch structures for the sphere (self-induction dominated deformation). The arrows indicate the orientation of the vorticity vector. 144

5.17 Distribution of velocity vector at $y = 0$ and $x/D = 0.5$ to 3. 145

5.18 Time-averaged, streamwise velocity, u, profiles at $y = 0$ and $x/D = 0.5$ to 3146

5.19 Time-averaged, streamwise velocity, u, profiles at $y/D = -0.25$ 147

5.20 Time-averaged, streamwise velocity, u, profiles at $y/D = -0.5$ 147

5.21 Time-averaged, streamwise velocity, u, profiles at $y/D = -0.25$ 148

5.22 Time-averaged, streamwise velocity, u, profiles at $y/D = -1$ 148

5.23 Time-averaged transverse velocity, v, profiles at $x/D = 0.5$ to 3 at $y = 0$. 149

5.24 Turbulent projected shear stress at $y = 0$ and $x/D = 0.5$ to 3 150

5.25 Turbulent projected shear stress at $y/D = -0.25$ and $x/D = 0.5$ to 1.5 . . . 151

5.26 Turbulent projected shear stress at $y/D = -0.5$ and $x/D = 0$ to 1.5 151

5.27 Turbulent projected shear stress at $y/D = -1$ and $x/D = 0$ to 1.5 152

5.28 Mean shear stress at $y = 0$ and $x/D = 0.5$ to 3 152

5.29 Mean shear stress at $y/D = -0.25$ and $x/D = 0.5$ to 1.5 153

5.30 Mean shear stress at $y/D = -0.5$ and $x/D = 0$ to 1.5 154

5.31 Mean shear stress at $y/D = -0.75$ and $x/D = 0$ to 1.5 154

5.32 Mean shear stress at $y = 0$ and $x/D = 0.5$ to 3 155

5.33 Contour plot of mean shear stress at $y = 0$ to -1 and $x/D = 0$ to 3 156

5.34 Total shear stress at $y = 0$ and $x/D = 0.5$ to 3 156

5.35 Total shear stress at $y/D = -0.25$ and $x/D = 0.5$ to1.5 157

5.36 Total shear stress at $y/D = -0.5$ and $x/D = 0$ to1.5 157

5.37 Total shear stress in streamwise direction at $y = 0$ and $x/D = 0.5$ to 3 . . 158

5.38 Total shear stress in streamwise direction at $y/D = -0.25$ and $x/D = 0.5$ to1.5 159

5.39 Total shear stress in streamwise direction at $y/D = -0.5$ and $x/D = 0$ to1.5159

5.40 Total shear stress in streamwise direction upstream of the sphereat $y/D = 0$ and $x/D = -1.1$ to -0.4 160

5.41 Average vertical profiles of shear stress estimated from Reynolds method over plexiglas with ADV 161

5.42 Contour plot of bed shear stress, τ_0, in z/D =0.035 at x/D = 0.5 to 3 and $y = 0$ 162

6.1 Graphic chart of future work for dynamic shedding behavior 168

6.2 An experimental setup for low relative submergence for upstream view at the open channel tests 169

6.3 An experimental setup for plan view measurement at low relative submergence for the open channel tests 169

CHAPTER 1
INTRODUCTION

Wall-mounted bodies in boundary layer flows are ubiquitous in nature and engineering applications such as nacelles and control surfaces on aircraft and underwater vehicles, buildings and exhaust stacks, bivalves inhabiting river beds and the ocean floor, and boulders, clusters and fish habitat structures in fluvial environments. Despite their geometric simplicity, a single wall-mounted obstacle in a boundary layer or channel flow creates an extremely complex, highly three-dimensional and unsteady flow field for which the transport mechanisms of momentum and scalars are still not well-understood (e.g. Martinuzzi and Tropea (1993); Palau-Salvador et al. (2009)). It is now understood that the flow field about a wall-mounted body is composed of a number of constituent vortex structures which are qualitatively robust for different obstacle geometries (Pattenden et al., 2005; Palau-Salvador et al., 2009) and interactions between these structures result in very large oscillations, making shedding characteristics significant to transport in this flow (Vlachos and Hajj, 2002). These local flow patterns around each obstacle, resulting from an interaction between the obstacle and the surrounding flow field, affect local transport of mass and momentum. An improved knowledge of the flow will provide insight into the related momentum, mass, and heat transfer processes in the vicinity of the body.

1.1 Motivation

The dissertation has been motivated by the need to better understand the fundamental fluid mechanics of the following topics:

1. Transport mechanisms in freshwater mussel populations.

2. Sediment transport in steep mountain streams and characterizing the effects of relative submergence (the ratio of flow depth to obstacle height, d/H) on flow-obstacle interaction such as bed shear stress distributions and mean flow.

Toward those ends, this dissertation presents a fundamental study of semi-ellipsoidal wall-mounted obstacle (representative of a fresh water mussel) and a spherical obstacle (representative of a bolder in a fluvial environment). To provide a basic understanding of these flows, flow structure and shedding characteristics are examined.

The importance of the first motivation is consideration of freshwater mussels as filter feeders. Mussels live at the water-sediment interface as shown in Fig. 1.1 and are believed to have a significant effect on water quality since they collectively process very large volumes of water. In recent years, the level of nitrogen concentration in the Mississippi River has elevated noticeably (Turner et al., 2008). The rise is due to the increased plantation of corn in the upper Midwest region, aimed at biofuel production as reported in National Center for Environmental Assessment (NCEA, 2011).

Freshwater mussels have historically existed in large quantities in the Upper Mississippi River (UMR). However, their populations have been declining substantially over the past several decades, mirroring the decline in the general health of the river due to factors which include overharvesting, destruction of habitats (e.g. the development and maintenance of locks and dams on the Mississippi River), pollution, and the introduction of invasive species (Strayer et al., 2004).

The local flow patterns around each mussel, which result from interaction between the mussel and the surrounding flow field, affect nutrient availability to the mussel in a competitive environment, and therefore contribute to the turbulent entrainment of nutrients into the benthic boundary layer, where nutrients are depleted due to consumption.

For the first motivation study, semi-ellipsoids, broadly representative of a freshwater mussel projecting from a river bed, have been considered. In the process of exploring these phenomena, the structures (vortices) have been observed in the

Figure 1.1: Freshwater mussel on the river bed (internetstones.com)

mean flow, and a high degree of control over the presence and strength of these vortices is demonstrated with changes in obstacle geometry. This serendipitous discovery of flow structure manipulation has led to the fundamental investigation that will be presented in this thesis and introduces an ellipsoidal geometries likely as a useful canonical geometry.

In addition to unique findings in the controlling flow pattern, this study differs from similar investigations in the geometry used for the experiments. Most investigations around bluff bodies have focused on isolated structures i.e. cylindrical or prismatic bodies which have flat tops with sharp edges and thus well-defined separation lines. Ellipsoids are more aerodynamically-shaped and align themselves with the flow. This study is, therefore, unique in its findings as they apply to ellipsoid-shaped obstacles.

The second motivation is the existence of varying relative submergences in mountain streams which yield strikingly different sediment depositional patterns. In steep mountain streams (Fig. 1.2), naturally-occurring obstacles or boulders have length scales comparable with flow depth and river width, introducing a parameter named relative submergence, d/H, (where d is the flow depth and H is the obstacle characteristic dimension). Findings in this area will give more insight on bed shear

Figure 1.2: Steep mountain stream (Rocky Mountain river, Photo by: Rolf Hicker)

stress distributions, mean flow, and sediment depositional patterns surrounding the obstacle and will elucidate the physical mechanisms governing these processes. It may also help in the prediction of sediment transport in mountain stream.

The flow regimes that exist for the different relative submergences, especially when $d/H < 1$, are suspected to have a large effect on the depositional patterns compared with large d/H and rates of sediment. Papanicolaou and Kramer (2005) have shown (Fig. 1.3) effects of different regimes of relative submergence on sedimentation and depositional patterns due to significant change in flow structures. Further insight into the dominant flow structures can provide us with valuable knowledge on prevalent issues of engineering including finding bed shear stress distribution and cluster formation.

1.2 Thesis Objectives and Overview

In this thesis, the mean and dynamics of streamwise vorticity around low-aspect-ratio wall-mounted obstacles were investigated. Experiments were conducted to examine the effects of shape and relative submergence on the wakes of different low-aspect-ratio wall-mounted obstacles such as semi-ellipsoids (broadly representative of a freshwater mussel projecting from a river bed) and a sphere (representative of a boulder). Particle Image Velocimetry (PIV) and thermal anemom-

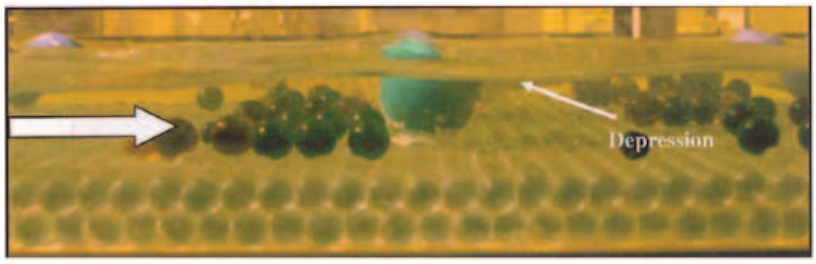

(a) Low Relative Submergence

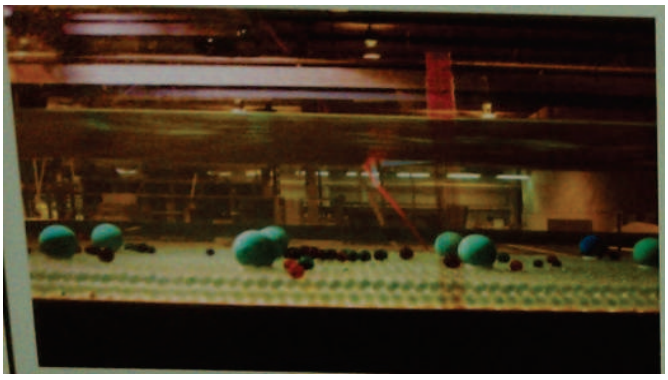

(b) High Relative Submergence

Figure 1.3: Effect of relative submergence (RS) on depositional pattern: (top) LRS-Low Relative Submergence-where particles deposit at the upstream face of the clast, (bottom) HRS-High Relative Submergence-where particles deposit at the wake of the clast (Papanicolaou and Kramer, 2005)

etry were employed to interrogate the flow. The sensitivity of the mean wake vorticity distribution to obstacle shape and relative submergence, quantified in this study, provides controls with which to further probe the dynamics of wake structures and the related transport mechanisms.

To simplify the governing physics and despite boulders existing in an open-channel environment, the experiments were conducted in a boundary layer flow. This approach was taken in order to simplify the flow field and provide a benchmark for further work. This approach also facilitates comparison with previous work which has most often been conducted in boundary layer flows. Equally important, this work aims at making fundamental contributions to the understanding

of the flow field surrounding a wall-mounted obstacle, particularly focusing on the evolution of flow structure with variation in shape and flow parameters such as relative submergence.

Chapter 2 reviews the related research in the literature and discusses the mean and dynamics of flow around low and high-aspect-ratio obstacles and controversies related to conditions under which base vortices are observed in the wake of obstacles. Chapter 3 describes the experimental methods and measurement techniques. The streamwise features observed in the mean wake and their shedding behavior for ellipsoidal and spherical geometries are demonstrated in Chapter 4 and 5, respectively. In addition, the fact that relatively subtle changes in geometry can provide such dramatic changes in flow patterns has implications for the transport of momentum and scalars in applications of flow around wall-mounted bodies. Based on the findings of the experiments, a vortex skeleton model is proposed for ellipsoids which is supported by spectral analysis at the flow field. This vortex skeleton model was found to be also largely applicable to the wake of the sphere, with some modification to take into account the convex geometry of the sphere at its interface with the base plane. Local bed shear stress measurements, estimated from Reynolds stress, have been computed in the wake of the sphere to provide insight into the sediment depositional patterns surrounding the obstacle. The bed shear stress measurements reveal that two areas at the side and close to reattachment length have the higher values. Finally, Chapter 6 includes conclusions and suggestions for future work.

CHAPTER 2
LITERATURE REVIEW

2.1 Flow Structure in the Wake of a Wall-Mounted Bluff Body

Wall-mounted obstacles are ubiquitous in a broad range of natural and engineered systems. Nevertheless, there are many aspects of this class of flows that are still poorly understood due to the complexity of the resulting highly three-dimensional unsteady flow and the sensitivity to a relatively large number of parameters including Reynolds number, obstacle characteristic length, aspect ratio, boundary layer characteristics, and free stream turbulence (Baker, 1980; Martinuzzi and Tropea, 1993).

2.2 Mean Flow Structure

The flow around two-dimensional cylindrical obstacles have been studied extensively. The characteristic of this flow include periodic alternate vortex shedding from the sides of the obstacle, which form the Kármán vortex street. In general, the behavior in the wake of a circular cylinder with finite height (one end free and the other fixed on the ground) is markedly different from that of two-dimensional bluff bodies (Etzold and Fiedler, 1976; Kawamura et al., 1984; Okamoto and Sunabashiri, 1992; Sumner et al., 2004). Several investigations have unveiled that the near wake of wall-mounted bodies depend on aspect ratio, $AR = H/D$, where H and D are the height and the characteristic width of a obstacle, respectively (Sakamoto and Arie, 1983; Kawamura et al., 1984; Okamoto and Sunabashiri, 1992; Sumner et al., 2004; Wang and Zhou, 2009). When H/D is less than critical value, vortex shedding changes from the anti-symmetrical Kármán type to the symmetric arch type as illustrated by Kawamura et al. (1984) in Fig. 2.1. For large-aspect-ratio cylindrical geometries Kármán shedding is frequently observed in the base region for sufficiently high aspect ratios, whereas symmetric shedding is present at the tip. The

minimum aspect ratio required for the existence of quasi-two-dimensional regions of Kármán shedding has been found to vary widely – between 1 and 7 in a range of studies (Sakamoto and Arie, 1983; Kawamura et al., 1984; Uematsu et al., 1990; Okamoto and Sunabashiri, 1992; Fox and West, 1993a,b; Sumner et al., 2004; bib; Frederich et al., 2008; Sumner and Heseltine, 2008; Palau-Salvador et al., 2009).

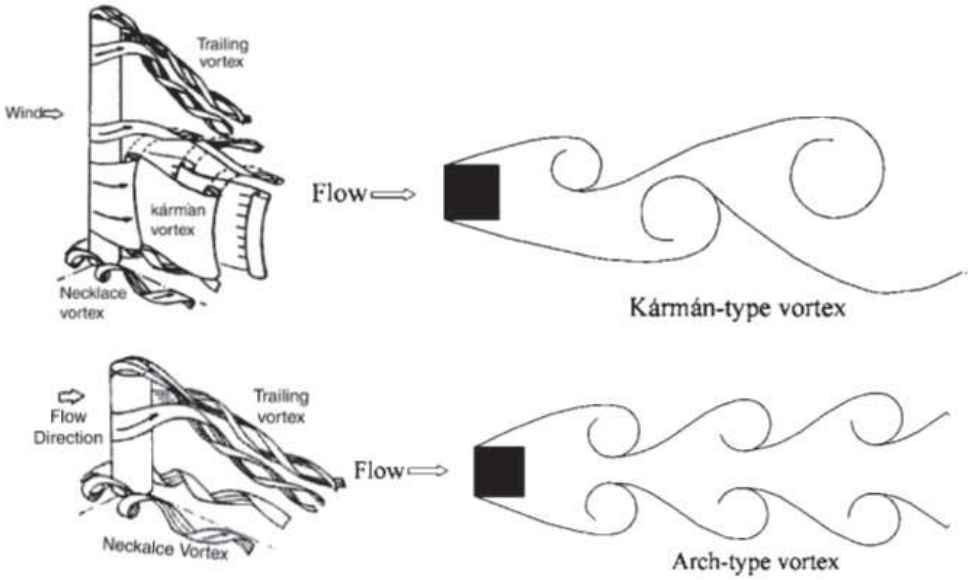

Figure 2.1: Flow around a finite circular cylinder (3D view and plan view) (a) $AR > criticalAR$, (b) $AR \leq criticalAR$ (from Kawamura et al. (1984)).

Fewer investigations have considered the flow structure in the wake of low-aspect-ratio wall-mounted obstacles. The mean flow in the near wake of the low-aspect-ratio obstacle is characterized by three dominant features that are qualitatively robust, as illustrated by Pattenden et al. (2005) in Fig.2.2: 1) a horseshoe vortex that forms at the junction between the obstacle and ground plane upstream of the obstacle, with legs that wrap around the obstacle and become primarily streamwise in the wake; 2) the streamwise tip vortices that appear to emerge from

the vicinity of the free end, and 3) the arch vortex consisting of the mean spanwise vortices shed from the obstacle sides, connected near the free end. Further downstream, the tip structures and horseshoe legs combine near the ground plane with vorticity generated due to the impingement of the downwash on the base plane to form large streamwise structures called the trailing vortices (Pattenden et al., 2005).

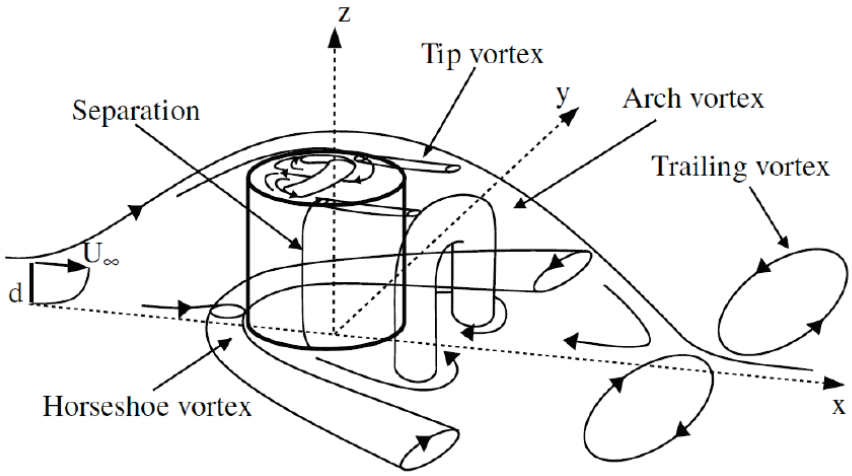

Figure 2.2: Three-dimensional vortex topology surrounding an obstacle ($AR = 1$) at high relative submergence (from Pattenden et al. (2005)).

Another mean flow pattern in the near wake of the low-aspect-ratio circular cylinder ($AR = 2$) has been proposed by Frederich et al. (2008) as shown in Fig.2.3 which is in agreemnt with Pattenden et al. (2005)'s model; however, the arch vortex has been presented differently. Frederich et al. (2008) showed the flow on the cylinder shell separates close to 80°, starting to generate a typical alternate vortex shedding. This vortex street is disturbed massively by the flow over the free end, and their combination leads to a recirculation arch vortex with tornado-like regions downstream of the cylinder.

A pair of streamwise vortex structures of opposite sign to the tip and horseshoe

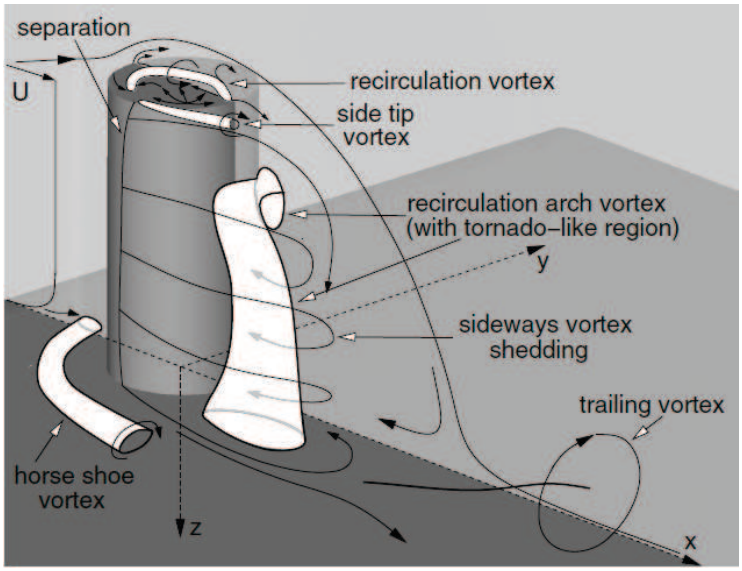

Figure 2.3: Three-dimensional vortex topology surrounding an obstacle ($AR = 2$) at high relative submergence (from Frederich et al. (2008)).

structures may also be found in the wake close to the ground plane, which induce an upwash on the symmetry plane of the wake (Etzold and Fiedler, 1976; Mason and Morton, 1987; Sumner et al., 2004; Wang and Zhou, 2009). However, these structures, often referred to as *base* vortices (Sumner et al., 2004), are much less robust than the other wake constituents and are frequently not observed.

2.2.1 Horseshoe Vortices

The dynamics and spatial extent of the horseshoe vortex system upstream of the obstacle depends on the ground plane boundary layer thickness, the cross-flow Reynolds number based on the obstacle diameter (or the boundary layer thickness), and the height and geometry of the obstacle (Baker, 1979, 1980; Seal et al., 1995; Ballio et al., 1998; Simpson, 2001). The dynamics of the horseshoe vortex upstream of the body have been studied extensively, and it is well-established that the horseshoe system may be comprised of several vortices evolving in a repetitive cycle of horseshoe vortex system formation, amalgamation, and decay (e.g. (Baker,

1979, 1980)).

Several investigations reported the existence of a bimodal velocity probability distribution function in the junction region upstream of the body as shown in Fig. 2.4, associated with very large turbulent stresses (Devenport and Simpson, 1987a,b, 1990; Dargahi, 1989; Larousse et al., 1991; Martinuzzi and Tropea, 1993; Olçmen and Simpson, 1997). Devenport and Simpson (1990) attributed the behavior to the intermittent entrainment of low-momentum boundary layer structures in the corner region between the wall and leading edge. Seal et al. (1995) and Paik et al. (2007) demonstrated that the primary vortex in the horseshoe vortex system (adjacent to the obstacle) is annihilated through the entrainment and mixing with opposite-sign vorticity lifted from the bed surface, and then replaced by the vortex advancing behind it. There has been little quantitative agreement in the literature about the relationship between flow parameters (e.g. Reynolds number) and the number of vortices present in the horseshoe system and their behavior, but most of the studies agree that the unsteadiness in the vortex system in front of the obstacle is independent of vortex shedding in the wake (Ballio et al., 1998; Wang and Zhou, 2009). However, Fu and Rockwell (2005); Rockwell (2008) showed that for very shallow flows there is interdependency between the horseshoe vortex oscillations upstream of the obstacle and vortex shedding in the wake.

The present work primarily focuses on the flow downstream of the obstacle. In particular, for the low-aspect-ratio obstacles investigated in this study, tip and base structures have been observed in the mean flow, and a high degree of control over the presence and strength of these vortices is demonstrated with changes in obstacle geometry and relative flow depth. In the following paragraphs, research on the origins, geometric characteristics, and dynamics is reviewed.

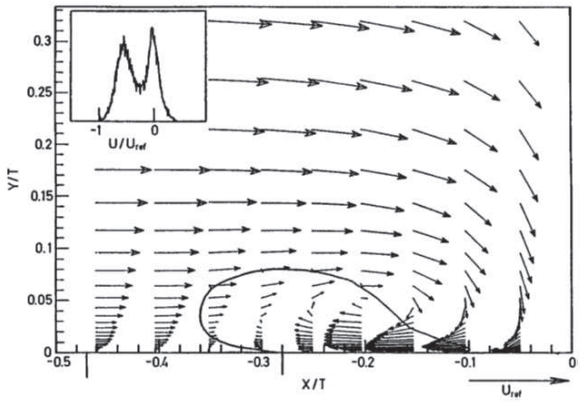

Figure 2.4: Time-mean velocity vectors in the plane of symmetry in front of a Rood wing at $Re = 6700$. Histogram of x-component velocity fluctuations at $x/T = 0.204$, $y/T = 0.0046$ inset. Bimodal flow zone for U velocity component enclosed by solid line (from Devenport and Simpson (1987b)).

2.2.2 Tip Vortices

In the mean flow, the tip vortices emerge from the free end of the obstacle and induce a downwash in the wake. Significant consideration has been given to the flow topology over the free end (Kawamura et al., 1984; Roh and Park, 2003; Park and Lee, 2004; Pattenden et al., 2005; Hain et al., 2008; Krajnović, 2011). Two foci are generally observed on the free end of flat-tipped finite cylinders, which were proposed by Roh and Park (2003); Hain et al. (2008) as shown in Fig. 2.5 to be the origins of the tip vortices; however, several other studies (Kawamura et al., 1984; Pattenden et al., 2005; Palau-Salvador et al., 2009; Krajnović, 2011) indicated that these foci are independent of the tip vortices and are rather connected to each other to form an arch within the recirculation region on top of the cylinder. These studies suggest that the tip vortex structures emerging from the free end are formed by the separation of the upwash flow at the sides of the cylinder.

The question has been raised as to whether the tip vortices are then continuous structures such as in the wakes of steady lifting bodies, or if they are intermittent (Sumner et al., 2004). Several recent studies have suggested that the tip vortices

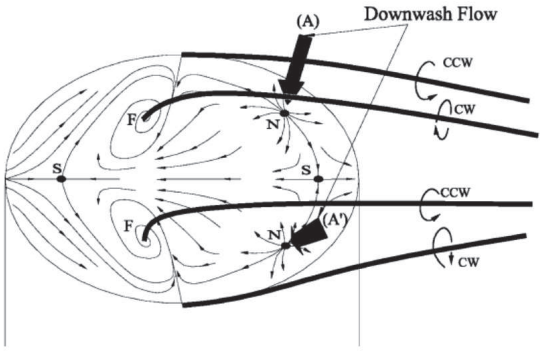

Figure 2.5: Topological flow pattern over the free end surface, the overall vortical structure over the free end surface is comprised of the tornado-like vortices evolving from the two spiral nodes and the side tip vortices. The adjacent vortices are counter-rotating each other. The arrows (*A*) and (*A'*) point out the down-wash flows (from Roh and Park (2003)).

emerging from the free ends of circular cylinders are often not apparent in instantaneous realizations of the flow, suggesting that they are not continuous streamwise structures (Pattenden et al., 2002; Hain et al., 2008; Krajnović, 2011). In fact, Hain et al. (2008) and Krajnović (2011) have observed instantaneous counter-rotating vortex pairs spatially coincident with the mean tip vortices near the free end of the cylinder. Furthermore, several studies of circular and square cylinders have proposed the streamwise tip vortices to result from the streamwise tilting of other structures previously thought to be distinct. For example, Tanaka and Murata (1999) used time-averaged measurements of the mean velocity field to support their assertion that the tip structures are consistent with the tilting of the tips of the arch structures in the upstream direction as shown in Fig. 2.6. Wang and Zhou (2009) used particle image velocimetry and thermal anemometry to deduce that the instantaneous structures are indeed a result of tilted spanwise vortices which intermittently switch between asymmetric (Kármán) and symmetric shedding. On the other hand, Bourgeois et al. (2011b) used phase-averaged PIV measurements to show that in the wake of their square prism of aspect ratio 4, only Kármán shedding

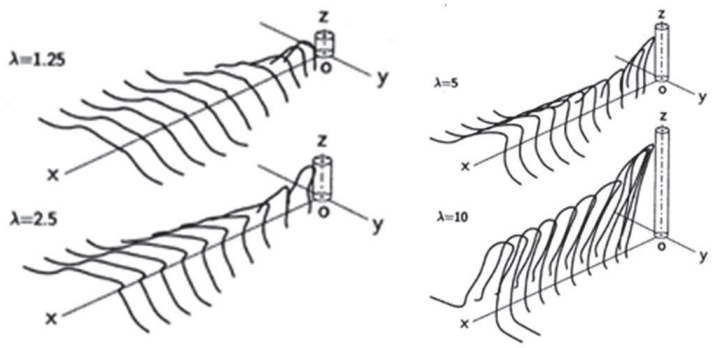

Figure 2.6: Arch vortex in the wake flow around cylinder AR=1.25 to 10 (from Tanaka and Murata (1999)).

was present, and that the mean tip structures are explained by quasi-streamwise vortex filaments connecting the Kármán vortices.

2.2.3 Base Vortices

In some cases, usually in the wakes of high-aspect-ratio geometries and where the boundary layer is not too thin (Etzold and Fiedler, 1976; Wang and Zhou, 2009), a streamwise vortex pair of opposite sign to the tip vortex pair may be observed in the mean flow near the ground plane (Mason and Morton, 1987; Sumner et al., 2004; Wang and Zhou, 2009) as shown in Fig. 2.7. The base vortex is not as robust a feature of wall-mounted bluff-body wakes as the tip and horseshoe structures, and the conditions of its existence are not well-understood.

Mason and Morton (1987) performed qualitative visualizations of the flow structure around low-aspect-ratio obstacles in steady flow at $Re_D = O(100)$, and noted that the wake was dominated by a streamwise vortex pair that may either induce upwash or downwash in the wake as shown in Fig. 2.8. At such low Reynolds number, they demonstrated that the upwash flow was generated by the tilting of vorticity generated in the region of adverse pressure gradient upstream of the obstacle to form a vortex similar, but of opposite sign to the horseshoe vortex. They

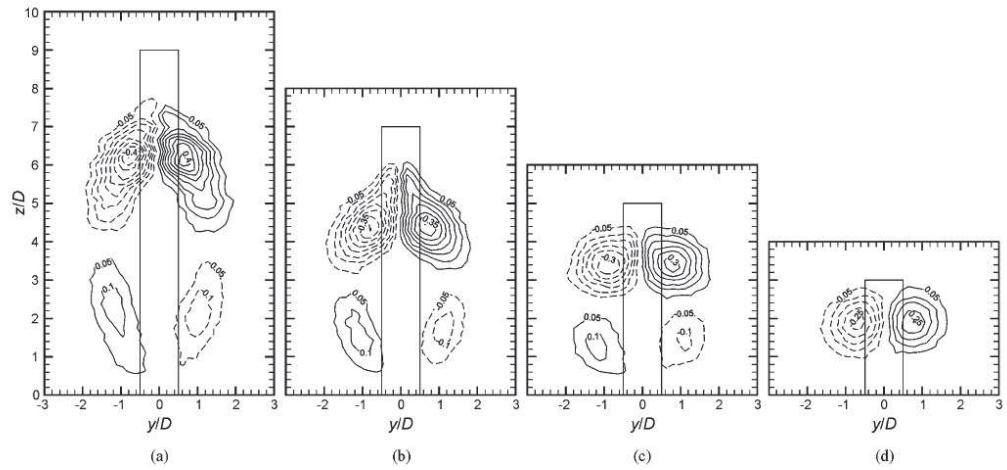

Figure 2.7: Non-dimensional, time-averaged, streamwise vorticity field in the wake of different aspect ratio cylinders in $x/D = 6$. a $AR = 9$. b $AR = 7$. c $AR = 5$. d $AR = 3$: no base vortices in low-aspect-ratio-cylinder. Vorticity contour increment 0.05, minimum vorticity contour ±0.05, solid lines represent positive (CCW) vorticity, dashed lines represent negative (CW) vorticity (from Sumner et al. (2004)).

proposed an empirical rule based on their observations: wide obstacles (aspect ratio ≤ 1), which direct more flow over their crest, produce a dominant vortex pair with a central upwash (i.e. a base vortex), while tall, narrower obstacles (aspect ratio ≥ 1), in which the flow is preferentially directed around the sides produce a dominant vortex pair with central downwash (i.e. a tip vortex).

The criteria of Mason and Morton (1987) are the converse of those proposed for flows of $Re_D = O(10^4)$ and higher over cylindrical bodies, suggesting that these vortices are generated by a fundamentally different mechanism. In studies where obstacle aspect ratio was varied and a base vortex was observed, the strength of the base vortex has been shown to be directly related to aspect ratio and inversely-related to downstream distance from the obstacle. For example, Wang and Zhou (2009) found a monotonic decrease in base vortex strength as the aspect ratio of their square prism was reduced from 7 to 3, and Sumner et al. (2004) made a similar observation when varying the aspect ratio of a circular cylinder between 9 and 3.

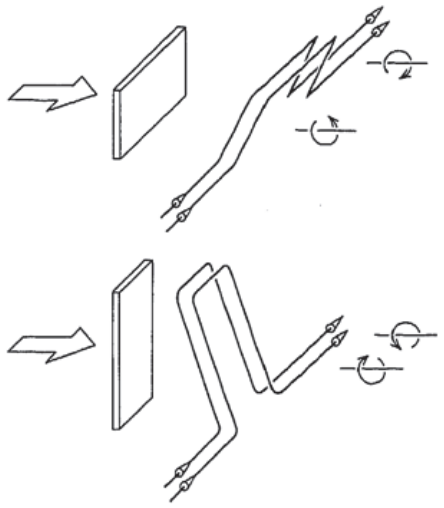

Figure 2.8: Schematic illustration of the dominant sense of vortex in the wake of obstacles at $Re_D = O(100)$ (from Mason and Morton (1987)).

In the work of Wang and Zhou (2009), the base structure was observed at $x/d = 1$ and 3 (where x is the streamwise distance measured from the center of the obstacle and d is the obstacle width), but not at $x/d = 5$. Likewise, the measurements of Sumner et al. (2004) revealed no base structure at $x/d = 6$.

The most frequent explanation cited in the literature for the existence of the base structures in the wakes of large-aspect-ratio obstacles is that, in the same manner as the tip vortices, they are projections of deformed spanwise vortices shed from the sides of the obstacle and are therefore not continuous streamwise structures. Mean vortex lines assembled by Tanaka and Murata (1999) were shown to be curved near the ground plane in addition to the free end, thus also accounting for the observed base structures. In addition, both Etzold and Fiedler (1976) and Wang and Zhou (2009) modeled the base vortex as the projection of inclined spanwise vortices near the wall. Sumner et al. (2004) hypothesized that the base vortices were, in particular, projections of Kármán vortices since they occurred under conditions when velocity spectra suggested the existence of Kármán shedding. Wang

and Zhou (2009) used PIV in multiple planes to capture instantaneous streamwise projections of symmetric and anti-symmetric shed vortices from high-aspect-ratio prismatic obstacles as shown in Fig. 2.9, demonstrating that such structures could, in fact, account for both the tip and base structures observed in the mean. Alternatively, the large eddy simulation (LES) reported by Krajnović (2011) for circular cylinder of $AR = 6$ revealed the streamwise base vortices to be joined through a transverse discrete vortex located in the base region near the wall as shown in Fig. 2.10. As seen in Fig. 2.10(right), the flow in the symmetry plane moves towards the cylinder near the ground and bends down after the stagnation point, forming the N_w vortex (base vortex). In the symmetry plane downstream of vortex N_w, a focus, F_{nw}, and a saddle point, S_{nw}, are visible in Fig. 2.10 (right), indicating the closure of the separation region in the near wake.

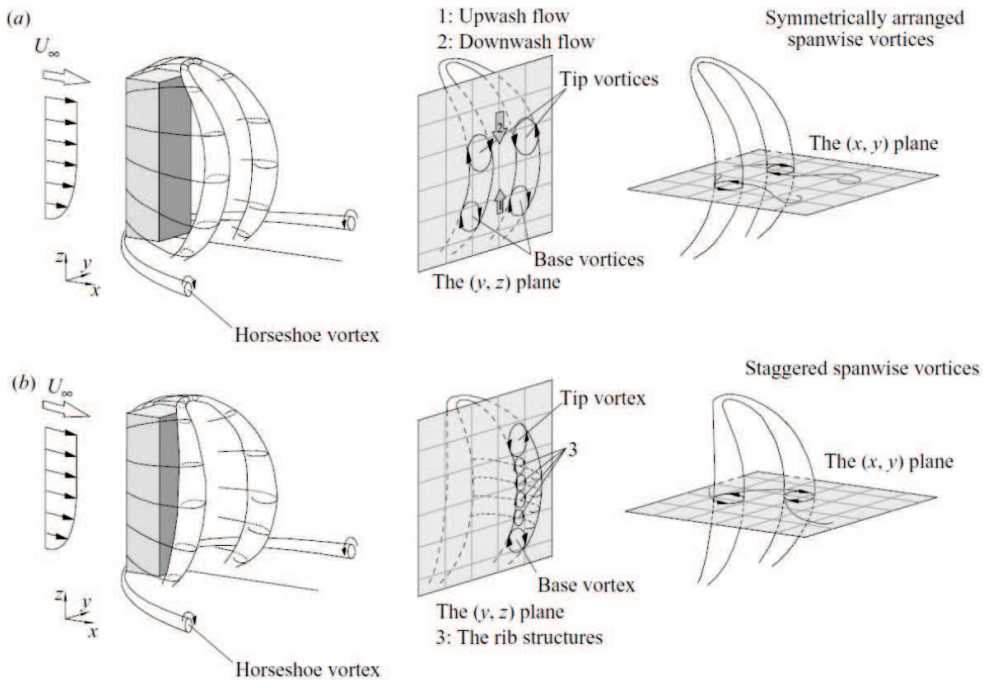

Figure 2.9: Model of the flow structure around a wall-mounted finite-length square cylinder: (a) symmetrically arranged two spanwise vortex roll, (b) staggered arranged spanwise vortex roll (from Wang and Zhou (2009)).

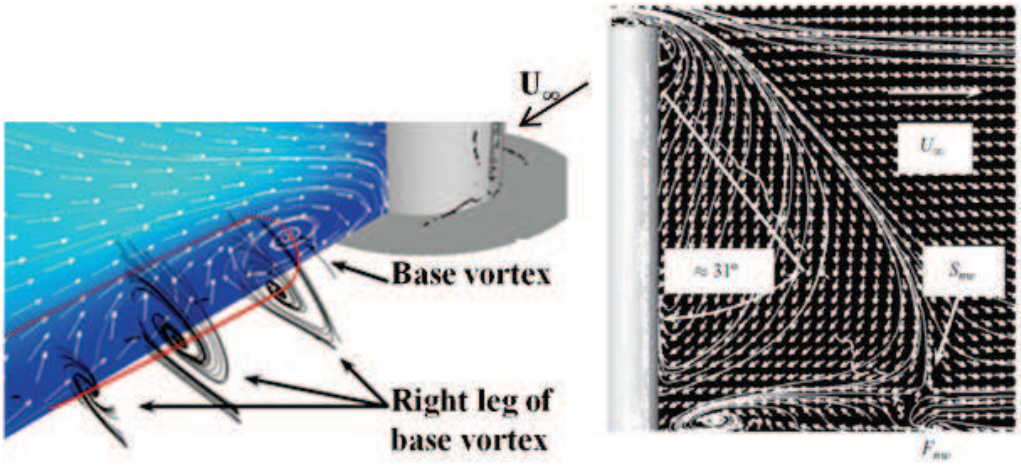

Figure 2.10: Circular cylinder of $AR = 6$: Streamlines and velocity vectors in the lower part of the near wake (left) and near wake visualized with vortex cores and streamlines and velocity vectors in plane $y = 0$ (right). The velocity vectors are not to scale for clarity (from Krajnović (2011)).

2.3 Effects of Obstacle Shape

While most investigations of the flow structure generated by wall-mounted obstacles have focused on circular cylinders and prisms, as suggested by the collection of literature described above, other geometries have been investigated. These include hemispheres and spheres (Okamoto, 1980; Savory and Toy, 1986, 1988; Shamloo et al., 2001; Strom and Papanicolaou, 2007; Tsutsui, 2008; Papanicolaou et al., 2011; Ozgoren et al., 2012; Papanicolaou et al., 2012a), tapered plates, pyramids and cones (Vosper et al., 1999; Castro et al., 2001; Martinuzzi and AbuOmar, 2003; AbuOmar and Martinuzzi, 2008; Martinuzzi, 2008), and modified cylinders and prisms (Savory and Toy, 1986, 1988; Leder, 2003; Sousa and Pereira, 2004). A few studies have also investigated on flow structure around an axisymmetric hill (Simpson et al., 2002; Byun and Simpson, 2006; Krajnović, 2008). Further insight into the shedding behavior and wake topologies of tapered structures will be re-

viewed in Sec. 4.2.5 and the flow structure around the sphere will be discussed in more details in Sec. 2.4.

A few studies have systematically investigated the effect of changing the shape of the free end of otherwise cylindrical or prismatic obstacles. While Tanaka and Murata (1999) did not observe significant changes in the wakes of cylinders of varying aspect ratio with varying end conditions, significant effects were noted in other investigations (Leder, 2003; Sousa and Pereira, 2004). Leder (2003) showed the tip vortices on a hemispherical-end cylinder of aspect ratio 2 to be significantly weaker than those on a flat-end cylinder. Furthermore, he noted that, compared to a flat-end cylinder, the reattachment point in the case of a hemispherical-end cylinder occurred further downstream, leading to a 10% longer separated flow region. For cylinders of aspect ratio 6, Park and Lee (2004) examined the flow structure around the free end having flat, radiussed, beveled, and hemispherical corner shapes. Similarly, they reported qualitative observation of a strong tip vortex structure for a flat-topped circular cylinder of aspect ratio 6, but not for cylinders with chamfered, radiussed, or hemispherical ends. They also noted a stronger downwash and shorter recirculation region in the wake. Measurements of the arch vortex near the tip showed that the modified ends significantly reduced vortex circulation. Sousa and Pereira (2004) showed that the addition of a gable roof of 30° pitch to a cubic obstacle had a strong impact on the vorticity field as indicated by the Q-criterion, although they did not specifically address the presence of tip structures.

For obstacles of aspect ratio of $O(1)$, wake structures can be quite varied. Savory and Toy (1986) examined a wall-mounted hemisphere of diameter, $D = 190$ mm and the $Re_D = 1.4 \times 10^5$ in turbulent boundary layers of thickness $\delta/H = 0.9$ to 3.9 where H is the obstacle height. Low-Reynolds-number flow visualizations ($Re_D = 1.6 \times 10^3$) revealed a series of vortex loops shed from the hemisphere that

tilted downstream such that their streamwise legs induced an upwash in the wake (i.e. base vortices) as shown in Fig.2.11. Similarly, Becker et al. (2002) observed slight tilting of the mean arch structure in the wake of broad prismatic obstacles.

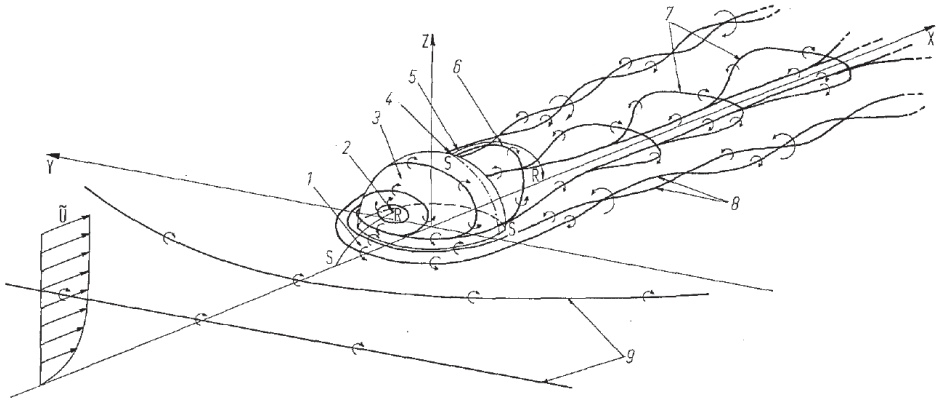

Figure 2.11: Distribution of vorticity in the flow regime associated with a hemisphere: 1 horseshoe vorticity, 2 stagnation point, 3 generation of vorticity, 4 separation line, 5 dividing streamline, 6 shear layer vorticity, 7 vortex loops, 8 trailing vortices, 9 boundary layer vorticity, S = separation, R = reattachment (from Savory and Toy (1986)).

Byun and Simpson (2006) employed fine-spatial-resolution three velocity component LDV measurements over the leeside of an axisymmetric hill with base radius= $2H$ in turbulent boundary layers of thickness $\delta/H = 0.5$ and showed one saddle and two foci mean separation points on the hill surface as shown in Fig. 2.13. The streamwise flow from the upstream and the backflow from the downstream spiral and converge toward $x/H = 1.2$ and $z/H = 0.7$. The flow at this point forms a focus separation. LDV measurements conducted at one transverse plane in the wake in $x/H = 3.26$ as shown in Fig. 2.12. The 3-D mean streamtraces by Byun and Simpson (2006) showed that the mean streamwise vortex generated by the focus separation on each side (upwash) is an opposite sense to what is observed (down-

wash) in the wake plane ($x/H = 3.26$). It means that the upwash flow observed is only inside the recirculation zone. Krajnović (2008) conducted LES simulation based on Byun and Simpson (2006)'s experimental study showing streaklines on the lee surface of a three-dimensional hill, consistent with upwash in the near wake. As time-averaging of the flow in Fig. 2.14 demonstrates, an arch vortex attached with its legs onto the leeward side of the hill. His results was in agreement with Byun and Simpson (2006)'s experimental study; however, the separation bubble was much ticker than that found in the experiment.

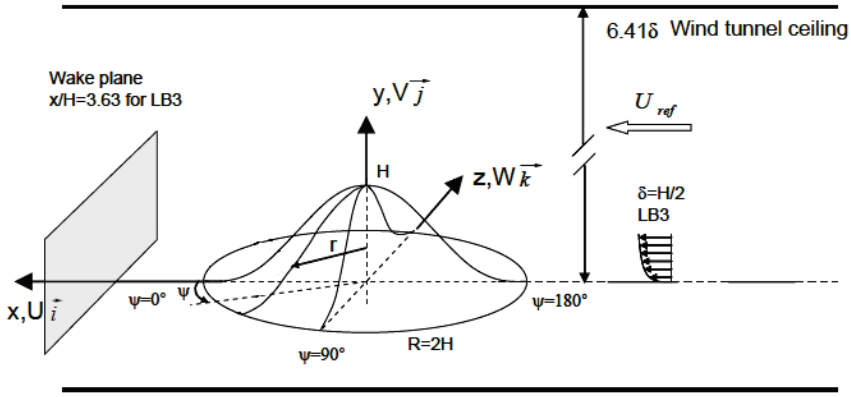

Figure 2.12: LDV measurements at one transverse plane in the wake of bump (from Byun and Simpson (2006)).

Martinuzzi and AbuOmar (2003) studied the mean flow in the wake of pyramids in thin boundary layers. They showed for a broad pyramids of $\zeta = 90°$ ($TR = 1$) a vortex core exists in the plane of symmetry directly downstream of the apex (tip) as shown in Fig. 2.15. This structure is referred to as a rotor vortex to emphasize its stability.

Surface visualization and instantaneous pressure measurements revealed a pair of bifurcation lines originating at the intersection of the leading edge corners of the

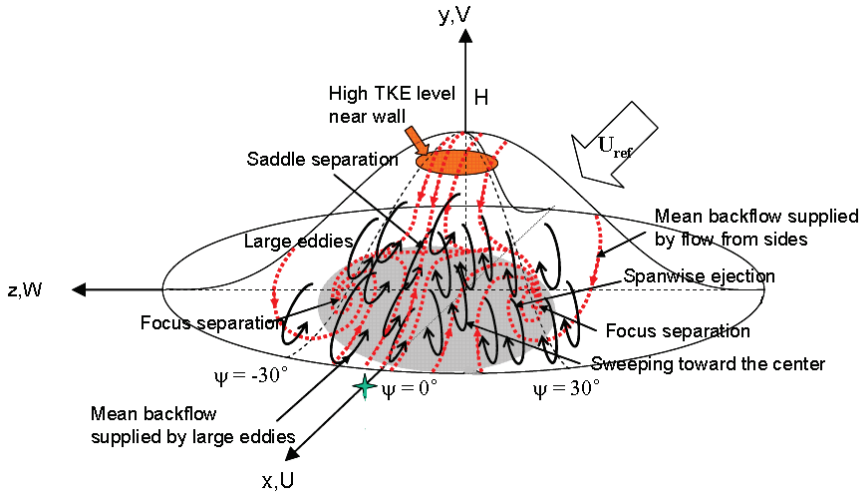

Figure 2.13: Flow structures on leeside of bump,behind the hill: large eddies shown in black; near surface flow patterns in dashed; mean backflow zone in gray (from Byun and Simpson (2006)).

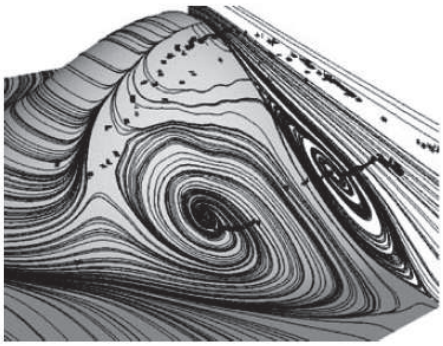

Figure 2.14: Streak lines on the surface of the hill, streamlines projected onto plane $z = 0$ (where z is the transverse axis) and vortex cores showing the extension of the vortices. View is from behind the hill on the surface of the hill (from Krajnović (2008)).

pyramid with the base plane as shown in Fig. 2.16, and extending upward and downstream along each side of the pyramid. These bifurcation lines were formed by three alternating-sign mean vortices along the surface. Further PIV studies by Martinuzzi (2008) and AbuOmar and Martinuzzi (2008) showed that these vortex

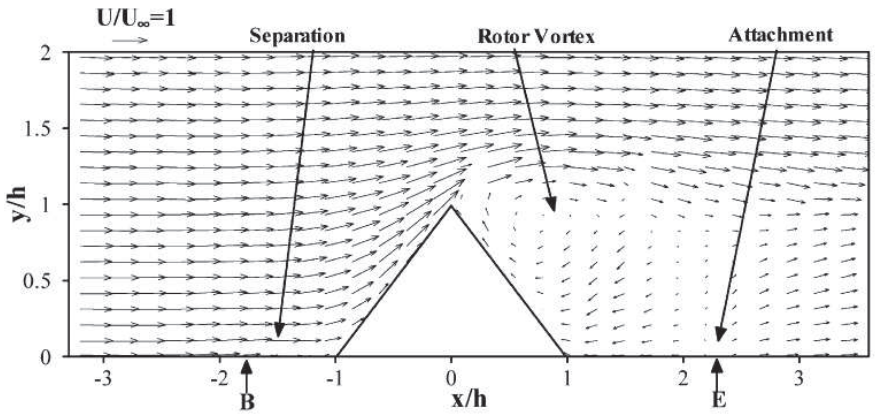

Figure 2.15: Mean velocity field, obtained with LDV, in the plane of symmetry (z/h =0) for $\zeta = 90°$ and $Re = 3.3 \times 10^4$ (from Martinuzzi and AbuOmar (2003)).

structures, which were oriented primarily streamwise in the wake, formed pairs inducing upwash and downwash downstream of the obstacle. Broad pyramids ($\zeta = 80°$ and 90°) were found to have a simpler flow field consisting of only a single arch (or hairpin) vortex structure which induced an upwash in the wake (Martinuzzi and AbuOmar, 2003) as shown in Fig. 2.17.

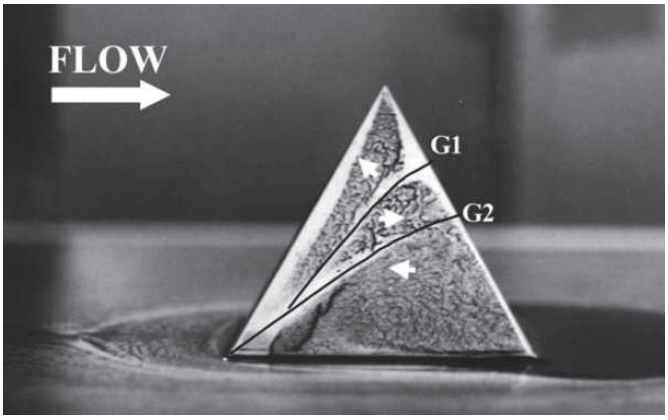

Figure 2.16: Surface-flow patterns on the side faces for a pyramid $\zeta = 60°$ (AR = 1.73) obtained using an oil-film technique. Arrows indicate general direction of pigment movement observed during experiments (from Martinuzzi (2008)).

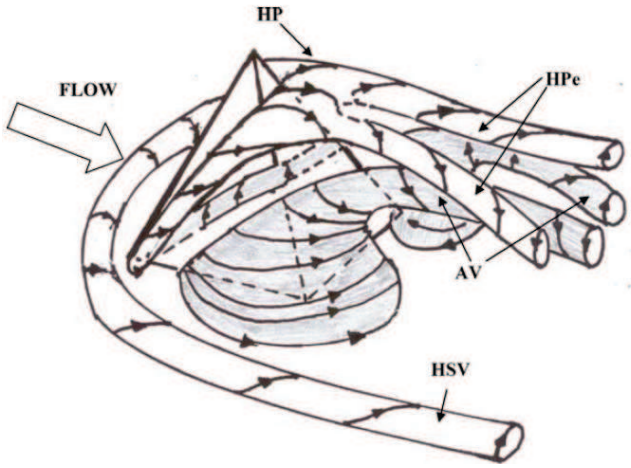

Figure 2.17: Vortex skeleton sketch for the flow around low-aspect-ratio pyramids (from Martinuzzi (2008)).

Hence, whereas high-aspect-ratio cylinders have been shown to produce base vortices under certain conditions and moderate-aspect-ratio cylinders generally do not, a new trend appears to emerge in the behavior of streamwise vorticity when the aspect ratio is near one (which we will refer to as low-aspect-ratio). The above discussion demonstrates that the wake structure and dynamics of these low-aspect-ratio obstacles can be highly varied as are the geometries that produce them. The so-called base vortices – we will use this term to describe any streamwise vortex pair inducing upwash in the wake – are apparently generated by very disparate mechanisms for different geometries.

2.4 Flow Characteristics around a Wall-Mounted Spherical Obstacle

As explained in Sec. 1.1, sediment transport around the sphere, representative of a boulder in a steep mountain stream, has been studied extensively by Papanicolaou and co-workers (Strom and Papanicolaou, 2007; Papanicolaou et al., 2011, 2012a). While the geometry of the sphere is simple, the flow structure around it is extremely

complex and has been one of the principal challenges for Computational Fluid Dynamics (CFD) (Constantinescu and Squires, 2004). The few experimental studies that have considered the flow structures around the sphere in boundary layer flows have only scratched the surface. None of these studies have proposed a model for flow around the sphere resulting from the interactions of wake components.

In Ch.5, the wake structure of a fully-submerged spherical obstacle, similar to the geometry in which the sediment observations were made by Papanicolaou et al. (2012a), will be investigated to provide insight into the flow-obstacle interaction with ramification to sediment transport and bed shear stress distrubution. As will be shown in Ch. 5, for a sphere, not only the dominant flow structures have been investigated but also the bed shear stress distribution has been quantified. Thus, the spherical geometry is being treated in this chapter separately.

Only a few studies have been considered and spherical bodies on boundary layer flow (Okamoto, 1980; Tsutsui, 2008; Ozgoren et al., 2012). The flow structure around sphere in the unbounded flow conditions has been studied extensively, either experimentally or numerically. Experimental investigation have been conducted via variety of approaches including flow visualization (Kim and Durbin, 1988; Sakamoto and Haniu, 1990) and thermal anemometry in the wake (Achenbach, 1974). Numerical investigation of flow field properties have been obtained by Achenbach (1972); Taneda (1978); Mittal and Najjar (1999); Constantinescu and Squires (2003, 2004); Jang and Lee (2008). Different flow regimes via varying Re_D and shedding mechanism around the sphere have been the primary interest in these investigations.

Okamoto (1980) conducted an experimental investigation on the flow past a sphere (D = 40 mm) and same aspect ratio hemisphere-cylinder (circular cylinder with hemisphere on top) placed on a ground plane with δ/D= 0.1 in the wind tunnel at the $Re_D = 4.74 \times 10^4$. Velocity measurements were conducted in x/D =0

to 28 via yawmeter and a wake model was proposed as illustrated in Fig. 2.18. To the authors knowledge, that is an only wake model proposed in the literature for the wake of wall-mounted spherical geometry. The vortex skeleton model is consistent with models of flow structure in the wake of low-aspect-ratio obstacles as obtained by Pattenden et al. (2005) containing arch and horseshoe vortices.

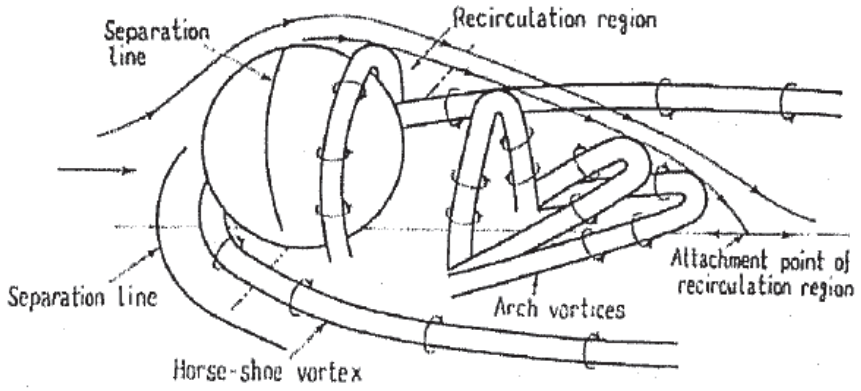

Figure 2.18: Proposed model for a wall-mounted sphere (Okamoto, 1980)

Pressure measurement by Okamoto (1980) demonstrated that the separation line on the ground upstream of the body was closer to the obstacle for sphere compare to cylinder. The intersections of the arch vortices with the ground plane were identified by the pressure distribution. The arch vortices were gradually inclined by the effect of strong downwash such that the inclined arches induced an upwash in the wake. An upwash was also reported in the near wake of a three-dimensional hill and wall-mounted hemisphere (Savory and Toy, 1986; Krajnović, 2008).

The horseshoe vortex was observed at $x/D = 2$ and 4 by Okamoto (1980) via using the tuft-grid method as illustrated in Fig. 2.19. It was observed that the

horseshoe vortex becomes flat at $x/D = 4$ and disappears at about $x/D = 5$. While Pattenden et al. (2005) reported the existence of trailing vortices at $x/D = 2.5$ for circular cylinder of $AR = 1$, resulting from the combination of tip structures and horseshoe legs near the ground plane, this observation was not reported by Okamoto (1980) in the wake of sphere.

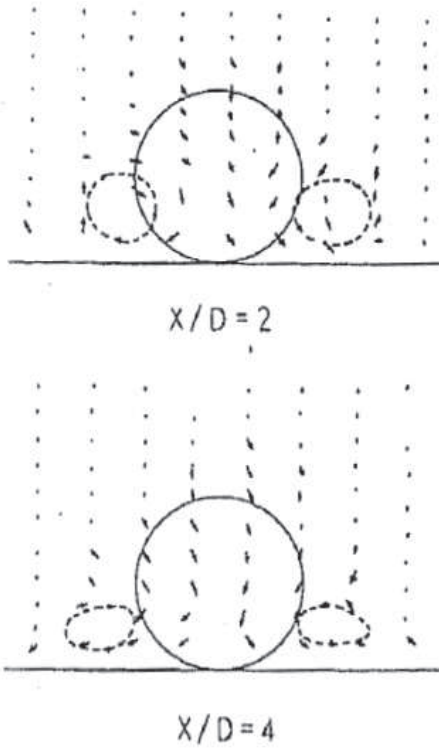

Figure 2.19: Horseshoe vortex behind the sphere observed by the tuft-grid method (Okamoto, 1980)

Tsutsui (2008) investigated the flow around a sphere ($D = 57$ mm) which was positioned in wind tunnel with varying gap above the boundary in $Re_D = 8.3 \times 10^4$. Three thick turbulent boundary layers of thickness δ/D =0.46, 1.26, and 2.11 were investigated. The flow was visualized by smoke-wire method and the surface oil-flow method and the surface pressure on the sphere and the plane

were measured. Figure2.20 is a photograph showing the flow visualization of the sphere. Tsutsui (2008) noted that the horseshoe and arch vortices exist when sphere was mounted on the plane. Arch vortices were formed downstream of the sphere and the separated shear layer from the top surface of the sphere reattaches at rear surface of the sphere.

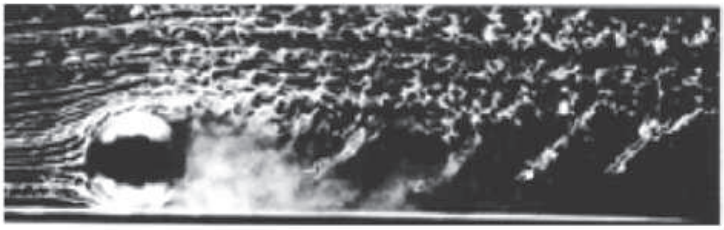

(a)

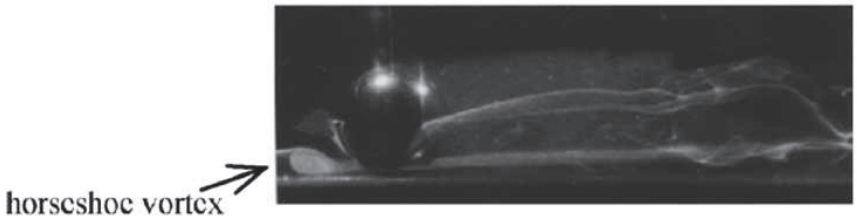

(b)

Figure 2.20: Flow visualization of the wall-mounted sphere ($\delta/D = 0.46$) using smoke-wire method: (a) $Re_D = 8.3 \times 10^4$, (b) $Re_D = 1 \times 10^4$ (Tsutsui, 2008).

The oil-flow pattern showing the surface flow over the sphere and the plane, the flow sketches and the fluctuating pressure coefficients along the centerline of the plane is shown in Fig. 2.21. He noted that a saddle point is existed at $x/d = 0.8$ on the plane and a peak in the Cp' ($= \Delta p/0.5\rho U^2$ where Δp is the r.m.s. value of the fluctuating pressure) distribution is observed at $x/d = 0.4$ (Cp' distribution has peaks at separation and attachment points). He deduced that these observations indicate the existence of a horseshoe vortex.

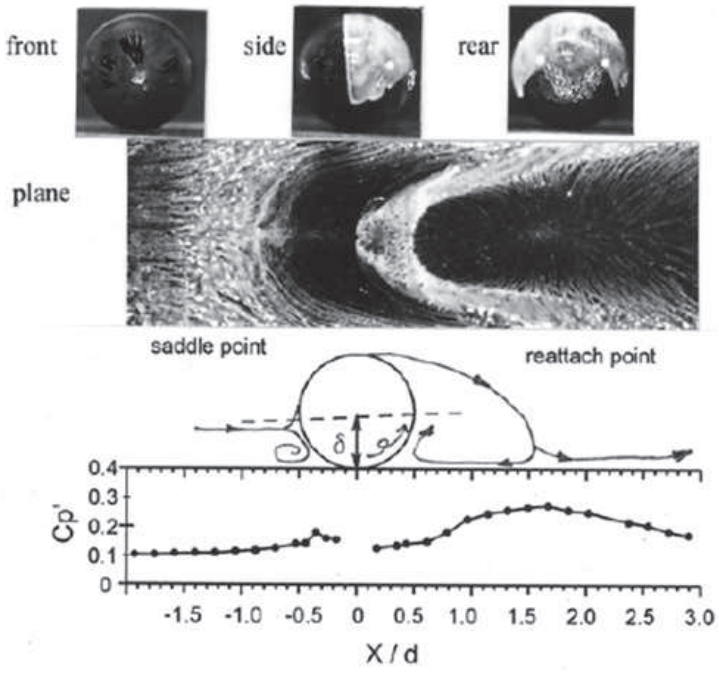

Figure 2.21: Surface oil-flow patterns of the wall-mounted sphere (δ/D = 0.46, $Re_D = 8.3 \times 10^4$ (Tsutsui, 2008)

The pressure coefficient distributions on the center line of the sphere and on the plane is shown in Fig. 2.22. The inside and outside of the sphere indicate positive and negative pressures, respectively. In addition, the upper and lower area from the ground line ($Cp = 0$ line) indicate negative and positive pressures, respectively. For a wall-mounted sphere case, the upper and lower Cp distribution of the sphere is asymmetric. The pressure acting on the forward-lower region of the sphere is positive, and that acting on the upper-rear area is negative.

Similar investigation on a sphere with varying gap on a flat plate was also conducted using PIV and dye visualization by Ozgoren et al. (2012) at Re_D = 5000 and thick boundary layer of δ/D = 1.58 to determine the flow-structure interaction with the plate boundary. Their results enhanced understanding of flow pattern in the streamwised symmetry plane which will be compared to results of this study in

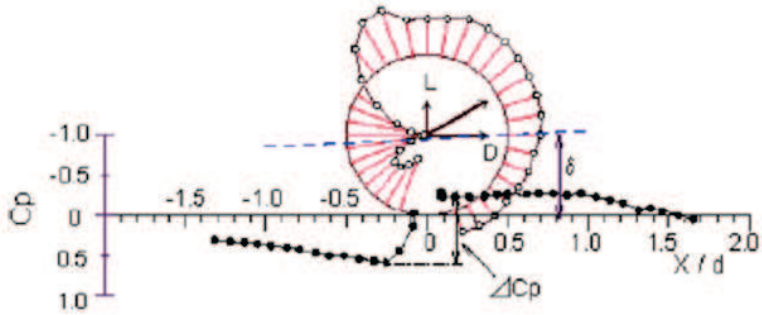

Figure 2.22: Pressure distribution of the wall-mounted sphere and the plane (δ/D = 0.46, $Re_D = 8.3 \times 10^4$ (Tsutsui, 2008)

the Sec.5.1. Figure 2.23 shows flow visualization image of instantaneous flow field with laser illumination of Rhodamine dye injection technique around the smooth sphere (the small scale vortices are designated by A to D). As Fig. 2.23 shows, small scale vortices in the wake region are formed around larger vortices with a wavy appearance due to Kelvin Helmholtz instability in the boundary layer.

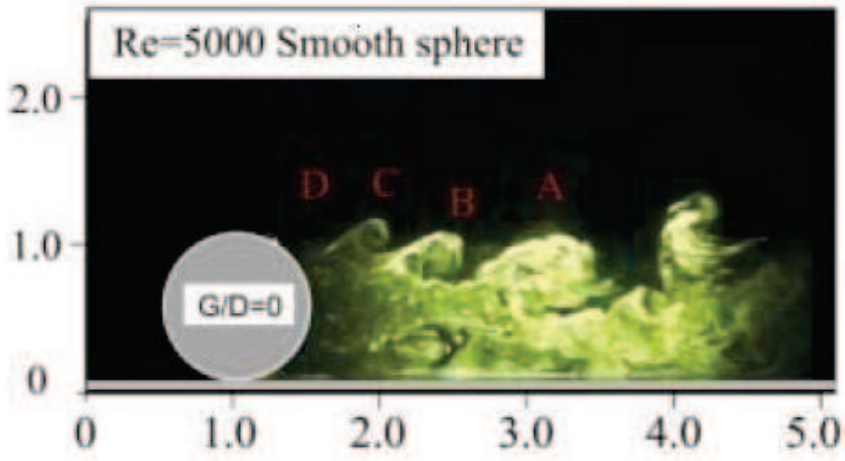

Figure 2.23: Flow visualization of flow structure with laser illumination of Rhodamine dye injection technique around the smooth sphere at Re_D = 5000 (Ozgoren et al., 2012)

The experimental study of Taneda (1978) by means of smoke-wire and the surface oil-flow method revealed a vortex skeleton model for a sphere supported by steel rod at the rear in the super critical regime ($3.8 \times 10^5 < Re < 10^6$). Taneda (1978) noted the vortex sheet separating from the sphere rolls up into a Ω-shaped structure to form a pair of strong streamwise vortices as shown in Fig. 2.24. He noted that in this flow regime, the wake is not axisymmetric.

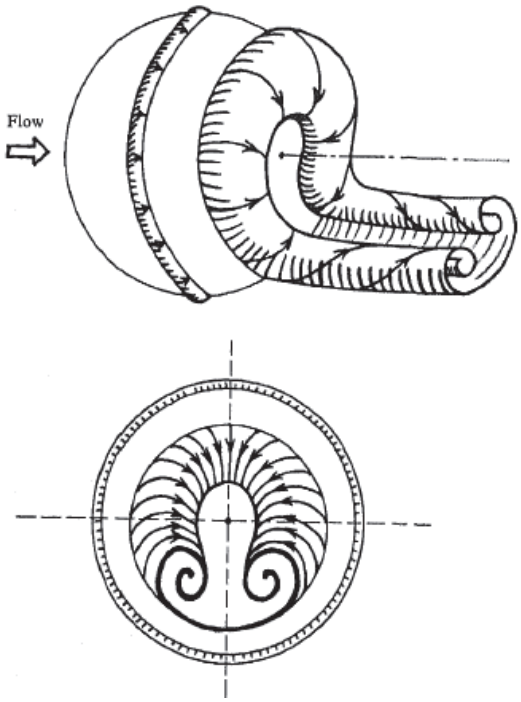

Figure 2.24: Proposed model for sphere supported by rod in the rear (Taneda, 1978)

Turbulent characteristics and mean flow around hemispherical and spherical geometries on the rough bed at open channel flow has also been investigated with implications to sediment transport (Shamloo et al., 2001; Strom and Papanicolaou, 2007; Dey et al., 2011; Papanicolaou et al., 2011, 2012a). The last two studies also documented flow field around sphere geometries within an array (Fig. 2.25) to

define mean flow and turbulent statistics in which the observations bring greater similarity to bed load transport studies.

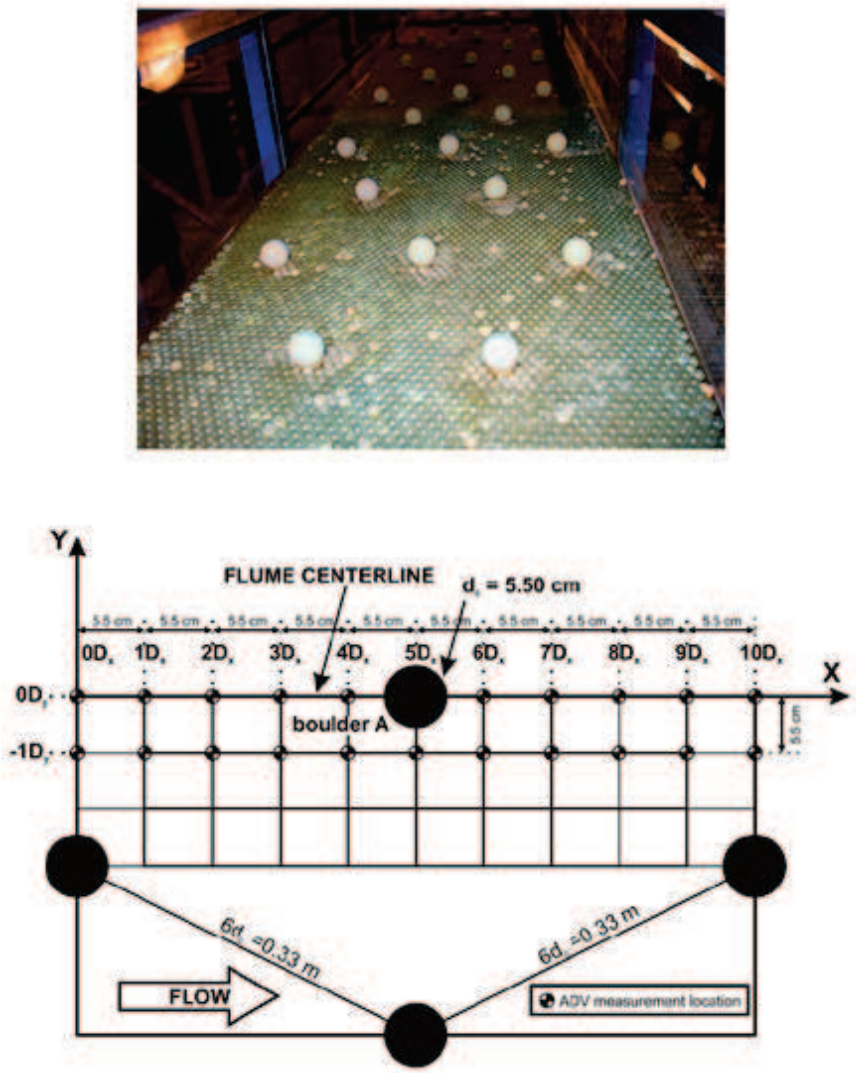

Figure 2.25: Perspective view of the experimental boulder section (top), and Plan view sketch of the ADV measurement locations (bottom). (Papanicolaou et al., 2012a)

Dey et al. (2011) considered the time-averaged characteristics of turbulent wall-wake flows downstream of a sphere placed on a rough wall. Vertical profiles of

u/u^* and τ/u^{*2} at different streamwise locations of sphere of D = 40 mm were measured as shown in Fig. 2.26. The u profiles in wall-wake flows exhibit a reversal velocity characteristic in the near-wake flow and a gradual recovery of the undisturbed boundary layer with an increase in x. It is visible from the τ/u^{*2} profile that immediately downstream of the sphere, τ starts with a positive value near the wall and sharply increases with z forming a peak at z/D =0.6.

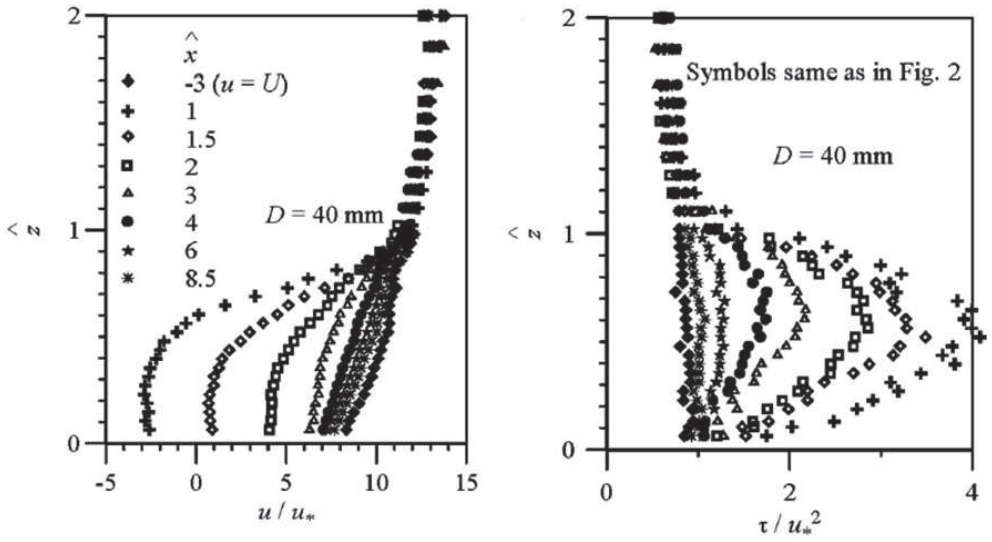

Figure 2.26: Vertical profiles of u/u^* (left) and τ/u^{*2} (right) at different streamwise locations of sphere of D = 40 mm (Dey et al., 2011).

Papanicolaou et al. (2012a) using the ADV measured the streamwise turbulence intensities, $rms(u')$, normalized with u^*, for symmetry, $0Dy$, and $-1Dy$ planes around a boulder compared with LES as illustrated in Fig. 2.27. The maximum in the profile observed at the crest of the boulder (sphere) in which the shear layer forms. The $rms(u)/u^*$ decreased near the bed which was related to increased roughness there. While the $rms(u)/u^*$ presents the maximum at z/H = 0.26 (where H= flow depth) in $0Dy$, it increased to z/H = 0.3 in transect $1Dy$ where the profiles

collapsed better and have lower magnitude than $0Dy$.

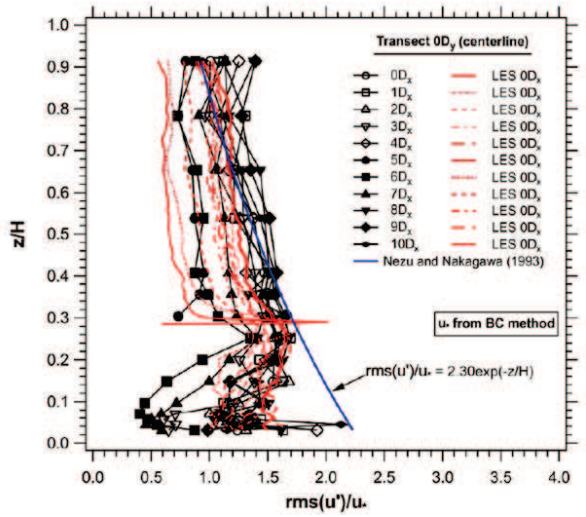

(a)

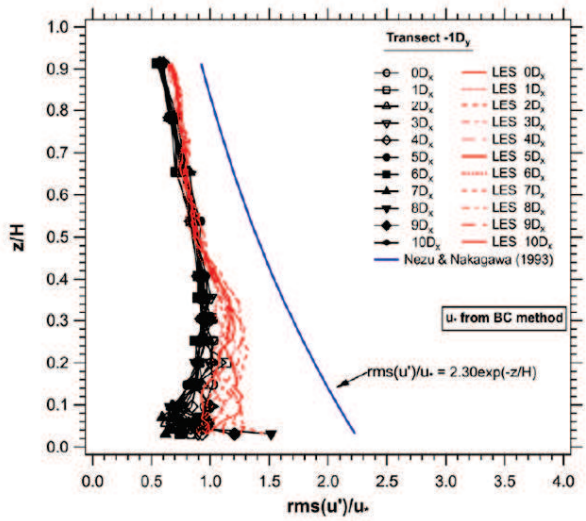

(b)

Figure 2.27: Comparison between the measured and simulated streamwise turbulent intensity profiles normalized with u^* from the boundary characteristics method for: (a) transect $0Dy$ (flume centerline), and (b) for transect $1Dy$ (from (Papanicolaou et al., 2012a).

Papanicolaou et al. (2012a) also employed LES for a sphere in an open channel

to resolve eddy structures around the boulder. However, the LES model considered a smooth, impermeable bed and therefore was not identical to the experiment. As illustrated in Fig. 2.28, the vortices are shed from top of the sphere into near wake region. In streamwise, the vortices sheared toward the base plane in the wake of sphere.

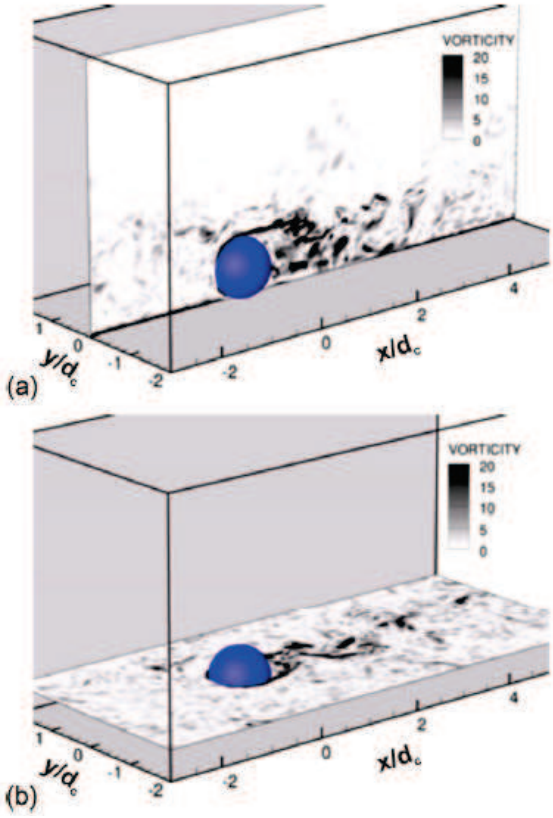

Figure 2.28: Magnitude of the instantaneous vorticity vector (a) in a longitudinal plane, and (b) in a horizontal plane at half boulder height (Papanicolaou et al., 2012a).

The contours of the time-averaged streamwise vorticity at $6Dx$, and $7Dx$ are shown in Fig. 2.29. Streamwise features observed in the mean wake include counter-rotating distributions of vorticity inducing downwash. The streamwise

vorticity distribution in the wake of the sphere at $x/dc = 6$ is similar to that observed by Pattenden et al. (2005) in the wake of a low-aspect-ratio cylinder and is dominated by the tip and horseshoe structures. At $x/dc = 7$ the tip vortices are significantly sheared toward the base plane in the wake of the sphere.

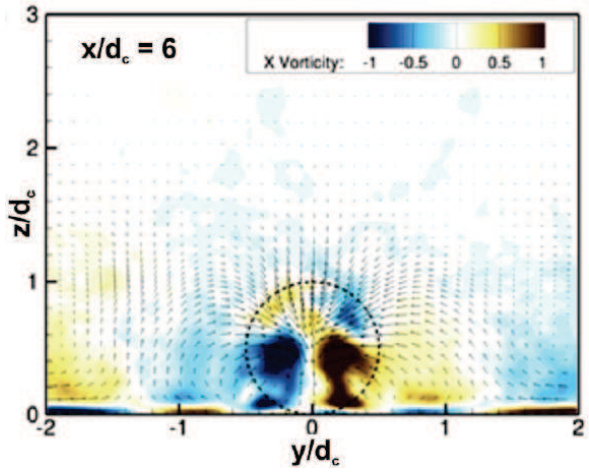

(a)

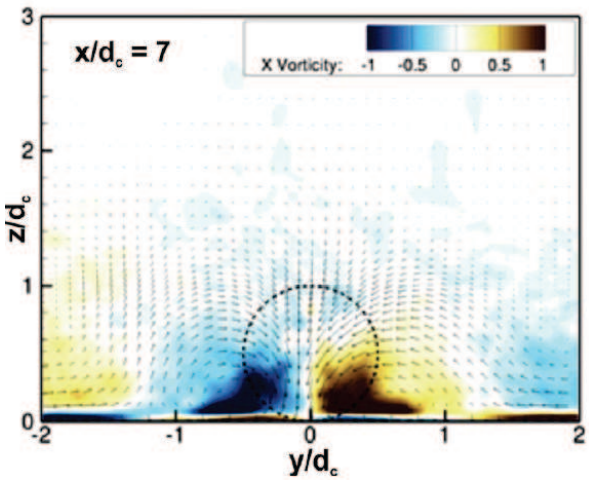

(b)

Figure 2.29: Contours of the time-averaged streamwise vorticity together with vectors of the secondary flow around a boulder (sphere) with LES at locations: (a) $6Dx(x/dc = 6)$, and (b) $7Dx(x/dc = 7)$ where dc is boulder (clast) diameter (from (Papanicolaou et al., 2012a).

2.5 Effects of Boundary Layer Thickness

The influence of boundary layer thickness on the structure of the wake has been documented in several studies (Sakamoto and Arie, 1983; Martinuzzi and AbuOmar, 2003; Wang et al., 2006; Bourgeois et al., 2011a). This is typically reported as the ratio δ/D for large-aspect-ratio obstacles (where δ is the boundary layer thickness and D is the width of the obstacle). For circular and square cylinders of aspect ratio significantly greater than one, increasing boundary layer thickness usually provides more favorable conditions for the existence of upwash. Wang et al. (2006) addressed the effect of δ/D (δ/D=0.51, 1.02 and 1.90) in a parametric study using particle image velocimetry in the symmetry plane of the wake of a square cylinder of $AR = 5$. They found the intensity of the upwash near the junction of the cylinder to increase with increasing δ/D as illustrated in Fig. 2.30.

Recently, Bourgeois et al. (2011a) proposed that the existence of upwash in the wake is determined by a threshold in δ/D which separates two fundamentally different wake structure types. For a square cylinder of $AR = 8$, with $\delta/D = 0.7$, only downwash was observed, and the wake dynamics were explained in terms of the half-loop structure introduced by Bourgeois et al. (2011b) as shown in Fig. 2.31. For $\delta/D = 2.6$, a full-loop structure, similar to the model proposed by Wang and Zhou (2009) was shown, resulting in both upwash and downwash in the wake. However, as suggested in Sec. 2.2.3, δ/D is not the sole parameter governing the selection, as Sumner et al. (2004) demonstrated the influence of obstacle height. As stated in Sec. 2.2.3, a notable exception is the wake topology proposed by Krajnović (2011) in which upwash is observed for a circular cylinder of $AR = 6$ with $\delta/D = 0.07$.

On the other hand, the influence of δ/D is less clear for low-aspect-ratio obstacles, which tend to have even more complex, three-dimensional wakes due to the proximity of the various elements of the wake. Using surface visualization ex-

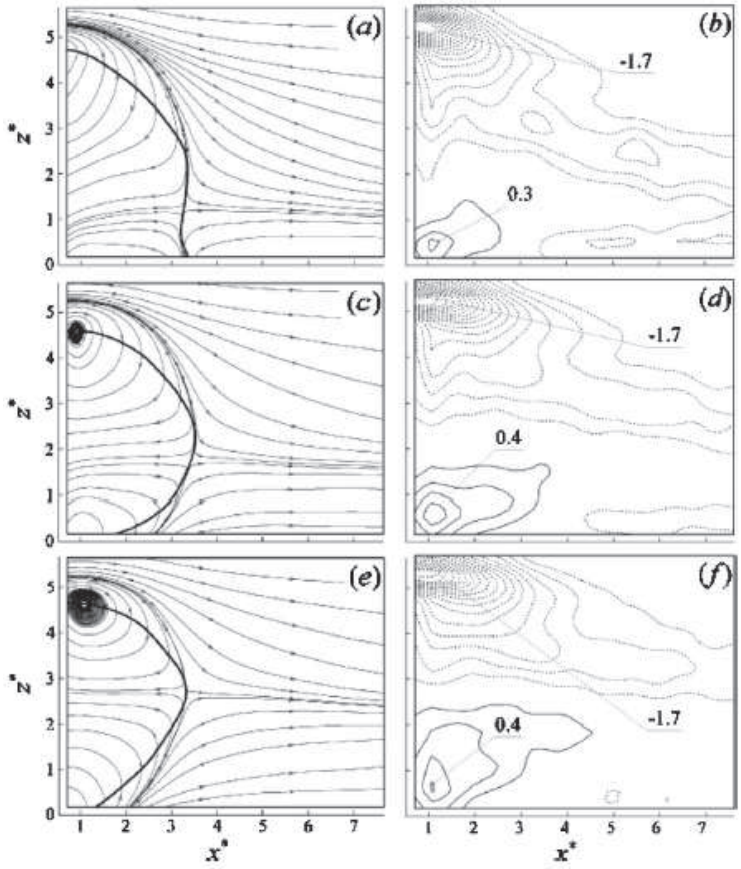

Figure 2.30: Averaged sectional streamlines (left) in the x-z plane at $y^* = 0$, viewed on a reference frame fixed on the wall, and the corresponding contours of lateral vorticity $\overline{\omega}_y^*$. (right), contour increment=0.2. (a), (b) δ/D=0.51, (c), (d) δ/D=1.02, (e), (f) δ/D=1.9. The thick solid line indicates the reverse flow region (from Wang et al. (2006)).

periments around low-aspect-ratio obstacles in thick boundary layers ($\delta/H = 2.5$), Chyu and Natarajan (1996) inferred the existence of an arch vortex in a pyramid wake that was inclined upstream such as to induce a downwash in that region. In contrast, Martinuzzi and AbuOmar (2003) reported the single arch structure, as described above, in a thick boundary layer ($\delta/H = 2$), tilted downstream from the leading edge corners, such as to induce an upwash. The latter observation is consistent with that of the high-aspect-ratio obstacles mentioned above, as well as

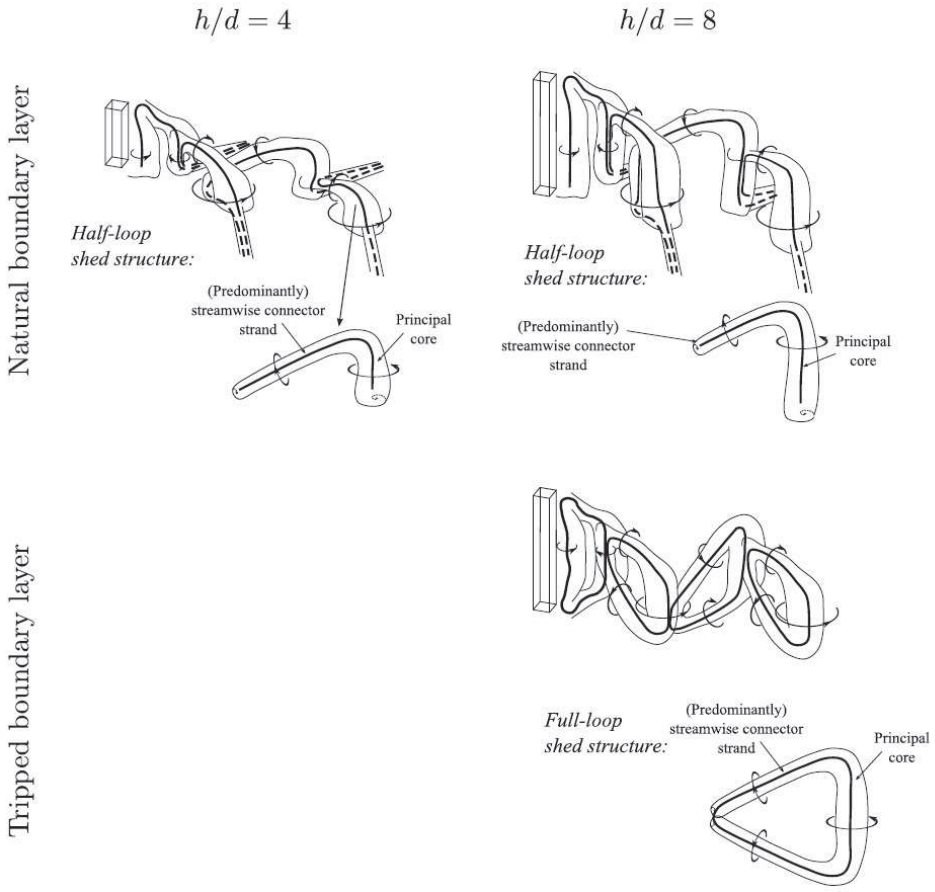

Figure 2.31: Effect of boundary layer thickness on flow topology (from Bourgeois (2012)).

that of Savory and Toy (1986) who presented data illustrating an increase in base vortex strength in transverse planes downstream of their hemispherical obstacle with increasing boundary layer thickness. In the low-Reynolds-number studies of Mason and Morton (1987), blunt plates with $AR < 1$ were found to produce upwash in boundary layers of thickness comparable to obstacle height. Interestingly, for $AR = 0.25$, the upwash was stronger for the thinner boundary layer, but this trend reversed for $AR \geq 1$.

To the authors' knowledge, there are no studies that report base vortices or upwash in the wakes of circular cylinders of $AR \approx 1$. The present study will

discuss data where this is the case.

2.6 Effect of Relative Submergence

The effect of relative submergence has been considered in hydraulic studies due to interest in fish habitat structures, flow structures around clasts, and sediment transport (Shamloo et al., 2001; Papanicolaou and Kramer, 2005; Tritico and Hotchkiss, 2005; Strom et al., 2007; Papanicolaou et al., 2011; Lacey and Rennie, 2012) and the study of Lacey and Rennie (2012) was undertaken to provide further insight into flow depth/wake structure relationships of a submerged surface mounted cube. In fact, most of the studies conducted on the topic of relative submergence have been in the context of open channel flow. Despite the considerable number of studies of flow around bridge-pier-like objects (Sadeque et al., 2008), we still have a limited knowledge of flow around submerged bluff bodies in open channels.

One study by Ozturk et al. (2008) was considered the boundary layer flow for cylinder of AR =0.4 in a RS = 1. Their study investigates the flow past a confined circular cylinder in a narrow rectangular duct with a Reynolds number , Re_d, in the range of 1500 to 6150 by using the PIV technique. For explaining downstream and upstream juncture regions of the cylinder and the dynamics of the horseshoe vortex system both time-averaged and instantaneous flow data were investigated. Ozturk et al. (2008) noted that there are concentrated vortices in the downstream corners of the cylinder at $d/H = 1$ and the size, intensity and interaction of the vortex systems vary substantially with the Reynolds number as shown in Fig. 2.32. The figure shows two symmetric primary vortices, Vp, and a pair of corner vortices, Vco, at the upper and lower junction regions. A pair of counter-rotating vortices, Vc, located between the primary, Vp, and developing, Vd, vortices, are also exist upstream of the cylinder for lower Reynolds number 1500.

Shamloo et al. (2001) examined the mean flow around hemispherical fish habi-

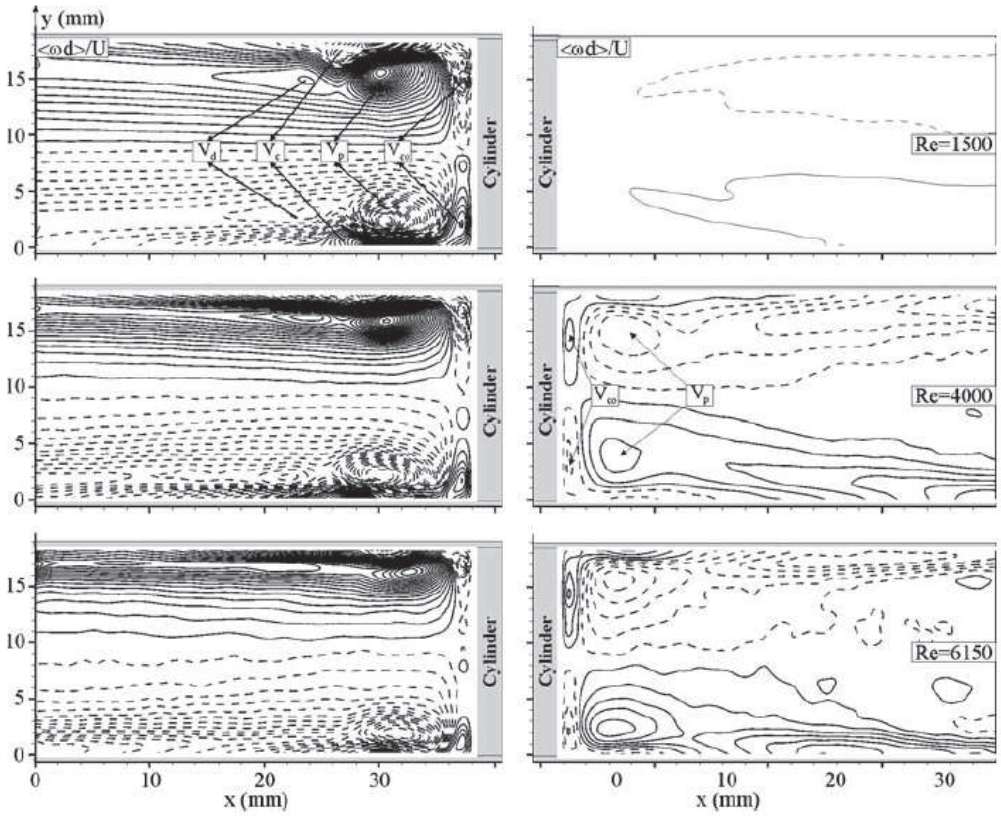

Figure 2.32: Side view of time-averaged normalized vorticity contours upstream and downstream of the cylinder in $RS = 1$. The positive and negative contours are displayed with solid and dashed lines (Ozturk et al., 2008).

tat structures in shallow open channel flows and proposed a classification of flow regimes based on d/h, where d is the flow depth and H is the characteristic obstacle length scale (e.g. the obstacle height) as shown in Fig. 2.33. For $d/h > 4$, the presence of the obstacle left no discernible signature on the free surface and flow patterns were qualitatively consistent with those observed around obstacles immersed in boundary layer flows. For $1.3 < d/h < 4$ surface wave appeared as illustrated in Fig. 2.33(c). When the relative depth of flow was in the range of 1.1 to 1.3 mixing of free shear layer through the whole depth was observed (Fig. 2.33d). For $d/h < 1$, standing waves formed around the obstacle, and a Kármán

vortex street was reported in the wake. A similar phenomenon occurs in stratified atmospheric flows around islands (Smith and Grubišić, 1993). Furthermore, Shamloo et al. (2001) measured shear stress distributions and scour patterns on those regimes. The results of their study, however, were difficult to generalize because the depth and discharge for different flow regimes in the study varied.

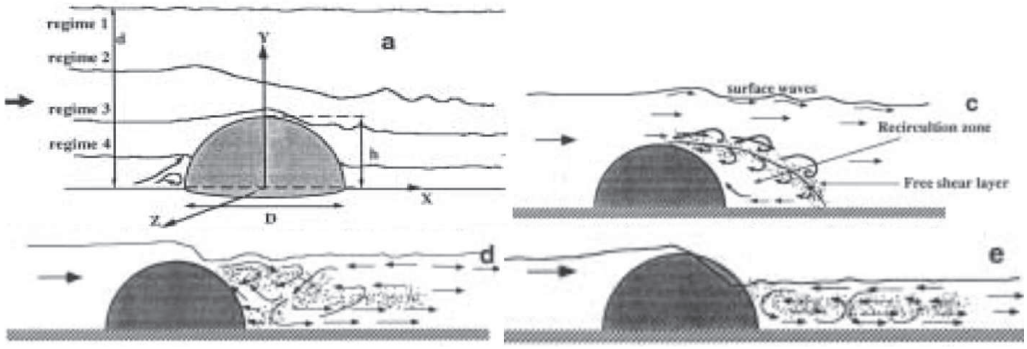

Figure 2.33: Details of flow for regimes 2, 3 and 4 (c, d, e) in Shamloos experiments (from Shamloo et al. (2001)).

Sadeque et al. (2008, 2009) further studied the effect of relative submergence on flow around cylindrical objects of aspect ratios between 0.48 and 2.6 in smooth and rough bed open channels and found that increasing relative submergence suppressed alternate vortex shedding and producing a more three-dimensional flow. In the case of slightly submerged and non submerged cylinders, wake vortices were found to shed in alternate style with a Strouhal number $St = 0.2$. The width of the wake, however, was smaller for the non submerged cylinder such that the dimensional shedding frequency was higher.

In addition, Papanicolaou and Kramer (2005) observed distinct patterns of sediment deposition around spherical obstacles for relative submergences of 0.8 and 3.5 as shown in Fig. 2.34, suggesting a significant change in flow structure. In the

high relative submergence experiment, the majority of clusters are deposited in the wake of the clasts. However, in the low relative submergence experiment, clusters are deposited in the stoss of the clasts and clasts appeared to control the areas where cluster formation occurred. Papanicolaou et al. (2011) also demonstrates more details for low relative submergence case and noted the existence of Kármán vortex street in the wake region of the clast using LSPIV.

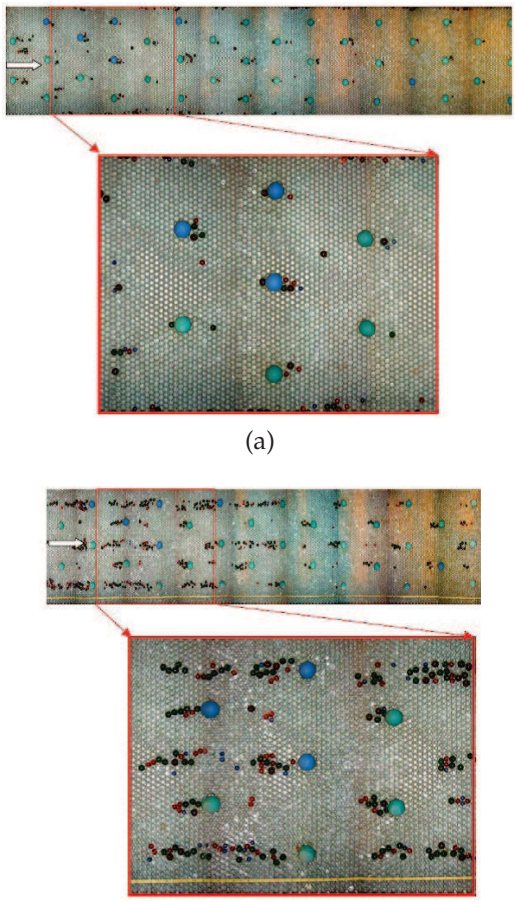

(a)

(b)

Figure 2.34: Plan view of the tests section for the: (a) d/d_{clast}= 3.5, (b) d/d_{clast}= 0.8, (from Papanicolaou and Kramer (2005)).

Sadeque et al. (2008) studied the effect of relative submergence with experimen-

tal study of flow around cylindrical objects in a smooth bed open channel. Cylindrical objects of equal diameter and four heights were tested while flow depth was kept the same producing four different levels of submergence. Horseshoe vortex systems were found to appear closer to the submerged cylinders compared to a surface piercing cylinder. The increase in dimensionless bed-shear stress is found to be inversely related to the level of submergence of the cylinders. Increasing submergence of the cylinder was found to suppress alternate vortex shedding and produce stronger three-dimensional flows in the downstream wake. They revealed that the upstream boundary layer separation point moves closer to the object as the cylinders become more deeply submerged. This results in a reduction of the size of the horseshoe vortex system. In the case of slightly submerged and non submerged cylinders, wake vortices were found to shed in alternate style with a Strouhal number St = 0.20. The width of the wake, however, was smaller for the non submerged cylinder such that the dimensional shedding frequency was higher.

Sadeque et al. (2009) also carried out the same tests on a rough bed in open channel flow. The vorticity structures on smooth and rough beds are similar, but the vortex strength is found to be 20 to 30% larger on the rough bed. Since the obstacles have changed during the tests, it is difficult to make a trend from Sadeque et al. (2008, 2009) experiments and the effect of relative depth on wake structure is not clear.

Lacey and Rennie (2012) observed further insight into flow depth/wake structure relationships of a submerged surface mounted prism of 0.2m width× 0.2m length×0.1m height (d/H=3, 2.5, 2) using ADV on a flat bed (thin layer of coarse sand, D_{50}=1 mm) open channel flume. According to the results of their study, with decreasing relative depth, substantial variations in the spatial distributions of mean and turbulence statistics were observed in the wake of submerged wall-mounted cube which have important implications for local sediment mobility and

fish habitat. The spatial distribution of turbulent kinetic energy, k_e, values shift downstream with decreasing depth as shown in Fig. 2.35a whereas increasing up to 50% of principal Reynolds shear stress ($-\overline{u'w'}$) close to the top of the cube was observed as illustrated in Fig. 2.35b. This has been related to the compression of shedding vortical structures. High wake values of k_e are in agreement with the results of previous studies (e.g, Tritico and Hotchkiss (2005)) and has been related to the existence of shear layers overtop and along the sides of the obstacle. While Sadeque et al. (2009) observed near-bed k_e values to decrease with relative depth, this trend was not observed in the Lacey and Rennie (2012)'s data. Lacey and Rennie (2012) also examined the spatial distribution of time-averaged vertical vorticity, $\overline{\omega}_z$. Results of their experiments demonstrated that the zones of intense vorticity expand downstream with decreasing flow depth. With interpretation of near-bed ($z^+ = 0.3$) variation in spatial pattern of $-\overline{u'w'}$, they noted that with decreasing flow depth, the flux of uw momentum changes location from the centerline toward the sides which results in bed shear stress reduction directly behind the cube.

2.7 Shedding Characteristics

In this section, the shedding characteristics and wake dynamics of wall-mounted bluff bodies (especially low-aspect-ratio) will be reviewed which depend on a number of factors including obstacle shape, aspect ratio, ratio of boundary layer thickness to obstacle width, and Reynolds number.

The wakes are often less organized and more highly three-dimensional for cylinders of aspect ratio $AR \approx 1$ in which a peak in the power spectrum has not been reported consistently. For a circular cylinder of $AR = 1$ at $Re_D = 4.7 \times 10^4$ and $\delta/D = \delta/H = 0.057$ (where δ is the boundary layer thickness, and D and H are the cylinder diameter and height, respectively), Okamoto and Sunabashiri (1992) reported a broad spectral peak around $St = 0.23$ suggesting that the shedding was not strongly coherent. At similar Reynolds number, Okamoto and Uemura (1991)

reported $St = 0.225$ in a slightly thicker boundary layer ($\delta/D = \delta/H = 0.086$). On the other hand, no dominant frequency was observed by Uematsu et al. (1990) for a circular cylinder of AR=1 at $Re_D = 4 \times 10^4$ where $\delta/D = \delta/H = 0.88$. Pattenden et al. (2005) reported only a very weak peak in the energy spectrum of the surface pressure signal at $St = 0.090$ for a circular cylinder of $AR = 1$ at $\delta/D = 0.1$ and a Reynolds number close to the critical condition. The power spectral density function was plotted on a linear axis as shown in Fig. 2.36. Similarly, no periodic shedding was detected by Sattari et al. (2010) for a circular cylinder of aspect ratio 0.5 in $Re_D = 6 \times 10^3 - 10^5$ and $\delta/D = 0.08$ ($\delta/H = 0.16$).

Obstacle cross-sectional shape also plays a significant role in vortex shedding. Okamoto and Uemura (1991) rounded the side corners of a cube placed on a ground plane and found that the shedding Strouhal number increases linearly with the corner radius. Whereas $St = 0.112$ was measured for a cube, a circular cylinder of $AR = 1$ was observed to shed at twice that frequency. A spectral peak at $St = 0.152$ was observed for the same aspect ratio hemispherical-end cylinder (Okajima, 1982), demonstrating that the shedding frequency is dependent on not only the cross-section but also the end condition. For a square cylinder of aspect ratio 0.5 at $\delta/H = 0.16$ ($\delta/D = 0.08$) and $Re_D = 6 \times 10^3 - 10^5$, Sattari et al. (2010) found a broad spectral peak centered around $St = 0.33$. The cross-correlation function revealed that the mean phase difference in fluctuation velocity signals on opposite sides of the wake is close to 180°, indicating antisymmetric shedding. Loss of power near the free end and in the wall junction region was observed. The latter was attributed to interference with the horseshoe vortex.

More complex shedding behaviors may be observed in the wakes of non-cylindrical obstacles. For example, cellular shedding has been observed in cones (Papangelou, 1992; Vosper et al., 1999; Vosper, 2000; Castro et al., 2001), tapered plates (Castro and Rogers, 2002; Castro and Watson, 2004), and pyramids (Mart-

inuzzi and AbuOmar, 2003; AbuOmar and Martinuzzi, 2008; Martinuzzi, 2008) in which either the shedding frequency or Strouhal number was found to be constant within each cell. The location and size of the cells are functions of the degree of taper, the aspect ratio, and the end conditions.

Papangelou (1992) found that the nature of cellular shedding by tapered cylinders and cones depends on Reynolds number and apex angle, ζ. Constant frequency cells were observed for tapered cylinders with $0.048^\circ \leq \zeta \leq 0.3^\circ$ at $Re = O(100)$, which broke down for increasing or decreasing Reynolds number ($Re < 80$ or $Re > 150$), and it was proposed that the existence of cellular shedding was sensitive to end conditions. Vosper et al. (1999) examined cones of significantly larger apex angle ($22^\circ < \zeta < 68^\circ$) at $Re = O(10^4)$ and found a single cell of constant frequency along the height in stably-stratified flow. On the other hand, Castro et al. (2001) observed periodic wake structures created by cones of aspect ratio less than one in strongly stratified flows in a towing tank. A cross-correlation analysis of point velocities measured in the wake indicated that the structures tilted upstream in this case, consistent with downwash. In the same study, experiments (in non-stratified flow) on wall-mounted triangular plates of aspect ratio 10 and 30 revealed cellular shedding patterns such that a significant portion of the lower wake exhibited constant-frequency shedding. Closer to the tip, either constant Strouhal number shedding was observed, or two frequencies, consistent with a bistable shedding regime.

Castro and Watson (2004) observed Kármán shedding of constant frequency corresponding to $St = 0.146$ across the entire span of bluff triangular plates of mild taper ratio, $1.2 < TR < 8$. The taper ratio TR is defined as (plate length / average width). For plates with a free end, this is equivalent to the aspect ratio, which we will denote AR_{av} to distinguish it from the aspect ratio defined in this thesis. Similar to cones, the mildly-tapered triangular plates (Castro and Watson, 2004;

Castro and Rogers, 2002) exhibited a constant-frequency cell in the base region as illustrated in Fig.2.37. The height of this cell was found to vary between 4 to 7 times the base width. However at small taper ratios (i.e. $TR = 3.73$) as shown in Fig. 2.37, the main vortex shedding peaks are visible all along the span. At $TR = 7.5$ the high-frequency, broad peaks can also be seen for $z/L > 0.25$.

While no vortex shedding was observed for $TR = 0.36$, weak Kármán-like shedding at $St = 0.18$ was observed for $TR = 0.58$ and 1, in relatively thick boundary layers ($\delta/H = 1.1$ and 0.68, respectively) despite the extreme taper and the spatial extent of the approaching shear flow. Notably, no coherent shedding was observed for a plate of $TR = 0.58$ with the size doubled, emphasizing the importance of boundary layer thickness, though still not well-understood.

Further insight into the shedding behavior and wake topologies of tapered structures was introduced by Martinuzzi and AbuOmar in their investigations of pyramid-shaped obstacles in thin boundary layers and shedding behavior was classified based on apex angle ζ.(Martinuzzi and AbuOmar, 2003; AbuOmar and Martinuzzi, 2008; Martinuzzi, 2008). For pyramids with apex angles, ζ, in the range $15° < \zeta < 75°$ (equivalent to taper ratios in the range $7.6 \geq TR \geq 1.3$), Martinuzzi and AbuOmar (2003) observed a cellular shedding pattern similar to that found by Vosper et al. (1999) and Castro et al. (2001), and Castro and Watson (2004). As shown in Fig. 2.16 a pair of bifurcation lines extend upward and downstream along each side of the pyramid. These bifurcation lines were found to delineate the cellular shedding regions. Martinuzzi and AbuOmar (2003) found $St = 0.33$ for a pyramid of aspect ratio 1. Also, no vortex shedding was observed for broad pyramids of $\zeta > 90°$ ($TR < 1$). On the other hand, Okamoto et al. (1977) reported periodic vortex shedding for $\zeta < 120°$.

Analysis of the phase shift between fluctuations at different positions in the wake has been previously employed by Castro et al. (2001), Martinuzzi and AbuO-

mar (2003), and Wang and Zhou (2009). For conical obstacles, Castro et al. (2001) reported vertical variations in the phase of vortex shedding with spanwise position, which are dependent on obstacle shape. They documented that for cones of aspect ratio less than one in strongly stratified flow, the vortex lines can be significantly tilted downstream, particularly in the upper part of the wake. Martinuzzi and AbuOmar (2003) also observed, for an aspect ratio of 1.73, a phase lag in pyramid wakes between a reference location (pressure signal on the side face of the pyramid) and the velocity fluctuations in the wake for several heights above the base plane, also suggesting tilting of wake vortices.

A few experimental studies have considered the shedding characteristic around the wall-mounted sphere. Most of the vorticity shed into the wake originates from shear layer separation at the sphere surface. Hot-wire anemometer were employed by Okamoto (1980) and Strouhal number of $St = 0.222$ was documented for sphere. Tsutsui (2008) demonstrated that power spectra have no prominent frequencies, when the sphere contact with boundary, indicating no organized vortex shedding from the wall-mounted sphere. This observation was confirmed with varying δ/D up to 2.11.

2.8 Summary

Compared to the number of studies on the subject of flow around bluff bodies, relatively few studies have focused on the turbulent wake of low-aspect-ratio bluff bodies. As a result, comprehensive information about the turbulence characteristics of the wake is not available in the prior studies.

For the flow structure around different low-aspect-ratio geometries, three dominant mean flow features are qualitatively robust: horseshoe vortex, tip vortex, and arch vortex. In addition to the three mentioned vortex structures, for higher aspect ratio obstacles, a pair of base vortex structures may be found close to the obstacle-wall junction (Etzold and Fiedler, 1976; Tanaka and Murata, 1999; Sumner

et al., 2004, Adaramola et al. (2006); Wang et al., 2006, 2009). They are distinguished from the tip and horseshoe structures by the fact that they induce an upwash on the symmetry plane of the wake.

Near the tip, vortex shedding is usually symmetric, and for sufficiently large aspect ratio H/D, the shedding mode may transition from the symmetric shedding (arch) near the tip to antisymmetric Karman shedding near the base. However, there is not general agreement about the aspect ratio at which the transition first appears (Wang and Zhou, 2009).

The base vortex is usually observed in relation to high-aspect-ratio geometries or in boundary layers that are thick of the order of the obstacle height (Sumner et al. 2004; Wang and Zhou, 2009). Interestingly, the base vortex is absent when the boundary layer is negligibly thin (Etzold and Fiedler, 1976; Okamoto and Sunabashiri, 1992; Park and Lee, 2000; Palau-Salvador et al., 2010). The base vortex induces upwash flow from the ground plane and is opposite in sense of rotation to the tip vortex (Sumner et al., 2004, Wang et al., 2006).

The role of the base vortex in the three-dimensional vortex structure of the wake is not well-understood. There is no consistent indication about nature of the base vortex. Furthermore, there is controversy about even the existence of the base vortex for a low-aspect-ratio obstacle. Most of the models here suggest that the base vortices are a projection of spanwise vortices. Sumner et al., (2004) proposed that vorticity emerging from free end suppresses spanwise vortex shedding at low-aspect-ratio. Therefore, the study concluded, the base vortices would not be expected at the lowest aspect ratio where spanwise vortex shedding expected to be suppressed. However, this is not a satisfying explanation since these vortices appear in time-averaged data, whereas the flow is unsteady periodic.

Vortex connectivity is another aspect of flow that poses many questions not resolved by the existing literature. For example, the base vortex connectivity

with other known vortical structures in the flow is not clear (even in mean-time averaged-flow). It is not evident whether the base (and tip) vortices are quasistationary, as in the case of a wing tip vortex, or if they are simply averages of many individual shed structures as in the model of Wang and Zhou (2009). Similarly, the question of whether the vertical vortices are connected across the tip shear layer or if they are merely bent back toward the obstacle at the free end are yet to be assessed conclusively. As a result, there is not a consistent 3-D model of wake structure (mean) for different geometries discussed.

In addition to the many questions and controversies in flow studies around bluff bodies, the literature reviewed here does not elucidate many concerns including the role of variation in geometry and especially the role of relative submergence (d/H) in the three-dimensional vortex structure of the wake. Besides, little research has been done on flow structure around bluff body in open channel and hydrodynamic effects on sediment transport around them. Also, characterization of fluctuations which govern scalar transport is not well-understood.

Therefore, the flow and sediment studies have not been combined to provide insight on total measures of bed shear stress that can be used to predict sediment transport characteristics in more complex riverine environments involving large obstacles. The time-averaged spatially-resolved bed shear stress distribution around the obstacles is key parameter for this kind of study. Also the bed shear stress has not been considered with varying Reynolds number, Froude number, Shields parameter, and relative submergence.

Finally, several open questions remain about interpretation of mean and instantaneous flow structure. Because the flow is aperiodic in time, a comparison of the mean and instantaneous flow characteristics shows that the flow deviates significantly with time such that the concept of a mean flow that consists of tip vortices and spanwise shedding and reattachment may be of limited physical significance

(Ballio et al., 1998; Vlachos and Hajj (2002); Pattenden et al., 2005). Therefore, the difference between the flow at any instant and the mean flow raises important questions as to the relevance of time averaged modeling methods to this class of flows.

On the way forward several key parameters will be considered. Table 2.1 lists several key parameters from selected studies relevant to the present work. For the constant $Re_H = 17,800$ will be used in this study, Re_D is in the range of 2 to 2.5×10^4. This is on the same order of magnitude as most studies presented in Table 2.1 and is an order of magnitude lower than the studies by Leder (2003) and Pattenden et al. (2005), which are in the critical Reynolds number range. Relative boundary layer thickness (δ/H) in this study will be 0.2 which is similar to the relative boundary layer thicknesses of most of the studies cited in Table 2.1. Also, while relative submergence varies considerably in some studies, there is considerable overlap between the values used in this study, and other works. However, similarities in relative submergence are often found for widely-varying obstacle aspect ratio.

Author(s)	$AR = H/D$	δ/D	d/H	$Re_D \times 10^4$
Tanaka and Murata (1999)	1.25-10	0.1	1.5-12	3.7
Leder (2003)	2	0.008	?	20
Sumner et al. (2004)	3-9	2.57	2.97-8.8	6
Pattenden et al. (2005)	1	0.1-0.2	3.63	20
Wang and Zhou (2009)	3-7	1.35	3.2-7.5	0.93
Palau-Salvador et al. (2009)	2.5, 5	0.25-0.5	1.96	4.3, 2.2
Krajnovic (2011)	6	0.067	3.33	2
Bourgeois et al. (2011b)	4	0.72	?	2
Present work	0.67, 0.89	0.2	1-5.5	1.96, 2.63

Table 2.1: Summary of previous experiments have been conducted on the wake of obstacles.

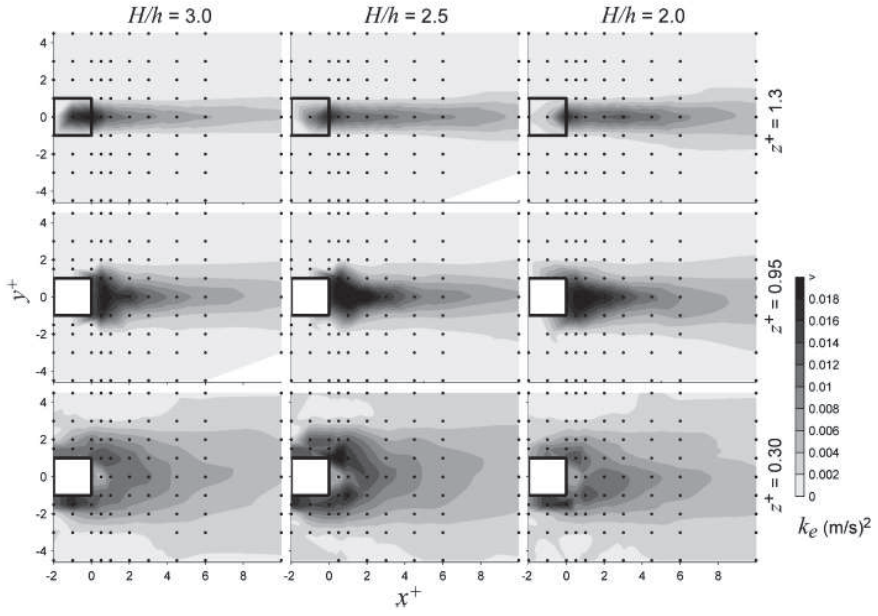

(a)

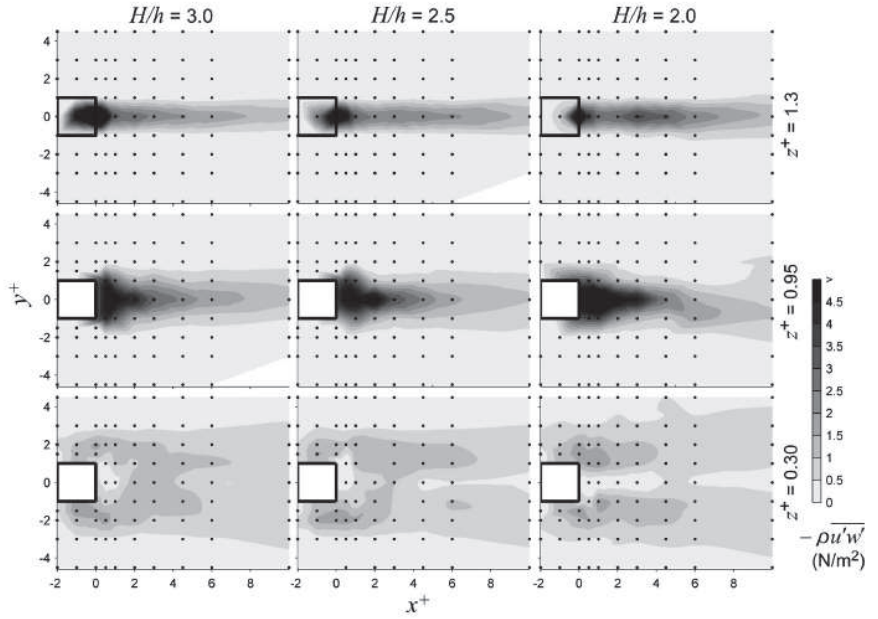

(b)

Figure 2.35: Spatial distributions are presented for experimental runs d/H=3.0, 2.5, and 2.0, and $x-y$ measurement planes $z^+ = 0.30$, 0.95, and 1.3: (a) Turbulent kinetic energy, k_e, in m^2/s^2, (b) Principal Reynolds shear stress $-\overline{u'w'}$ in N/m^2 (from Lacey and Rennie (2012).

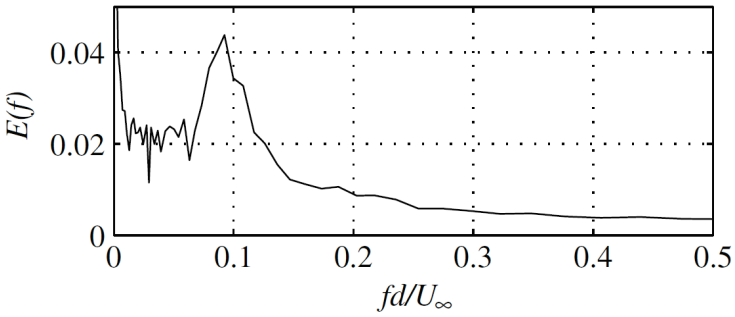

Figure 2.36: Power spectral density function of pressure measurements for cylinder of $AR = 1$ at midspan ($z/h = 0.5$), $U = 20$ m/s. The plot shows a peak in the energy spectrum of the pressure signal at 12 Hz (from Pattenden et al. (2005)).

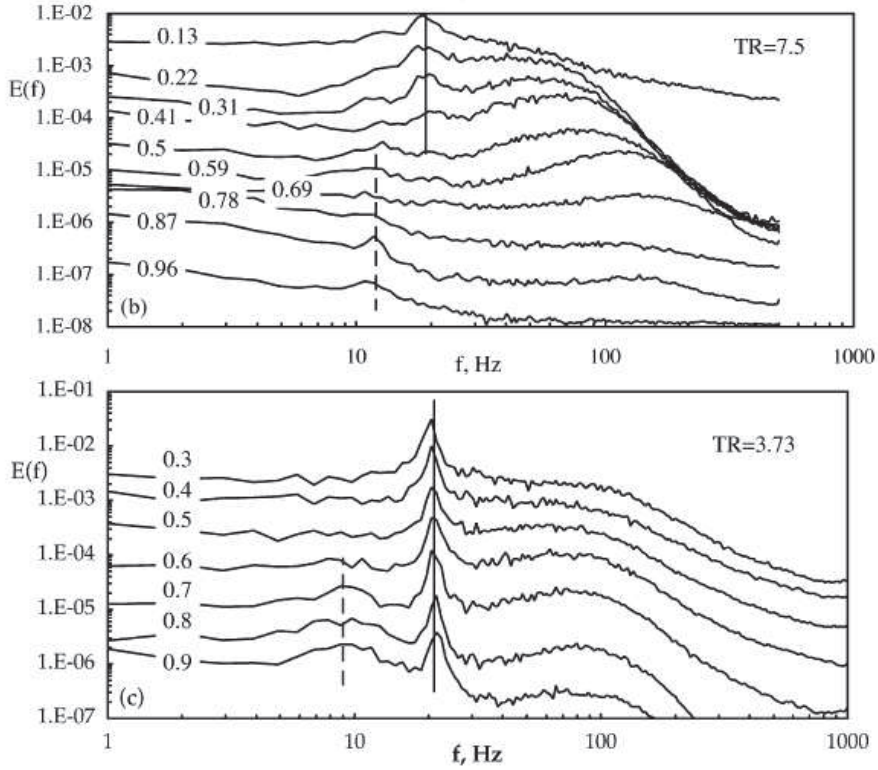

Figure 2.37: Spectral sequences for $TR = 7.5$ (top) and 3.73 (bottom). Curves are ordered vertically as indicated by the $z' = z/L$ values shown for each. The dashed line in follows the successive peaks which correspond to lower base frequency (Castro and Watson, 2004).

CHAPTER 3
EXPERIMENTAL FACILITY AND TECHNIQUES

In this chapter, the experimental set-up and the instrumentation used for this study are discussed. A water channel facility and the associated instrumentation– Digital Particle Image Velocimetry (DPIV), and thermal anemometry– are described. Measurements of the flow field and resulting wake structures were accomplished in a boundary layer flow for semi-ellipsoidal, cylindrical, and spherical obstacles. Flow visualization has been conducted at low Reynolds number to provide a qualitative understanding of the wake structure (Hajimirzaie et al., 2012). Two sets of experiments were conducted in high and low free stream turbulence. After completion the preliminary results, the plenum of the water channel was modified as will be described in Sec. 3.1.2. Most of measurements of this thesis were made after the overhaul in low free stream turbulence. Digital Particle Image Velocimetry (DPIV) and thermal anemometry were employed to interrogate the flow structures, shedding behavior, and turbulent characteristics in and around the wake.

3.1 Water Channel Facility and Flow Quality

Experiments were conducted in a closed-return, free-surface water channel of width 0.6 m, depth 0.3 m, and length 10 m. Two sets of experiments were conducted in high and low free stream turbulence. The free-stream streamwise turbulence intensity u'/U measured using DPIV where:

$$\frac{u'}{U} = \frac{1}{\overline{u(z)}} \sum_{i=1}^{N} \left(\frac{[u(z) - \overline{u_i(z)}]^2}{n} \right)^{1/2} \tag{3.1}$$

Here n=2500. In both conditions, the time-averaged flow outside of boundary layer was uniform to within 1%.

The honeycomb and screens were frequently cleared of tracer particles using a

jet of water, to prevent localized blockages and inhomogeneities in the flow.

An acrylic plate of length 1 m placed on the free surface eliminated surface waves, and allowed optical access from above the water channel in both high and low free stream turbulence experiments.

3.1.1 High Free-Stream Turbulence Flow

In the first set, the flow was conditioned with a honeycomb flow straightener, two stainless steel screens and two-dimensional 3 : 1 contraction. After measurements of mean flow velocity and turbulence intensity profiles at multiple locations in the test section, it was determined that measurements would be conducted approximately 5 m from the inlet due to favorable flow uniformity and comparatively low streamwise turbulence intensity of 7% as shown in Figs. 3.1 and 3.2.

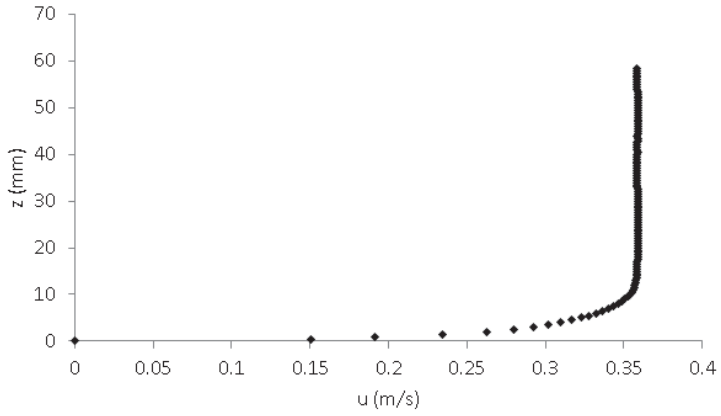

Figure 3.1: Mean velocity profile of boundary layer at high free stream turbulence flow on the plate at the location of the obstacle.z measured from the plate.

The integral length scale of the streamwise fluctuations in the free stream was measured from DPIV velocity measurements as demonstrated in ONeill et al. (2004). Integral length is determined from the autocorrelation function using the

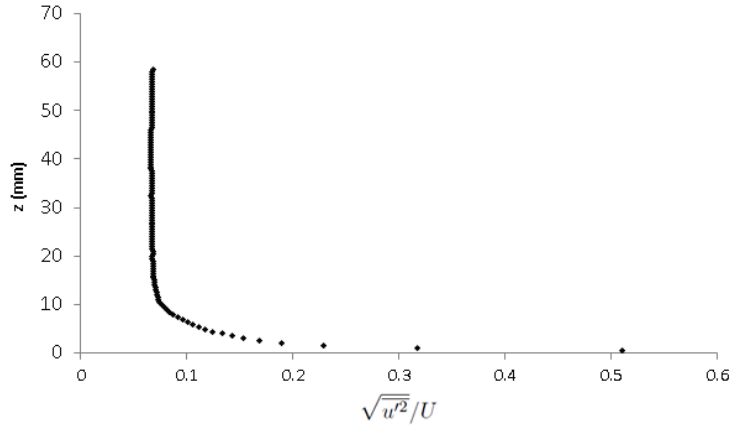

Figure 3.2: rms velocity profiles in the absence of the obstacle. z measured from the flume bed.

available spatial domain. The integral length scale of the velocity defined by:

$$L = \int_0^\infty R_{ii}(r,t)dr \tag{3.2}$$

where the double-i subscript in $R_{ii}(r,t)$ indicates the autocorrelation function (i.e. correlation of a velocity component with itself) defined by:

$$R_{ii} = \frac{\overline{u_i(x_i,t)u_i(x_i+r,t)}}{\overline{u_i^2}} \tag{3.3}$$

and r is the distance between two points in the flow and u_i, is the root-mean square velocity in the i-direction. The integration domain for the determination of the integral length as a representative length scale of the turbulence can be specified in a number of ways (ONeill et al., 2004). Here we calculate the integral length via integration over the entire available domain as shown in Fig. 3.3. The integral length scale of the streamwise fluctuations was found to be 10.7 mm approximately 0.3 m upstream of the base plate.

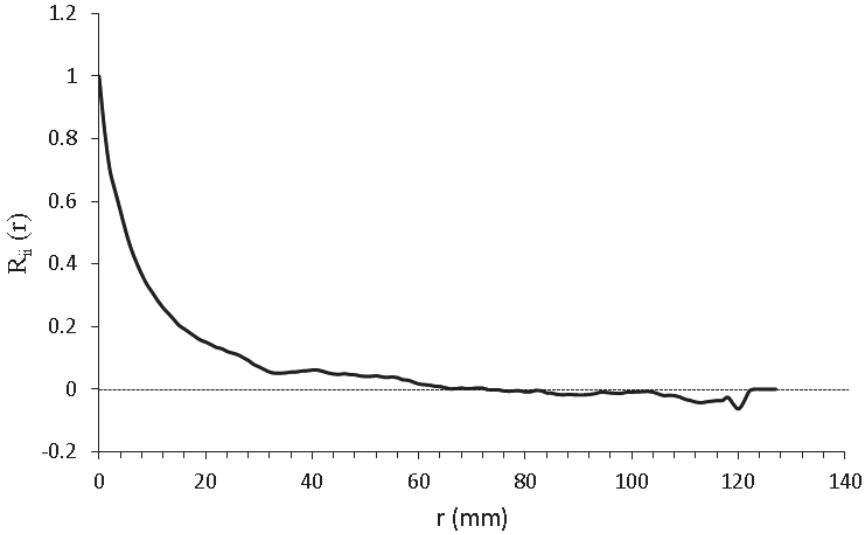

Figure 3.3: Longitudinal velocity auto-correlation function from PIV data

3.1.2 Low Free-Stream Turbulence Flow

After a significant overhaul of the flow conditioning apparatus, a three-dimensional 8 : 1 contraction, honeycomb, and screens were installed as visible in 3.4. Figure 3.5 illustrates the velocity profile obtained by DPIV. The turbulence intensity was found to be $\leq$ 0.3% as shown in Fig. 3.6. The results of measured turbulence intensity was confirmed in thermal anemometry experiments.

3.1.3 Measurement Conditions

The measurement conditions were kept constant in two sets of high and low free stream turbulence experiments. All the geometrical configurations for experiments were investigated at Reynolds numbers based on the height of the obstacle, $Re_H = UH/\nu = 17,800$, where U is the freestream velocity. For ellipsoids and cylinders, the flow depth d above the base plate was varied between 50 mm and 275 mm, providing relative submergences d/H between 1 and 5.5 as shown in Fig.3.7. With decreasing relative submergence, there is a concomitant reduction in flow velocity due to the slight redirection of flow around the test region. This results

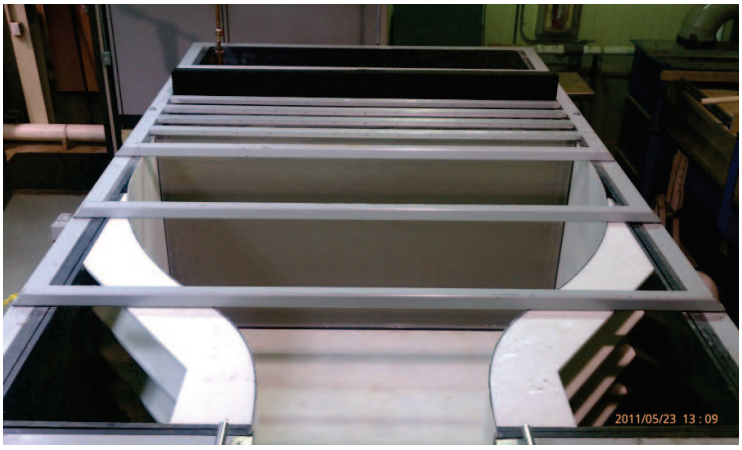

Figure 3.4: Plan view of head-box of the flume after overhaul.

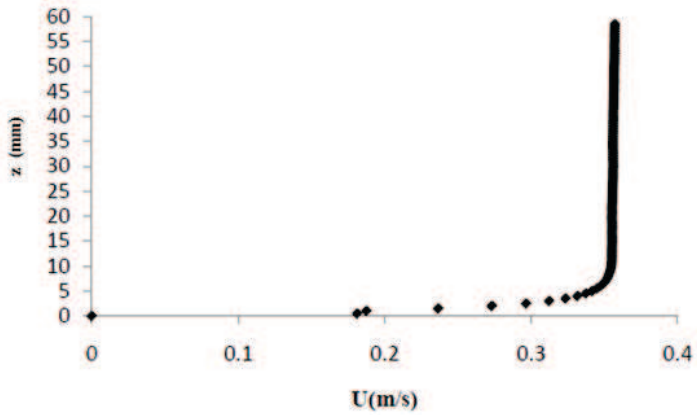

Figure 3.5: Mean velocity profile of boundary layer at low free stream turbulence flow on the plate at the location of the obstacle. z measured from the plate.

in a maximum reduction of Reynolds number of 3% and 8% at $d/H = 2.5$ and 1, respectively. This velocities were used to calculate Strouhal number in each relative submergence. For experiments around the sphere a constant relative submergence, d/H of 3.5 was investigated due to similarity to experiments of Papanicolaou et al. (2012a).

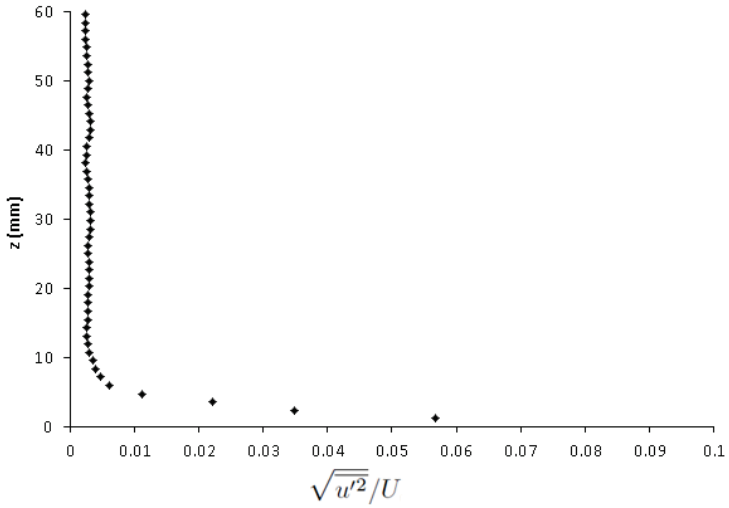

Figure 3.6: rms velocity profiles in the absence of the obstacle at low free stream turbulence. z measured from the flume bed.

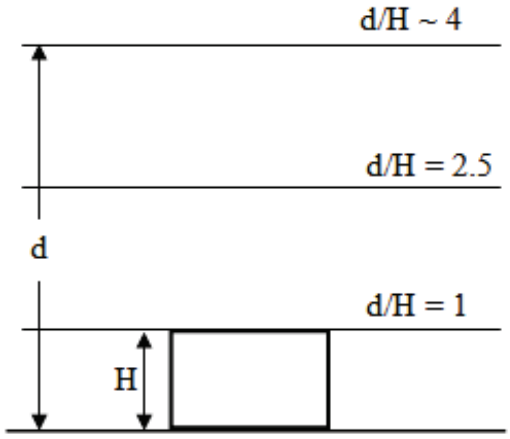

Figure 3.7: Schematic of different level of relative submergence.

3.2 Obstacle Geometries and Experimental Setup

Obstacle geometries and experimental setup were kept constant in high and low free stream turbulence experiments. Five wall-mounted obstacle geometries were investigated. The first two were formed by a semi-ellipsoidal body having a base ellipse with major and minor axes of 75 mm and 56 mm, respectively, and a height of

50 mm, as shown in Fig. 3.8. The obstacle was positioned with its major axis aligned with the flow (streamwise orientation) and perpendicular to the flow (transverse orientation). The shape was chosen to be broadly representative of a freshwater mussel emerging from the sediment on a river bed, but (more importantly for this study), they can be considered somewhat of a canonical geometry since they produce a relatively simple flow compared with other geometries. The relative dimensions of the three axes were determined from measurements of more than 50 mussel shells representing 14 species. The mussels were collected in a quadrat in Pool 16 of the Mississippi River near Fairport, IA (Nakato et al., 2007) as shown in Fig.3.9. However, this research focuses on the fundamental effects of shape on flow structure and not specifically mussel hydrodynamics. Defining the aspect ratio as the ratio of obstacle height, H, to base width, D, gives $H/D = 0.89$ and 0.67 for the streamwise and transverse ellipsoids, respectively. The other two geometries are circular cylinders of aspect ratios matching the ellipsoids, as illustrated in Fig. 3.11. The circular cylinders are included as a reference (baseline) since they bear greater similarity to geometries investigated in other studies. A sphere of diameter, D, 50 mm was employed for comparison with past and ongoing experiments on sediment transport in open channel flow (Papanicolaou and Kramer, 2005; Papanicolaou et al., 2012a). It should be noted that this thesis focuses on the flow structure in the wake and not specifically sediment transport hydrodynamics.

A 12 mm thick base plate of streamwise length 0.60 m and width 0.60 m with semi-circular leading edge was installed parallel to the bed. The top surface was offset 0.1 m from the bed. In the subsequent low-turbulence experiments, a similar plate with a super-elliptic leading edge was used to avoid the flow separation (Narasimha and Prasad, 1994). By analyzing the development of a laminar boundary layer on a two-parameter family of nose shapes, Narasimha and Prasad (1994)demonstrated that a cubic super-ellipse of axis ratio 6 or higher is a reason-

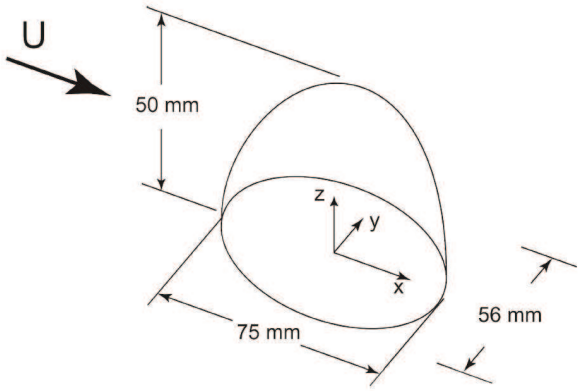

Figure 3.8: Coordinate system definition and idealized mussel geometry. The streamwise configuration is shown.

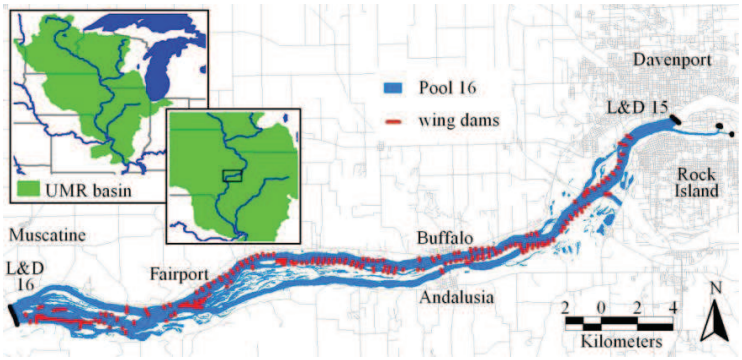

Figure 3.9: Mussels location map

able optimum shape for avoiding separation on or due to such nose-pieces. A super-ellipse equation was defined in Eq. (3.4).

$$[\frac{a-x}{a}]^n + (\frac{y}{b})^n = 1 \tag{3.4}$$

where a is the length of the nose $0 < x < a$ and $2b$ is the plate thickness. As shown in Fig. 3.12, the minimum axis-ratio for no separation is obtained for $n = 3.5$. As fig. 3.12 illustrates, with $n = 3.5$, the $a/2b$ can be defined from the y-axis, $a/2b =$

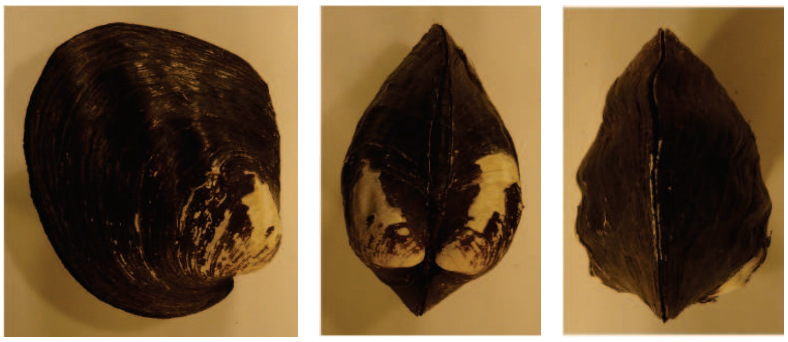

(a) musselside (b) musselupst (c) musseltop

Figure 3.10: Photographs of a Threeridge (Amblema plicata) mussel shell collected from Pool 16 of the Upper Mississippi River near Fairport, IA. (a) side view (flow left to right), (b) upstream-looking view, (c) top view (flow top to bottom).)

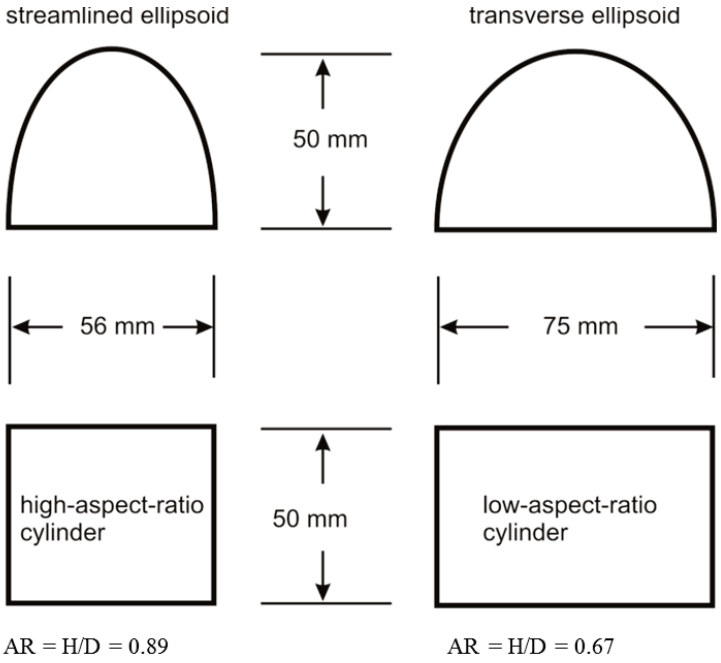

Figure 3.11: Streamwise projections of obstacle cross sections.

2.9. The thickness of plate for experiments in this thesis is 12 mm, therefore $2b = 12$ mm and a, the length of the nose for these experiments, was defined as $a = 35$ mm.

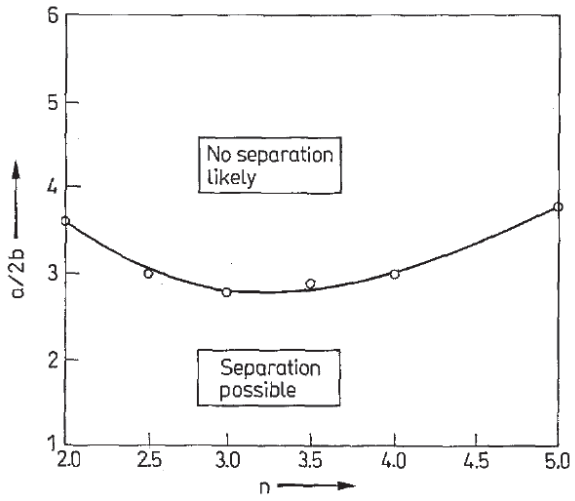

Figure 3.12: The boundary between separated and unseparated flow in the plane of the two nose shape parameters, axis ratio a/b and exponent n (Narasimha and Prasad, 1994).

Measurements of the flow in the vicinity of the leading edge verified that the flow over the leading edge was symmetric with the stagnation point on the center of the superelliptic edge and no flow separation was observed. The obstacle was centered 152 mm from the leading edge of the plate in each case. A schematic of the PIV and thermal anemometry setup, plan view of probe positions, and positions of Reynolds shear stress measurement around the sphere are shown in Fig. 3.13 through Fig. 3.15.

3.3 Flow Measurement Techniques

3.3.1 Digital Particle Image Velocimetry (DPIV)

Digital Particle Image Velocimetry (DPIV) (Adrian, 2005) is a whole-flow-field technique providing approximately instantaneous velocity vector measurements in a planar region of a flow. For seeding the flow, Potters Industries Inc.'s SPHERICEL Hollow Glass Spheres (mean diameter 10-11 μm) were used with a density of 1.1 g/cc.

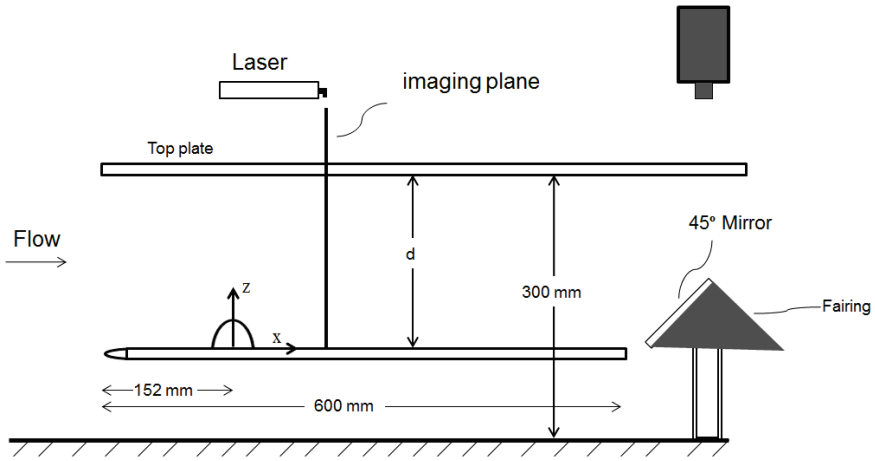

Figure 3.13: Side view of PIV experimental setup.

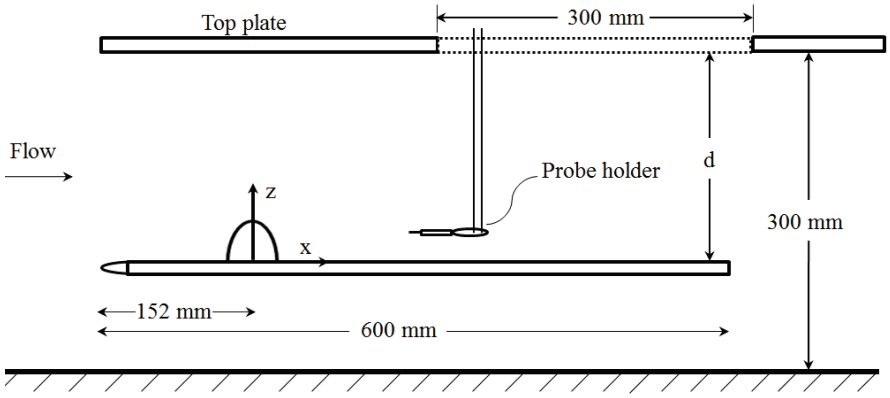

Figure 3.14: Side view of thermal anemometry experimental setup.

Two-component digital particle image velocimetry was used to characterize the freestream flow characteristics, the boundary layer on the plate in the absence of the obstacle, and the highly three-dimensional, unsteady flow surrounding the obstacle. A LaVision Inc. Flowmaster system was employed, consisting of a 2048×2048 pixel CCD camera with 14-bit dynamic range and a frame rate of approximately 7.2 frames/second, a dual-cavity 200 mJ/pulse Nd:YAG laser with

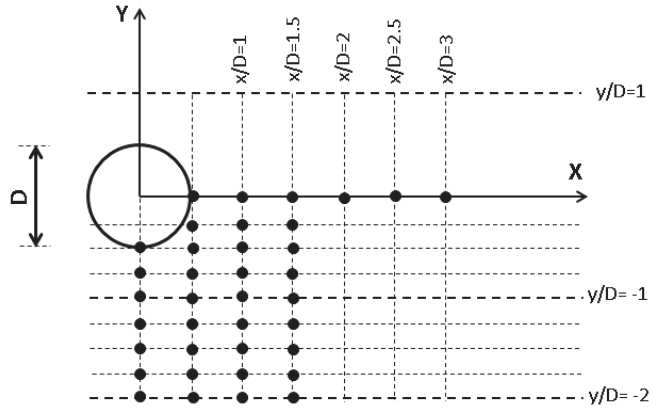

Figure 3.15: Plan view of probe positions in thermal anemometry experiments. Dotted-line shows the access window cut into the upper plate to facilitate positioning of hot-film probes.

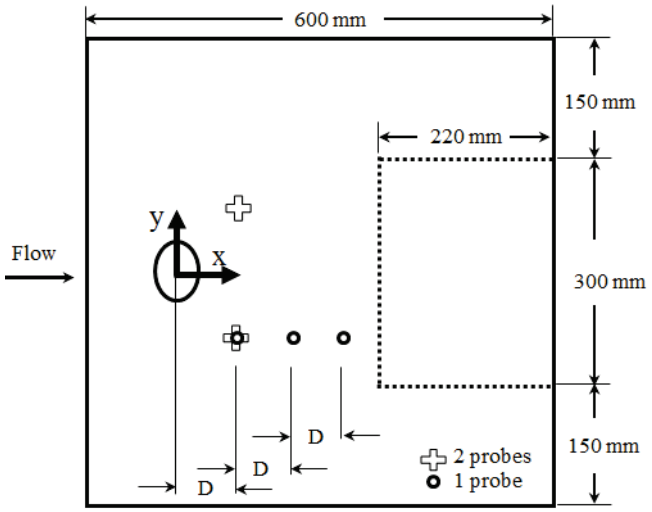

Figure 3.16: Locations of Reynolds shear stress measurement around the sphere.

light sheet optics, and a PC-based timing and data acquisition system managed by LaVision DaVis 7.2 and DaVis 8.1 software. The camera was equipped with Nikon 105-mm Micro-Nikkor lenses. To obtain images in transverse planes, a front surfaced mirror with dimensions 60 × 85 mm was installed at a 45° angle

downstream of the base plate (approximately 0.5 m downstream of the obstacle trailing edge) as shown in Fig. 3.13. The transfered images by mirror were such that positions and consequently velocities in the transverse direction were reversed, and a correction was applied to the computed velocity field.

Standard cross-correlation analysis was employed in multiple passes on window sizes of 64×64 pixels and 32×32 pixels with 50% overlap, to produce $128 \times 128 = 16384$ vectors. A local median filter was used to eliminate outliers. DPIV data were acquired by illuminating a plane of the seeded flow twice with a laser sheet in two orthogonal sets of planes: the symmetry plane ($y = 0$), *side view* images, downstream of the obstacle, and transverse ($y - z$) planes, *upstream* images, at $x/H = 1.00$, 1.50, 2.00, and 3.00 as shown in Fig. 3.17. The spatial resolution of the resulting velocity vector fields was approximately 0.625 mm, or $H/80$. For experiments around the sphere, DPIV data were also acquired in two orthogonal sets of planes: the symmetry plane ($y = 0$) downstream of the sphere, and transverse (y-z) planes at $x/H = 0.5$, 1.00, 1.50, 2.00, 3.00, and 4.00. The spatial resolution of the resulting velocity vector fields was approximately 0.55 mm, or $D/90$. In addition to these measurements, the fine transverse (y-z) planes with the increment of x/D =0.1 is considered in the wake of the sphere from $x = 0$ to $x = 12.5$ mm to shed more lights on the evolution of the structures in the wake. The obtained DPIV data in upstream view ($y - z$) and side view ($x - z$) of sphere were used to measure the Reynolds shear stress distribution around the sphere as shown in Fig. 3.15 where the Reynolds shear stress is:

$$\tau_{t,p}(x, y, z) = [(-\rho\overline{u'w'})^2 + (-\rho\overline{v'w'})^2]^{1/2} \tag{3.5}$$

where u', v', and w' are the velocity fluctuations of the streamwise, transverse, and vertical components and denotes an average. Figure 3.18 illustrates one example of defining shear stress locations from intersection of $x - z$ and $y - z$ planes.

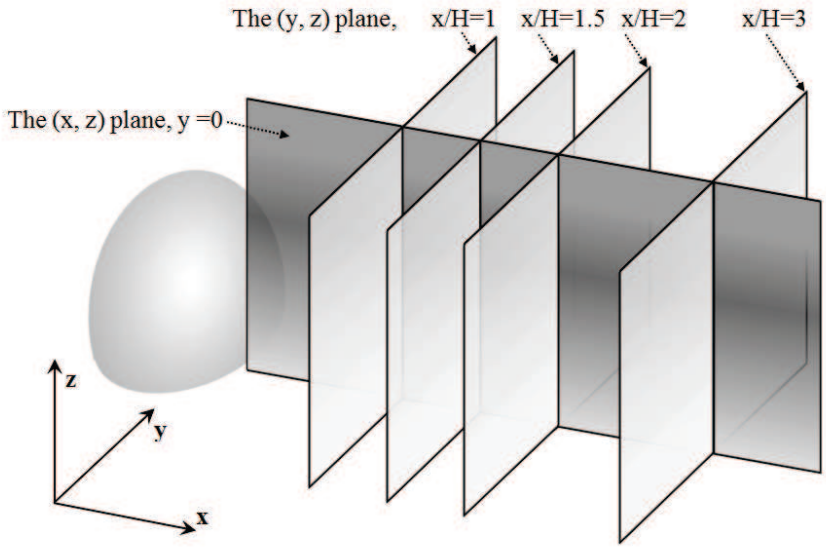

Figure 3.17: Experimental DPIV measurement planes.

Since the DPIV data in the upstream view and the side view of sphere were obtained separately, the z-axis magnitude, i.e. the spacing between vectors created in the PIV vector files in the vertical direction (z-direction), in DPIV images of side and upstream planes were not constant (using a data file exported from LaVision). Therefore a Matlab code was developed to interpolate the Reynolds stress in a constant specific locations in both planes. Although the spacing between vectors, Z_g, in the side and upstream planes were close to each other (for instance at $y = 0$, one of the planes' intersection, Z_g =0.853699 and in $x/D = 1$, Z_g =0.8571), the spline quadratic interpolation method was employed to define constant specific locations (similar z values) for the Reynolds shear measurements.

To calculate the total shear stress, the mean shear stress has also been measured from the velocity profile in $(x - z)$ and $(y - z)$ planes and added to corresponding Reynolds shear stress, $-\rho\overline{u'w'}$ and $-\rho\overline{v'w'}$. The mean shear stress for $(x - z)$ plane is:

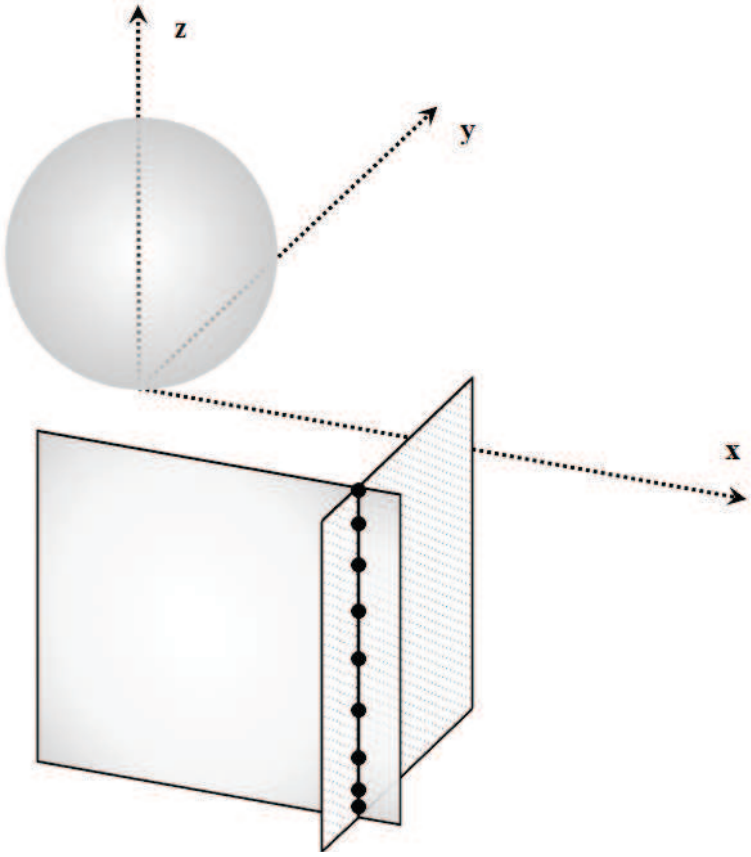

Figure 3.18: Intersection of $x-z$ and $y-z$ planes for Reynolds shear stress measurement around the sphere. Planes in figure are $x-z$ plane at y/D =-1 and $y-z$ plane at x/D =2.

$$\tau_{x,z} = \mu \frac{du}{dz} \tag{3.6}$$

where μ is dynamic viscosity. Similarly, the mean shear stress defined for $(y-z)$ plane.

From the velocity field, the out-of-plane vorticity can be calculated discretely by taking the curl of the velocity field as shown by Eq. 3.7.

$$\omega_x = \frac{\partial U_z}{\partial y} - \frac{\partial U_y}{\partial z} \approx \frac{U_{z_{j+1}} - U_{z_{j-1}}}{2Y_g} - \frac{U_{x_{k+1}} - U_{x_{k-1}}}{2Z_g} \tag{3.7}$$

Where j is in the y-direction while k is in the z-direction. U_y and U_z are the velocities in the y- and z-direction, respectively, and Z_g and Y_g are the grid spacing between the velocity vectors in the z- and y-direction, respectively.

Circulation (Eq. 3.8) was computed for various streamwise structures identified in the flow in different relative submergences. A user defined threshold was chosen such that the circulation was insensitive to changes in the threshold.

$$\Gamma = \int_A \omega_x dA \approx \sum_N \omega_{x_{kj}} \Delta z \Delta y \tag{3.8}$$

3.3.2 Hot-Film Anemometry

Measurements of the vortex shedding frequency and phase relationship between different points in the flow field were obtained using constant-temperature anemometry with a TSI IFA-300 anemometer, a single-sensor, cylindrical hot-film probe (TSI model 1210-20), a National Instruments (NI 6216, 16-bit resolution) data acquisition board and collected using LabVIEW. The probe dimensions have been presented in Fig. 3.19.

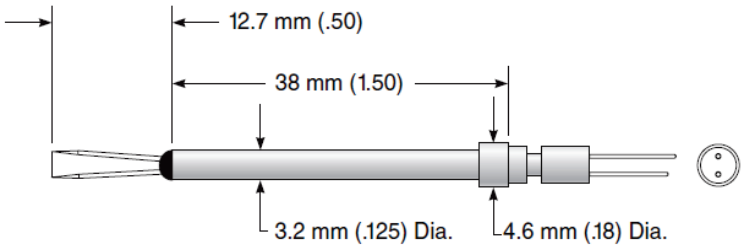

Figure 3.19: Cylindrical hot-film probe (TSI model 1210-20)

Thermal anemometry is a technique that utilizes heat transfer to measure the

instantaneous velocity. The operation of constant-temperature anemometer (CTA) which has been employed here is based on dependency of resistance on temperature. The anemometer keeps resistance constant by employing the wire in a Wheatstone bridge with feedback control.

The hot-film probes were calibrated against a propeller-type current meter (Nixon-type 430) in the free-stream in the range 0.1 $m/s < U <$0.45 m/s. In all cases, the axis of the hot-film sensor was horizontal and the overheat ratio was 1.06.

In low free stream turbulence experiments, a window (void) was cut in the acrylic surface plate with dimensions 300×300 mm, with the upstream edge of the window 168 mm downstream of the center of the obstacle to allow access for the hot-film probe supports. For comparison, a plate with only a narrow streamwise slot 25×300 mm was also employed for probe access. The velocity and spectral results were in agreement in both cases, so the window was used since it provided much greater flexibility for probe positioning and model access.

For each geometry, the probe was positioned in the range $1 \leq y/D \leq 3$ and $0.5 \leq x/D \leq 3$. The probe was moved along the obstacle height in increments of $0.25H$. The signal from the hot-film was offset, low-pass filtered at a cutoff frequency of 300 Hz, and then sampled at a frequency of 1 kHz. The sampling duration for each record was 80 seconds. Power spectral density plots shown here were generated from an average of 20 spectra.

Cross-correlation functions as shown in Eq. 3.9 were calculated via two single hot-film probes positioned symmetrically at $x/D = 1$, $y/D = \pm 1$, with varying spanwise position $0.25 \leq z/H \leq 1$.

$$R_{u_1 u_2}(\tau) = \int_{-\infty}^{\infty} u_1(t) u_2(t+\tau) dt \tag{3.9}$$

To further explore the ellipsoid wake model proposed in Ch. 4 and Sec. 4.2.4, two-point hot-film measurements were performed at $x/D = 1$ and $y/D = 1$, for both ellipsoids, with one probe fixed at $z/H = 0.25$ and the other traversed in the range $0.5 \leq z/H \leq 1$ with increments of $\Delta z/H = 0.25$ as shown in 3.20. Figure 3.21 illustrates the orientation of the sensor in the flow.

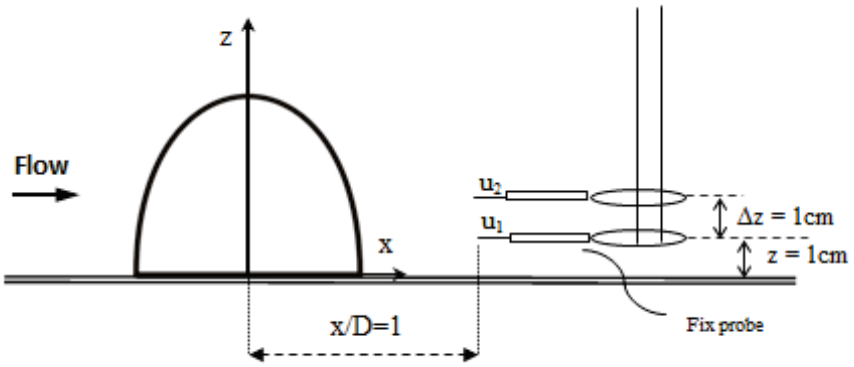

Figure 3.20: Two-point hot-film measurements

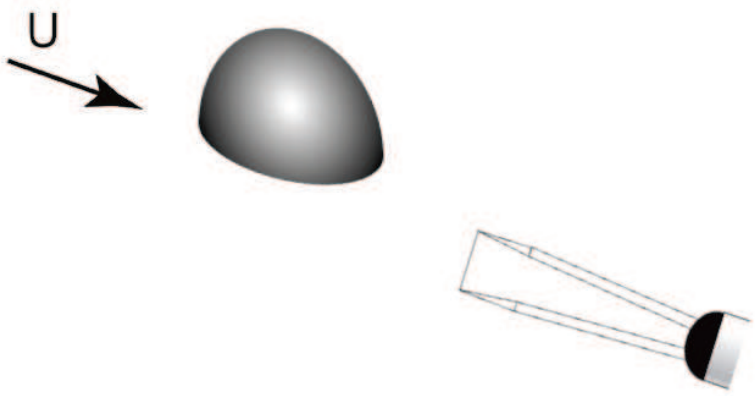

Figure 3.21: The orientation of the sensor in the flow]

By the Wiener-Khintchine theorem, the cross-spectral density function for signals u_1 and u_2 (Eq. 3.10) form a Fourier transform pair with the cross-correlation function (Ochi, 2005).

$$S_{u_1u_2}(f) = 2\int_{-\infty}^{\infty} R_{u_1u_2}(\tau)e^{-i2\pi ft}d\tau = C_{u_1u_2}(f) + iQ_{u_1u_2}(f) \tag{3.10}$$

The real part of the cross-spectral density, $C_{u_1u_2}(f)$ (co-spectrum) and imaginary part, $Q_{u_1u_2}(f)$ (quadrature spectrum), defines the phase shift between the two signals at frequency f:

$$\phi(f)_{u_1u_2} = tan^{-1}\frac{Q(f)_{u_1u_2}}{C(f)_{u_1u_2}} \tag{3.11}$$

The spectral coherence was also computed as shown in Eq. 3.12.

$$\mathrm{Coh}_{u_1u_2}(\mathrm{f}) = \frac{\mathrm{C}^2_{u_1u_2}(\mathrm{f}) + \mathrm{Q}^2_{u_1u_2}(\mathrm{f})}{\mathrm{S}_{u_1}(\mathrm{f})\mathrm{S}_{u_2}(\mathrm{f})} \tag{3.12}$$

CHAPTER 4
FLOW CHARACTERISTICS AROUND A WALL-MOUNTED SEMI-ELLIPSOID

In this chapter, dye visualization, DPIV, and thermal anemometry are used to investigate the effect of shape and relative submergence (the ratio of flow depth to obstacle height, d/H) on the wake around four different low-aspect-ratio wall-mounted obstacles and its evolution with downstream distance. A vortex skeleton model is also proposed through observation of the wake structures and their shedding behaviors.

Two sets of experiments are conducted in high and low free-stream turbulence. As described in Sec. 3.1, the plenum of the water channel was modified resulting in a low free-stream turbulence intensity. Therefore, the preliminary results of Sec. 4.1 have been completed in low free stream turbulence flow, Sec. 4.2.

4.1 High Free-Stream Turbulence Flow

4.1.1 Boundary Layer Characteristics

Boundary layer characteristics have been measured from the profile of the streamwise mean velocity on the plate at the location of the obstacle as it has been illustrated in Fig. 3.5. In the absence of obstacles, a boundary layer of thickness $\delta_{99}/H = 0.2$ was present on the plate at the location of the obstacle center in the high free-stream turbulence flow. Therefore δ/D were 0.133 and 0.179 for the streamwise and transverse ellipsoids, respectively, and the similarly-dimensioned cylinders. The displacement thickness (δ^*) and momentum thicknesses (θ) were δ^*=0.94 mm and $\theta = 0.66$ mm, providing a shape factor of 1.44. Despite the relatively low boundary layer Reynolds numbers - $Re_x \approx 54,000$, the profiles are not very representative of a Blasius profile (shape factor $H_{sf} = 2.59$), likely due to the relatively high free stream turbulence intensities.

4.1.2 Flow Patterns in the Streamwise Symmetry Plane

Some basic properties of the flow are first characterized by examining the velocity, vorticity, and Reynolds shear stress fields on the symmetry plane in the wake of the obstacle. Figures 4.1 through 4.3 contain the mean streamlines, each obtained from 2000 velocity fields, in the symmetry plane upstream and downstream of each of the geometries. The cross section of the time-averaged horseshoe vortex can be seen upstream of the obstacle junction (Fig.4.1). Similar results were observed in the upstream of the cylinders in agreement with Baker (1980). The horseshoe vortex is smaller for the streamwise ellipsoid than transverse ellipsoid. Figure 4.2 shows the topology of the time-averaged horseshoe vortex system in a closer view upstream of transverse ellipsoid. Similar topology is observed for the streamwise ellipsoid. The vortices are numbered 1 and 2, with vortex 1 being the called primary vortex and 2 the secondary vortex. The height of the primary vortex is $z/H = 0.05$ or 0.25δ. The streamlines reveal that there is also a saddle point in the horseshoe system of transverse ellipsoid which is also observed at the upstream of the cylinders in other studies (Baker, 1980; Pattenden et al., 2005). Similar to Pattenden et al., (2005), a third thin vortex between vortex 1 and 2 which has been suggested by Baker (1980) was not found in the present work.

Table 4.1 contains the reattachment lengths on the symmetry plane non-dimensionalized by the obstacle height and width. Reattachment lengths were defined where the velocity gradient off the wall is zero or in other words, where the wall shear stress is zero. The longest reattachment lengths (x_r/H) are observed for the low-aspect-ratio cylinder ($AR = 0.67$) and the transverse ellipsoid, which have the same aspect ratio and very similar reattachment lengths ($x_r/H = 2.45$ and $x_r/H = 2.41$, respectively). However, the streamwise ellipsoid and cylinder of matching aspect ratio have more disparate reattachment lengths; the streamwise ellipsoid having a much

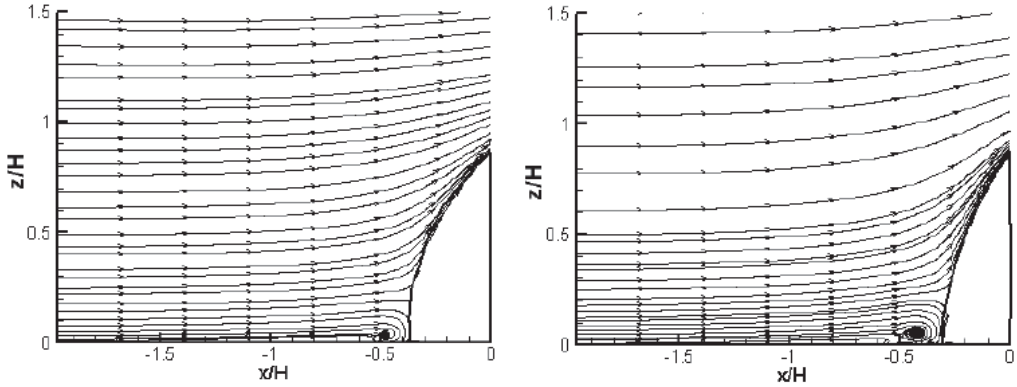

Figure 4.1: Mean streamlines upstream of the ellipsoids in $d/H = 3.9$: Streamwise ellipsoid (left), and transversely-oriented ellipsoid (right).

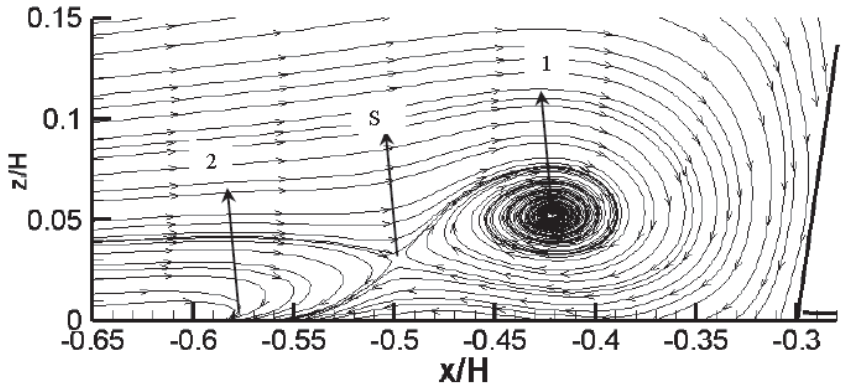

Figure 4.2: Topology of horseshoe vortex system upstream of the transverse ellipsoid in $d/H = 3.9$.

shorter reattachment length ($x_r/H = 1.9$) than the cylinder. The same conclusions can be made by comparing values of x_r/D, which are more commonly reported, and are also presented in Table 4.1. In general, these measurements are similar to others reported in the literature for low-aspect-ratio wall-mounted bodies. Hunt et al. (1978) and Hussein and Martinuzzi (1996) observed reattachment lengths of $1.6D$ for a surface-mounted cube. For a circular cylinder of aspect ratio 1, Okamoto

and Sunabashiri (1992) found $x_r/D = 2.9$. For $AR = 2$, Leder (2003) and Frederich et al. (2008) found $x_r/D = 2.2$ and $x_r/D = 2.9$, respectively, and Sumner et al. (2004) noted $x_r/D = 3$ for $AR = 3$. Pattenden et al. (2005) reported $x_r/D = 1.6$ for a circular cylinder of $AR = 1$ at $Re_D = 20 \times 10^4$. For a hemisphere, more representative of the ellipsoid geometries studied here, Savory and Toy (1986) reported reattachment lengths between $1.1D$ and $1.25D$ (varying with boundary layer parameters) in boundary layers significantly thicker than that in the present study.

Obstacle	x_r/H	x_r/D
Streamwise ellipsoid	1.90	1.70
Transverse ellipsoid	2.41	1.61
Cylinder (AR=0.89)	2.24	2.00
Cylinder (AR=0.67)	2.45	1.63

Table 4.1: Mean dimensionless reattachment lengths on the symmetry plane measured from the obstacle center line, and nondimensionalized by obstacle height (which remains constant for all obstacles) and obstacle diameter.

Isocontours of non-dimensional transverse vorticity ($\omega_y^* = \omega_y H/U$) are shown in Fig. 4.4. In addition to the regions of large positive ω_y (counter clockwise rotation) located in the vicinity of the shear layer separating from the top of the obstacle, significant negative vorticity is found for each geometry adjacent to the base plane in the vicinity of the recirculation region. Large negative values of vorticity also exist on the lee faces of the ellipsoids.

The distributions of kinematic Reynolds shear stress ($-\overline{u'w'}/U^2$) in the wake of the obstacles are shown in Fig. 5.5. The lowest magnitudes occur for the streamwise ellipsoid. There is a fundamental difference between the flow field over the two

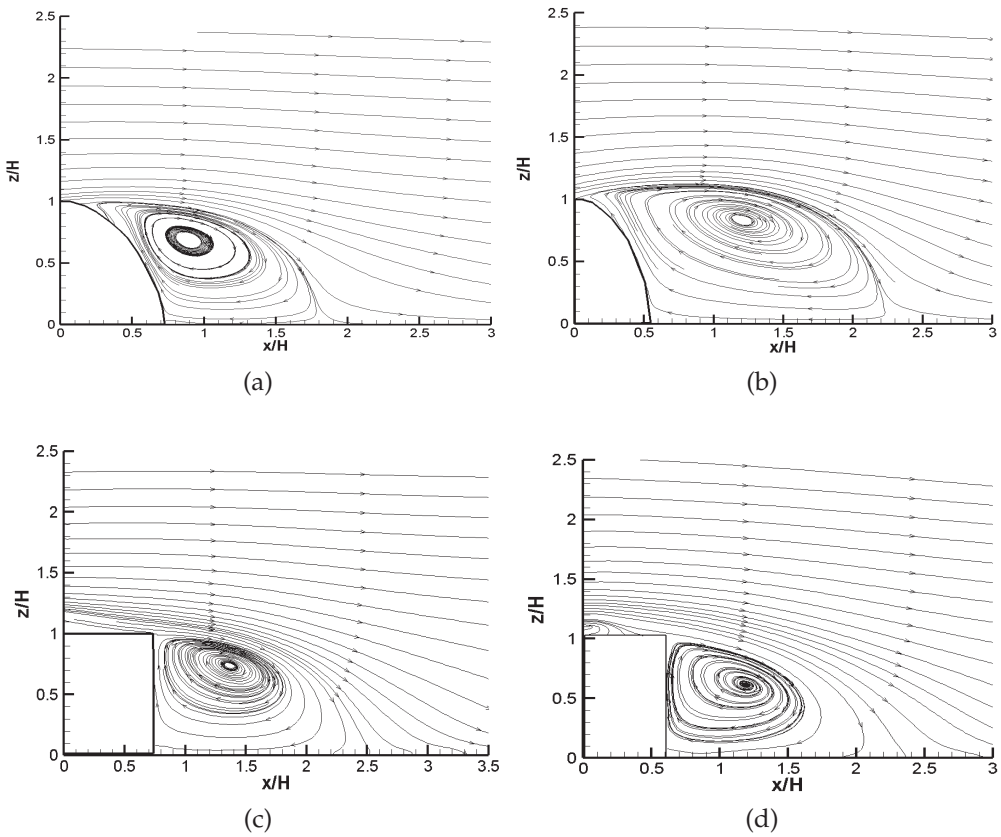

Figure 4.3: Mean streamlines downstream of the obstacle in $d/H = 3.9$ for: (a) Streamwise ellipsoid, (b) transverse ellipsoid, (c) cylinder (H/D=0.89) and (d) cylinder (H/D=0.67).

ellipsoids and that over the cylinders. On the symmetry plane, the cylinders have separation points on the top surface at the leading and trailing edges. The shear layer over the separated region on the end of the cylinders transitions to turbulence before reattaching, and therefore, there are higher turbulence intensities in the shear layer separating from the downstream edge of the cylinders. In contrast, for the ellipsoids, there is only one separation point, near the top of the structure, and therefore the Reynolds stresses are significantly lower just after separation.

Distributions of the turbulence intensities $(v'^2 + w'^2)/U^2$ measured in transverse planes as shown in Fig. 4.6 which indicate peak values near the symmetry plane

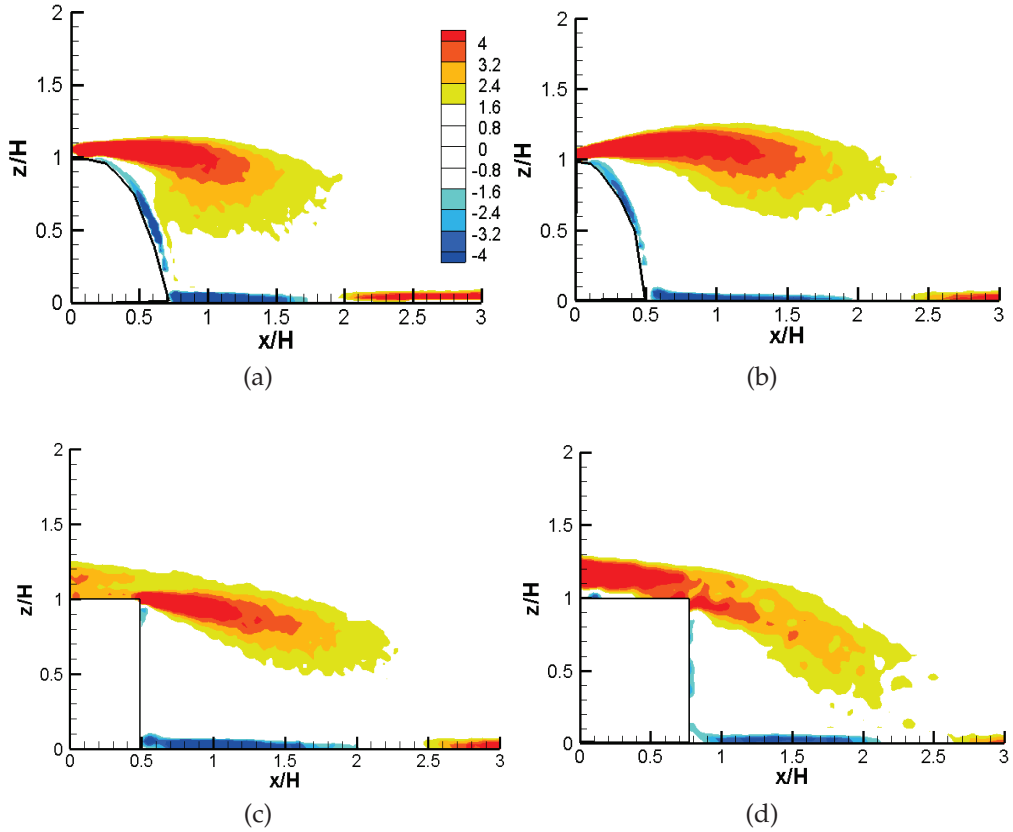

Figure 4.4: Isocontours of non-dimensional spanwise vorticity, ω_y^*, downstream of the obstacle in $d/H = 3.9$ for: (a) streamwise ellipsoid, (b) transverse ellipsoid, (c) cylinder (AR=0.89) and (d) cylinder (AR=0.67). Red shades indicate counter-clockwise rotation and blue shades indicate clockwise rotation.

coincident with the locations of high Reynolds stresses shown in Fig. 5.5. However, maximum turbulence intensities in the cylinder wakes appear near the lateral edges of the cylinder.

4.1.3 Streamwise Vorticity Distributions

Figures 4.7 through 4.11 display isocontours of streamwise dimensionless vorticity ($\omega_x^* = \omega_x H/U$) in the wakes of the obstacles in transverse (y-z) planes between $x/H = 1$ and 4, with $d/H = 3.9$ using the experimental configuration shown in Fig. 3.13. Comparison with Table 4.1 indicates that the planes at $x/H = 1$, 1.5 and 2

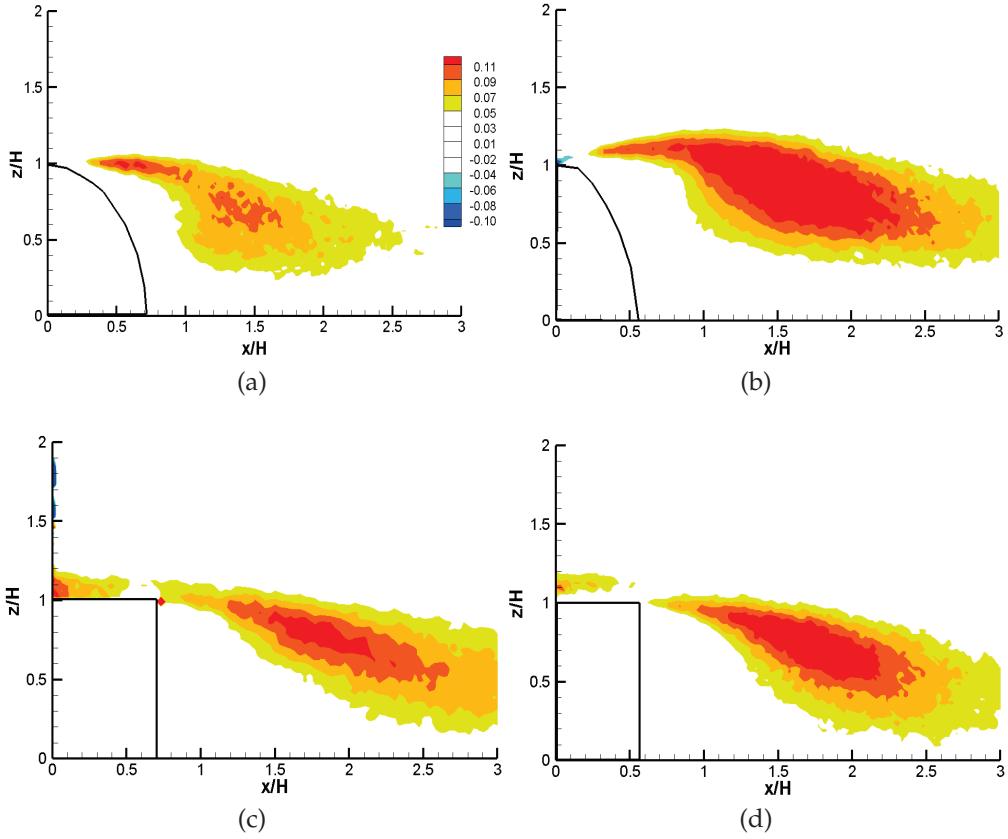

Figure 4.5: Isocontours of Reynolds shear stress, $-\overline{u'w'}/U^2$, downstream of the obstacle in $d/H = 3.9$ for: (a) streamwise ellipsoid, (b) transverse ellipsoid, (c) cylinder (AR=0.89) and (d) cylinder (AR=0.67).

fall within the recirculation region for all obstacles except the streamwise ellipsoid (where $x/H = 2$ is downstream of the reattachment point). Each mean vorticity field was obtained from 3000 instantaneous velocity fields.

Fig. 4.7 contains streamwise vorticity located at $x/H = 1$ for the four geometries. The streamwise vorticity distribution in the wake of the streamwise ellipsoid at $x/H = 1$ (Fig.4.35a) is similar to that observed by Pattenden et al. (2005) in the wake of a low-aspect-ratio cylinder and is dominated by the tip and horseshoe structures. Results reported in the literature and summarized in section 2.5 suggest that this might be expected for a low-aspect-ratio geometry in a thin boundary

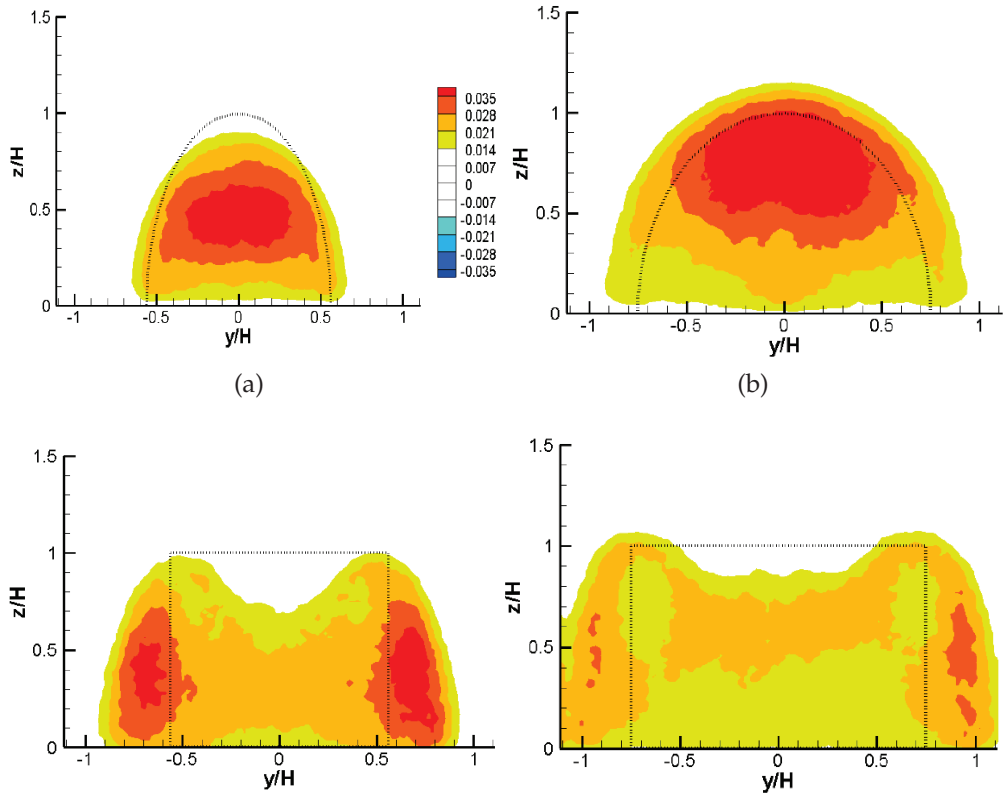

Figure 4.6: Isocontours of non-dimensional turbulence intensities $(v'^2 + w'^2)/U^2$, downstream of the obstacle at $x/H = 1.5$ and d/H =3.9 for: (a) streamwise ellipsoid, (b) transverse ellipsoid, (c) cylinder (AR=0.89) and (d) cylinder (AR=0.67).

layer. However, for the transverse ellipsoid (Fig.4.35b), a relatively subtle change in obstacle geometry, the flow is dominated by a strong vortex pair inducing upwash. It is noteworthy that the presence of upwash or downwash in the ellipsoid wakes is consistent with the empirical rule of Mason and Morton (1987) for very low-Reynolds number flows ($Re_H = O(100)$). Mason and Morton (1987) proposed: wide obstacles (aspect ratio< 1), which direct more flow over their crest, produce a dominant vortex pair with a central upwash (i.e. a base vortex), while tall, narrower obstacles (aspect ratio>1), in which the flow is preferentially directed around the sides produce a dominant vortex pair with central downwash (ie. a tip vortex).

As Figs. 4.7c and 4.7d show, base structures also exist, concurrently with the tip vortices, in the wakes of the cylinders at $x/H = 1$. This is contrary to the results of Pattenden et al. (2005) in which a similar geometry was examined at $Re_H = 200,000$.

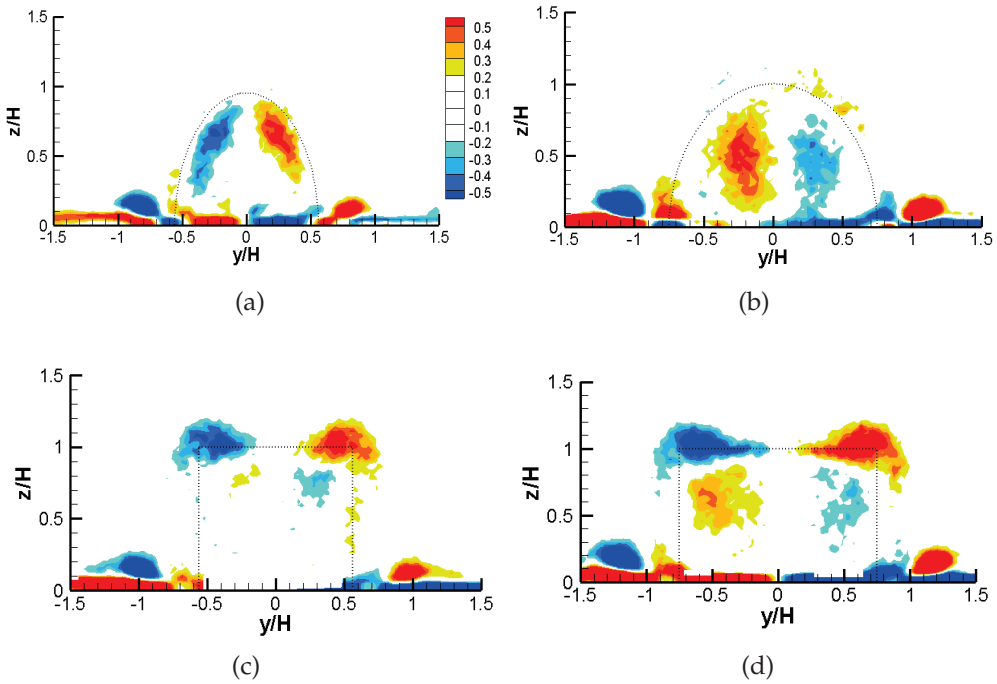

Figure 4.7: Isocontours of non-dimensional streamwise vorticity, ω_x^*, in the plane $x/H = 1$ at $d/H = 3.9$ for: (a) streamwise ellipsoid, (b) transverse ellipsoid, (c) cylinder (H/D=0.89), and (d) cylinder (H/D=0.67). Red shades indicate counter-clockwise rotation and blue shades indicate clockwise rotation.

Fig. 4.8 illustrates the streamwise vorticity patterns at $x/H = 1.5$. Here also, the tip vortex pair is dominant in the wake of the streamwise ellipsoid and the base vortex pair is dominant in the transverse ellipsoid. The distribution of the tip vortices is very different for the high- and low-aspect-ratio cylinders (Figs. 4.8c and 4.8d). For the low-aspect-ratio cylinder (AR=0.67) the tip vortices remain at approximately the same vertical position, but they are significantly sheared toward

the base plane in the wake of the higher-aspect-ratio cylinder. Furthermore, at $x/H = 1.5$ the base vortex is no longer evident in the wake of the high-aspect-ratio cylinder, and the wake of the low-aspect-ratio cylinder now contains a tertiary vortex pair of the same sign as the tip vortex near the base plane (Fig. 4.8d).

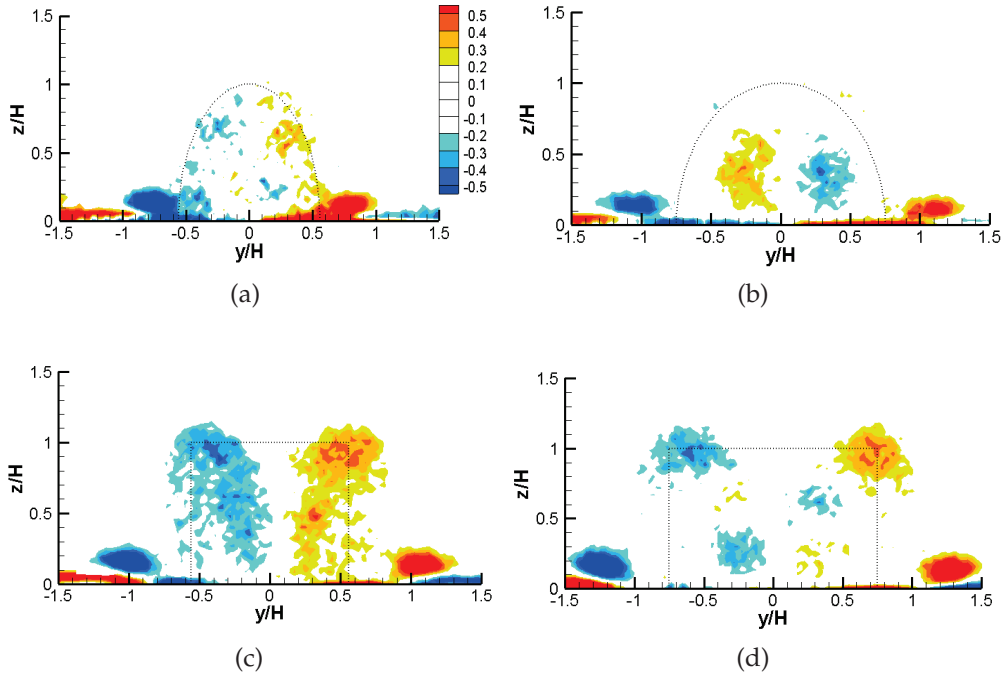

Figure 4.8: Isocontours of non-dimensional streamwise vorticity, ω_x^*, in the plane $x/H = 1.5$ in $d/H = 3.9$ for: (a) Streamwise ellipsoid, (b) transverse ellipsoid, (c) cylinder (AR=0.89), and (d) cylinder (AR=0.67). Red shades indicate counter-clockwise rotation and blue shades indicate clockwise rotation.

Similarly, Fig. 4.9 shows streamwise vorticity distributions at $x/H = 2$. At this position, the base vortex pair is not visible for either of the cylinders. The shearing of the tip structure created by the low-aspect-ratio cylinder is now evident (Fig. 4.9c), as it was for the higher-aspect-ratio cylinder wake at $x/H = 1.5$. The comparatively delayed evolution of the tip vortices for the low-aspect-ratio cylinder is consistent

with the longer separated region of the low-aspect-ratio cylinder quantified in Table 4.1. Although the base structure is still evident in the wake of the transverse ellipsoid, it is significantly weakened.

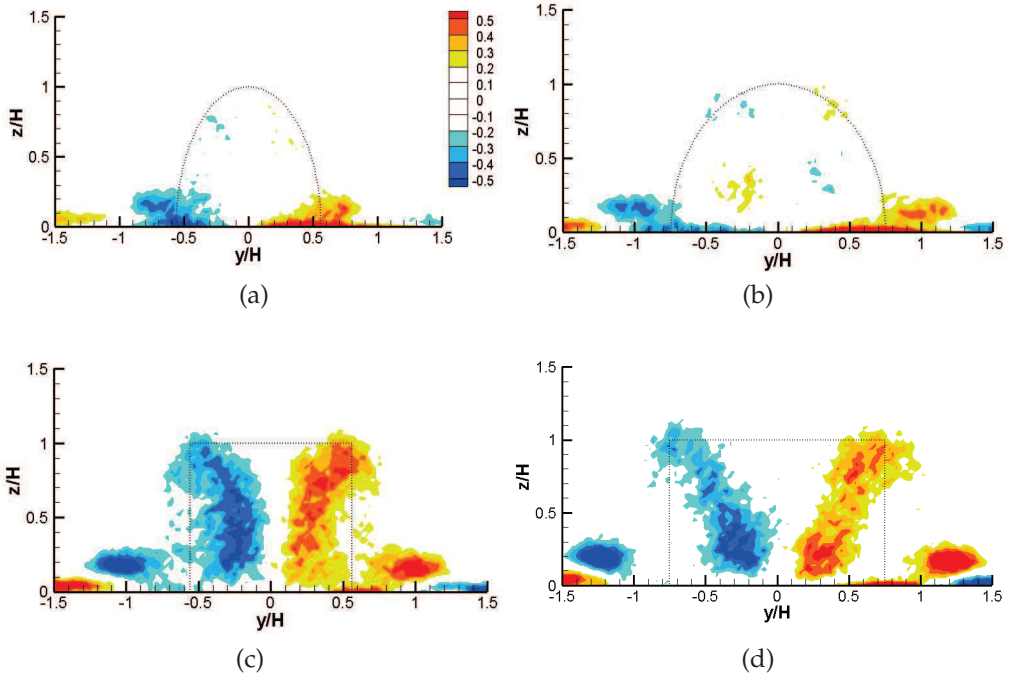

Figure 4.9: Isocontours of non-dimensional streamwise vorticity, ω_x^*, in the plane $x/H = 2$ in $d/H = 3.9$ for: (a) Streamwise ellipsoid, (b) transverse ellipsoid, (c) cylinder (AR=0.89), and (d) cylinder (AR=0.67). Red shades indicate counter-clockwise rotation and blue shades indicate clockwise rotation.

Further downstream, only the low-aspect-ratio cylinder ($H/D = 0.67$) and transverse ellipsoid are considered. Fig. 4.10 and Fig. 4.11 show the streamwise vorticity at $x/H = 3$ and 4, respectively. In these layers, the tip vortices merge with the legs of the horseshoe vortex, which have the same sense of rotation, and finally end up in fairly large trailing vortices as sketched in Pattenden et al. (2005).

It can be deduced from a comparison of Fig. 4.3 and Figs. 4.7 to 4.11 that the

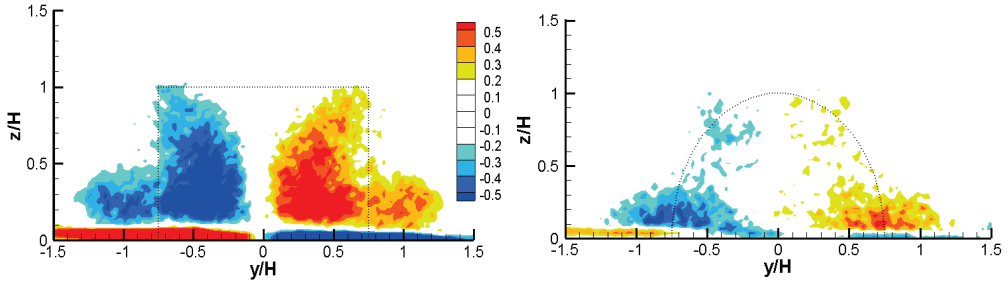

(a) (b)

Figure 4.10: Isocontours of non-dimensional streamwise vorticity, ω_x^*, in the plane $x/H = 3$ in $d/H = 3.9$ for: (a) cylinder (AR=0.67), (b) transverse ellipsoid. Red shades indicate counter-clockwise rotation and blue shades indicate clockwise rotation.

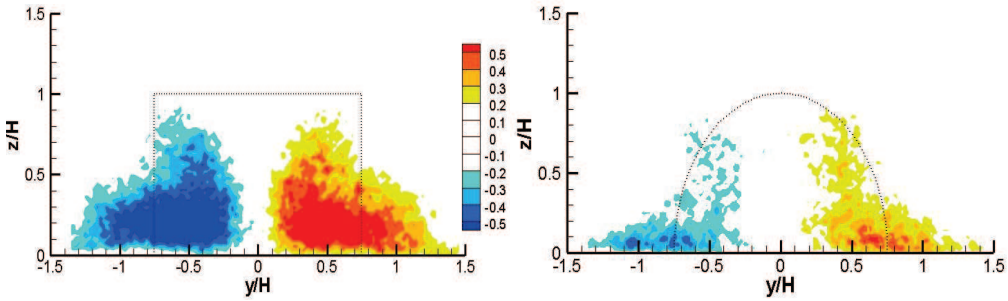

(a) (b)

Figure 4.11: Isocontours of non-dimensional streamwise vorticity, ω_x^*, in the plane $x/H = 4$ in $d/H = 3.9$ for: (a) Cylinder (AR=0.67), (b) Transverse ellipsoid. Red shades indicate counter-clockwise rotation and blue shades indicate clockwise rotation.

base vortex exists only inside the recirculation area, suggesting that the vortex lines visible in the transverse planes of Figs. 4.7 through 4.11 may be connected through the shear layer bounding the separated region. The dimensionless circulations $\Gamma^* = \Gamma/(UH)$ of each of the identified structures in the wakes of the ellipsoids were computed by integration of the streamwise component of the vorticity field within

an isocontour of $\omega^* = 0.07$ (at this value, the circulation was found to be insensitive to small changes in ω^*). The results are given in Figs. 4.12 and 4.13. Differences in the circulations of the left and right structures represent a larger error than that due to the PIV measurements, and therefore, the sizes of the error bars are given by Equation 4.1:

$$\pm \delta\Gamma^* = \pm \left(|\Gamma_L^* - \Gamma_R^*| \right) / (2|\overline{\Gamma^*}|) \times 100\% \tag{4.1}$$

where Γ_L^* and Γ_R^* are the circulations of the left- and right-vortices in a given pair, respectively.

Due to the ambiguity in the definition of the tip structure boundaries when it descends to the base plane and combines with the horseshoe vortex (Figs. 4.9c and 4.9d, 4.10 and 4.11), no attempt has been made to distinguish the tip structure from the connected like-signed vorticity, and therefore this contributes to the increase in circulation of the tip vortices in the streamwise ellipsoid and cylinder wakes, as shown in Figs. 4.12 and 4.13.

The mean circulation magnitude of the transverse ellipsoid base structures decreases monotonically in the range $1 \leq x/H \leq 2$, whereas the magnitude of the tip structure increases slightly such that both vortex pairs have similar magnitude at $x/H = 2$. Whereas the base structure in the wake of the streamwise ellipsoid is very weak at all three locations, the tip structure undergoes a rapid initial decrease in strength and remains approximately constant between $x/H = 1.5$ and 2. In contrast, as Fig. 4.13 illustrates, the tip vortex strengths for both cylinders increase significantly between $x/H = 1$ and 2, an artifact of the way they are defined in these instances, as described above. The cylinder base structures diminish monotonically with streamwise position. The streamwise decay of structures is expected, and may be explained by turbulent diffusion of vorticity resulting in the mixing and mutual annihilation of opposite-signed vortices on either side of the wake. However, since there is no source of vorticity away from the boundaries, the strengthening of the

base structures in the transverse ellipsoid wake with streamwise distance must be explained by tilting of vorticity into the streamwise orientation, as will be described later in a discussion of the instantaneous structure and dynamics of the wakes in section 4.2.4.

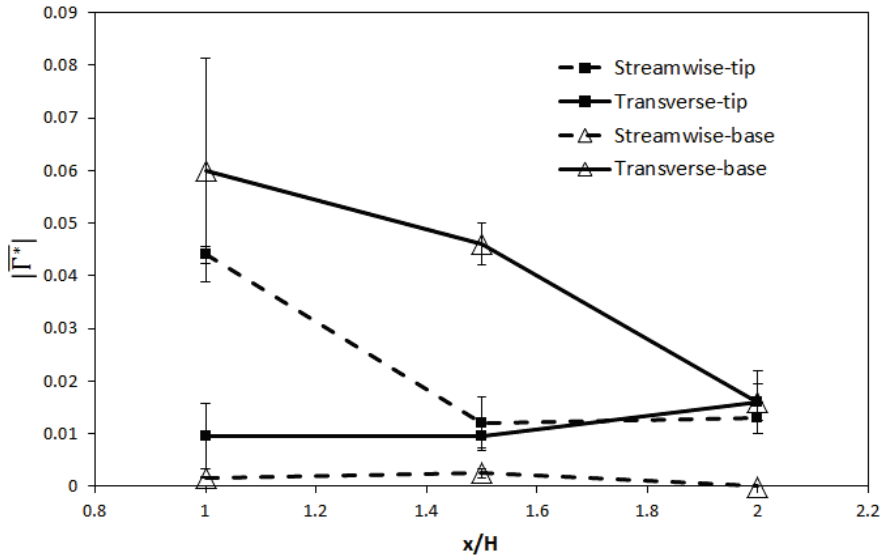

Figure 4.12: Average dimensionless circulations of structures identified for ellipsoids in Fig. 4.7 to Fig. 4.9a and 4.9b, and the left/right deviation.

4.1.4 The Role of Relative Submergence

Further experiments were conducted on the ellipsoids while varying the ratio d/H, which we refer to as the relative submergence, as it is called in open channel flows.

Given the sensitivity of the streamwise structures in the wakes of the ellipsoids to the relatively subtle changes in geometry, the relative submergence was varied to assess the extent that the boundaries are influencing the flow field. Figs. 4.14 and 4.15 show the influence of relative submergence on the distributions of streamwise

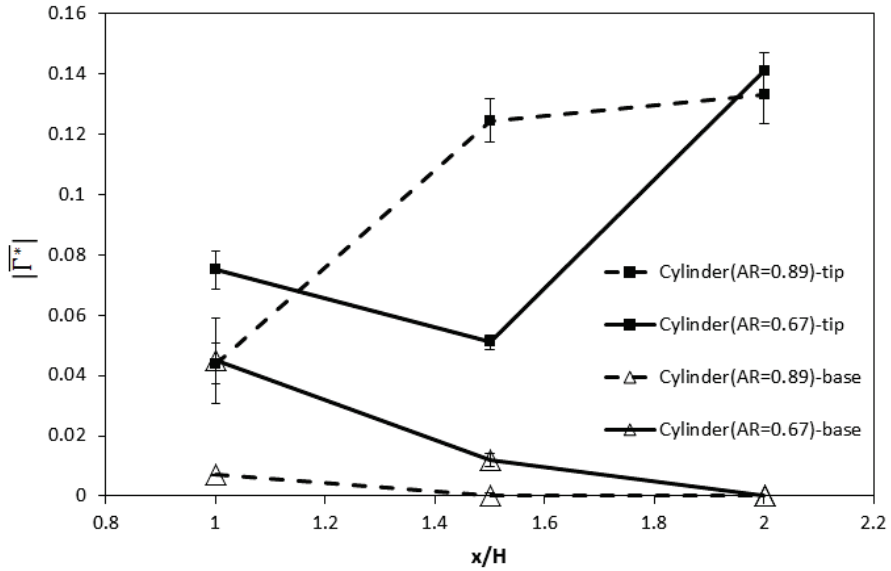

Figure 4.13: Average dimensionless circulations of structures identified for cylinders in Fig. 4.7 to Fig. 4.9c and 4.9d, and the left/right deviation.

vorticity in the wakes of the transverse and streamwise ellipsoids, respectively, at $x/H = 1.5$. Table 4.2 shows the circulation measurements for structures in the wake of transverse ellipsoid quantitatively. Fig. 4.14 qualitatively demonstrates an inverse relationship between the strength of the base vortex and relative submergence for the transverse ellipsoid. In contrast, Fig. 4.15 suggests that, for the streamwise ellipsoid, the strength of the base vortex is only sensitive to relative submergence as d/H approaches 1. In comparison with the circulations of the base vortices at $d/H = 1$, the tip vortices in both cases are rather weak and experience modest variations with changes in relative submergence.

It is noteworthy that, at $d/H = 1$, the domain is no longer simply connected, and a junction now occurs also at the tip of the obstacle. Thus, a weak horseshoe vortex is observed adjacent to the top boundary in addition to the tip vortex, which still persists. In the case of the streamwise ellipsoid, the tip structures transition from elongated patches of vorticity following the projected perimeter of the body

at $d/H = 2.5$ to concentrated and compact vortices at $d/H = 1$.

Fig. 4.16 illustrates the non-dimensional circulations of the tip and base vortices in the ellipsoid wakes for the relative submergence values shown in Figs. 4.14 and 4.15. The base vortex circulation of the transverse ellipsoid increases linearly with diminishing flow depth for relative submergence between $d/H = 3.9$ and 1. However, base vortex strength is quite insensitive to relative submergence for $d/H \geq 3.9$, which is consistent with the result of Shamloo et al. (2001). For the streamwise ellipsoid, base vortex circulation is negligible at $d/H = 2.5$ and 3.9, and then suddenly rises to nearly that of the transverse ellipsoid at $d/H = 1$. In contrast, the tip vortex structures are much weaker than the base structures at $d/H = 1$, and relatively insensitive to relative submergence.

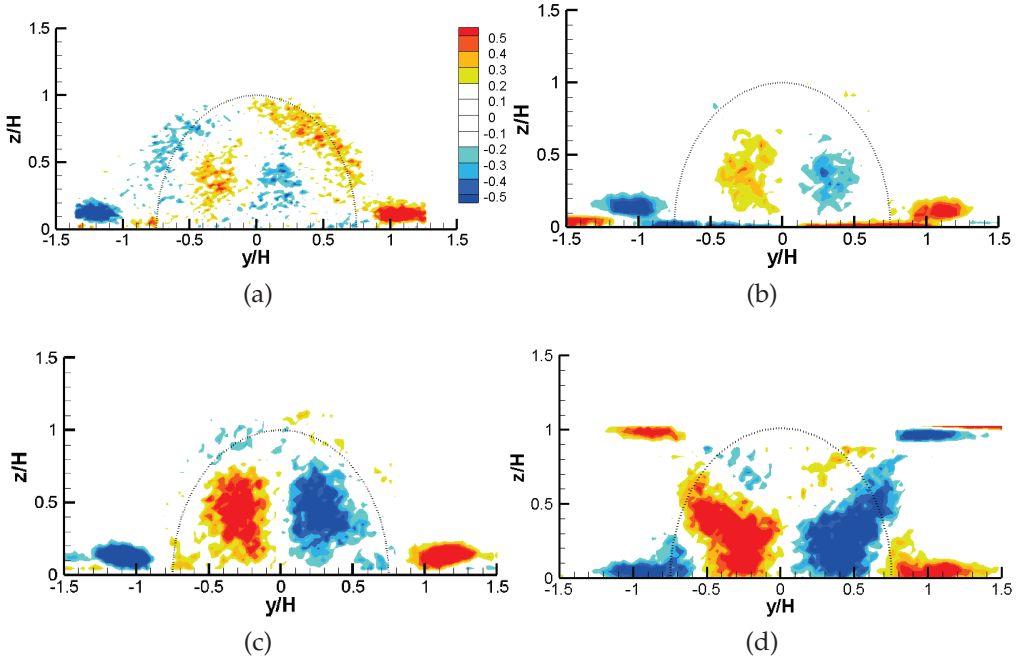

Figure 4.14: Isocontours of non-dimensional streamwise vorticity distribution, ω_x^*, with varying relative submergence for the transverse ellipsoid at $x/H = 1.5$. (a) $d/H = 5.5$ (b) $d/H = 3.9$, (c) $d/H = 2.5$ and (d) $d/H = 1$. Red shades indicate counter-clockwise rotation and blue shades indicate clockwise rotation.

Transverse ellipsoid	Structure	$\overline{\lvert\Gamma^*\rvert}$
Very HRS, $d/H = 5.5$	tip	0.685
	base	0.039
HRS, $d/H = 4$	tip	0.101
	base	0.046
MRS, $d/H = 2.5$	tip	0.007
	base	0.084
LRS, $d/H = 1$	tip	0.012
	base	0.135

Table 4.2: Circulation of base vortex in different relative submergence in Figure 4.14.

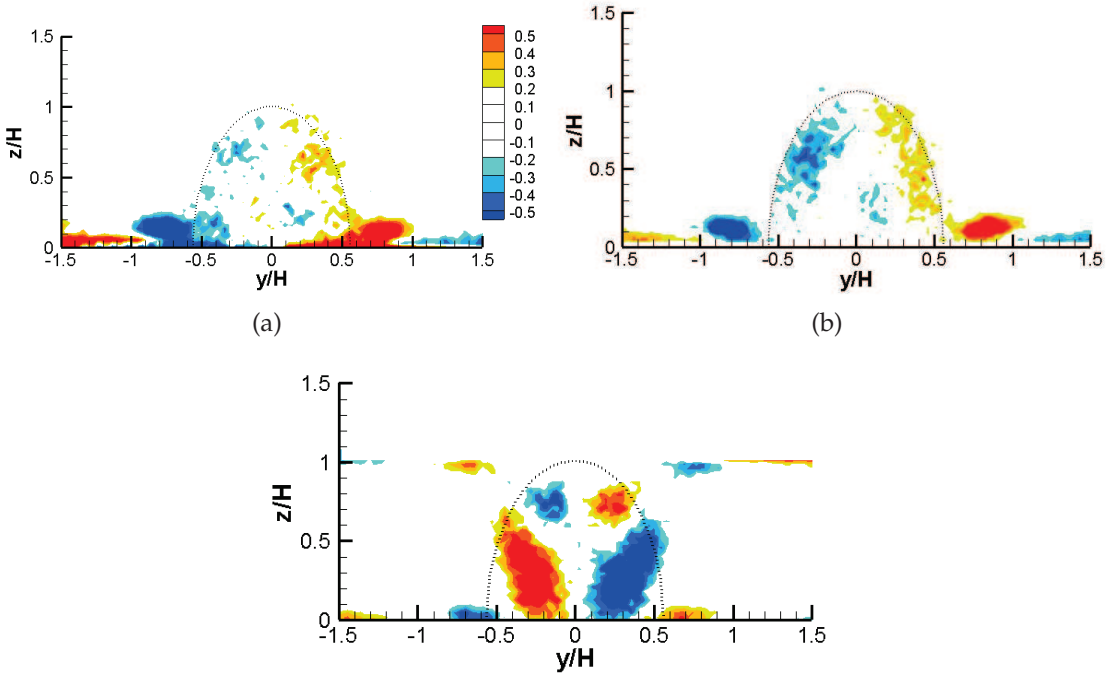

Figure 4.15: Isocontours of non-dimensional streamwise vorticity distribution, ω_x^*, with varying relative submergence for the streamwise ellipsoid at $x/H = 1.5$. (a) $d/H = 3.9$ (b) $d/H = 2.5$ (c) $d/H = 1$. Red shades indicate counter-clockwise rotation and blue shades indicate clockwise rotation.

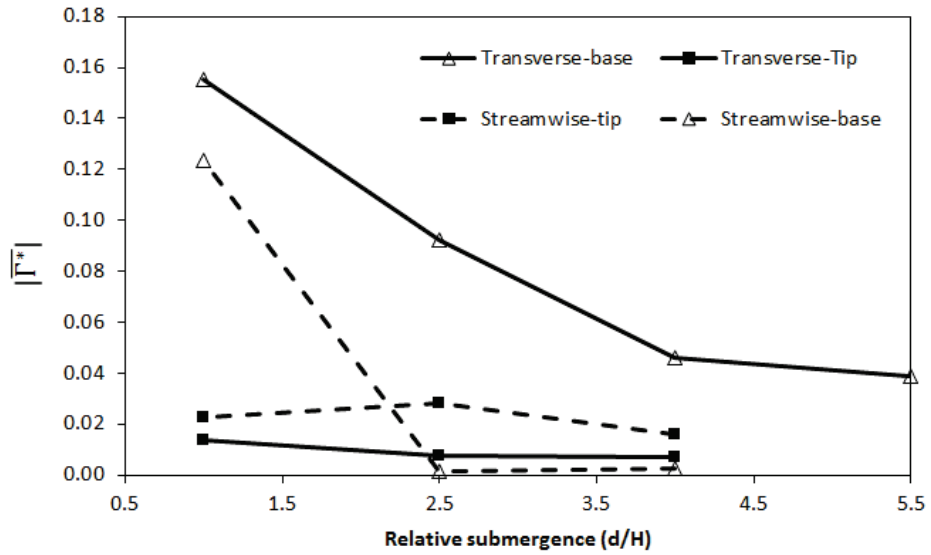

Figure 4.16: Tip and base vortex strengths with varying relative submergence for streamwise and transverse ellipsoids.

To better understand the dynamics of the flow and to compare the global wake structures for the low- and high-relative-submergence cases, dye visualizations of the transverse ellipsoid wake were conducted at $Re_H = 5500$ for $d/H = 3.9$ and 1, as shown in Fig. 4.17. At low-relative submergence (where the strongest base vortex is found), the wake is sinuous and has the appearance of a Kármán vortex street. In contrast, the wake is much more broad at high relative submergence, with a Kelvin-Helmholtz-like instability developing on the separated shear layer. These results are qualitatively in agreement with the consensus in the literature, which reports the absence of Kármán shedding in the wakes of deeply-submerged low-aspect-ratio obstacles, and the existence of Kármán shedding behind low-aspect-ratio obstacles in shallow or stratified flows ($d/H \leq 1$). (Smith and Grubišić, 1993; Castro et al., 2001; Shamloo et al., 2001). As Figs. 4.14 through 4.16 show, the sharply contrasting shedding modes illustrated in Fig. 4.17 are accompanied by not only significant increases in the strengths of the base vortices, but also more

concentrated tip structures.

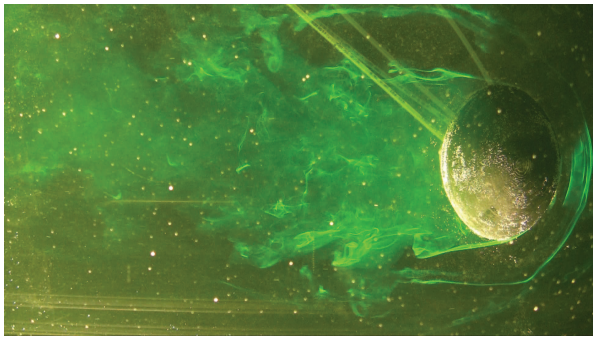

(a)

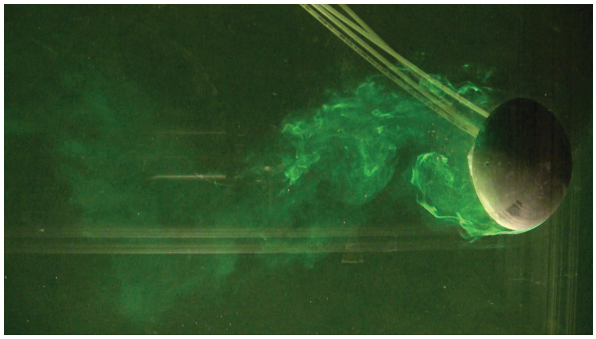

(b)

Figure 4.17: Dye visualizations of the flow around the transverse ellipsoid at $Re_H = 5500$. (a) $d/H = 3.9$, (b) $d/H = 1$.

Whereas ellipsoid aspect ratio controls the relative strengths of the tip and base structures, Fig. 4.16 shows that the parameter d/H controls the strength of the base vortex. There are three ways in which reducing d/H modifies the flow structure: 1) by modifying pressure gradients on and around the obstacle due to solid and wake blockage as well as streamwise pressure gradients due to boundary layer growth; 2) by modifying pressure gradients on and around the obstacle due to increasing interactions with the upper boundary; and 3) in the case of $d/H = 1$, by a fundamental change in the domain topology such that it is no longer simply

connected.

It is well-known (Zdravkovich, 1997) that increasing blockage on two-dimensional circular cylinders in the transitional shear layer Reynolds number range delays separation, decreases base pressure, strengthens the shed vortices, and increases drag. Farell et al. (1977) investigated the effects of blockage ratio on cooling towers, and found the base pressure coefficient in wind tunnel measurements to drop approximately 76% at 10% blockage. In the present work, the effects of blockage ratio are most severe for $d/H = 1$, where the solid blockage ratios are 7.3% and 9.8% for the streamwise and transverse ellipsoids, respectively.

The reduction of three-dimensionality (increasingly horizontal streamlines) commensurate with decreasing relative submergence is also expected to increase the magnitudes of pressure gradients and vortex strengths, and without further investigation, it is difficult to distinguish these effects from blockage. It is noteworthy that a reduction in d/H from 3.9 to 2.5 (where the blockage ratios are 2.9% and 3.9% for the streamwise and transverse ellipsoids, respectively) increases the strengths of the tip vortices in the streamwise ellipsoid wake and the base vortices in the transverse ellipsoid wake. This change can be explained by an increase in shed vortex strength by either of the mechanisms discussed above, in the context of the model presented in Fig. 4.25.

For $d/H = 1$, the flow topology is necessarily different since boundary layer vorticity on the upper plate forms a horseshoe at the upper junction. In addition, the severe constraint on flow three-dimensionality results in quasi-two-dimensional Kármán-like vortex shedding. However, it is evident that pressure gradients still exist in the z-direction due to the significant upwash observed in the wake, indicated by the strong base structures in Fig. 4.14d. Fig. 4.18 contains streamlines in the symmetry plane of the low-relative-submergence wake of the streamwise and transverse ellipsoids. A vertical bifurcation line is present, centered around

$x/H = 1.5$, which separates upstream flow in the vortex formation region from downstream flow in the wake. There are no concentrated vortices present in this plane as in, for example, the base of the high-aspect-ratio cylinder examined by Krajnović (2011), or the similar structures observed by Ozturk et al. (2008) in the downstream corners of a circular cylinder at $d/H = 1$. Thus, the tip structures observed in Fig. 4.14d are not connected through the symmetry plane, and must therefore originate through either the generation of streamwise vorticity on the surface of the ellipsoid or top boundary, or they must be formed by the tilting of spanwise ($z-$) vorticity into the streamwise direction. Additional experiments conducted in the low-turbulence-intensity facility as illustrated in Fig. 4.20 show similar flow topology as that given in Fig. 4.18; however, while the tip structures robustly appear downstream of the bifurcation line, they are not present upstream of it. This suggests that the tip structures observed in Fig. 4.14d form as a result of tilting of the Kármán vortices by the velocity gradient in the upper boundary layer. Similar tilting is expected near the base plane; however, this effect is masked due to its co-location with additional streamwise *base* vorticity. In this case, it is anticipated that the base vorticity is formed on the ellipsoid surface by strong vertical pressure gradients – low-turbulence experiments (Sec. 4.2.7) reveal that the streamwise distribution of base vorticity is distributed along the projected perimeter of the ellipsoid at $x/H < 1$, and rotates and evolves into the form shown in Figs. 4.14 and 4.15 by self-induction.

4.2 Low Free-Stream Turbulence Flow

Given the relatively high free-stream turbulence levels present for the measurements reported in Sections 4.1.2 through 4.1.4, the preliminary results of Sec. 4.1 have been completed in low free-stream turbulence flow section. The boundary layer characteristics have been measured and flow patterns in the streamwise symmetry planes have been accomplished. Similar ($y - z$) transverse layers were

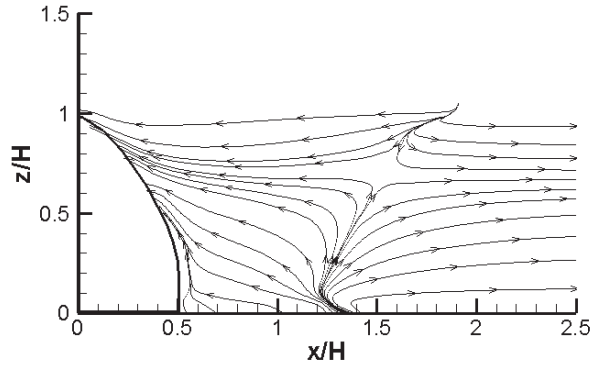

(a)

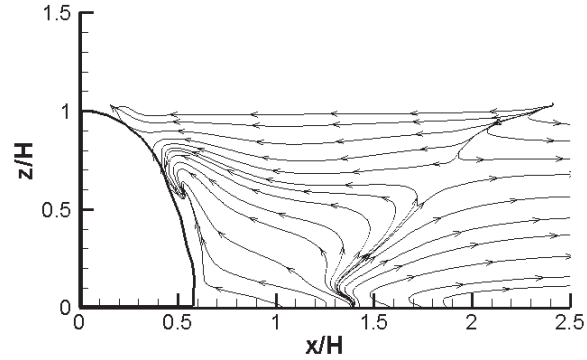

(b)

Figure 4.18: Mean streamlines in the wake of the streamwise and transverse ellipsoids at $d/H = 1$.

considered to measure streamwise vorticity distributions in the wake of ellipsoids and cylinders. Based on this vorticity distributions, a vortex skeleton model has been proposed for ellipsoidal geometry which later will be verified by spectra and correlation analysis in the wake. Relative submergence has been revisited in this section and the spectral analysis and streamwise vorticity distributions in $(y - z)$ transverse layers will be discussed.

The comparison of wake structures through the high and low free-stream turbulence flow is also interesting since not many studies have investigated the effects of free-stream flow characteristics on the flow structures around finite bluff bodies.

Existing studies that have been conducted note only a small effect on the wake (Lee, 1975; Bearman and Morel, 1983). Bearman and Morel (1983) reviewed the effects of free stream turbulence on the flow around bluff bodies and identified the main FST influences as accelerated transition to turbulence in separated shear layers and increased spreading. Lee (1975) presented measurements of the mean and fluctuating pressure field on a two-dimensional square cylinder in grid-generated turbulence. With increasing free-stream turbulence intensity in the range 0.5 to 12.5%, Lee (1975) found a 73% increase in the base pressure and a reduction in drag of the body. While the study did not heavily focus on the effects of FST on flow structure, pressure measurements revealed that the strength of the vortex shedding reduced as the intensity of the incident turbulence increased. Nakamura (1993) considered the effects of FST on square prisms with aspect ratios of 1 and 10 with turbulence intensities of 10 to 12%. It was shown that if turbulence length scale was comparable to top shear-layer thickness and body size, FST could have an effect on the flow separation and reattachment.

4.2.1 Boundary Layer Characteristics

After completion of the experiments reported in the previous sections, the plenum of the water channel was modified as described in Chapter 3.1, resulting in a free-stream turbulence intensity below 0.3%. For the low-turbulence case, in the absence of obstacles, a boundary layer of thickness $\delta_{99}/H = 0.14$ was present on the plate at the location of the obstacle center in the high free-stream turbulence flow. Therefore δ/D were 0.125 and 0.093 for the streamwise and transverse ellipsoids, respectively, and the similarly-dimensioned cylinders. The displacement thickness (δ^*) and momentum thicknesses (θ) were δ^*=2.07 mm and θ = 0.78 mm, providing a shape factor of H_{sf} = 2.66. The profiles are representative of a Blasius profile (shape factor H_{sf} = 2.59).

4.2.2 Flow Patterns in the Streamwise Symmetry Plane

Some basic properties of the flow are characterized again in low free-stream turbulence by examining the velocity, vorticity, and Reynolds shear stress fields on the symmetry plane in the wake of the obstacle. The results of symmetry plane are qualitatively in agreement with high turbulence flow. Therefore, just results for ellipsoids have been shown in the following section. The reattachment length remained in the range of the results in the Sec. 4.1.2, therefore they have not been shown here for brevity. Isocontours of non-dimensional transverse vorticity ($\omega_y^* = \omega_y H/U$) are shown in Fig. 4.19. In addition to the regions of large positive ω_y (counter clockwise rotation) located in the vicinity of the shear layer separating from the top of the obstacle, significant negative vorticity is found for each geometry adjacent to the base plane in the vicinity of the recirculation region. With comparison to Fig. 4.4a, in low turbulence flow, large negative values of vorticity was not observed on the lee faces of the ellipsoids.

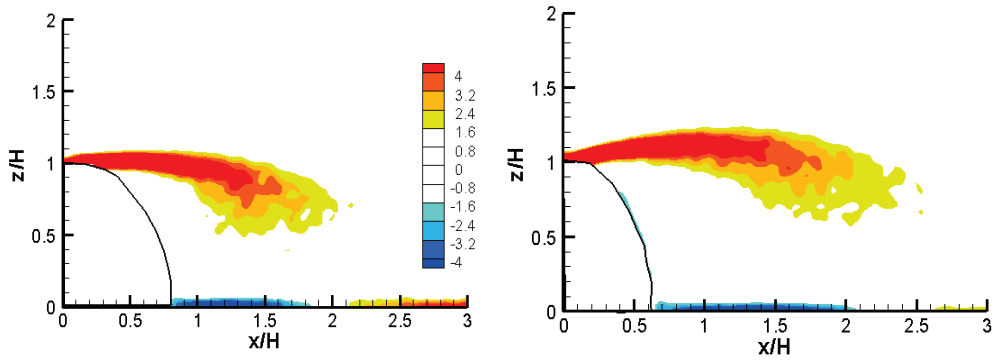

Figure 4.19: Isocontours of non-dimensional spanwise vorticity, ω_y^*, downstream of the obstacle in $d/H = 3.9$ for: (a) streamwise ellipsoid, (b) transverse ellipsoid low free stream turbulence. Red shades indicate counter-clockwise rotation and blue shades indicate clockwise rotation.

The distributions of kinematic Reynolds shear stress ($-\overline{u'w'}/U^2$) in the wake of the ellipsoids are shown in Fig. 4.20. Here also the lowest magnitudes occur for the streamwise ellipsoid. Similar to high turbulence flow, for the ellipsoids, there is only one separation point, near the top of the structure.The Reynolds stress values shown in Fig. 4.4 are approximately five times those measured in the low free-stream turbulence flow.

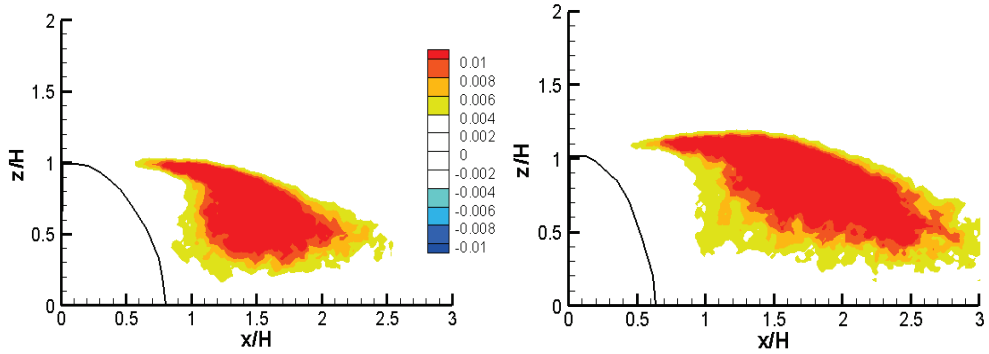

Figure 4.20: Isocontours of Reynolds shear stress, $-\overline{u'w'}/U^2$, downstream of the obstacle in $d/H = 3.9$ for: (a) streamwise ellipsoid, (b) transverse ellipsoid low free stream turbulence.

4.2.3 Streamwise Vorticity Distributions

Figures. 4.21 and 4.24display isocontours of streamwise dimensionless vorticity ($\omega_x^* = \omega_x H/U$), at the significantly reduced turbulence level, in the wakes of the obstacles in transverse (y-z) planes between x/H= 0.5 and 1.5, with $d/H = 3.9$ using the experimental configuration shown in Fig. 3.13. Each mean vorticity field was obtained from 3000 instantaneous velocity fields.

The streamwise structures are qualitatively similar to the vorticity distributions in Figs. 4.7 and 4.8. However, the circulation magnitudes of these streamwise

structures are much larger in the low-turbulence case, and all of the structures except the tip structure on the transverse ellipsoid increase in strength significantly between $x/H = 1$ and 1.5 as shown in Fig. 4.22. These increases provide important clues about vortex dynamics in the wake, which will be discussed in section 4.2.4.

Transverse	**Structure**	$\lvert\overline{\Gamma^*}\rvert$	$\delta\Gamma^*$ (%)
Turbulence intensity 7%	tip	0.0095	20.71
	base	0.0456	8.5239
Turbulence intensity 0.3%	tip	0.021	37.72
	base	0.163	9.55
Streamwise			
Turbulence intensity 7%	tip	0.016	31.822
	base	0.002	36.630
Turbulence intensity 0.3%	tip	0.078	2.34
	base	0.0196	41.83

Table 4.3: Average dimensionless circulations of structures identified for streamwise and transverse ellipsoid at $x/H = 1.5$ in two different turbulence intensity, and the left/right deviation.

Figure. 4.23 contains streamwise vorticity located at x/H =0.5 to 1.5 for the two cylinders. The streamwise structures are qualitatively robust with change in turbulence intensity and are similar to the vorticity distributions in Figs. 4.7 and 4.8. However, the circulation magnitudes of these streamwise structures are much larger in the low-turbulence case, and all of the structures except the base structures on the high-aspect-ratio cylinder increase in strength significantly between $x/H = 1$ and 1.5 as shown in Fig. 4.24.

Also, another pair of vortex structures is visible in the upper wakes of the cylinders (Figs. 4.23a and 4.23b)) between the tip vortices inducing upwash. The existence of the observed vortices is controversial in existing literature and is ques-

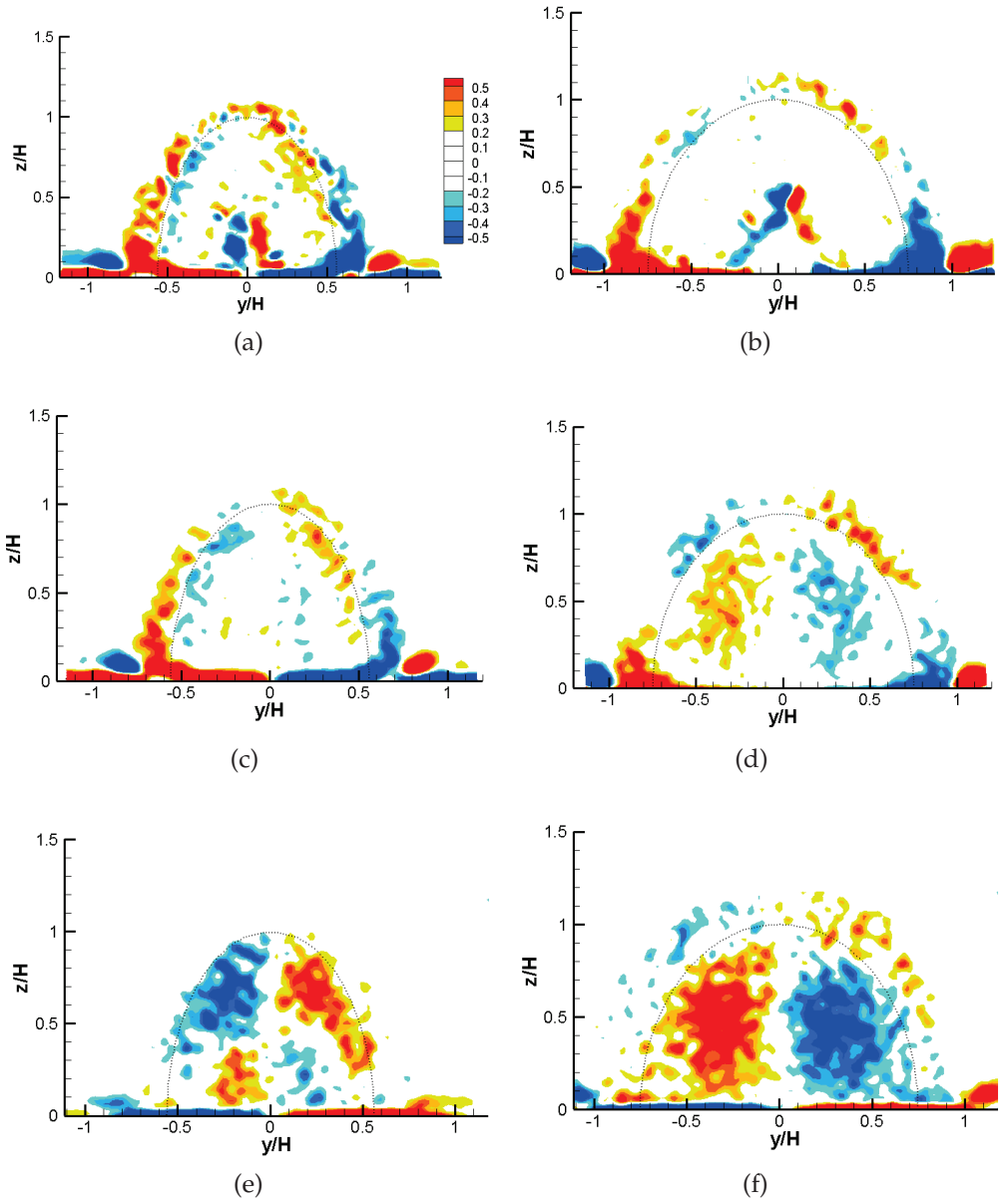

Figure 4.21: Isocontours of non-dimensional streamwise vorticity, ω_x^*, in the plane $x/H = 0.5, 1, 1.5$ (top to bottom) in $d/H = 3.9$ at low free stream turbulence intensity 0.3% for: (a) (c) (e) Streamwise ellipsoid, (b) (d) (f) transverse ellipsoid. Red shades indicate counter-clockwise rotation and blue shades indicate clockwise rotation.

tioned by Pattenden et al (2005), Palau-Salvador et al. (2010), and Krajnovic (2011).

To the authors knowledge, the only other studies that have noted the existence of

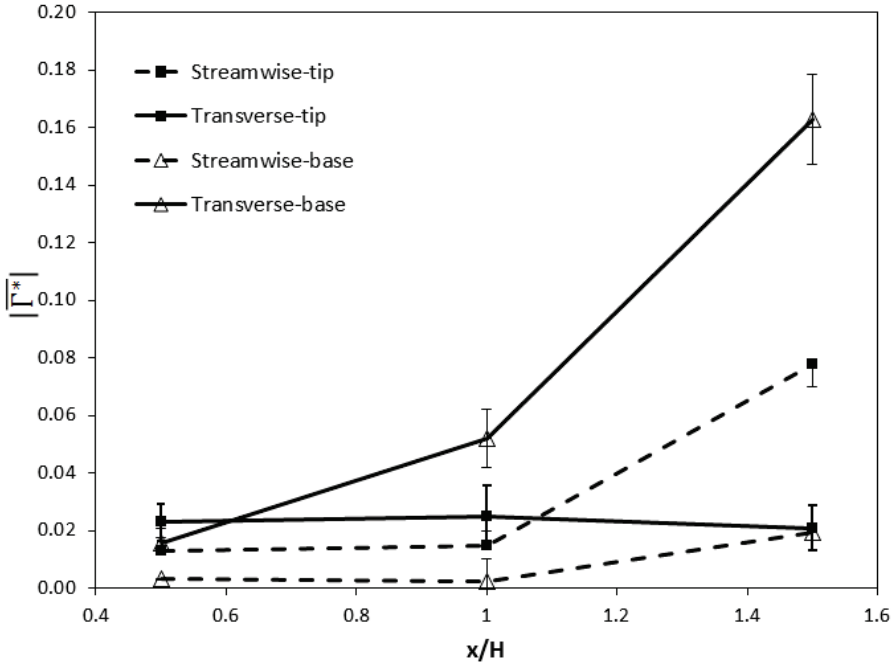

Figure 4.22: Average dimensionless circulations of structures with FST=0.3% identified in Fig. 4.21 and the left/right deviation.

these vortices are Roh and Park (2003) and Hain et al. (2008).

4.2.4 Proposed Model for Ellipsoid Wakes and Its Application to Cylinder Wakes

The results of this work show that dominant streamwise structures in the wake of the ellipsoids, and to some extent also the cylinders, can be controlled with relatively minor changes in geometry. In the subsequent discussion, we consider these results in the context of previous work, propose a vortex model of the wake that elucidates the mechanisms of selection between tip and base vortices, and then examine the implications of relative submergence on this model.

The streamwise vorticity distribution shown in Fig. 4.35b, in which strong base vortices are observed, corresponds to the same obstacle geometry and relative submergence as the dye visualization in Fig. 4.17a. In accordance with previous

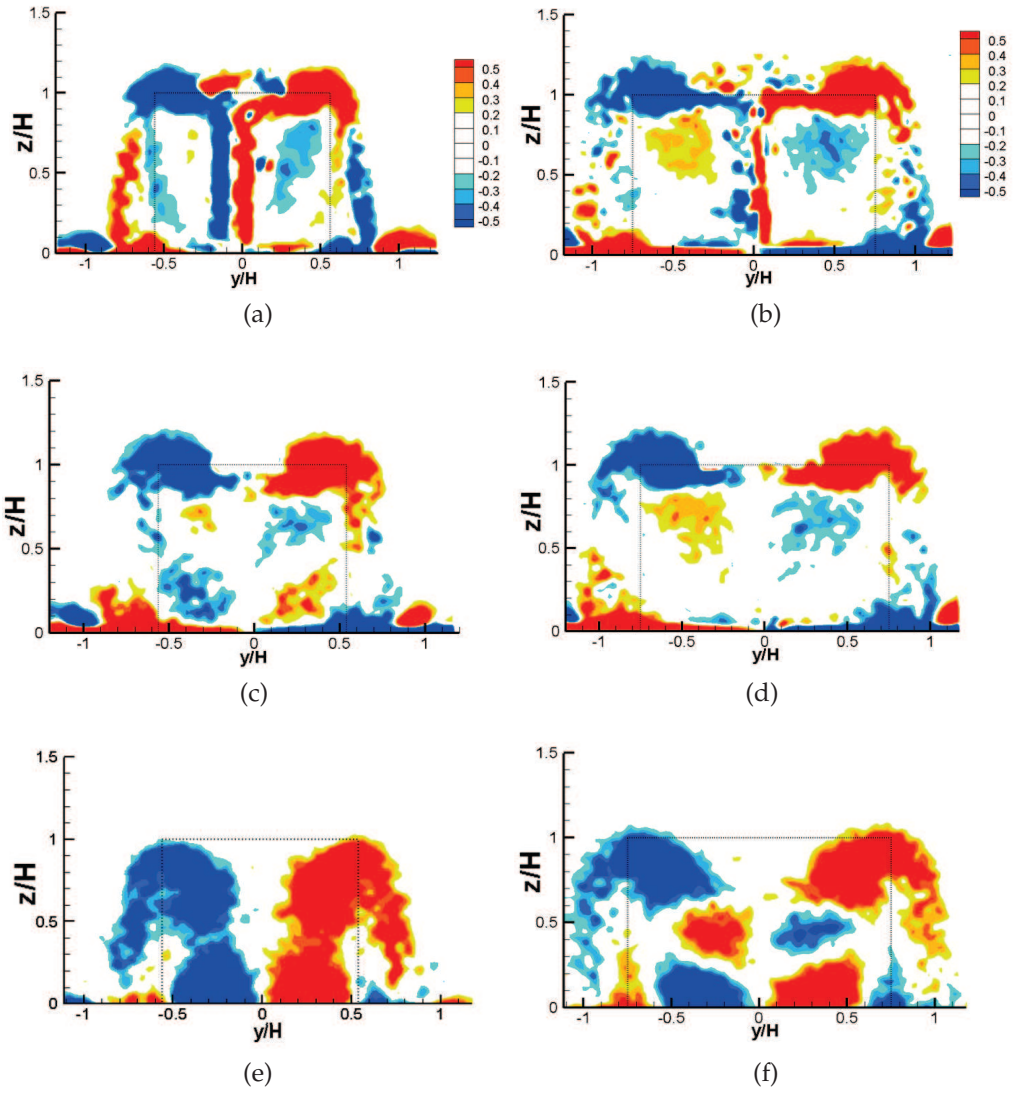

Figure 4.23: Isocontours of non-dimensional streamwise vorticity, ω_x^*, in the plane $x/H = 0.5, 1, 1.5$ (top to bottom) in $d/H = 3.9$ at low free stream turbulence intensity 0.3% for: (a) (c) (e) Cylinder (AR=0.89), (b) (d) (f) Cylinder (AR=0.67). Red shades indicate counter-clockwise rotation and blue shades indicate clockwise rotation.

studies on low-aspect-ratio geometries, Fig. 4.17a indicates that Kármán shedding is not present. Models for higher-aspect-ratio bodies presented in the literature (Sumner et al., 2004; Wang and Zhou, 2009; Bourgeois et al., 2011b) suggest that tip and base structures are streamwise projections of individual curved Kármán

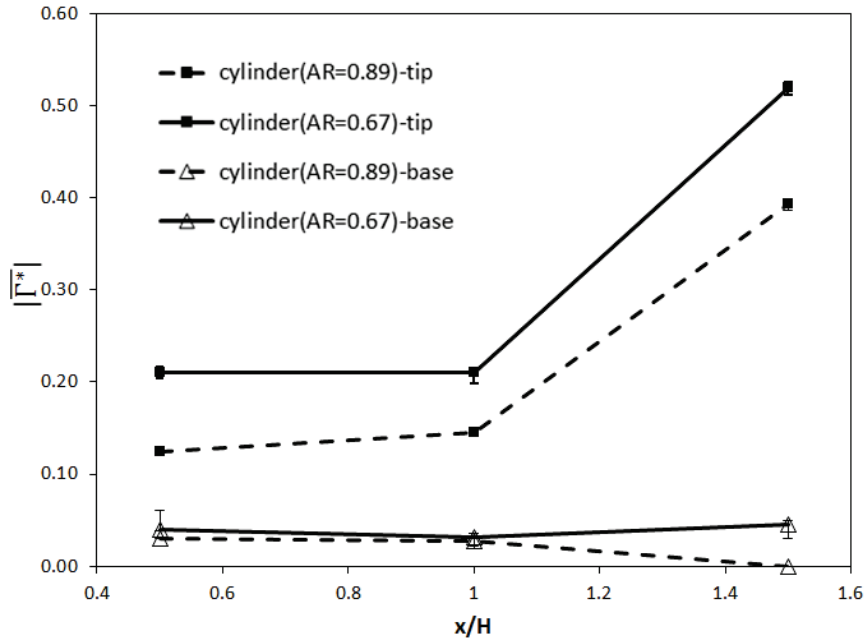

Figure 4.24: Average dimensionless circulations of structures with FST=0.3% identified in Fig. 4.23 and the left/right deviation.

vortices or filaments connecting the vortices. The model proposed by Wang and Zhou (2009) does not fit well with the present measurements in the wake of the ellipsoids due to a) the significant disparities in the circulations of the tip and base vortices in the near wake (idealizing the Kármán vortices as vortex tubes would require equal circulation in the tip and base structures), b) the close proximity of the tip and base structures, and c) the absence of Kármán shedding or large-scale symmetric shedding as indicated in Fig. 4.35b.

The low-aspect-ratio cylinder wake model presented by Pattenden et al. (2005) also does not account for the presence of base structures observed in either the transverse ellipsoid or the cylinders despite similarities in aspect ratio, relative submergence and boundary layer thickness. However, we do not believe that the results presented here are in contradiction to those of Pattenden et al. (2005). Two key differences separate the two studies: the aspect ratio investigated by

Pattenden et al. (2005) is approximately 12% higher than the high-aspect-ratio cylinder investigated here, and their Reynolds number is an order of magnitude higher. Since both studies consider time-averaged flow fields in transverse planes, information on the instantaneous structure and dynamics of the wakes are largely lost, preventing direct comparison of those characteristics; however, it is likely that enhanced turbulent mixing at the higher Reynolds number will increase mixing and annihilation of base structures in the wake. Perhaps more importantly, Figs. 4.7c and 4.7d show a strong inverse relationship between base vortex strength and cylinder aspect ratio within the range investigated here. This dependence is quantified in Fig. 4.13 which shows that the base vortex circulation drops by approximately 85% as the aspect ratio increases from 0.67 to 0.89. It is therefore plausible that this trend will continue with increasing aspect ratio such that a much weaker base vortex might exist for a cylinder with aspect ratio 1.

The wake model proposed by Mason and Morton (1987) to support their empirical rule for obstacle wakes at $Re = O(100)$ consists of arch vortices that are either tilted upstream such as to produce downwash in the case of taller obstacles, or tilted downstream such as to produce upwash in the case of wider obstacles. The ellipsoid wake vorticity distributions presented in sections 4.1.2 and 4.1.3 are consistent with both the empirical rule and the vortex model presented by Mason and Morton (1987). However, the cylinder wakes are more complex and contain features that are not accounted for by their model. The vortex loops shown in hemisphere wakes by Savory and Toy (1986) are also consistent with this model. Likewise, the low-aspect-ratio pyramid wakes observed in thick boundary layers by Chyu and Natarajan (1996) and Martinuzzi and AbuOmar (2003) also appear to have similarities with the arch model of Mason and Morton (1987). However, unlike all of these results which were obtained in boundary layers with thicknesses on the order of obstacle height (or width), in the present work, the boundary layer

is thin.

As suggested in the previous section, the model of Mason and Morton (1987) reasonably emulates the primary features observed in the wakes of the streamwise and transverse ellipsoids. However, no explanation is provided for the physical mechanisms governing the selection of upwash or downwash in the wake. For the ellipsoid wakes, we propose a similar model, shown in Fig. 4.25, which does account for the selection. The dominant structures in the deeply-submerged ellipsoid wakes are the horseshoe vortex system (not shown in the figure) and the arch-shaped shear-layer containing the Kelvin-Helmholtz instability shown in Fig. 4.17a. We suggest that two dominant mechanisms govern the dynamics of the resulting arch structures to produce the observed mean flow: 1) Biot-Savart self-induction due to the curvature of the vortex which, due to the vorticity orientation, would tend to drive the top of the arch upstream as shown in Fig. 4.25a; and 2) the shear flow onto which the vortex is superimposed (due to the ground plane boundary layer and other wake constituents), which would advect the top of the arch downstream more quickly than the base as shown in Fig. 4.25b.

For the case of the ellipsoids, obstacle aspect ratio governs the balance between these two mechanisms through the curvature of the arch vortices (which is determined by the curvature of the projected obstacle perimeter when viewed in the streamwise direction). The streamwise ellipsoid generates arch structures of higher curvature, which are deformed upstream by Biot-Savart self-induction, forming the observed tip structures in the mean (Fig. 4.25a). On the other hand, the transverse ellipsoid produces arch structures of lower curvature which have weaker self-induction so that the influence of the external shear flow dominates, bending the structures downstream to produce the base structures (Fig. 4.25b).

This model of wake structure and dynamics correlates well with the observations of wakes in the low-turbulence flow, as shown in Figs. 4.21 and 4.22, in which

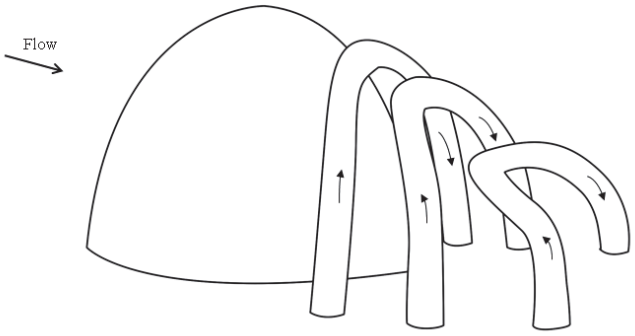

(a)

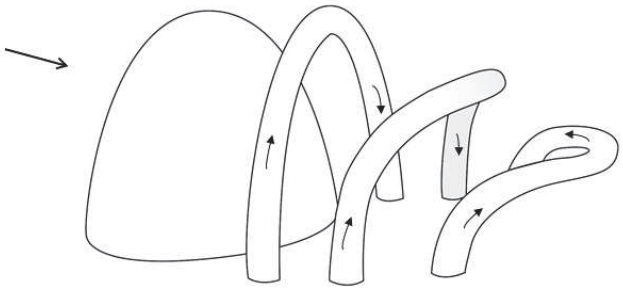

(b)

Figure 4.25: Proposed evolution of the arch structures for (a) the streamwise ellipsoid (self-induction dominated deformation) and b) the transverse ellipsoid (external shear dominated deformation). The arrows indicate the orientation of the vorticity vector.

the dominant structures increase in strength with increasing downstream distance (thus, more arch filaments penetrate the measurement plane as they become more inclined). However, as Fig. 4.12 indicates, these structures are generally decreasing in strength with increasing x/H in the high turbulence flow. This may be attributed to enhanced turbulent diffusion and cross-cancellation of the streamwise structures. For example, the Reynolds stress values shown in Fig. 4.20b are approximately five times those measured in the low free-stream turbulence flow (see Fig. 4.19).

The model presented in Fig. 4.25 is an idealization that describes the dominant

wake dynamics; however, minor features, such as the residual base and tip vortices for the streamwise and transverse ellipsoids, respectively, are not accounted for by the model. This is likely due to the generation of streamwise vorticity on the surfaces of the obstacle and base plane. For example, Figs. 4.21d and 4.21f contain strong base vortices, explained by the model of Fig. 4.25b with an opposite-signed tip vortex. That the tip vortex does not increase in strength with downstream distance, as shown in Fig. 4.22, supports that it is fundamentally a different type of structure than that shown in Fig. 4.25.

The flow structures observed in the cylinder wakes are more complicated due to the square corners and flat tip which govern the separation and reattachment processes at the leading- and trailing edges of the free end. Unlike the ellipsoid wakes, a dominant tip vortex exists in the wakes of both cylinders due to this robust separation and the vorticity persists at this location in the transverse plane for a considerable distance downstream (see, for example, Fig. 4.10a). These tip vortices are similar in appearance to those observed by Pattenden et al (2005), and it is expected that they have been formed by the separation of the upwash flow on the sides of the cylinder as described in Sec. 2.2.2. Vortical structures of opposite sign (akin to the base vortices) also form in the near wake directly below the tip structures for both low- and high-aspect-ratio cylinders (Figs. 4.7c and 4.7d or Figs. 4.23c and 4.23d). To the authors' knowledge, this is the first observation of such structures in the wakes of low-aspect-ratio cylinders. It is plausible that these base structures are also generated by the deformation of arch structures shed into the wake, as described in Sec. 4.2.4. However, due to the rectangular profile of the cylinders, the shape of the arch structures shed, and their self-induced deformation, the wake structure of the cylinder is necessarily more complex than that of the ellipsoids. This is evidenced by a tertiary vortex pair (of the same sign as the tip vortices) directly beneath the base vortices in Fig. 4.8dor in Fig. 4.21f, which

suggests the presence of a higher-order bending instability in the vertical legs of the arch structures. Although the wakes of the low- and high-aspect- ratio cylinders are not as dramatically different as the low- and high-aspect-ratio ellipsoids, a similar (but weaker) trend is still evident as the base vortices are weaker in the wake of the high-aspect-ratio cylinder.

4.2.5 Spectra and correlation analysis in the wake

The present section focuses on the spectra and phase characteristics in the wakes of low-aspect-ratio ellipsoidal obstacles of aspect ratios $H/D = 0.67$ and 0.89 (where H is the ellipsoid height and D is the base width), and circular cylinders of matching H/D. Mean vorticity distributions in the wakes of these obstacles were investigated Sec. 4.1.3. In the present section, these wakes are further interrogated using thermal anemometry, and spectral and cross-correlation analysis to elucidate the origins of the mean flow structures and their dynamics.

Figures 4.27 and 4.28 show the power spectral density (PSD) functions of the streamwise velocity component measured for the transverse and streamwise ellipsoids at $d/H = 3.9$. The hot-film probe was placed at spanwise locations $x/D = 1$, 2 and 3, and for $z/H = 0.25$, 0.5, 0.75, and 1. The z-axis of the power spectra is offset to allow comparison between measurements at different locations. Due to symmetry, the power spectra from either side are nearly identical and only the spectra from one side of the obstacles are shown.

Weak spectral peaks are apparent in the wakes of both the transverse and streamwise ellipsoids. For all streamwise and spanwise positions shown in Fig. 4.27, the power spectral density for the transverse ellipsoid exhibits a peak at $St = 0.188$ ($f_s = 0.875$ Hz) at all values of z/H at $x/D = 1$, 2, and 3. A more broad peak, which is almost exactly 1/3 the frequency of the higher-frequency mode, is centered around $St = 0.058$ ($f_s = 0.273$ Hz) at $z/H = 0.25$ for $x/D = 1$, and up to z/H=0.5 for $x/D = 2$. These low-frequency peaks significantly weaken between

$x/D = 2$ and 3. Similar peaks were observed by Castro and Watson (2004) for low-taper-ratio triangular plates. They surmised that the origin of the low-frequency mode was plausibly a beat frequency since the shedding frequency was not well-defined at lower taper ratios. That explanation seems unlikely in the present case since, as we will show in the following paragraph, other geometries exhibit a similar low-frequency peak even in the absence of higher-frequency shedding. Whereas the base shedding mode was antisymmetric in the tapered plate wakes, the low-frequency mode was symmetric and found only near the tip. As will be shown later in this section, the shedding is predominantly in-phase for the ellipsoids at $d/H = 3.9$.

Dye visualizations of the transverse ellipsoid at $Re_H = 5500$ reveal a somewhat intermittent plunging of the shear layer in the near wake (i.e. penetration of the arch vorticity into the recirculation region), which occurs with frequency consistent with the broad peaks observed in the spectra. A sequence of PIV images in the streamwise symmetry plane at $Re = 17,800$ also confirm the existence of the plunging phenomenon; however, the PIV sequence is not sufficiently long to assess the frequency of occurrence. Some snapshots of dye visualizations have been illustrated in Fig. 4.26. Inserted white arrows show plunge occurrence.

The power spectral density function is similar for the streamwise ellipsoid, as shown in Fig. 4.28. In this case, the primary peak is observed at $St = 0.183$ ($f_s = 1.14$ Hz) which is only a marginally measurable difference from that of the transverse ellipsoid. Notably, this peak is essentially non-existent at $x/H = 1$ for all streamwise positions. This may be due to the increased tilting of structures in the case of the streamwise ellipsoid, as will be quantified in Sec. 4.2.6. For the streamwise ellipsoid, the broad, low-frequency peaks occur at Strouhal numbers of $St = 0.041$, 0.0358, and 0.0256 ($f_s = 0.256$, 0.224, and 0.160 Hz), at positions of $z/H = 0.25$, 0.5, and 0.75 and then increase to $St = 0.031$ ($f_s = 0.188$ Hz) at $z/H = 1$ for

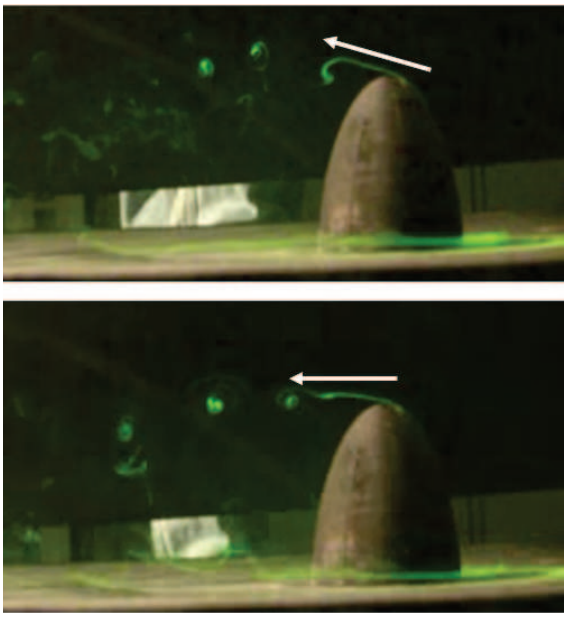

(a)

(b)

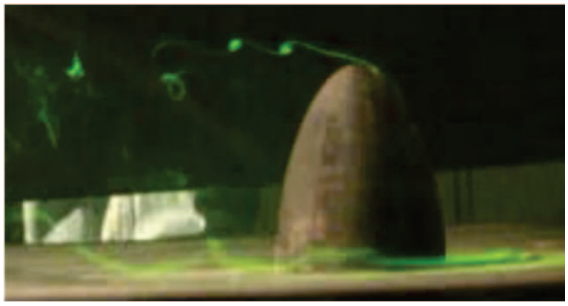

(c)

Figure 4.26: Snapshots of dye visualizations of the transverse ellipsoid at Re_H = 5500 unveiling intermittent plunging of the shear layer by a time interval of 8 s. Inserted white arrows show plunge occurrence.

all streamwise locations. Contrary to the transverse ellipsoid, the low-frequency peaks persist at all three streamwise measurement locations.

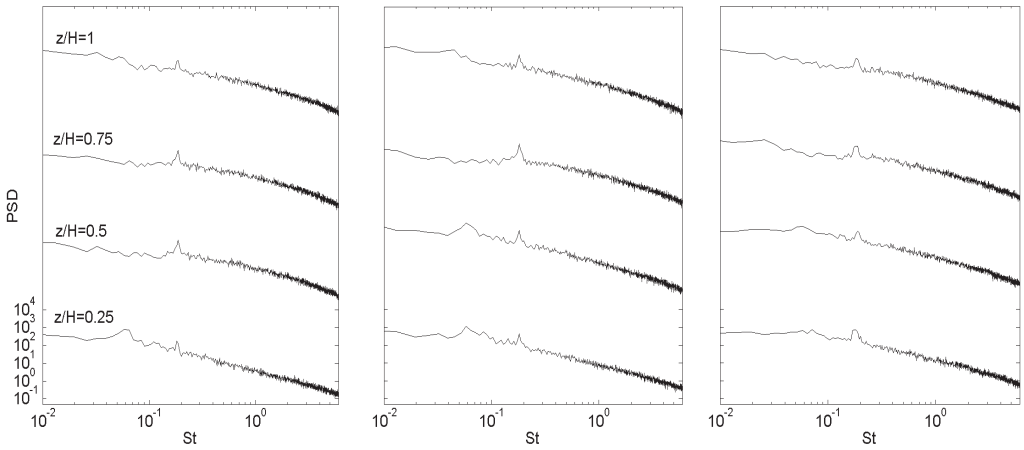

Figure 4.27: The power spectral density function, PSD, of the of the streamwise velocity component in $d/H = 3.9$ for transverse ellipsoid at $y/D = 1$: (a) $x/D = 1$, (b)$x/D = 2$ and (c) $x/D = 3$. Each spectrum is the average of 20 individual spectra. Spectra are off-set by constant factor for clarity.

For circular cylinders of matching H/D, Fig. 4.29 shows the spectra at $x/D = 1$ and $y/D = 1$. Whereas the cylinder of aspect ratio $H/D = 0.67$ displays no discernible peak in the frequency spectrum, the cylinder of $H/D = 0.89$ exhibits a weak peak of $St = 0.065$. Similar to the streamwise ellipsoid (with matching H/D), the broad, low-frequency peaks occur at Strouhal numbers of $St = 0.0200$ ($f_s = 0.125$), at positions of $z/H = 0.25$, 0.5, and 0.75 and then increase to $St = 0.0240$ ($f_s = 0.15$ Hz) at $z/H = 1$. If the power spectral density function for the lower-aspect-ratio cylinder is plotted on a linear axis as shown in Fig. 4.30, a weak peak at $St = 0.084$ is found for the cylinder of $H/D = 0.67$, which is very similar to the weak dominant frequency observed by Pattenden et al. (2005) at $St = 0.09$ for a

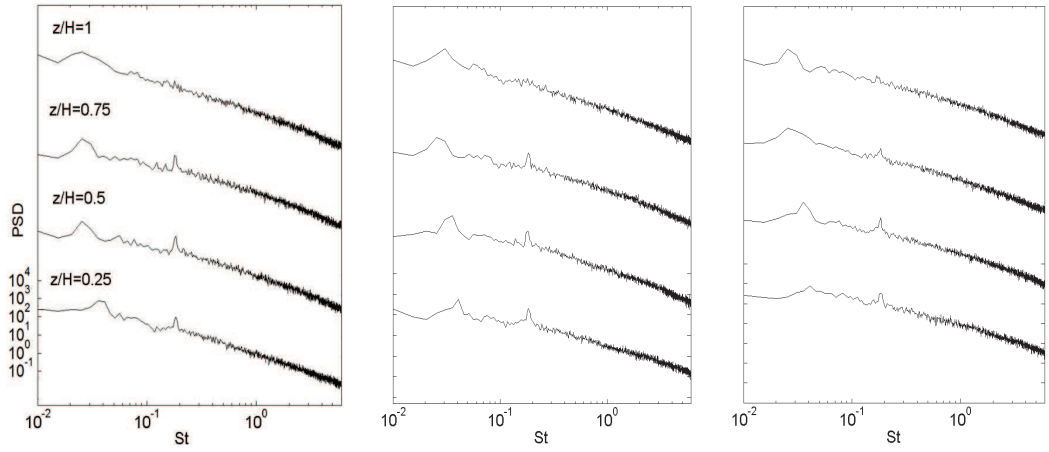

Figure 4.28: The power spectral density function Eu of the of the streamwise velocity component in $d/H = 3.9$ for streamwise ellipsoid at $y/D = 1$: (a) $x/D = 1$, (b)$x/D = 2$ and (c) $x/D = 3$. Each spectrum is the average of 20 individual spectra. Spectra are off-set by constant factor for clarity.

cylinder of aspect ratio 1 as shown in Fig. 2.36.

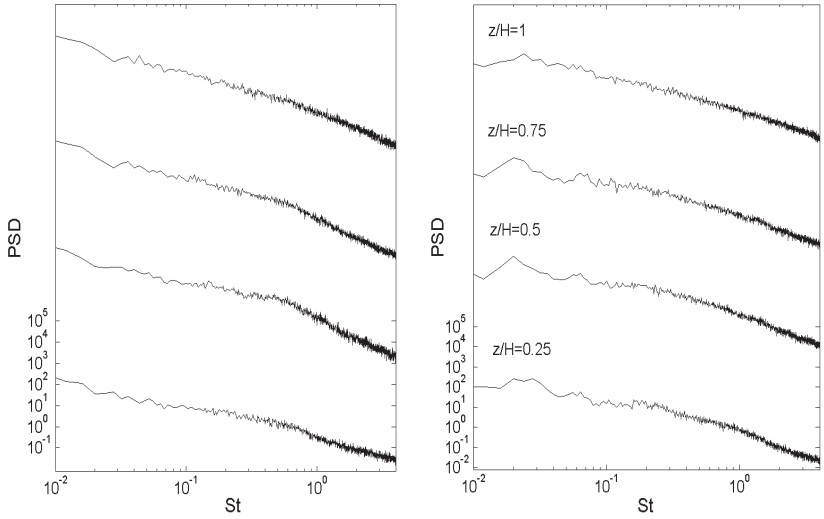

Figure 4.29: The power spectral density function of the streamwise velocity component in $d/H = 3.9$ for cylindrs of AR=0.67 (left) and AR=0.89 (right) at $x/D = 1$ and $y/D = 1$. Each spectrum is the average of 20 individual spectra. Spectra are off-set by constant factor for clarity.

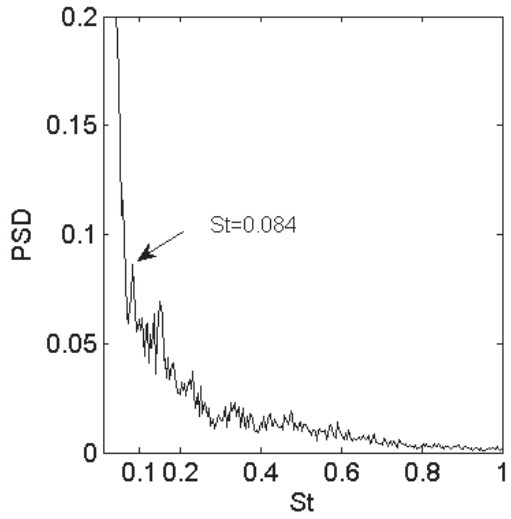

Figure 4.30: The power spectral density function of the streamwise velocity component in $d/H = 3.9$ for cylindrs of AR=0.67 in linear axis and at $x/D = 1$, $y/D = 1$, and $z/H = 0.5$

Figure 4.31a shows cross-correlations of velocity fluctuations for measurements at symmetric positions in the wake of the transverse ellipsoid at $x/D = 1$, $y/D = \pm 1$, and equal, varied values of z/H. The auto-correlation function at $x/D = 1$, $y/D = 1$, and $z/H = 0.25$ is also shown in the figure. The spatial cross-correlations, $\tau = 0$ s, are positive for each wall-normal position, indicating in-phase shedding on opposite sides of the ellipsoid. Also, the values increase monotonically with distance from the wall, similar to the pyramid measurements of Morrison et al. (2006). A small-amplitude, high-frequency component is superimposed on the auto- and cross-correlation functions at $z/H = 0.25$, unlike the cross-correlations further from the base plane. These fluctuations are likely caused by unsteadiness in the horseshoe vortex. In comparison, Seal et al. (1995) observed the cycle of vortex generation, amalgamation, and decay to occur at a frequency of 4.65 times that of the shedding frequency in the wake of a low-aspect-ratio rectangular block, which is consistent with the features shown in the correlations at $z/H = 0.25$ shown in Fig. 4.31a.

Cross-correlations at symmetric positions in the wake of the streamwise ellipsoid are given in Fig. 4.31b. A positive spatial correlation is evident at $z/H = 0.25$ and 1; however, the values are close to zero near the mid-span of the ellipsoid and the cross-correlation function is less periodic than for the transverse ellipsoid, suggesting increased unsteadiness in the flow separation lines on the more streamlined obstacle and thus a higher degree of randomness in the formation and evolution of the arch structures.

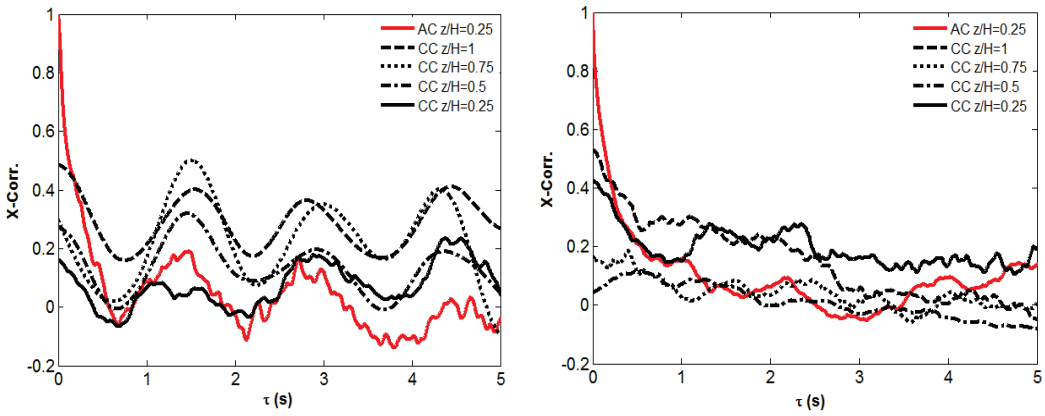

Figure 4.31: Correlations of the fluctuating velocity at d/H=3.9, x/D=1, and y/D=±1 for the (a) transverse and (b) streamwise ellipsoid.

4.2.6 Model for Ellipsoid Wakes

The models shown in Fig. 4.25 imply that the presence of upwash or downwash in the wakes of the transverse and streamwise ellipsoids, respectively, can be attributed to the tilting of the arch vortex tips upstream or downstream, as explained in Sec. 4.2.4. Here, we further consider and validate this model by examining local relative phases of vortex shedding.

Simultaneous thermal anemometry measurements were acquired with two

probes at $x/D = 1$ and $y/D = 1$. The reference probe u_1 was positioned at $z/H = 0.25$ while the other probe u_2 was positioned at $z/H = 0.5$, 0.75, and 1. The spectral coherence between the two signals, $Coh_{u_1u_2}$, contained a pronounced peak at all spanwise locations for the transverse ellipsoid but not at $z/H = 1$ in the wake of the streamwise ellipsoid. The peak value of $Coh_{u_1u_2}$ ranges from 0.46 at $z/H = 0.2$ to 0.15 at $z/H = 1$ for the streamwise ellipsoid and from 0.56 at $z/H = 0.2$ to about 0.25 at $z/H = 1$ for the transverse ellipsoid as shown in Fig.4.32. In comparison, Castro and Watson (2004) found a cross-spectral coherence of approximately 0.2 at the spectral peak associated with weak shedding in the wake of plates with taper ratios of 0.58 and 1. For a square cylinder of aspect ratio 7, Wang and Zhou (2009) reported values varying from 0.9 at $z/D = 2$ to 0.3 at $z/D = 7$.

The relative phase shift between signals u_1 and u_2 was calculated from the spectral coherence, as discussed in Ch.3.1. Figure 4.33 shows the variation of the phase shift, $\phi_{u_1u_2}(f_s)$ as a function of shedding frequency f_s for the transverse ellipsoid. A plateau occurs at $\phi_{u_1u_2}$ at $f_s = 0.875$, the dominant shedding frequency shown in Fig. 4.27, where $\phi_{u_1u_2} = 0.0068\pi$ radians, supporting the conclusion obtained from the cross-correlation analysis that the velocity fluctuations on opposite sides are in phase.

Fig. 4.34 shows the dependence of $\phi_{u_1u_2}$ on z/H in the wake of the transverse and streamwise ellipsoids at the respective dominant frequencies (f_s=0.875 Hz and 1.14 Hz). Positive phase shifts indicate u_1 leading u_2. The phase shifts, which are positive in the case of the transverse ellipsoid, indicate tilting of the tip of the arch structure in the downstream direction, as indicated in Fig. 4.25b. Likewise, the negative phase shifts observed in the streamwise ellipsoid are consistent with upstream tilting of the arch shown in Fig. 4.25a. There is no plateau in $\phi_{u_1u_2}$ for the streamwise ellipsoid at $f_s = 1.14$ Hz for $z/H = 1$, due to the low spectral coherence for that location. Therefore, there is no point at $z/H = 1$ in Fig. 4.34b. This

observation is consistent with larger magnitudes of the phase shifts observed for the streamwise ellipsoid, compared to the transverse ellipsoid, closer to the base plane, which suggest greater tilting of the arch structures.

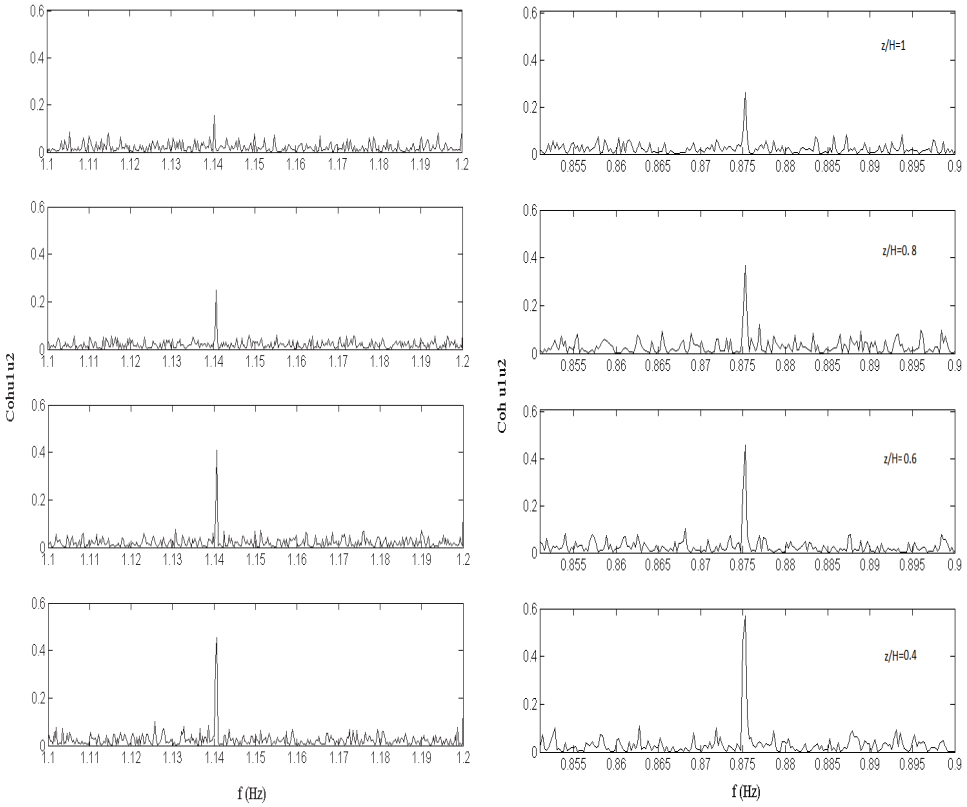

Figure 4.32: Spectral coherence $Coh_{u_1u_2}$ between streamwise fluctuating velocity u_1 and u_2 for (a) streamwise, and (b) transverse ellipsoid at $x = y = 1D$. u_1 was measured at $z/H = 0.2$ and u_2 was measured from $z/H = 0.4$ to 1.

4.2.7 Relative Submergence Revisited

The effect of relative submergence at high free-stream turbulence flow on the wake structures located at one specific transverse plane, $x/H = 1.5$, is described in Sec. 4.1.4. To better understand the effect of relative submergence on the wake

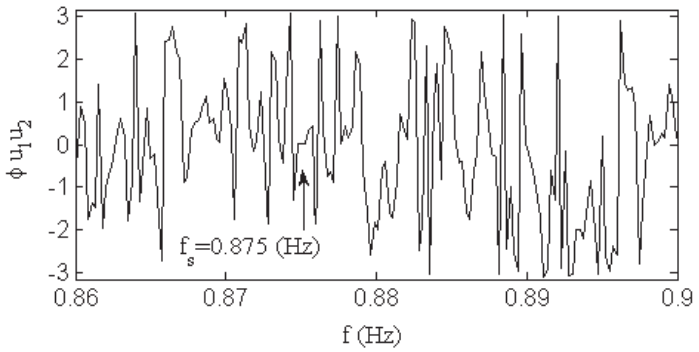

Figure 4.33: The phase shift between u_1 and u_2 for transverse ellipsoid at $x = y = 1D$. u_1 was measured at $z/H = 0.2$ and u_2 was measured from $z/H = 0.4$ to 1. Results with u_2 at $z/H = 0.4$ have been illustrated as an example.

structures and their evolutions with downstream distance, some of the experiments reported in Sec. 4.1.4 have been completed. These results are qualitatively in agreement with the findings observed in Sec. 4.1.4.To shed more lights on the dynamics of the low-relative-submergence wake, spectral analysis has been conducted for d/H =2.5 and 1.

At $d/H = 1$, the flow topology is necessarily different since boundary layer vorticity on the upper plate forms a horseshoe at the upper junction. It is noteworthy that at $d/H = 1$, the domain is no longer simply connected and a junction now occurs also at the tip of the obstacle. Thus, a weak horseshoe vortex is observed adjacent to the top boundary in addition to the tip vortex, which still persists. In the case of the streamwise ellipsoid, the tip structures transition from elongated patches of vorticity following the projected perimeter of the body at $d/H = 2.5$ (Fig. 4.15b) to concentrated and compact vortices at $d/H = 1$. An inverse relationship was observed between the relative submergence and the strength of the base structures for the ellipsoids, which is attributed to the modified pressure gradients on the surface of the structure and the tilting of Kármán vortices by the shear in the boundary layer.

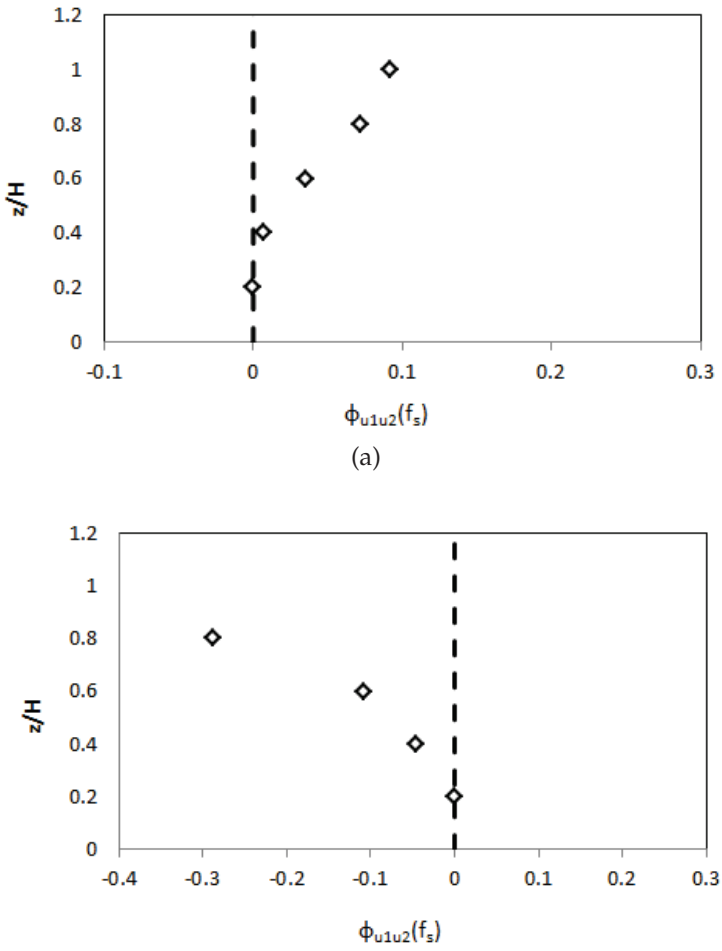

Figure 4.34: Dependence of the phase angle $\phi_{u_1u_2}(fs)$ between streamwise fluctuating velocities u_1 and u_2 at $x/D = 1$ and $y/D = 1$ at varying spanwise locations, where u_1 was measured at $z/H = 0.2$ and u_2 was measured from $z/H = 0.4$ to 1. (a) Streamwise ellipsoid, (b) Transverse ellipsoid.

Figures 4.35 through 4.38 display isocontours of streamwise dimensionless vorticity ($\omega_x^* = \omega_x H/U$) in the wakes of the ellipsoids in transverse ($y - z$) planes between $x/H = 0.5$ and 2, at $d/H = 1$. Figure 4.35 contains streamwise vorticity located at $x/H = 0.56$ and 0.75 (trailing edges) for the two ellipsoids. The horseshoe and strong base vortices are visible in both ellipsoids. The base structures are stronger for the streamwise ellipsoid than transverse.

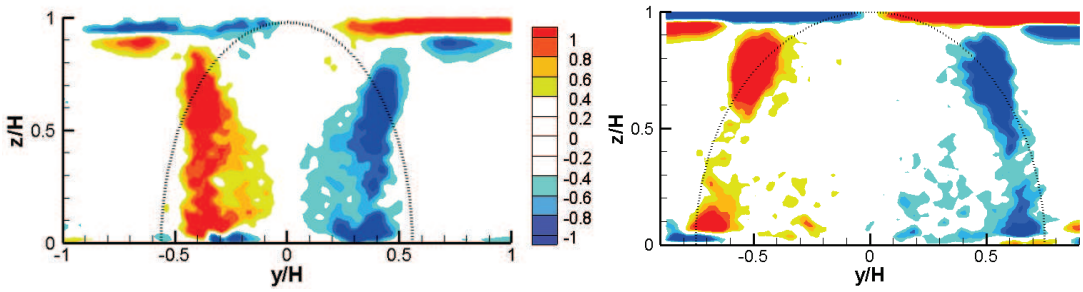

Figure 4.35: Isocontours of non-dimensional streamwise vorticity, ω_x^*, in the plane $x/H = 0.56$ and 0.75 at $d/H = 1$ for: (a) streamwise ellipsoid, (b) transverse ellipsoid. Red shades indicate counter-clockwise rotation and blue shades indicate clockwise rotation.

Figure. 4.36 illustrates the streamwise vorticity patterns at $x/H = 1$. In this location, the wake of the streamwise ellipsoid contains a concentrated transverse vortex observed just downstream of the ellipsoid. This structure is analogous to the rotor vortex observed in pyramid wakes as shown in Fig. 2.15, which appears to be connected to the tip structures observed in the wake. The concentrated transverse vortex was not observed for transverse ellipsoid in at $x/H = 1$. Figure 4.37 shows streamwise vorticity distributions at $x/H = 1.5$. The tip structures in the wake of the streamwise ellipsoid at $x/H = 1.5$ are stronger than tips at $x/H = 1$ due to the tilting of the structures downstream. The wake of the transverse ellipsoid at $x/H = 1.5$ presents the similar concentrated transverse vortex (analogous to the rotor vortex) observed for the streamwise ellipsoid at $x/H = 1$. As shown in Fig. 4.18, this delay is in agreement with the existence of bifurcation further downstream. Figure. 4.38 shows the streamwise vorticity at $x/H = 2$. The structures in the wake are weak at this location probably due to an increase in shear flow between the top plate and base plate.

As mentioned in Sec. 4.1.4, an inverse relationship was observed between the

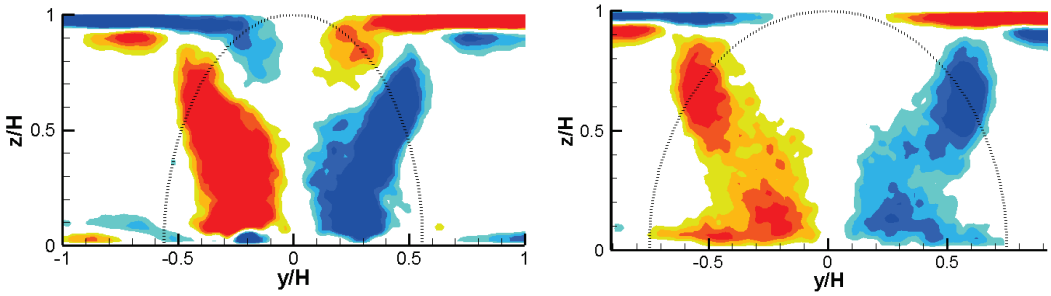

Figure 4.36: Isocontours of non-dimensional streamwise vorticity, ω_x^*, in the plane $x/H = 1$ in $d/H = 1$ for: (a) Streamwise ellipsoid, (b) transverse ellipsoid. Red shades indicate counter-clockwise rotation and blue shades indicate clockwise rotation.

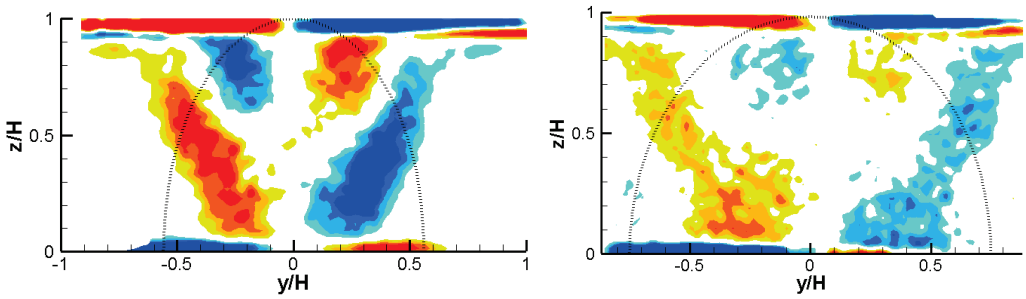

Figure 4.37: Isocontours of non-dimensional streamwise vorticity, ω_x^*, in the plane $x/H = 1.5$ in $d/H = 1$ for: (a) Streamwise ellipsoid, (b) transverse ellipsoid.Red shades indicate counter-clockwise rotation and blue shades indicate clockwise rotation.

relative submergence d/H and the strength of the base structures in the transverse and streamwise ellipsoid wakes. A dominant base structure was even observed in the streamwise ellipsoid wake at $d/H = 1$, despite that it was barely detectable for $d/H \geq 2.5$. Furthermore, dye visualizations conducted by Hajimirzaie et al. (2012) around a transverse ellipsoid at $Re_H = 5500$ showed that, while the wake is quite symmetric at $d/H = 3.9$, antisymmetric shedding is observed at $d/H = 1$.

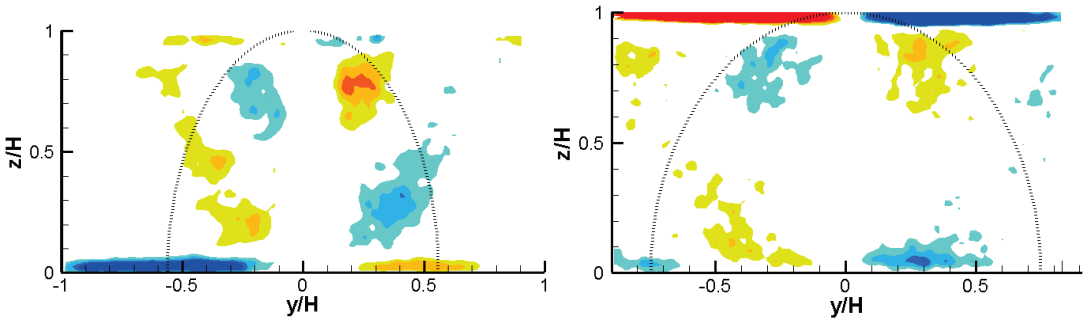

Figure 4.38: Isocontours of non-dimensional streamwise vorticity, ω_x^*, in the plane $x/H = 2$ in $d/H = 1$ for: (a) Streamwise ellipsoid, (b) transverse ellipsoid. Red shades indicate counter-clockwise rotation and blue shades indicate clockwise rotation.

As also discussed in Sec. 4.1.4, reduction in relative submergence results in significant increases in blockage ratio. For wall-mounted cylinders with aspect ratios between 4 and 10, West and Apelt (1982) found Strouhal number to be unaffected for blockage ratios less than 6% at Reynolds numbers between 2×10^4 and 6×10^4. For higher blockage ratios, the Strouhal number was found to rise rapidly with blockage ratio. While this may quantitatively affect the observed shedding frequencies, it is not expected to change the qualitative shedding behavior, which we discuss below.

To better understand the dynamics of the low-relative-submergence wake, the spectral analyses reported above have been conducted for d/H=2.5 and 1. Figs. 4.39 and 4.40 show the power spectral density function for the streamwise and transverse ellipsoids at multiple spanwise positions for $d/H = 2.5$, with $y/D = 1$ and x/D=1 to 3. Weak dominant frequencies are apparent in the wakes of both the transverse and streamwise ellipsoids. The Strouhal numbers are $St = 0.188$ and 0.183 for the transverse and streamwise ellipsoids, which is unchanged from the Strouhal numbers observed at $d/H = 3.9$ for both ellipsoids. However the

peaks in the power spectral density are somewhat more broad at d/H=2.5 for both ellipsoids. At x/D=2 and 3 the power spectrum for the streamwise ellipsoid exhibits weaker peaks (Figs. 4.40b, 4.40c) compared to the same locations in the transverse ellipsoid wakes (Figs. 4.39b and 4.39c). The power spectral density functions for the cylinders at d/H=2.5 are not significantly different than those at d/H=3.9, and therefore these data have not been shown.

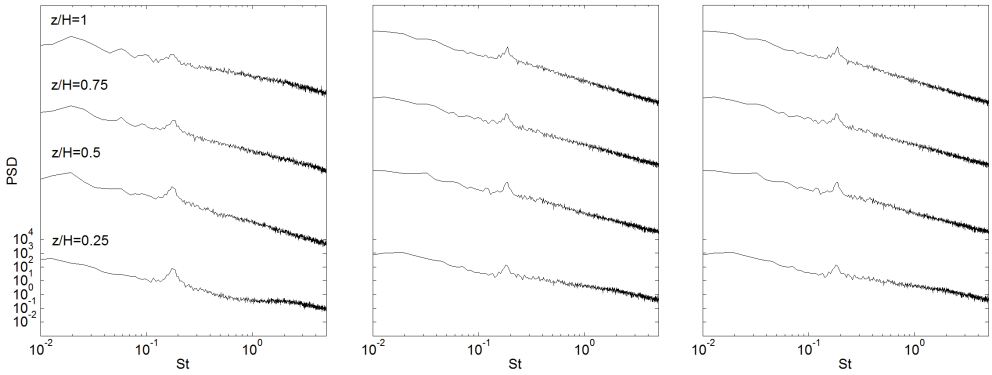

(a) (b) (c)

Figure 4.39: The power spectral density function of the of the streamwise velocity component at d/H=2.5 and y/D=1 for the transverse ellipsoid at (a) x/D=1, (b) x/D = 2 and (c) x/D = 3. Each spectrum is the average of 20 individual spectra. Spectra are off-set by constant factor for clarity.

Figure 4.41 shows the power spectral density functions for all four obstacle geometries with d/H = 1, at x/D = 1 and y/D = 1. Since z/H = 1 now corresponds to the location of the upper plate, the top measurement position has been changed to z/H = 0.85. It should be noted that, since the top and bottom plates are not identical, slight differences exist in the boundary layers on the base plane and top plate. The relative boundary layer thickness on the top plate was δ_{99}/H = 0.18.

The dominant peaks are more distinct than at d/H = 3.9 in all cases except the streamwise ellipsoid, which has actually further weakened compared with

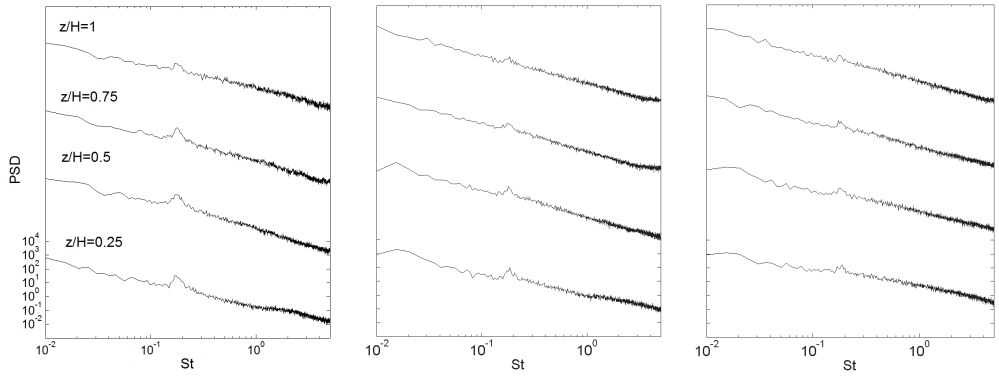

(a) (b) (c)

Figure 4.40: The power spectral density function of the of the streamwise velocity component at d/H=2.5 and y/D=1 for the streamwise ellipsoid at (a) x/D=1, (b) $x/D = 2$ and (c) $x/D = 3$. Each spectrum is the average of 20 individual spectra. Spectra are off-set by constant factor for clarity.

$d/H = 2.5$. Most notably, however, both cylinders now have a dominant shedding frequency as well as a secondary, higher-frequency peak.

At $d/H = 1$, the Strouhal number has significantly increased to 0.357 and 0.345 for the streamwise and transverse ellipsoid respectively. It is expected that the increase in Strouhal number is due to a combination of reduced three-dimensionality due to the proximity of the top surface, the change in topology as the obstacles now span the entire height of the domain, and blockage effects. The shedding behavior is very similar for both cylinders, also with essentially the same shedding Strouhal numbers, which were measured to be $St = 0.248$ for the $AR = 0.67$ cylinder and $St = 0.243$ for the $AR = 0.89$ cylinder. The secondary peaks occur at St =0.694, 0.488 ,and 0.486 in the wakes of the transverse ellipsoid, and cylinders of AR=0.67 and AR=0.89, respectively, which represents the second harmonic of f_s, as also observed by Wang and Zhou (2009) and Okamoto and Sunabashiri (1992) for a square cylinder of aspect ratio 7. It is particularly interesting that this only occurs at $d/H = 1$ where the shedding behavior begins to approach that of much higher-aspect-ratio

cylinders, as will be discussed in the following paragraph. Furthermore, Wang and Zhou (2009) did not observe the second harmonic near the tip where the Kármán shedding does not exist.

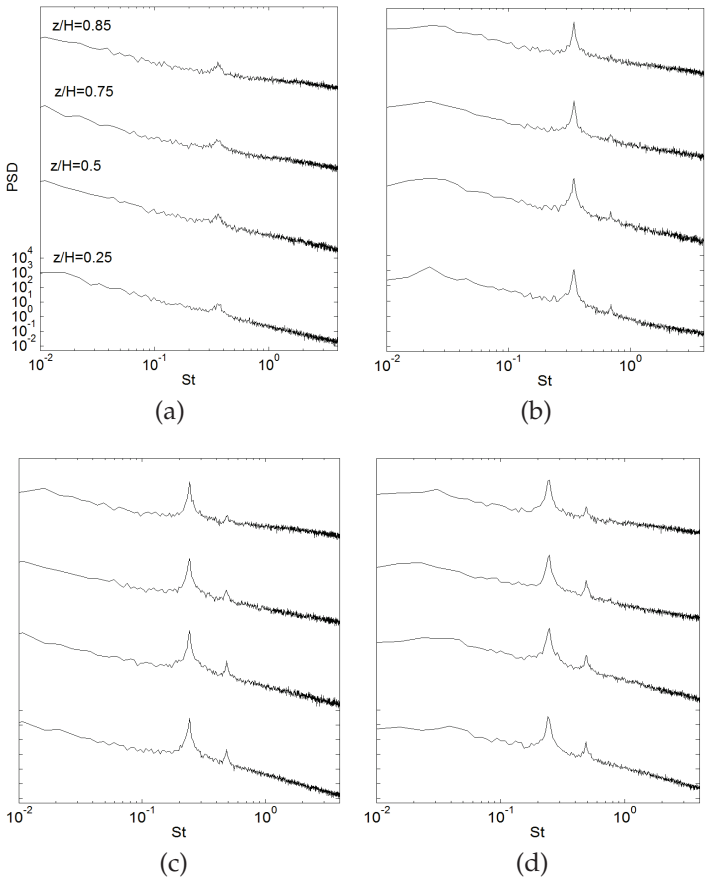

Figure 4.41: The power spectral density function of the streamwise velocity component at $d/H = 1$ for: (a) streamwise ellipsoid, (b) transverse ellipsoid, (c) cylinder ($H/D = 0.67$), (d) cylinder ($H/D = 0.89$) at $x/D = 1$ and $y/D = 1$. Each spectrum is the average of 20 individual spectra. Spectra are off-set by constant factor for clarity.

Auto- and cross-correlations of the velocity fluctuations were performed for symmetrically-positioned sensors in the wakes of each of the four geometries at $d/H = 1$. Figure 4.42 shows the results for $x/D = 1$ and $y/D = \pm 1$ in the wake of

the transverse ellipsoid. The cross-correlation values are now negative at $\tau = 0$ s, indicating that the shedding is antisymmetric, consistent with the reduced-Reynolds-number flow visualizations of Sec. 4.1.4. The cross correlation for the streamwise ellipsoid is shown in Fig. 4.43, again exhibiting negative values at $\tau = 0$ s. Somewhat surprisingly, the magnitude of the auto-correlation near the tip is two to four times that at the other positions.

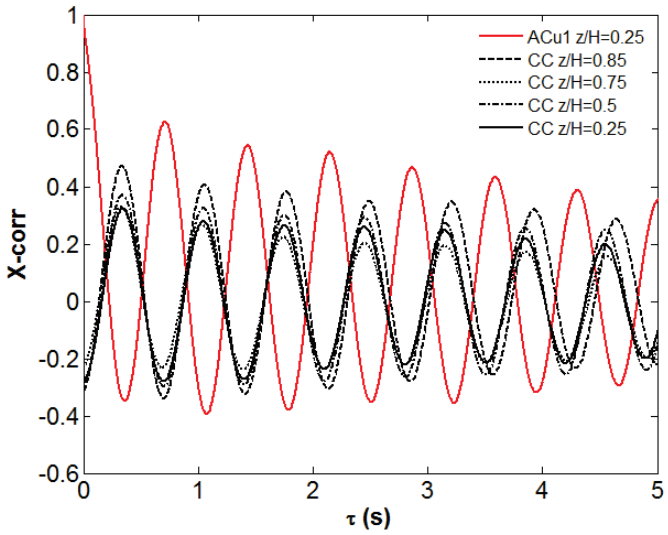

Figure 4.42: Auto- and cross-correlation of fluctuating velocity on opposite side for transverse ellipsoid an $d/H = 1$ in $x/D = 1$, $y/D = \pm 1$, and $z/H = 0.25$ to 0.85 .

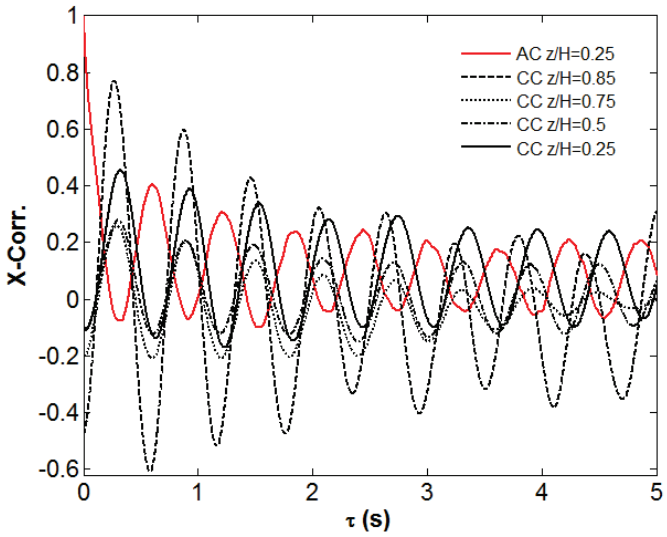

Figure 4.43: Auto- and cross-correlation of fluctuating velocity for streamwise ellipsoid at d/H=1 and x/D=1,$y/D = \pm 1$, z/H = 0.25 to 0.85

CHAPTER 5
FLOW CHARACTERISTICS AROUND A WALL-MOUNTED SPHERE

The motivation of this part of the study is to provide detailed flow characteristics around a fully submerged, wall-mounted, isolated spherical obstacle representative of a boulder in a steep mountain stream. The results of this study can provide insight to predict sediment transport characteristics in more complex riverine environments involving large obstacles. Of primary interest in this study are the effects of dominant flow structures and their dynamics on the bed shear stress distributions surrounding the obstacle. These measurements will inform future work to predict sediment transport characteristics in shallow flows.

The experiments reported in this chapter have been conducted in low free stream turbulence. As it has been shown in Sec.3.1, boundary layer characteristics have been measured and for the sphere, $\delta_{99}/H = 0.14$ which provided ratios $\delta/D = 0.14$, as well.

5.1 Flow Patterns in the Streamwise Symmetry Plane

Some basic properties of the flow are first characterized by examining the velocity, vorticity, and Reynolds shear stress fields on the symmetry plane in the wake of the sphere. Fig. 5.1b contains the mean streamlines, obtained from 2000 velocity fields, in the symmetry plane upstream and downstream of the sphere. The reattachment length on the symmetry plane non-dimensionalized by the obstacle width is $x_r/D = 1.90$. In other investigations of wall-mounted spheres, Okamoto (1980), Tsutsui (2008), and Ozgoren et al. (2012) determined $x_r/D = 2.50$, 1.65, and 1.42, respectively. This magnitude is also similar to other measurements reported in the literature for wall-mounted bodies of aspect ratio $O(1)$ as reviewed in Sec. 4.1.2. Okamoto (1980) reported $x_r/D = 2.40$ for hemisphere cylinder with matched aspect ratio of sphere. For a hemisphere, Savory and Toy (1986) reported reattach-

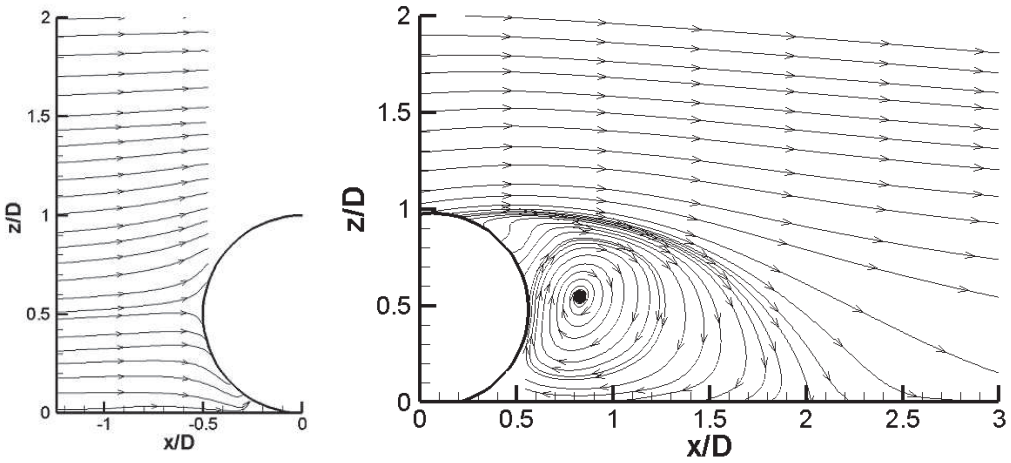

(a) (b)

Figure 5.1: Mean streamlines of the sphere: (a) upstream (b) downstream.

ment lengths between 1.1D and 1.25D (varying with boundary layer parameters) in boundary layers significantly thicker than that in the present study. As it has been reported in Sec. 4.1.2 for low-aspect-ratio ellipsoid and cylinder (AR=0.89) of diameter 56 mm, x_r/D are 1.70 and 2.00, respectively. Figure 5.1b, shows the streamlines upstream of the sphere. It should be noted that the well-known horseshoe vortex should be located in this region although it cannot be discerned in Fig.5.1b. The profiles of the time-averaged streamwise velocity, u, at different streamwise positions at $y/D = 0$ are illustrated in Fig. 5.2.

Isocontours of non-dimensional transverse vorticity ($\omega_y^* = \omega_y H/U$) are shown in Fig. 5.3. In addition to the regions of large positive ω_y (counter clockwise rotation) located in the vicinity of the shear layer separating from the top of the obstacle, significant negative vorticity is found for each geometry adjacent to the base plane in the vicinity of the recirculation region. Some negative values of vorticity also exist on the lee faces of the sphere.

To shed more light on the flow structures upstream of the sphere, especially

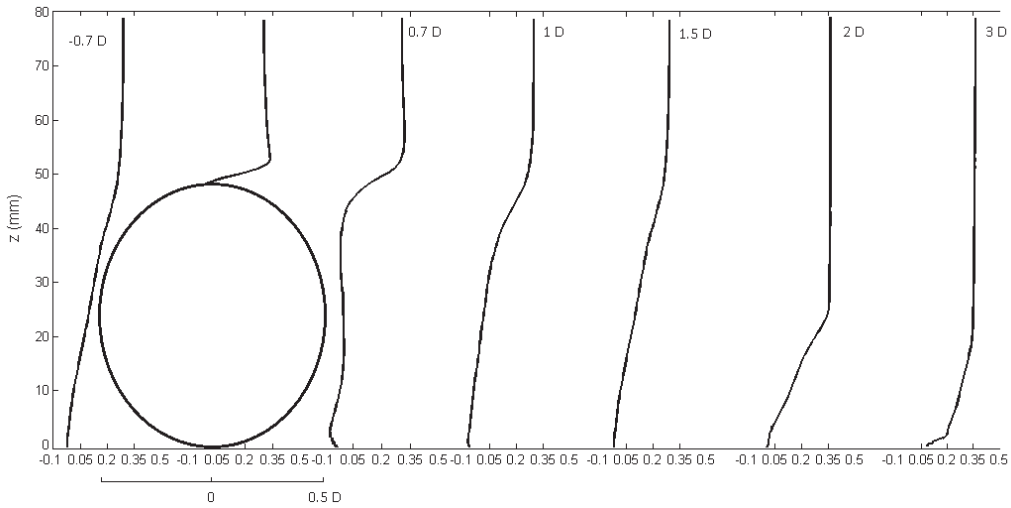

Figure 5.2: Time-averaged, streamwise velocity, u, profiles along the centerline at $y/D = 0$

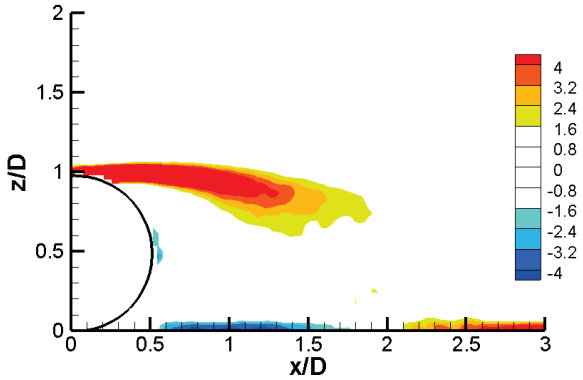

Figure 5.3: Isocontours of nondimensional spanwise vorticity, ω_y^*, downstream of the sphere. Red shades indicate clockwise rotation and blue shades indicate counter-clockwise rotation.

the existence of a horseshoe vortex, laser illumination was employed under the flume as shown in Fig. 5.4. This particular positioning of the laser was done so to prevent shadowing around the junction that occurs when the laser is used from top of the obstacle. While the spatial resolution was high enough ($D/90$, where D is sphere diameter), the horseshoe vortex was not observed upstream of the sphere probably related to convex shape of the sphere at the junction (D goes to zero) which may increase strong interaction of vortex with the boundary in agreement with the studies of Ballio et al. (2012). The non-dimensionalized streamwise velocity profiles, u/U_∞, upstream of the sphere will be later shown in Fig. 5.15 which shows the adverse pressure gradient is weaker near the base plane than it is at higher levels.

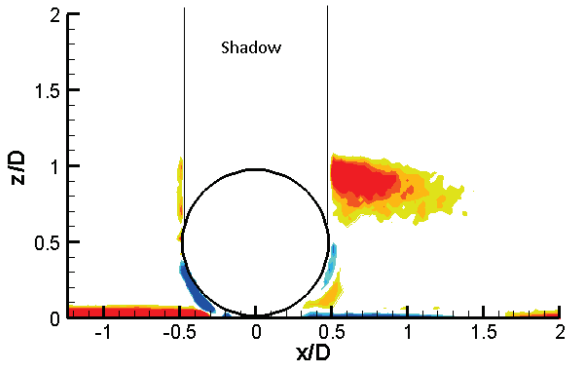

Figure 5.4: Isocontours of nondimensional spanwise vorticity, ω_y^*, upstream and downstream of the sphere using the laser under the flume. Red shades indicate clockwise rotation and blue shades indicate counter-clockwise rotation.

Seal et al. (1995) noted the spanwise vorticity in the incoming boundary layer at the junction of a rectangular obstacle moves toward the leading edge and presents reorganized discrete vortices. This system of vortices interact with vorticity of the opposite sign generated on the surfaces of the junction. The resulting structure

is a complex pattern of primary and secondary vortices around the obstacle, undergoing mutual annihilation and deformation by the main flow. In the sphere geometry, it is therefore expected that the pressure gradient is weak and the vorticity of the opposite sign is not produced and separated in the same way. Ballio et al. (2012) demonstrated that for different symmetrical geometries, the obstacle diameter is the main length scale parameter that controls the horseshoe vortex system upstream of the body. They showed that with reduction in obstacle diameter, the vortex system can be expected to vanish and only the weak primary vortex observed.

In the same boundary layer characteristics, the horseshoe vortex observed upstream of the ellipsoids at z/H =0.05 or 0.25δ as shown in Fig. 4.2, where H is the hight of ellipsoids which is equal to the sphere diameter. A strong horseshoe vortex was observed upstream of the sphere in the study of Tsutsui (2008) at $Re_D = 1 \times 10^4$ while $\delta/D = 0.46$ was 3 times of this study. However, Ozgoren et al. (2013) did not observe the horseshoe vortex upstream of the sphere, using the laser under the flume similar to this study, at $\delta/D = 1.5$. Therefore the effect of δ/D is not clear on existing of the horseshoe vortices on the sphere junction. It will be shown in Sec. 5.2 for the upstream view results that a weak horseshoe vortex exists in the wake similar to observation of Okamoto (1980) in the same range of δ/D of this study.

The distributions of kinematic Reynolds shear stress ($-\overline{u'w'}/U^2$) in the wake of the sphere is shown in Fig. 5.5. Two zones with higher turbulence level occur: the transitional region of the separated shear layer (downstream of the separation point at the top of the sphere), and near the bed around the reattachment point. This observation is quite similar to results of Ozgoren et al. (2012, 2013) for a wall-mounted sphere. There is only one separation point, near the top of the sphere, and the Reynolds stresses are significantly lower just after separation compare to what was observed for the cylinder geometries investigated here. Similar results

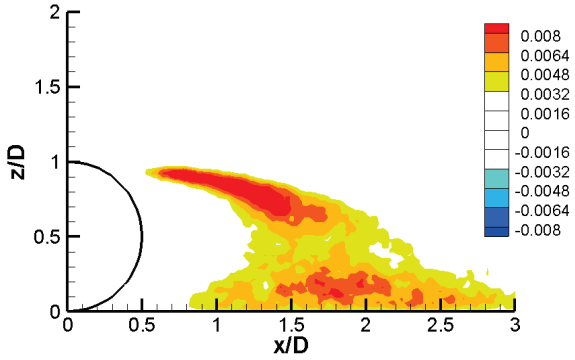

Figure 5.5: Isocontours of Reynolds shear stress, $-\overline{u'w'}/U^2$, downstream of the sphere.

were observed for the ellipsoids, as reported in Sec. 4.1.2. Further downstream, the Reynolds stresses increase significantly due to the transition of the shear layer.

The streamwise turbulence intensities, $rms(u')$ are illustrated for $y/D = 0$ and -1 in Figs. 5.6 and 5.7 to compare with Papanicolaou et al. (2012b) which investigated fully-developed open-channel flow over a rough bed. Values of $rms(u')$ at $y/D = 0$ show a maximum at z/D =1 which is the crest of sphere. This is in good agreement with Papanicolaou et al. (2012b); Ozgoren et al. (2013) and Strom and Papanicolaou (2007) who observed the maximum of $rms(u')$ at the crest of a sphere and pebble cluster. Near the bed, the $rms(u')$ decreases. At $y/D = -1$, the $rms(u')$ profiles are similar, therefore the $rms(u')$ profiles have been considered up to z/D =1.5. At $y/D = -1$, $rms(u')$ shows lower magnitude than $y/D = 0$. The $rms(u')$ values rise near the bed in this location.

Figure 5.8 shows profiles of mean wall-normal , w, velocity along the lines at $z = 0.25D$, $0.5D$, $0.75D$ and $z = 1D$ on the center plane for the sphere. Near the bed, at $z/D = 0.25$, there is a downward flow upstream of the sphere. At this height, there is also upflow downstream of the sphere. The downwash reaches its maximum at $x/D = 1$. At z/D =0.5 and 0.75, also an upwash is evident.

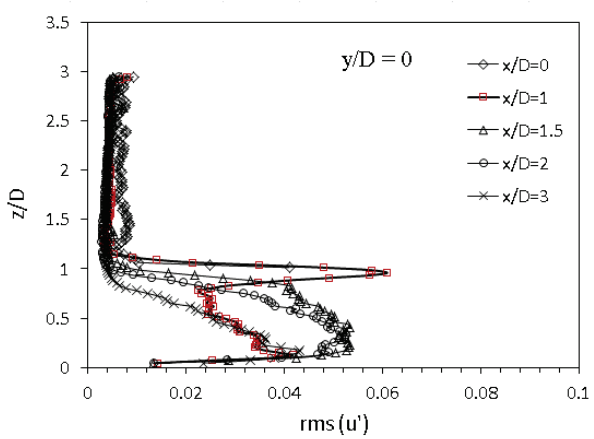

Figure 5.6: Streamwised turbulence intensity profiles at $y/D = 0$

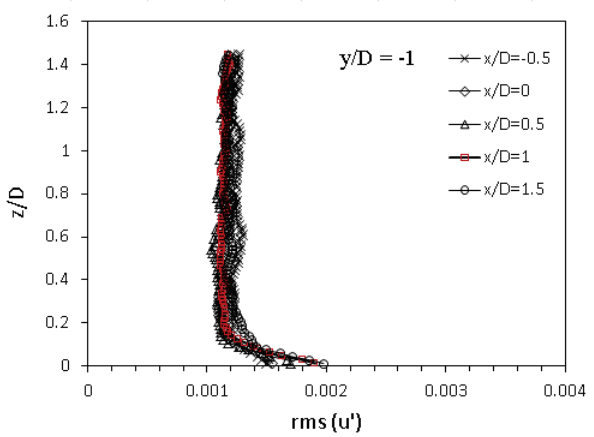

Figure 5.7: Streamwised turbulence intensity profiles at $y/D = -1$

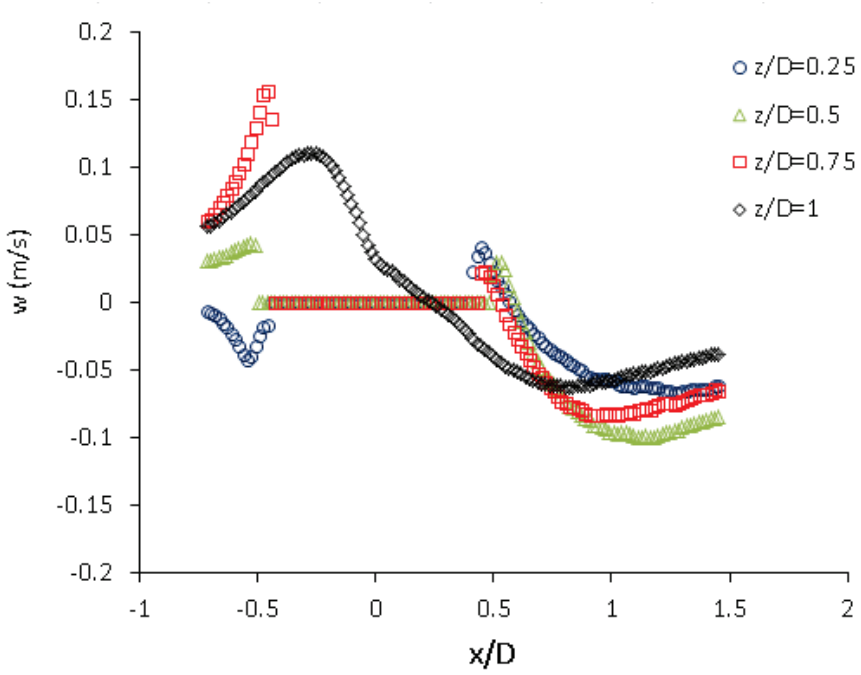

Figure 5.8: Time-averaged, wall-normal velocity, w, profiles along the centerline at $y/D = 0$

5.2 Streamwise Vorticity Distributions

Figure 5.9 and 5.10 display isocontours of streamwise dimensionless vorticity ($\omega_x^* = \omega_x D/U$) in the wake of the sphere in transverse (y-z) planes at x/D =0, 0.2, 0.4, 0.5, 0.6, 0.7, 0.8, 1, 1.2, 1.6, 2, and 2.5, with $d/H = 3.5$ using the experimental configuration shown in Fig. 3.13. Comparison with the reattachment length, x_r/D =1.90, indicated that the planes at x/D =0 to 1.6 fall within the recirculation region. Each mean vorticity field was obtained from 3000 instantaneous velocity fields.

Figure 5.9 contains streamwise vorticity located at x/D =0 to 1 for the sphere. Figures 5.9a through 5.9c contain streamwise vorticity located at x/D =0 through 0.4 which are before the trailing edge of the sphere. The generation of vorticity into the streamwise direction (even before shedding) appears to be much more significant

than in the case of the ellipsoids. At $x/D = 0.4$, as shown in Fig. 5.9c, the strong vortices generated on the circumference of the sphere and shed downstream while after trailing edge ($x/D = 0.5$) have been tilted downstream as can be interpreted from Fig. 5.9d.

The streamwise vorticity distribution in the wake of the sphere at x/D =0.5 is similar to that observed for the streamwise ellipsoid. This distribution is also similar to that observed by Okamoto (1980) and Pattenden et al. (2005) in the wake of a sphere and a low-aspect-ratio cylinder and is dominated by the tip and horseshoe structures. For the sphere (as with the ellipsoid), the tip structures are almost certainly the streamwise projection of a complex $3D$ vorticity field shed around the perimeter of the sphere.

Near the base plane, two pair of vortices are visible in the wake of the sphere, which have the same sense of rotation, as named in Fig.5.9b: close to the side of the sphere (hereafter lobes) and further from the obstacle in the transverse planes (well-known horseshoe vortex) as shown in Fig. 5.9b and 5.9c. The lobes (inner vortices) are stronger and the further one is weaker. The circulation of these structures and their evolution will be discussed. At x/D =0.5 and 0.6 (Fig. 5.9d and 5.9e), a weak vortex pair inducing upwash is observed at the top of the wake. This vortex pair (hereafter upper vortices) was not reported in Okamoto's (1980) study.

Figure 5.9f illustrates the streamwise vorticity patterns at x/D =0.7. The tip vortices remain at approximately the same vertical position, but they are significantly sheared toward the base plane in the wake. The upper vortices are no longer evident close to the top of the sphere in the wake. It can be deduced from a comparison of Fig. 5.1b and Figs. 5.9d to 5.9e that this vortex pair (upper vortices) exists only inside the recirculation area and remains distinct from the tip vortices. From x/D =0.7 to further downstream at x/D =1, the tip and lobe vortices amalgamate within the recirculation region as shown in Figs 5.9f to 5.9h.

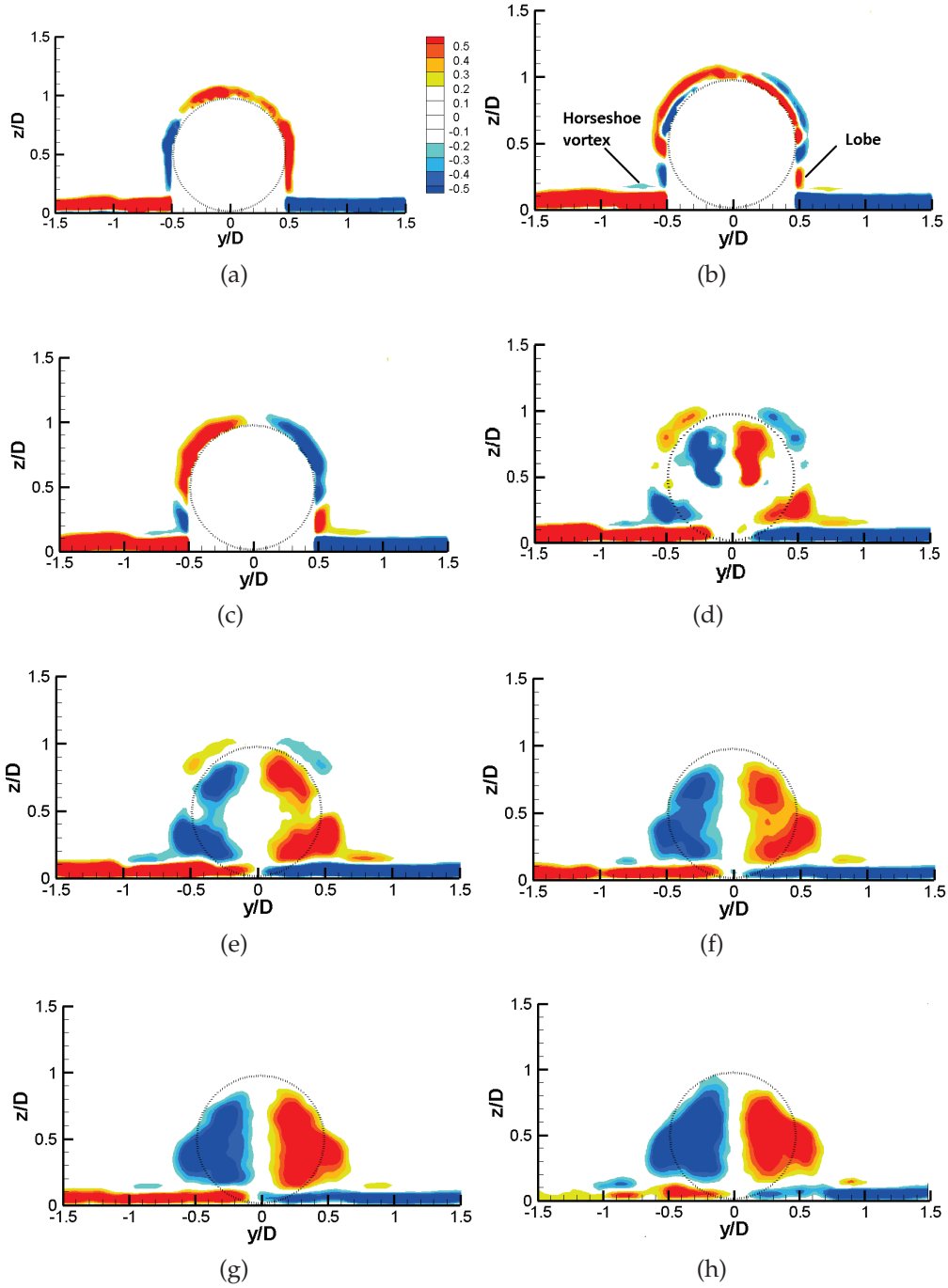

Figure 5.9: Isocontours of non-dimensional streamwise vorticity, ω_x^*, in the plane $x/D = 0, 0.2, 0.4, 0.5, 0.6, 0.7, 0.8$, and 1 (left to right and top to bottom) in $d/H = 3.5$. Red shades indicate counter-clockwise rotation and blue shades indicate clockwise rotation.

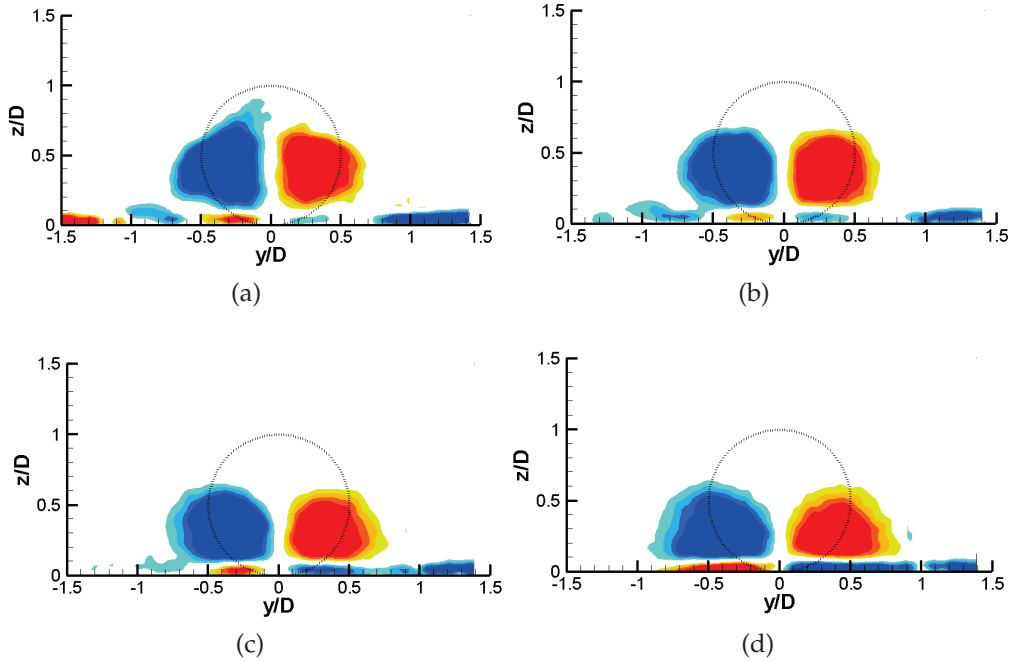

Figure 5.10: Isocontours of non-dimensional streamwise vorticity, ω_x^*, in the plane x/D = 1.2, 1.6, 2, and 2.5 (left to right and top to bottom) in d/H = 3.5. Red shades indicate counter-clockwise rotation and blue shades indicate clockwise rotation.

Figure 5.10 shows the streamwise vorticity at x/D =1.2 to 2.5. As Figs. 5.10a through 5.10d display, tip vortices are significantly sheared toward the base plane in the wake of the sphere and the horseshoe lobes are no longer evident in the wake. In these layers, the tip vortices merge with the legs of the horseshoe vortex, which have the same sense of rotation, and finally end up in fairly large trailing vortices as sketched in Pattenden et al (2005). The trailing vortices are quite axisymmetric in these layers. Similar results were observed further downstream at x/D = 3 and 4. There is a striking resemblance to the streamwise vorticity field around the wall-mounted sphere demonstrated in Papanicolaou et al. (2012b) despite significant differences in approach flow and bed characteristics.

The dimensionless circulations $\Gamma^* = \Gamma/(UD)$ of each of the identified structures at x/D = 0.4 to 0.7 in the wakes of the sphere were computed by integration of

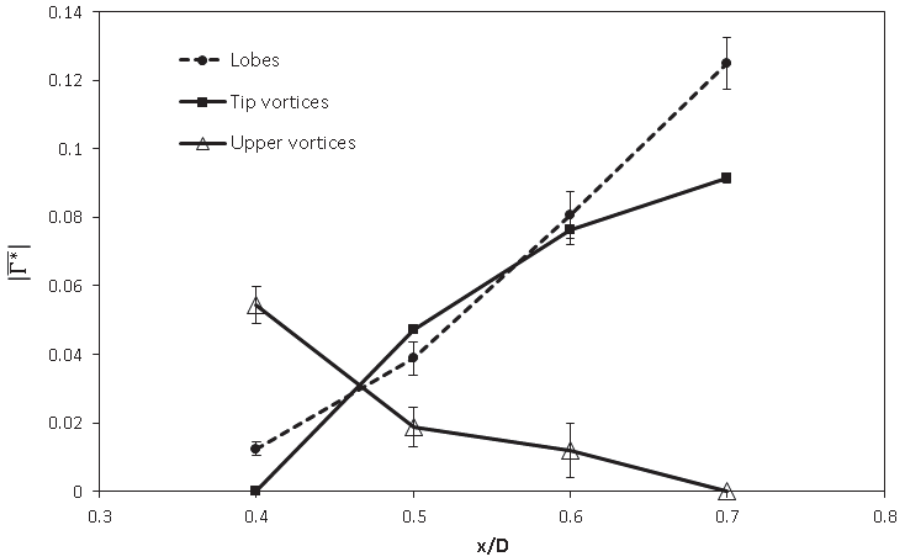

Figure 5.11: Average dimensionless circulations of structures identified for the sphere in Fig. 5.9c to Fig. 5.9f and the left/right deviation.

the streamwise component of the vorticity field within an isocontour of $\omega^* = 0.07$ (at this value, the circulation was found to be insensitive to small changes in ω^*). Further downstream, due to the ambiguity in the definition of the tip structure boundaries when it descends to the base plane and combines with the horseshoe lobes (Figs. 5.9g through 5.10d), no attempt has been made to measure circulation and distinguish the tip structure from the connected like-signed vorticity. Evidentially, this amalgamation contributes to the increase in circulation of the tip vortices in the sphere wake. The results are given in Fig. 5.11. Differences in the circulations of the left and right structures represent a larger error than that due to the PIV measurements, and therefore, the sizes of the error bars are given by Equation 4.1.

The mean circulation magnitude of the upper vortices decreases monotonically in the range $0.4 \leq x/D \leq 0.7$, whereas the magnitude of the tip and lobes structures increase such that both vortex pairs have similar magnitude at x/D =0.5 and 0.6.

The circulation of the lobes is larger than the horseshoe (HS) vortex circulation of a streamwise ellipsoid, but smaller than the HS vortex circulation of a transverse ellipsoid at the same location. The circulation of well-known HS vortex (weak vortex) has not been illustrated in Fig. 5.11. The streamwise decay of upwash structures is expected, and may be attributed to enhanced turbulent diffusion and cross-cancellation of the streamwise structures. However, since there is no source of vorticity away from the boundaries, the strengthening of the tip structures in the wake with streamwise distance must be explained by tilting of vorticity into the upstream orientation by a similar mechanism as described in Sec. 4.1.3, which will be described later in a discussion of the instantaneous structure and dynamics of the wakes in Sec. 5.4.

5.3 Shedding Characteristics

Figure 5.12 illustrates the power spectral density function (PSD) of the streamwise velocity component measured for the sphere at relative submergence of $d/H = 3.5$. The hot-film probe was placed at spanwise locations $x/D = 1$, 2 and 3, and for $z/D = 0.25$, 0.5, 0.75, and 1. The z-axis of the power spectra is offset to allow comparison between measurements at different locations. Due to symmetry, the power spectra from either side are nearly identical and only the spectra from one side of the obstacles are shown. In this case, the broad, weak peak is observed near the bed at $St = 0.21$ ($f_s = 1.47$ Hz) which is only a marginally measurable difference from that of the transverse ellipsoids. Taneda (1978) reported the Strouhal number around 0.2 in the subcritical Reynolds number around the sphere which is consistent with this study observation. Notably, this peak is essentially non-existent at $x/H = 1$ for all streamwise positions. The peak continues up to $z/H = 0.5$ further downstream at $x/D = 2$, suggesting that the shedding region in the wake grows outward from the wall with increasing x. It is plausible that this is the shedding frequency from the spanwise edges of the sphere since the structures shed would

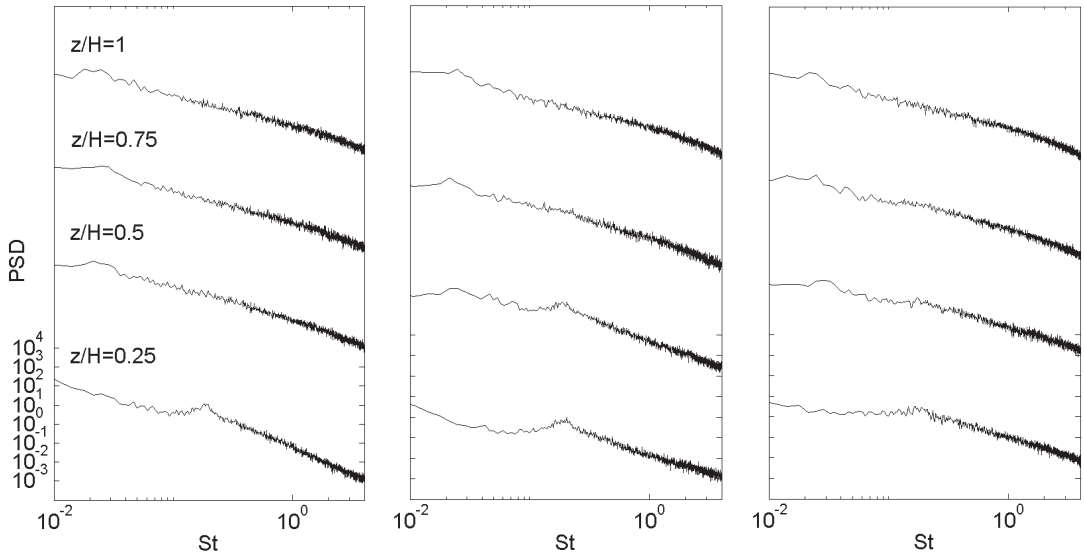

Figure 5.12: The power spectral density function of the of the streamwise velocity component in $d/H = 3.5$ for sphere at $y/D = 1$: (a) $x/D = 1$, (b) $x/D = 2$, and (c) $x/D = 3$. Each spectrum is the average of 20 individual spectra. Spectra are off-set by constant factor for clarity.

have a highly three-dimensional vorticity field, and only the streamwise projection of it is seen in the vorticity plots.

A more broad peak is centered around $St = 0.025$ ($f_s = 0.175$ Hz) at $z/D = 0.5$ to 1 for $x/D = 1$ to 3. Similar to the streamwise ellipsoid, the low-frequency peaks persist at all three streamwise measurement locations. As illustrated in Sec. 4.2.5, similar peaks were observed for ellipsoidal geometry and low-taper-ratio triangular plates observed by Castro and Watson (2004). The ratio of primary (high) peak to low-frequency peak (broad peak) is 8.4 which is closer to this ratio in the streamwise ellipsoid. The ratio of primary (high) peak to low-frequency peak (broad peak) is 7.2 and 3.2 for streamwise and transverse ellipsoid, respectively.

Figure 5.13 shows cross-correlations of velocity fluctuations for measurements at symmetric positions in the wake of the sphere at $x/D = 1$, $y/D = \pm 1$, and

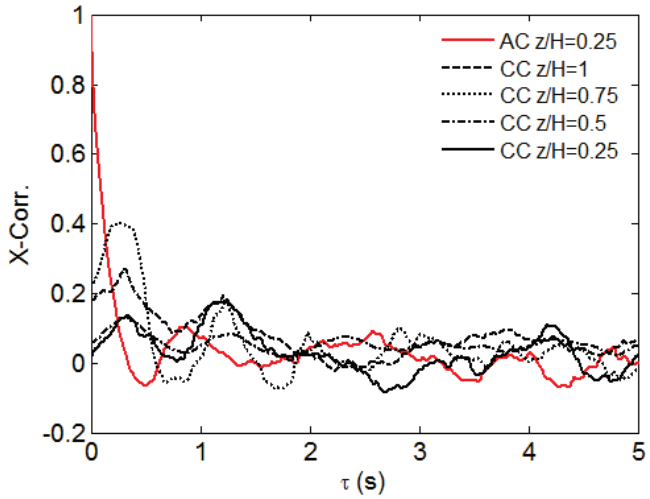

Figure 5.13: Cross-correlation of fluctuating velocity on opposite side for the sphere at $x/D = 1$ and $y/D = \pm 1$ and $z/H = 0.25$ to 1.

equal, varied values of z/H. The auto-correlation function at $x/D = 1$, $y/D = 1$, and $z/H = 0.25$ is also shown in the figure. The spatial cross-correlations, $\tau = 0$ s, are positive for each wall-normal position, indicating approximately in-phase shedding on opposite sides of the sphere. A positive spatial correlation is evident at $z/H = 0.75$ and 1; however, the values are close to zero near the mid-span and bed of the sphere. Similar to the streamwise ellipsoid the spatial cross correlation values are considerably larger at $z/H = 1$ and 0.75, on the upper part of the sphere they are possibly weaker near the base due to the interaction with the horseshoe lobes.

The cross-correlation function is less periodic than for the transverse ellipsoid, suggesting less organized shedding due to the nearly axisymmetric nature of the spherical geometry.

5.4 Proposed Model for the Sphere Wake

As suggested in Sec. 5.2, the model by Okamoto (1980) shown in Fig.2.18 describes some of the preliminary features observed in the wake of the sphere. However, no explanation is provided for the physical mechanisms governing the upwash or downwash in the wake. As noted in Sec. 4.2.4, for the ellipsoid wakes, we propose a model, shown in Fig. 4.25, which does account for the upwash or downwash in the wake. The dominant structures in the deeply-submerged sphere wake are the horseshoe vortex (not shown in the Fig. 4.25) and the arch-shaped shear-layer. As suggested for the streamwise ellipsoid, the dominant mechanism governing the dynamics of the resulting arch structure to produce the observed mean flow is Biot-Savart self-induction due to the curvature of the vortex which, due to the vorticity orientation, would tend to drive the top of the arch upstream as shown in Fig. 4.25a. However, Okamoto (1980) proposed a model for a wall-mounted sphere, with inclined arch vortices in the downstream direction such that their streamwise legs induce an upwash.

As noted in Sec. 5.2, near the base plane, two sets of strong (lobes) and weak (horseshoe) vortices are observed in the wake. The weak horseshoe vortex, further from the obstacle in transverse planes, is a well-known horseshoe vortex which is shown in Okamoto (1980)'s model as shown in Fig. 2.18. The strong vortices (lobes) are also observed in Okamoto (1980)'s investigation as shown in Fig. 5.14a; however, he did not discuss the source of these lobes upstream of the obstacle, so his wake structure is incomplete. Figure 5.14 shows the existence of lobes on the side of the sphere in both investigations. These lobes have not been illustrated in Okamoto's model therefore it is not clear how they fit into a 3D model of the wake. It is noteworthy that the horseshoe vortex upstream of sphere are weak (in this study) compared with the approaching boundary layer, therefore they have not been observed in Fig. 5.1a.

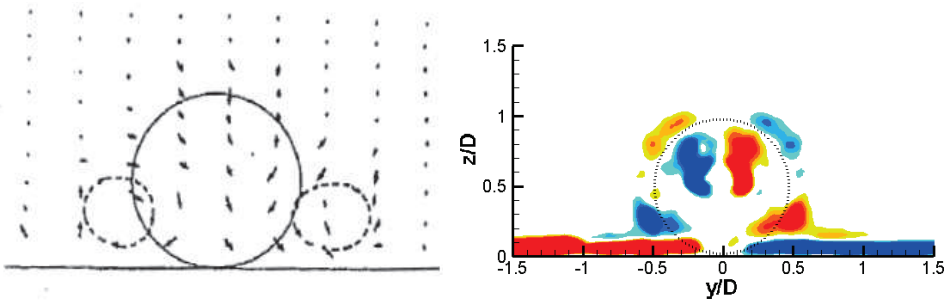

(a) (b)

Figure 5.14: Existence of horseshoe lobes on the side of the sphere: (a) Horseshoe vortex behind the sphere observed by the tuft-grid method (Okamoto, 1980), (b) Isocontours of non-dimensional streamwise vorticity, ω_x^*, in the plane $x/D = 0.5$ in $d/H = 3.5$. Red shades indicate counter-clockwise rotation and blue shades indicate clockwise rotation.

A model of the arch vortex dynamics was proposed to explain the observed streamwise vorticity distributions in the sphere wake as shown in Fig. 5.16. The data presented in Fig. 5.15 offers insight into the origin of the lobes structures.

A wall jet is present as the flow approaches the obstacle, indicating that the adverse pressure gradient upstream of the obstacle is weaker near the base plane than it is at higher levels (up to $z/D = 0.5$). Such a strong vertical gradient of streamwise velocity over the bottom half of the sphere would be expected to tilt vorticity shed in that region into the streamwise direction. Thus, a plausible mechanism for the origin of the lobes is "arch" structures tilted in the streamwise direction. So from the side, the arches would take on an "*S*" shape as illustrated in Fig. 5.16.

The experimental study of Taneda (1978) around the sphere showed that the orientation of the wake is determined by small perturbations on the surface of the sphere (Fig. 2.24). For a wall-mounted sphere, there is a large perturbation due to the pressure of the wake but the results are still in surprising agreement with his study. This model of wake structure and dynamics correlates well with the observations of wakes as shown in Fig. 5.11, in which the dominant structures increase in

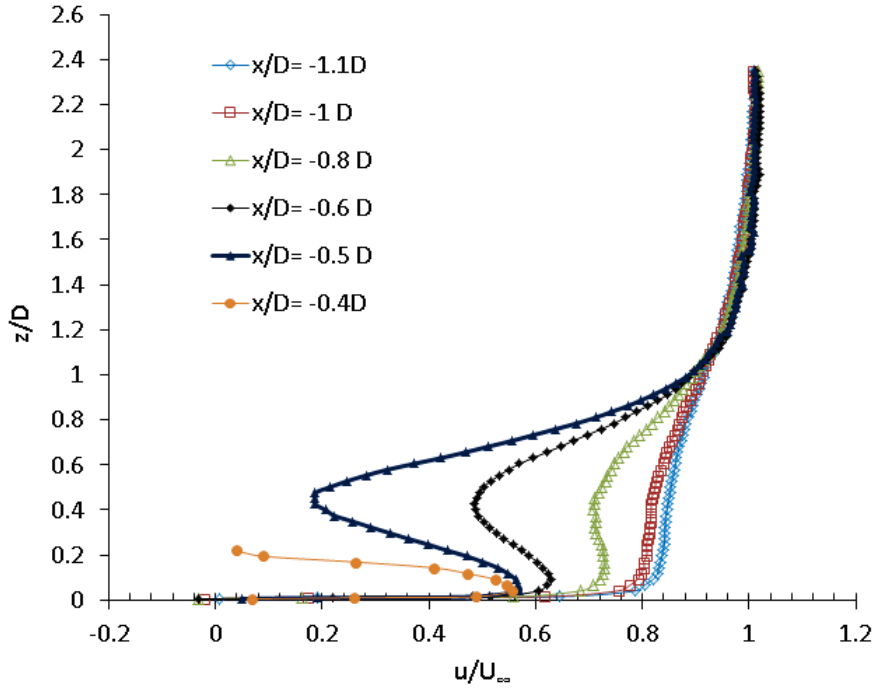

Figure 5.15: Mean streamwise velocity profile, u, upstream of the sphere at $y/D = 0$ and $x/D = -1.1$ to -0.4

strength with increasing downstream distance. Also, the cross-correlation analysis shown in Fig. 5.13 demonstrated that the shedding is relatively symmetric, similar to the ellipsoids at high relative submergence.

Due to the existence of strong lobe vortices at $x/D = 0.5$ to 1, it will be expected that the bed shear stress increases on these regions. It will be shown in Sec. 5.5 that strong shear stress is found on the bed on those locations ($z/D = 0.4$) in agreement with this observation as shown Figs. 5.35 and 5.36.

5.5 Shear Stress Distribution

As illustrated in Fig. 3.15 in Sec. 3.3.1, the shear stress distribution was measured around a wall-mounted sphere as a benchmark for future study. Streamwise velocity profiles and vectors have been computed for each measurement location around the sphere. The velocity profiles in the symmetry plane ($y = 0$) have been

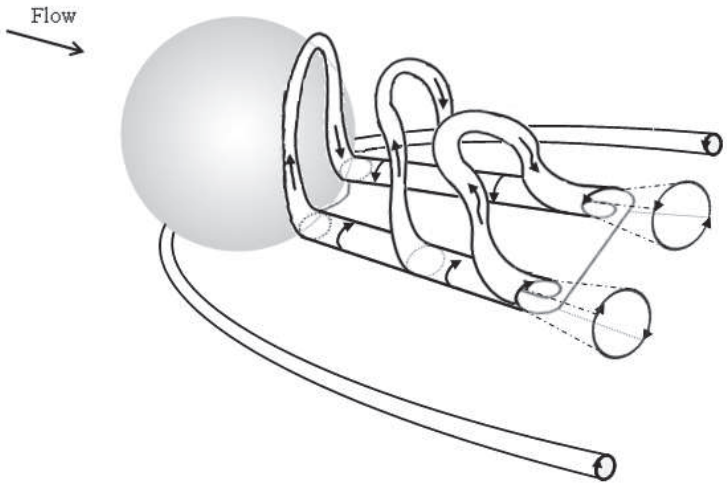

Figure 5.16: Proposed evolution of the arch structures for the sphere (self-induction dominated deformation). The arrows indicate the orientation of the vorticity vector.

illustrated in Fig. 5.17 and 5.18 .

The velocity profiles at $y/D = -0.25$ and -0.5 have been illustrated in Fig. 5.19 and 5.20 indicating the reverse flow zone. At y/D =-0.5 and at the side of the obstacle (x/D =0) a strong reverse flow was observed which shows a complex 3D flow field around the perimeter of the sphere near the mid-span.

The streamwise velocity profiles are similar at $y/D = -0.75$ and -1 as shown in Figs. 5.21 and 5.22, which demonstrates that the effect of sphere is not apparent in the profiles. A quantitative comparison of the boundary layer characteristics in these profiles with the boundary layer characteristics measured on the plate at the absence of the obstacle confirms similar findings for δ/D and the shape factor H_{sf}. The boundary layer thickness, of δ/D= 0.15 is present at the location of obstacle (x/D =0) and shape factor H_{sf} = 1.87. Therefore, the shear stress measurements from y/D = 0 to -0.5 are of particular interest. In addition, the shear stress up to $y/D = -1$ has been presented.

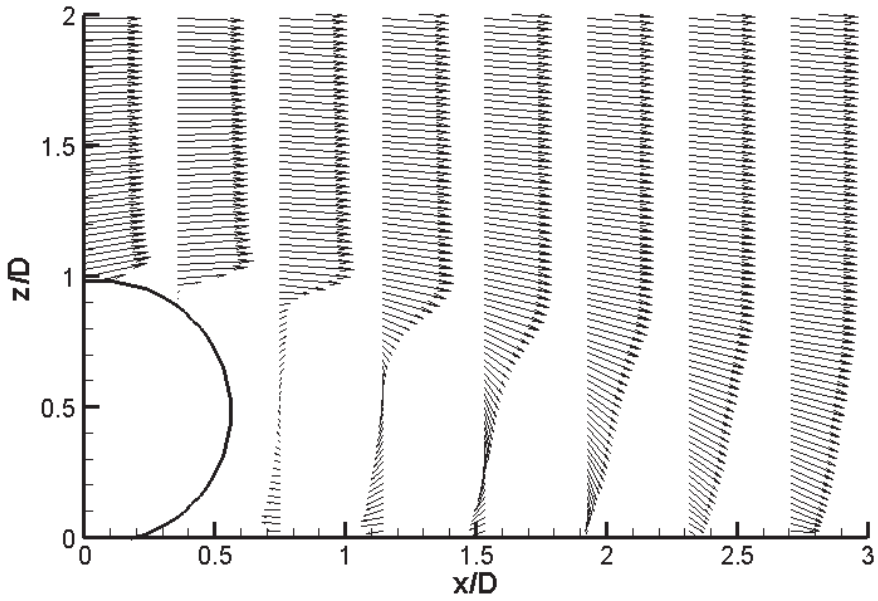

Figure 5.17: Distribution of velocity vector at $y = 0$ and $x/D = 0.5$ to 3.

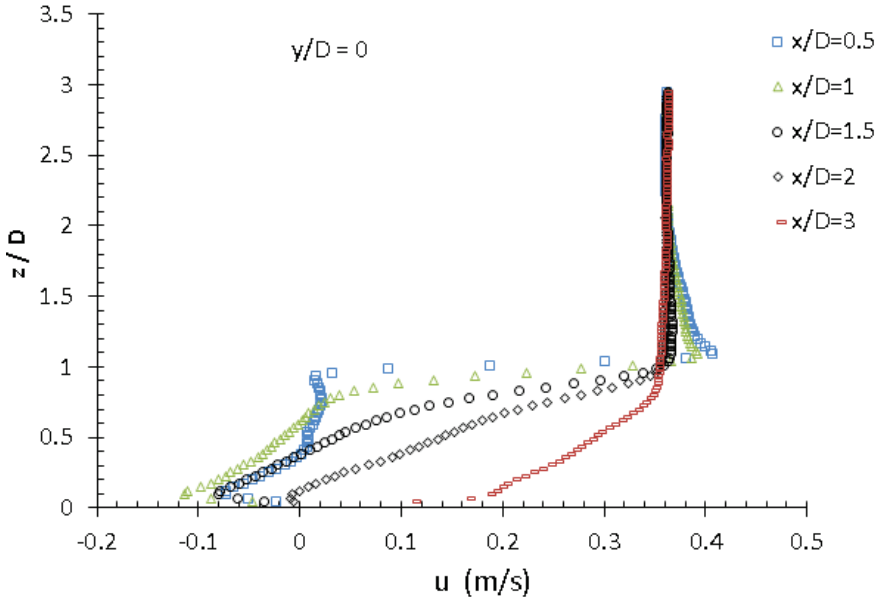

Figure 5.18: Time-averaged, streamwise velocity, u, profiles at $y = 0$ and $x/D = 0.5$ to 3.

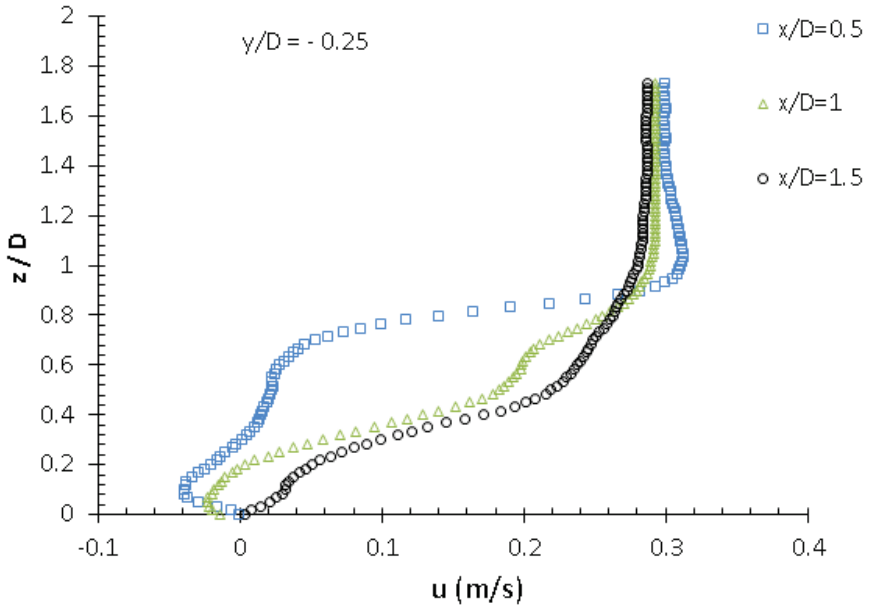

Figure 5.19: Time-averaged, streamwise velocity, u, profiles at $y/D = -0.25$

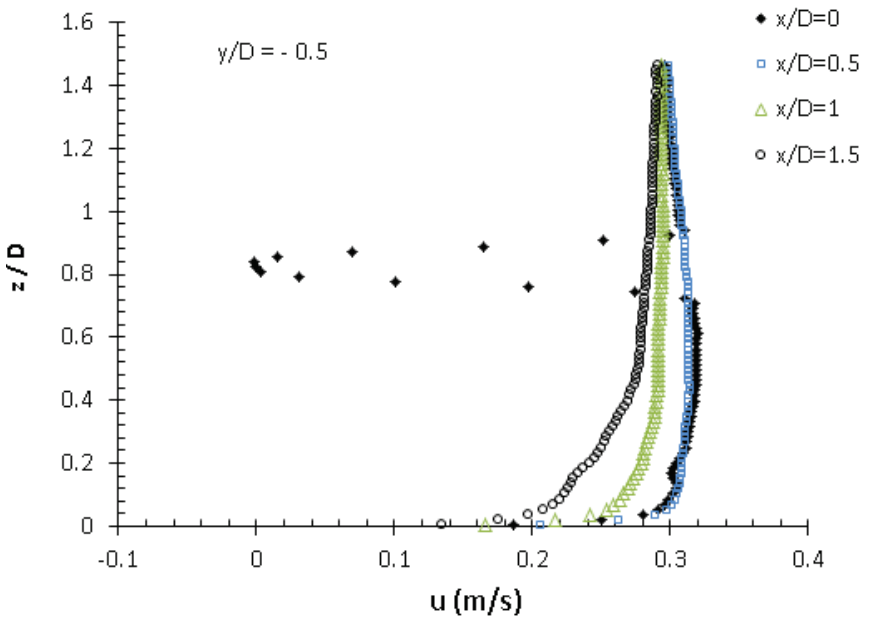

Figure 5.20: Time-averaged, streamwise velocity, u, profiles at $y/D = -0.5$

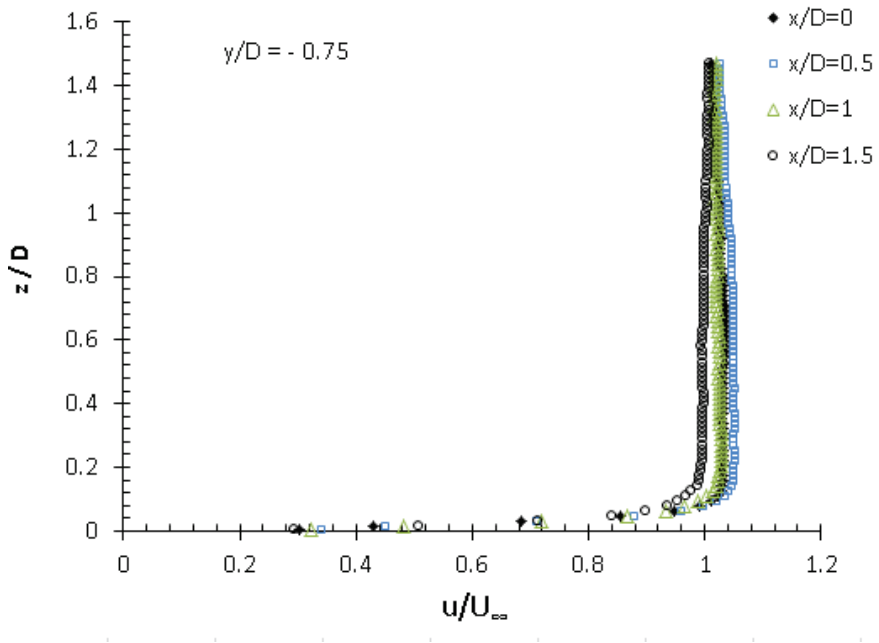

Figure 5.21: Time-averaged, streamwise velocity, u, profiles at $y/D = -0.75$

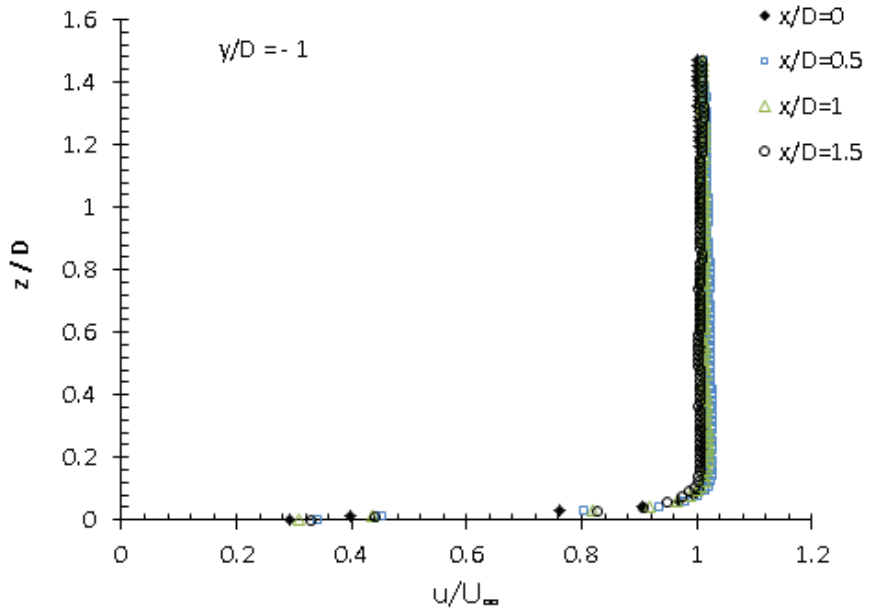

Figure 5.22: Time-averaged, streamwise velocity, u, profiles at $y/D = -1$

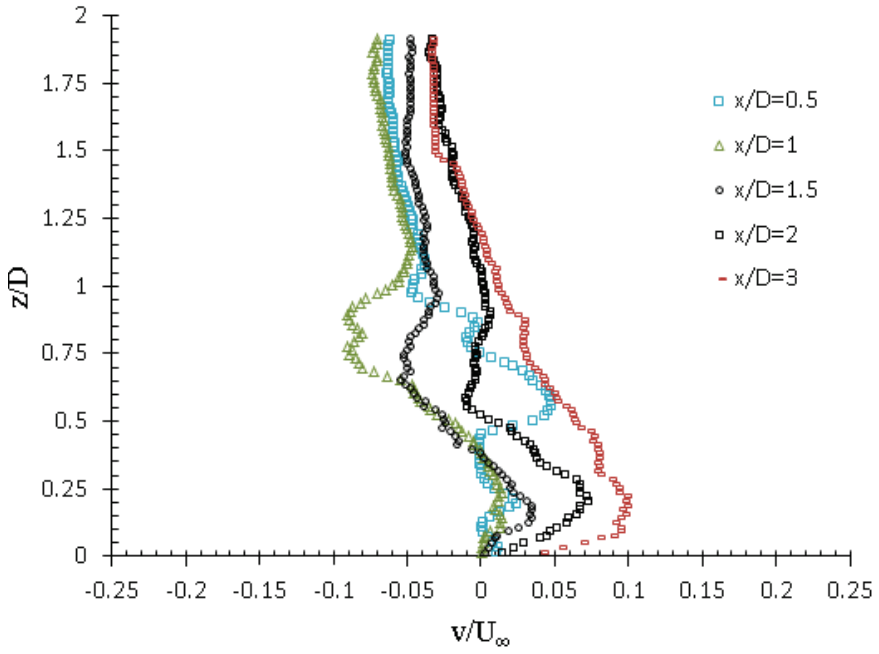

Figure 5.23: Time-averaged transverse velocity, v, profiles at $x/D = 0.5$ to 3 at $y = 0$

The time-averaged transverse velocity profiles, v, have been computed for each measurement location around the sphere. As presented in Fig. 5.23, the mean v profile, along the z-axis at $y = 0$ and $x/D = 0.5$ to 3 have values close to zero. The results in $y = 0$ have been shown as an example.

Figures 5.24 to 5.27 illustrate the turbulent projected shear stress, $\tau_{t,p}$, calculated in different locations as noted in Sec. 3.2 and based on Eq. (3.5). As illustrated in Fig. 3.15, the data are available from x/D =0.5 to x/D =3 along the centerline, $y = 0$, and not in other $x - z$ locations. At $y = 0$, the profile shows maximums at the location of shear layer before the reattachment length ($x/D = 2$) as shown in Fig. 5.24. At the trailing edge, x/D =0.5, the profile contains a maximum at the crest of the sphere (z/D =1). With descent of the shear layer toward the ground, the profile's maximums fall to z/D =0.8. After the reattachment point, at $x/D = 2$ and 3, the maximum of $\tau_{t,p}$ occurs at z/D =0.2. The $\tau_{t,p}$ reduces near the bed at all

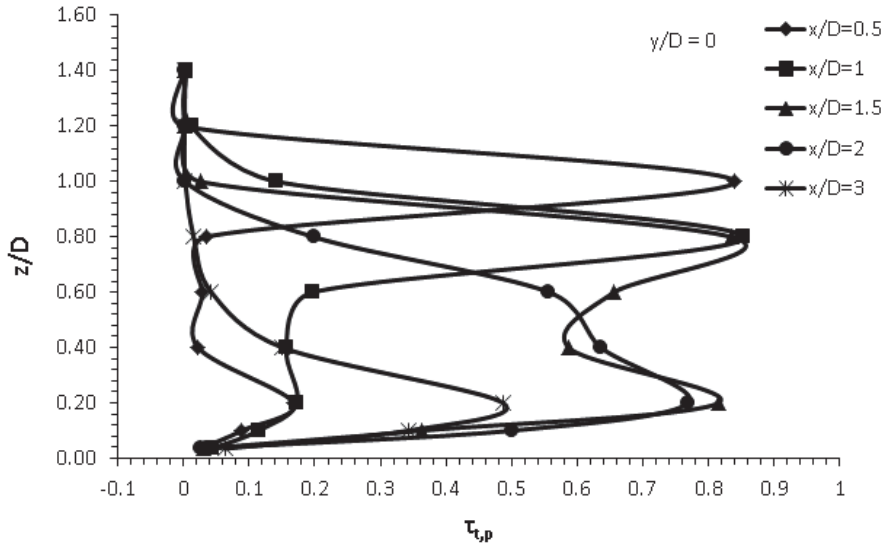

Figure 5.24: Turbulent projected shear stress at $y = 0$ and $x/D = 0.5$ to 3

measurement locations.

At $y/D = -0.25$ and at the streamwise locations investigated here, the $\tau_{t,p}$ values collapse along most of the depth except for when z/D =0.8 as shown in Fig. 5.25. This location is the same as locations where maximum $\tau_{t,p}$ occurred at $y = 0$. At $y/D = -0.5$, which is right on the sphere's side, no maximum is observed at x/D =0. At x/D =0.5 to 1.5, the maximum $\tau_{t,p}$ is visible at z/D =0.4 and the values of $\tau_{t,p}$ increase in streamwise direction as shown in Fig. 5.26.

The occurrence of $\tau_{t,p}$ maximum values at z/D =0.4 is likely due to the presents of the lobes at the side of the sphere as shown in Figs. 5.9d and 5.9e. As shown in Fig. 5.27, the shear stress distribution has also been considered in $y/D = -1$ where the profiles collapse in together and the values are close to zero.

The mean shear stress profiles at $x - z$ planes have been computed for each measurement location around the sphere as illustrated in Figs. 5.28 through 5.31. Figure 5.28 presents the mean shear stress from the velocity profiles in $(x-z)$ planes as noted in Eq. 3.6.

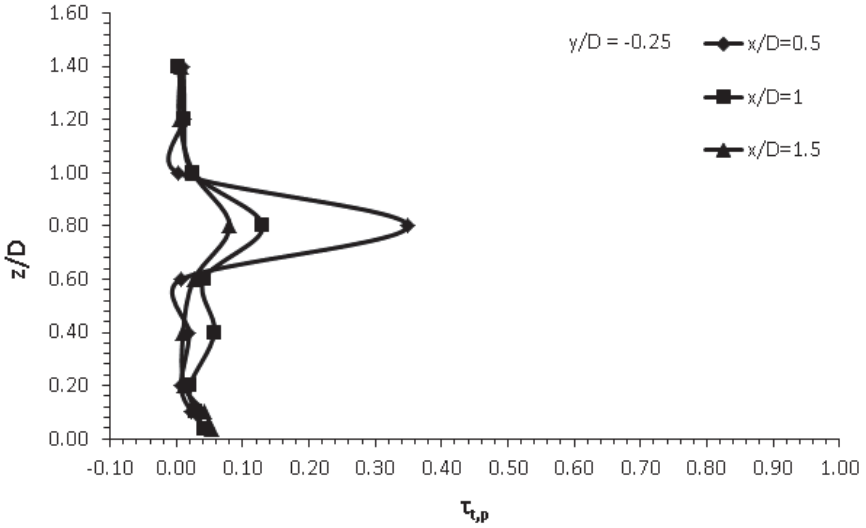

Figure 5.25: Turbulent projected shear stress at $y/D = -0.25$ and $x/D = 0.5$ to 1.5

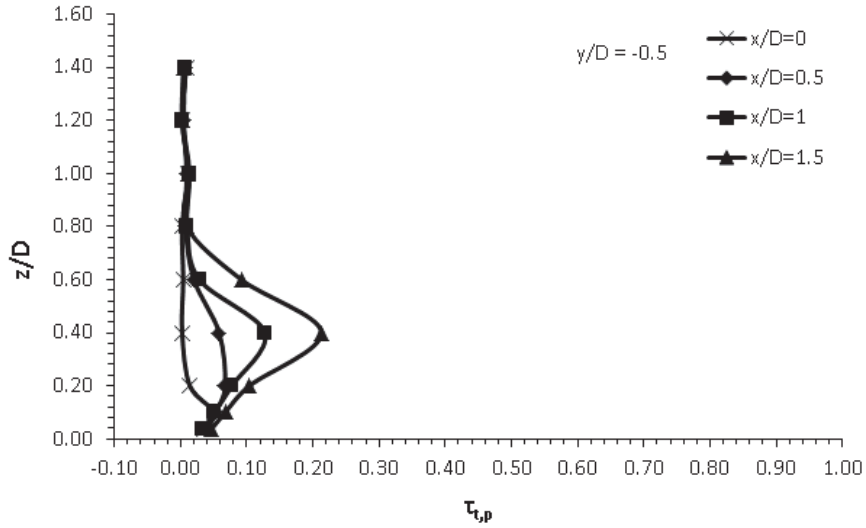

Figure 5.26: Turbulent projected shear stress at $y/D = -0.5$ and $x/D = 0$ to 1.5

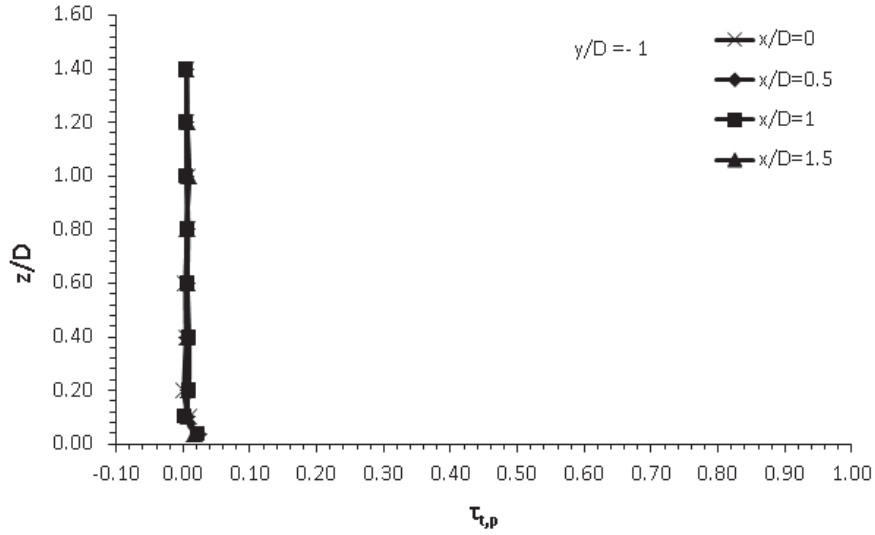

Figure 5.27: Turbulent projected shear stress at $y/D = -1$ and $x/D = 0$ to 1.5

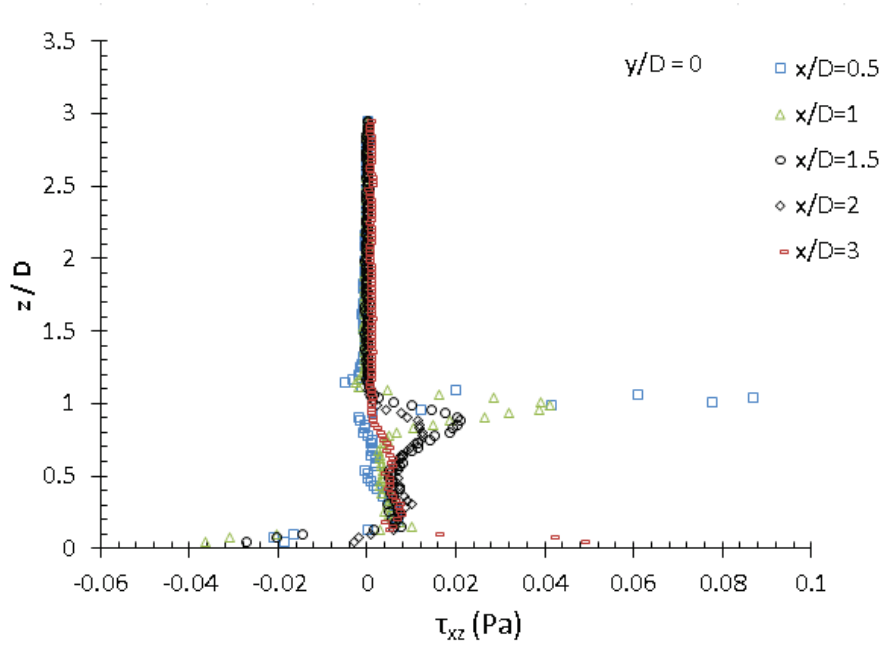

Figure 5.28: Mean shear stress at $y = 0$ and $x/D = 0.5$ to 3

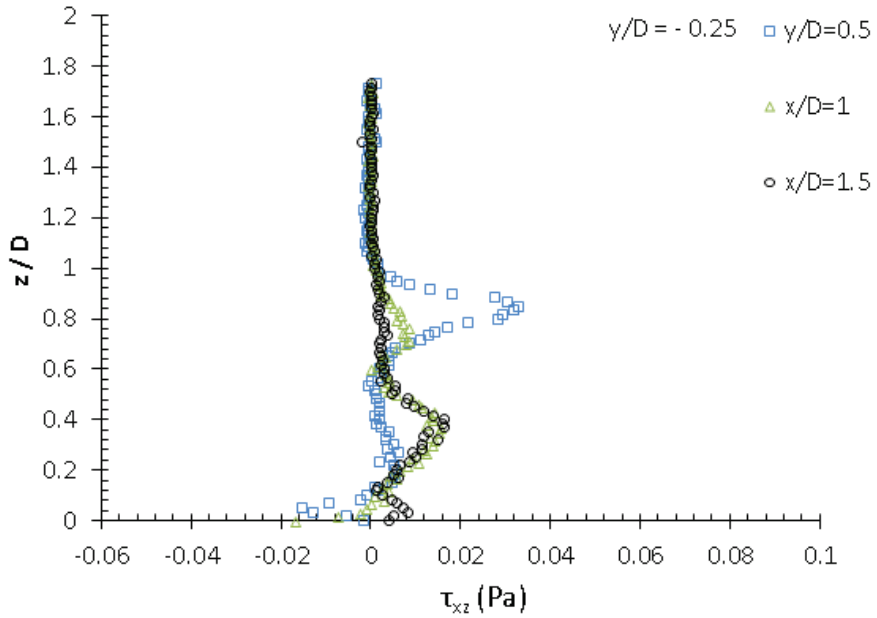

Figure 5.29: Mean shear stress at $y/D = -0.25$ and $x/D = 0.5$ to 1.5

These plots demonstrate the gradient of the u velocity in the streamwise direction, du/dx, along the height of the sphere. At $y = 0$, the flow decelerates ($du/dx < 0$) near the bed up to location $x/D = 2$ as shown in Fig. 5.28. After this location at $x/D = 2$, the flow accelerates ($du/dx > 0$) as visible in Fig. 5.17. At $y/D = -0.25$, the maximum value of mean shear was observed at z/D =0.9 and x/D =0.5 while at other streamwise locations, as shown in Fig. 5.29 the maximums are slightly below midspan in agreement with velocity profiles observed for this location as shown in Fig. 5.19. At the sphere side in $y/D = -0.5$, the mean shear values at x/D =0 and above the midspan, are varying between negative and positive values as shown in Fig. 5.30. At other streamwise locations, τ_{xz} reaches the maximum value near the bed as expected from the observation of velocity profiles in this location as shown in Fig. 5.20. For comparison the mean shear stress was also measured at $y/D = -0.75$ as shown in Fig. 5.31 in which the velocity profiles (Fig. 5.21) have not been shown the reverse flow zone.

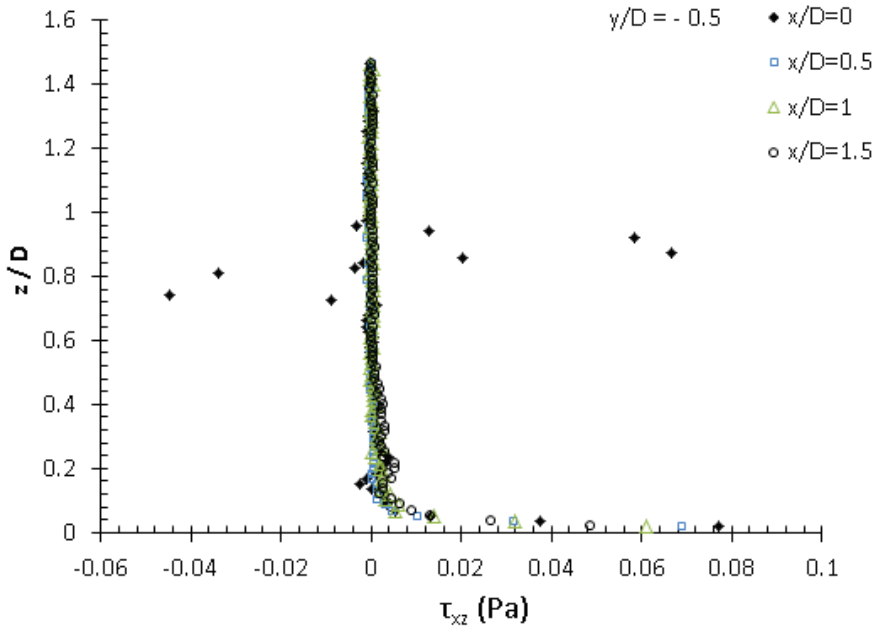

Figure 5.30: Mean shear stress at $y/D = -0.5$ and $x/D = 0$ to 1.5

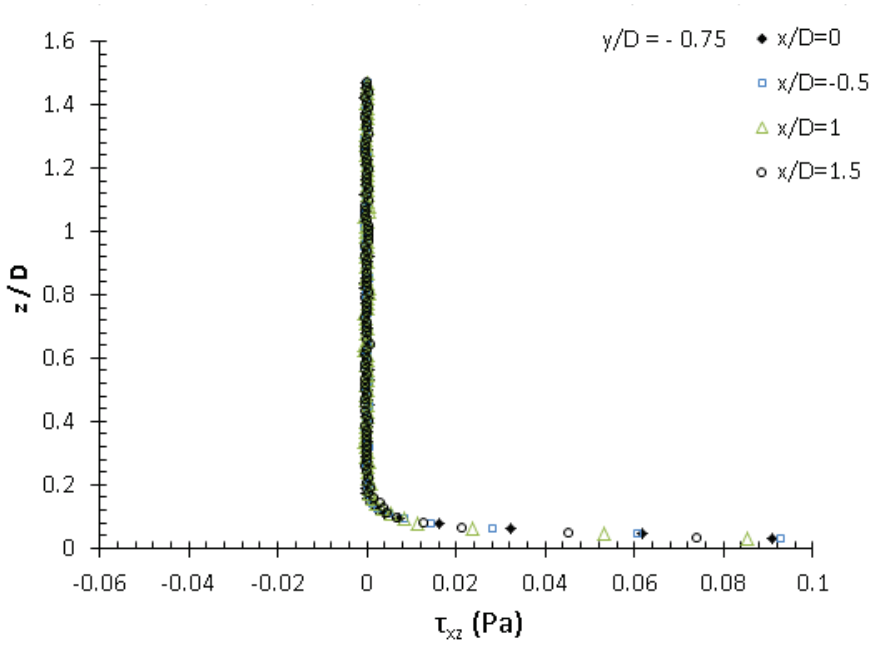

Figure 5.31: Mean shear stress at $y/D = -0.75$ and $x/D = 0$ to 1.5

The mean shear stress profiles at $y-z$ planes (τ_{yz}) have also been computed for each measurement location around the sphere as an example illustrated in Figs. 5.32 for $y = 0$. As expected from the velocity profiles (Fig. 5.23), the shear stress values are small and their effect in total shear stress will be marginal.

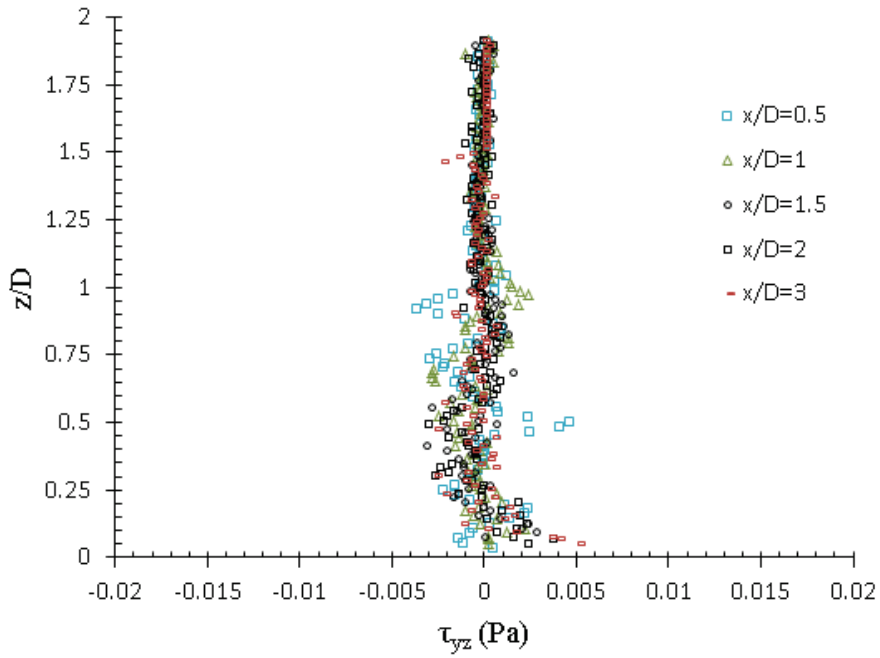

Figure 5.32: Mean shear stress at $y = 0$ and $x/D = 0.5$ to 3

While the contour is coarse, the contour plot of mean shear stresses has been illustrated in Fig. 5.33 in which mean shear stress have been superimposed indicating the the direction of shear stress.

Figures 5.34 through 5.36 illustrate the total shear stress distribution resulting from adding mean shear stress found in these locations as an example shown in Fig. 5.28. The mean shear values have been added to their corresponding Reynolds shear stress. Compared to $\tau_{t,p}$ in the streamwise symmetry plane, shown in Fig. 5.24, the effect of mean shear stress on total τ along the height and near the bed

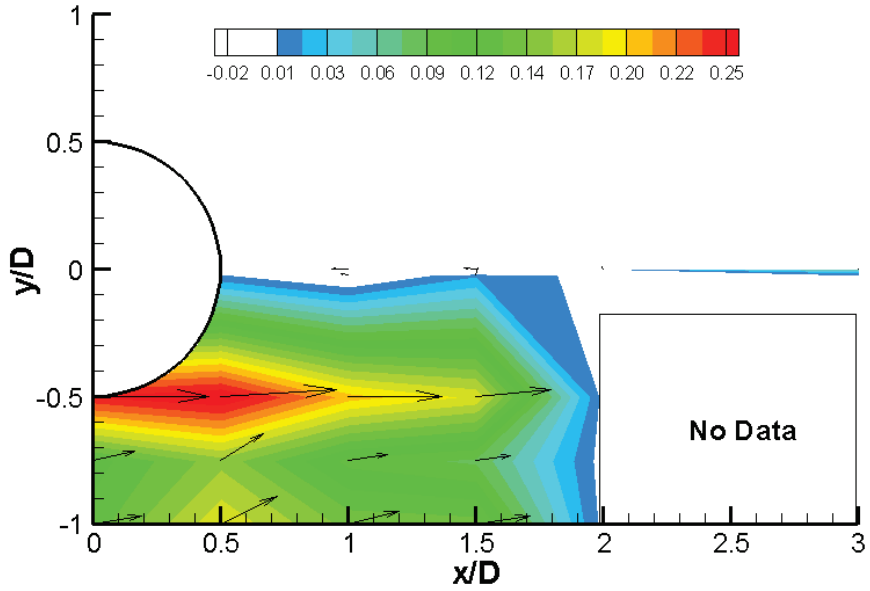

Figure 5.33: Contour plot of mean shear stress at $y = 0$ to -1 and $x/D = 0$ to 3

is trivial and no notable change is observed on the τ values. However, the total τ values increase near the bed at y/D =-0.25 and -0.5, which can be seen by comparing Fig. 5.35 with Fig. 5.29 and Fig. 5.36 with Fig. 5.30.

In summary, Figs. 5.37 through 5.39 illustrate the total shear stress distribution in streamwise direction along the height around the sphere. In all the results here, at z/D =1.2 and 1.4, the total shear does not vary in the streamwise direction as expected for the area far from the obstacle. At the symmetry plane, $y = 0$, except $z/D = 1$ which is right at the crest of sphere, the total shear increases in streamwise direction up to reattachment length, $x/D = 2$, and reduces after that. However, close to the bed at $z/D = 0.035$, the total shear stress increases in agreement of higher stress location near the reattachment point. Similarly Fig. 5.38 and 5.39 demonstrates that close to bed at $z/D = 0.035$ the shear stress rises toward $x/D = 1.5$. At $y/D = -0.25$, the highest shear stress observed at x/D =0.5 and z/D =0.8 as shown in Fig. 5.38 which is the location of the free shear layer.

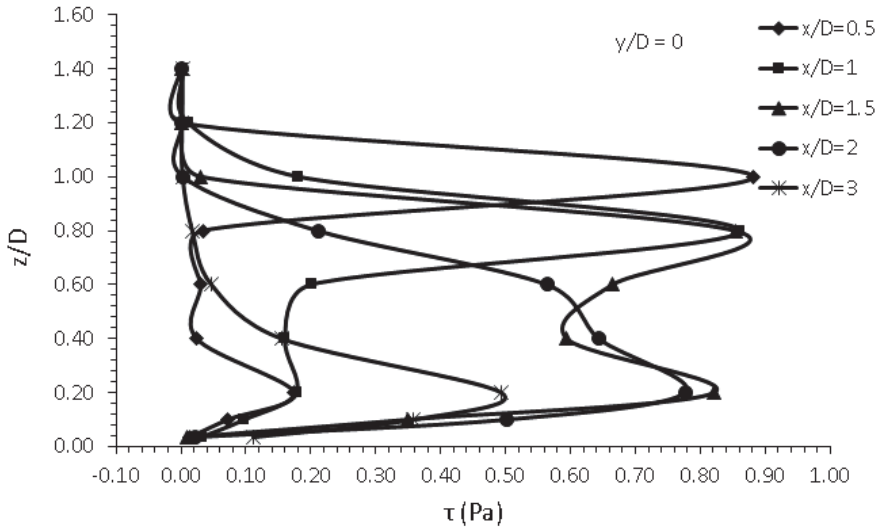

Figure 5.34: Total shear stress at $y = 0$ and $x/D = 0.5$ to 3

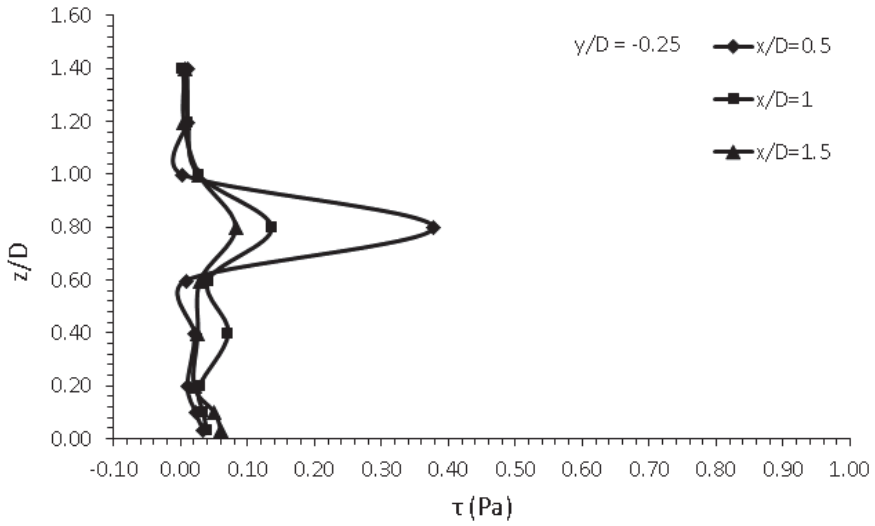

Figure 5.35: Total shear stress at $y/D = -0.25$ and $x/D = 0.5$ to1.5

The total shear stress distribution is computed upstream of the sphere at $y/D = 0$ and $x/D = -1.1$ to -0.4 using the imaging configuration employed for Fig. 5.4. The streamwise velocity profiles have been illustrated in Fig. 5.15. In agreement with the other studies (Sadeque et al., 2008, 2009; Shamloo et al., 2001; Papanicolaou et

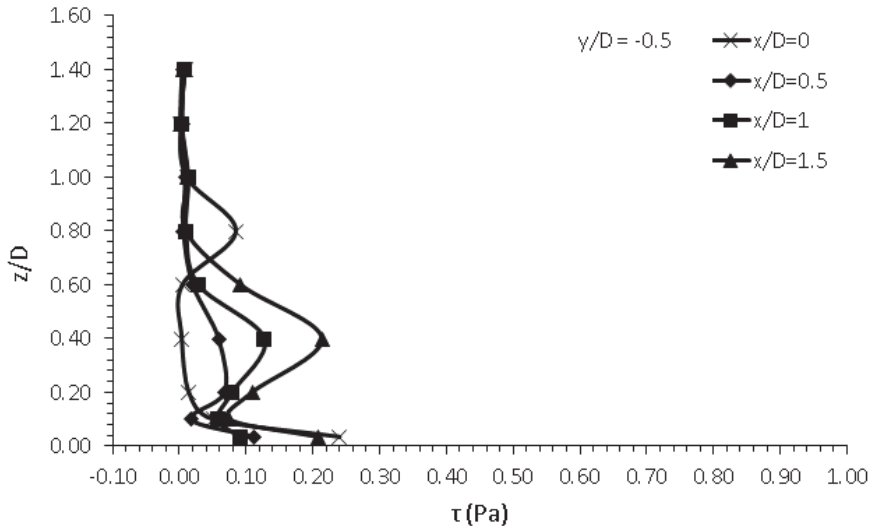

Figure 5.36: Total shear stress at $y/D = -0.5$ and $x/D = 0$ to1.5

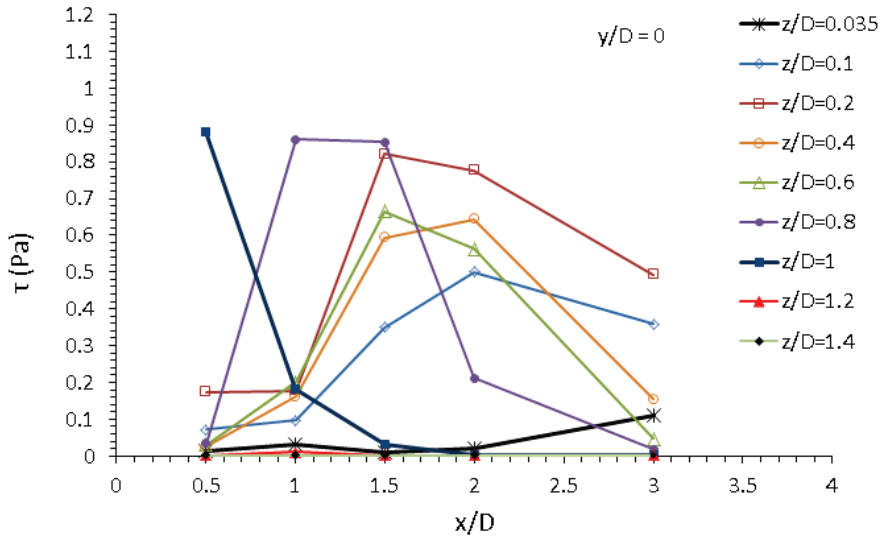

Figure 5.37: Total shear stress in streamwise direction at $y = 0$ and $x/D = 0.5$ to 3

al., 2011; Papanicolaou et al., 2012a), the stress on the bed near the sphere increases in the streamwise direction, an observation that can be considered for erosion study and sediment depositional pattern.

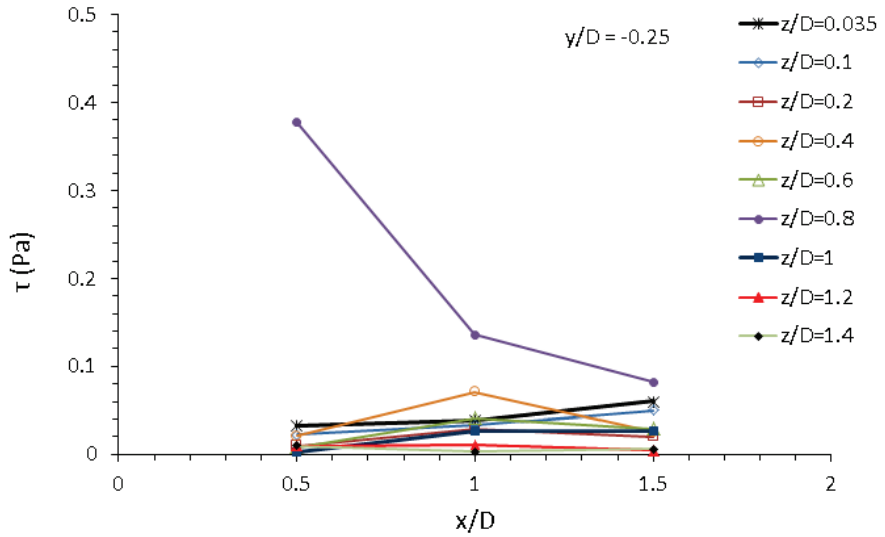

Figure 5.38: Total shear stress in streamwise direction at $y/D = -0.25$ and $x/D = 0.5$ to1.5

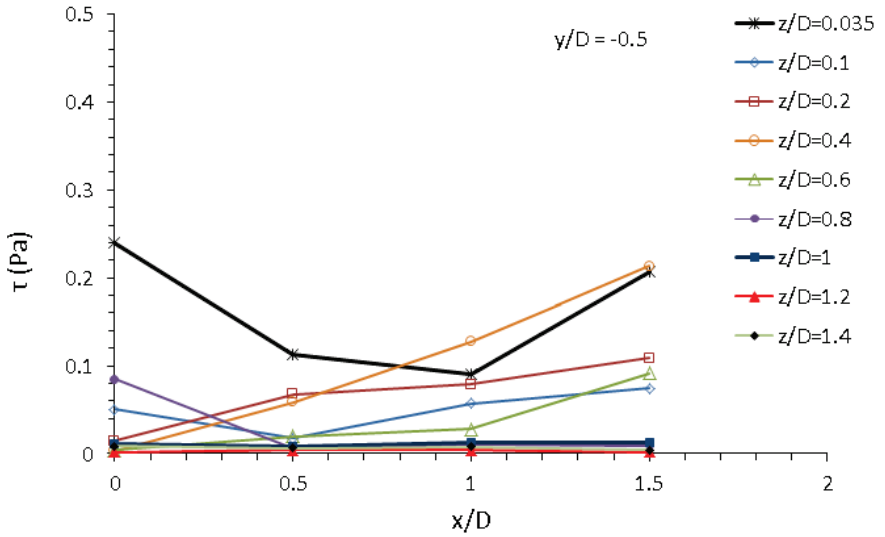

Figure 5.39: Total shear stress in streamwise direction at $y/D = -0.5$ and $x/D = 0$ to1.5

From the measurement reviewed above, the bed shear stress, τ_0, has been computed in each measurement location. Determining the bed shear stress has

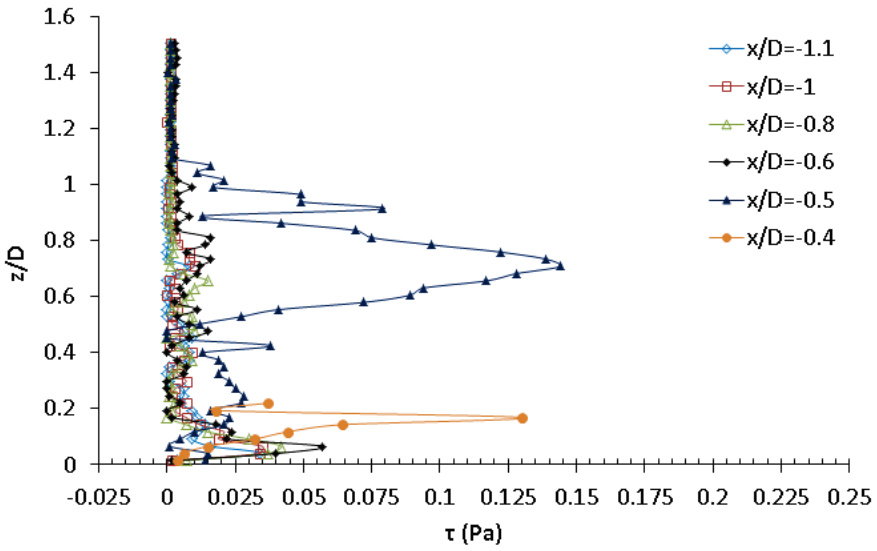

Figure 5.40: Total shear stress in streamwise direction upstream of the sphere at $y/D = 0$ and $x/D = -1.1$ to -0.4

been a challenge in sediment transport studies (Biron et al., 2004; Rowinski et al., 2005). Biron et al. (2004) conducted a set of experiments on a simple boundary layer over plexiglas using an acoustic Doppler velocimeter (ADV). The study showed that Reynolds shear stress varies with height above the bed and reaches a maximum value at z/d =0.1 (z = 6.2 mm) in open channel flow, where d is the flow depth. The Reynolds shear stress decreases as the non-dimensional height falls below 0.1, but as illustrated in Fig. 5.41, it occasionally rises after the initial decrease. It is not clear whether the decrease in shear stress values in the findings of Biron et al. (2004) below z/d =0.1 is related to the difference in the instrument measurement. These observations raise the question of the most appropriate distance from the bed to obtain a representative shear stress value.

Having more accurate velocimeters which can measure close to the bed, the question that remains unanswered is the best location for measurements and the proximity of the location to the bed. In the current study, based on the DPIV

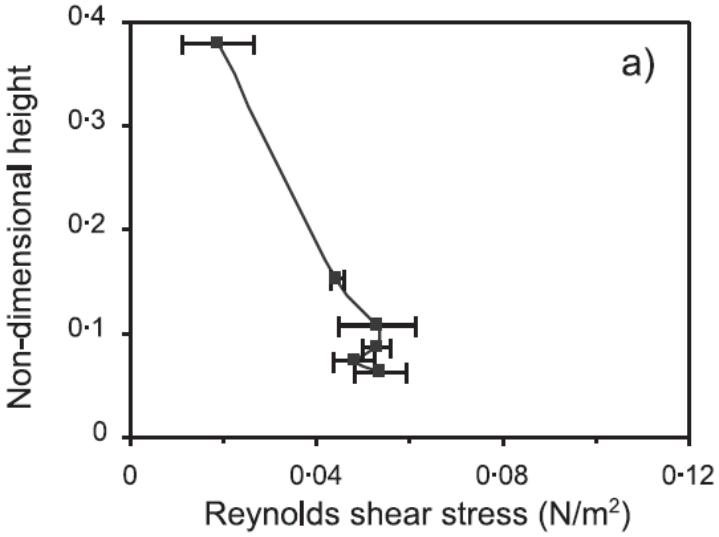

Figure 5.41: Average vertical profiles of shear stress estimated from Reynolds method over plexiglas with ADV (from Biron et al. (2004))

spatial resolution of the velocity vector fields, z/D =0.035 (z = 1.75 mm) has been determined as the representative height to obtain reliable bed shear stress estimates. This is the height that the correlation windows used to determine the bottom row of vectors in all the measurement locations do not include portions of the bed image. The bed images are stationary and would thus skew the vector magnitude. It is not clear whether the results would change much if we were able to look closer to the bed.

The τ_0 values in the centerline at x/D = 0.5 to 3 have been shown in Table 5.1. Even though the data is coarse, the contour plot has also been illustrated as shown in Fig. 5.42 in which bed shear stress vectors have been superimposed indicating the direction of shear stress. Two area of higher shear stress are visible at the side of the sphere and near the reattachment point. The higher shear stress at the side of the sphere is probably related to existence and development of the lobe structures.

	τ_0				
	$y/D = 0$	$y/D = -0.25$	$y/D = -0.5$	$y/D = -0.75$	$y/D = -1$
x/D =0			0.240	0.0204	0.0028
x/D =0.5	0.014	0.033	0.112	0.02	0.0048
x/D =1.0	0.031	0.039	0.090	0.028	0.0023
x/D =1.5	0.010	0.060	0.207	0.030	0.007
x/D =2.0	0.022				
x/D =2.5	0.069				
x/D =3.0	0.111				

Table 5.1: Bed shear stress, τ_0, in z/D =0.035 at x/D = 0.5 to 3 and y = 0

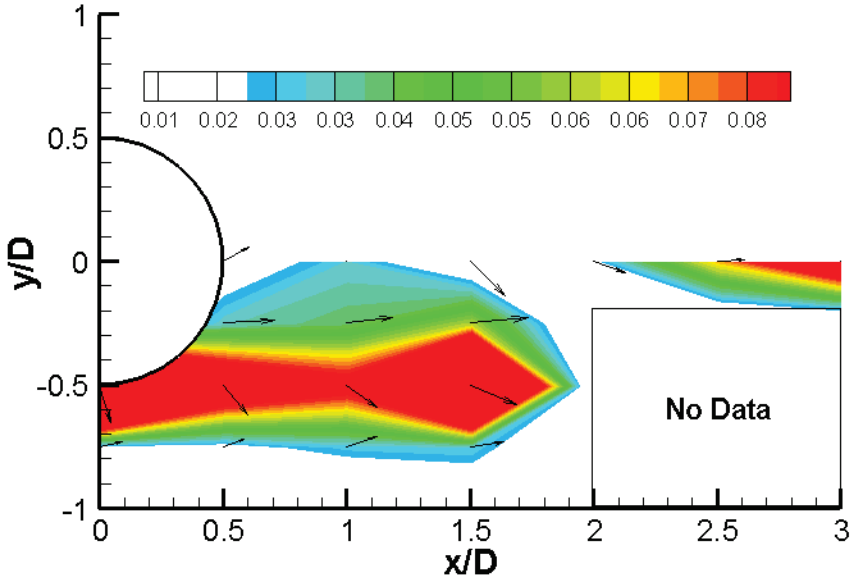

Figure 5.42: Contour plot of bed shear stress, τ_0, in z/D =0.035 at x/D = 0.5 to 3 and y = 0

CHAPTER 6
CONCLUSIONS AND FUTURE WORK

6.1 Conclusions

Particle image velocimetry and thermal anemometry were used to investigate the shedding characteristics and the wake structures generated by five different low-aspect-ratio obstacles: ellipsoids of aspect ratio (H/D) 0.67 (transverse ellipsoid) and 0.89 (streamwise ellipsoid), two cylindrical obstacles of the same aspect ratios as the ellipsoids, and a sphere. Despite the relatively subtle difference between the two ellipsoid geometries, the time-averaged streamwise vorticity distribution in the wakes revealed striking disparities. Whereas the the dominant structures in the wake of the streamwise ellipsoid consisted of a *tip* vortex pair inducing downwash and the horseshoe vortices near the ground plane, the transverse ellipsoid exhibited a dominant *base* vortex pair oriented such as to induce an upwash in the wake. This latter observation is unique in that base vortices have not been previously reported for low-aspect-ratio obstacles in thin boundary layers with thickness significantly smaller than the obstacle dimensions. The flow structures were shown to be qualitatively robust with significant variations in free-stream turbulence intensity; however, the circulations of the mean streamwise structures were significantly greater in the low-turbulence case. In contrast, both cylinder wakes contained strong tip vortices with weaker base vortices also present. Following a similar trend to the ellipsoids, the strength of the base structures in the cylinder wakes was inversely related to aspect ratio. Streamwise features observed in the mean wake of the sphere, included tip and horseshoe structures, and a weak opposite- sign vortex pair near the top of the obstacle.

A model of the arch vortex dynamics was proposed to explain the observed streamwise vorticity distributions in the ellipsoid wakes in which the evolution of the arch structures is governed by two competing mechanisms: Biot-Savart self-

induction and the deformation due to the external shear flow. It is proposed that the balance between these mechanisms is governed by the curvature of the obstacle profile. While the cylinder wake is more complex due to the separation of arch and tip structures from the square corners at the free end, the general trend of base vortex strength with variation in cylinder aspect ratio is consistent with that observed in the case of the ellipsoids. The phase measurements verified downstream and upstream tilting of structures shed by the transverse and streamwise ellipsoids, respectively, as hypothesized by Hajimirzaie et al. (2012). The relative simplicity of the ellipsoid wakes make them an archetypical model for understanding somewhat more complex flows such as that of the sphere wake.

The dominant structures in the deeply-submerged sphere wake are the horseshoe vortex and the arch-shaped shear-layer. As suggested for the streamwise ellipsoid, the dominant mechanism governing the dynamics of the resulting arch structure to produce the observed mean flow is Biot-Savart self-induction due to the curvature of the vortex which, due to the vorticity orientation, would tend to drive the top of the arch upstream. Near the base plane, two pair of vortices are observed in the wake of the sphere, which have the same sense of rotation: close to the side of the sphere (lobes) and further from the obstacle in the transverse planes (well-known horseshoe vortex). The origin of these was proposed to be streamwise tilting of the base of the arch structures due to a wall jet that forms in the vicinity of the junction.

Spectral measurements at high relative submergence of $d/H = 3.9$ revealed that transverse and streamwise ellipsoids exhibited weak dominant shedding frequencies at $St = 0.188$ and 0.183, respectively. Cross-correlation analysis demonstrated that the shedding was symmetric in nature. Broad, lower-frequency peaks were observed in many cases, which were also apparent in other studies. A previously-proposed hypothesis, that these peaks are essentially beat frequencies, seems un-

likely in this case since, in the present study, spectra have been observed which contain only these peaks. Alternatively, we have observed an intermittent collapse of the recirculation region which is consistent with these features. Much weaker peaks were observed at $St = 0.084$ for the low-aspect-ratio cylinder (AR=0.67) and 0.065 for the high-aspect-ratio cylinder (AR=0.89). In the wake of the sphere, a weak dominant frequency is observed at $St = 0.20$ close to the obstacle junction and the cross-correlation function for symmetric measurements in the wake indicates symmetric shedding.

Relative submergence (d/H) was varied systematically for the two ellipsoids. For the transverse ellipsoid, the base vortex circulation was found to vary approximately with the inverse of the flow depth for $d/H \leq 4$ while it was relatively insensitive to flow depth for $d/H \geq 4$, consistent with previous observations in free surface flows. In contrast, for the streamwise ellipsoid, a strong base vortex was observed at $d/H = 1$, and essentially no base vortex for $d/H \geq 2.5$. While reducing relative submergence to 2.5 had no effect on the dominant Strouhal numbers for the transverse and streamwise ellipsoids, the peaks were found to broaden slightly, indicating that the increased proximity of the top boundary has an effect on the shedding behavior. Likewise, in the wake of the streamwise ellipsoid, Hajimirzaie et al. (2012) did not find the circulations of vortex structures measured in streamwise planes to vary significantly; however, for the transverse ellipsoid, base vortex circulation was found to vary inversely with relative submergence. At $d/H = 1$, the dominant shedding Strouhal numbers increased to $St = 0.345$ and 0.357 for the transverse and streamwise ellipsoids, respectively. This change was concomitant with significantly-increased base vortex strengths for both ellipsoids, as shown by Hajimirzaie et al. (2012). The shedding behavior also changed from a symmetric mode to a antisymmetric mode with increased coherence for the transverse ellipsoid and cylinders, likely due to the reduction in three-dimensionality and the change

in topology of the domain as the obstacle now spans the entire height. Surprisingly, the streamwise ellipsoid wake actually experienced decreased coherence.

Other studies of tapered obstacles (plates, cones, and pyramids) have defined a taper ratio or aspect ratio (of which the definitions are equivalent for obstacles that do not penetrate through the boundary) AR_{av}, as defined in Sec. 4.2.5. Whereas the values of the cylinder aspect ratios AR and AR_{av} are identical by this definition, the transverse and streamwise ellipsoids have equivalent aspect ratios of $AR_{av} = 0.794$ and 1.031, respectively. For this range of AR_{av}, the presence and nature of periodic vortex shedding is highly varied as indicated in Sec. 4.2.5. Comparing similarly tapered geometries, Castro and Watson (2004) observed $St = 0.18$ – nearly identical to that observed for the ellipsoid geometries at $d/H = 3.9$ – for triangular plates of $AR_{av} = 0.58$. On the other hand, Martinuzzi and AbuOmar (2003) measured $St = 0.33$ for a pyramid of $AR_{av} = 1$. However, they also proposed a complex multi-vortex wake structure that evidently relies on distinct separation points at the pyramid edges as well as important afterbody effects, so it is not surprising that the shedding frequency is quite distinct from the ellipsoids.

Local bed shear stress measurements, estimated from Reynolds stress, have been computed in the wake of the sphere to provide insight into the sediment depositional patterns surrounding the obstacle. The bed shear stress measurements reveal that two areas at the side and close to reattachment length have the higher values. The higher stress near the side of the sphere are probably related to lobe structures observed at the side of the sphere.

The sensitivity of the mean wake vorticity distribution to obstacle shape and relative submergence, quantified in this dissertation, provides controls with which to further probe the dynamics of wake structures and the related transport mechanisms. In addition, the fact that relatively subtle changes in geometry can provide such dramatic changes in flow patterns has implications for the transport of mo-

mentum and scalars in applications of flow around wall-mounted bodies.

The shear stress distribution measured around the sphere may help in the prediction of sediment transport in mountain stream.

6.2 Future Work

In a general sense, the observations presented in Ch. 4 and the methods developed provide a framework that can be used to increase our understanding of turbulent flow dynamics and structure. Therefore, this work provides insight into the modeling and control of flow over wall-mounted bodies. These results can also elucidate roles of shape and relative submergence which is not previously discussed in the literature, and introduces new wake vorticity fields that cannot be explained by existing models.

While the mean wake structure and shedding characteristics have been documented around the low-aspect-ratio obstacles of interest, and correlated with bed shear stress in the case of the sphere, many details of the dynamics of these wakes are still unresolved. As described in Fig. 6.1, conditional averaging of DPIV data can be employed based on, for example the phase of a hot film signal determined from *FFT* or wavelet analysis, to better understand the dynamics of large-scale structures in the wake.

Also using the knowledge gained and methods developed in this boundary layer experiment, we can consider the more complex problem of open-channel flow over a submerged obstacle on a rough bed. This configuration has direct application to sediment transport in mountain streams and is additionally complicated at low relative submergence by an active free surface. In particular, the following questions are of interest:

1. What is the time-averaged spatially resolved bed shear stress distribution around the spherical obstacle with varying Reynolds number, Froude number, Shields parameter, and relative submergence?

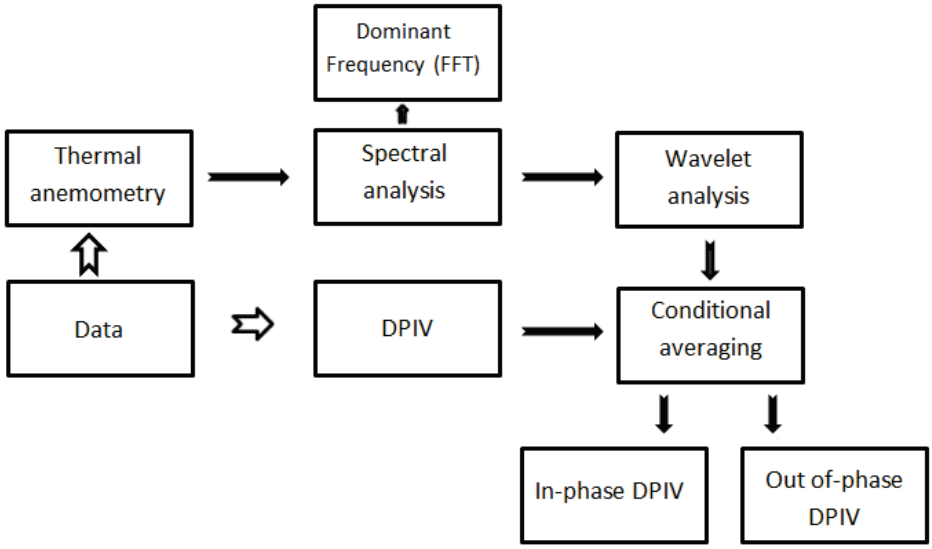

Figure 6.1: Graphic chart of future work for dynamic shedding behavior

2. How do the mean flow structure and its dynamics govern these stresses?

Figures 6.2 and 6.3 illustrate an experimental setup, which will be facilitate flow measurements around a sphere atop a rough bed under the high (d/D =3.5), intermediate (d/D =1.2), and low (d/D = 0.8), relative submergence regimes.

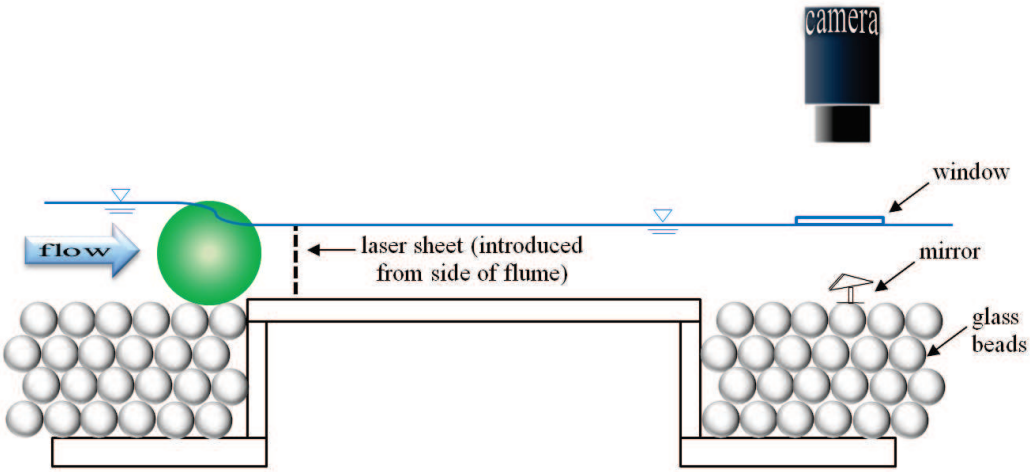

Figure 6.2: An experimental setup for upstream view at low relative submergence for the open channel tests

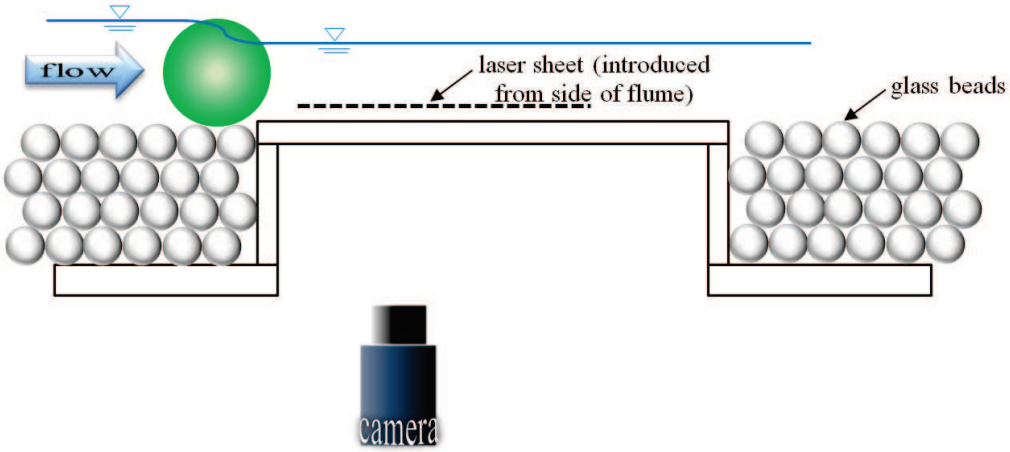

Figure 6.3: An experimental setup for plan view measurement at low relative submergence for the open channel tests

APPENDIX A
UNCERTAINTY ANALYSIS-DPIV

Based on the literature and quality of the data, an uncertainty in the PIV data was assumed and from the assumed values, a general uncertainty for each of the terms was calculated, designated by σ.

A.1 Transverse Plane

Factors that influence PIV errors are large particle sizes, improper seeding of particles, particle displacement, and out-of-plane motion (Adrian, 2005; Huang et al., 1997; Raffel et al., 2007). Huang et al. (1997) proposed a representative uncertainty in the displacement determined by DPIV analysis to be approximately 0.1 pixels. Obtaining accurate estimates of PIV uncertainty in situ is not possible due to the widely-varying sources of error from vector to vector. With the influence of these publications, advancements in technology, and the quality of the data obtained, the assumed uncertainties for the change in pixel position for $\sigma_{\Delta x}$, $\sigma_{\Delta y}$, $\sigma_{\Delta z}$ were 0.1 pixels.

Y_g and Z_g are spacing between vectors generated in the PIV vector files in the spanwise direction, and spacing between vectors created in the PIV vector files in the vertical direction (z-direction), respectively. For transverse (y-z) plane, $Y_g = Z_g$=1.3699 mm. In this analysis, the uncertainties in the vector spacing (σ_{X_g}, σ_{Y_g}, and σ_{Z_g}) are assumed to be negligible. For a transverse plane, the pixel shift was approximately 2-3 pixels which resulted in an uncertainty in the z- and y-component of the velocity to be approximately 3%.

A conservative estimate for the uncertainties in the spanwise velocity and streamwise vorticities were calculated and are demonstrated in the subsequent equations. The velocity vectors are calculated using PIV by first using a cross-correlation analysis to determine a mean particle displacement within a sub-window of the domain between the two images and dividing by the time interval

separating the image pair (Raffel et al., 2007). The spanwise velocity, U_z, can be defined in this manner and is shown in Eq. A.1.

$$U_z = \frac{\Delta z}{M \Delta t} \tag{A.1}$$

Where M is the magnification ratio. The total uncertainty in the spanwise velocity can be obtained by once again taking partial derivatives of U_z with respect to the terms that will contribute error. The cameras were calibrated with the laser plane using a ruler. Since the calibration was of high quality, the uncertainty in the magnification ratio is assumed to not be a major component of uncertainty in the spanwise velocity. The resulting uncertainty for the spanwise velocity is given in Equation A.2.

$$\sigma_{U_Z} = \left[\left(\frac{\partial U_z}{\partial \Delta z} \sigma_{\Delta z} \right)^2 + \left(\frac{\partial U_z}{\partial \Delta t} \sigma_{\Delta t} \right)^2 \right]^{\frac{1}{2}} \tag{A.2}$$

The uncertainty associated with Δt is determined by the laser timing and and assumed to be negligible. The resulting uncertainty used in the analysis for the spanwise velocity is:

$$\sigma_{U_z} = \frac{\sigma_{\Delta z}}{M \Delta t} \tag{A.3}$$

During the processing of the DPIV images, a window size of 32×32 was used. This implied the magnification ratio was 0.0428 mm/pixel. Lastly, the Δt used between laser pulses for the data acquired was 2200 microseconds. Using these values, the uncertainties can be obtained as seen below:

$$\sigma_{U_z} = 1.9455 \frac{mm}{s} \tag{A.4}$$

In similar way, σ_{U_y} can be calculated 1.9455 $\frac{mm}{s}$. Out-of-plane vorticity components

were calculated using the central difference scheme presented in Equation 3.7. To determine the uncertainty in the vorticity values, the potential sources of errors were added in quadrature as demonstrated below with simplifications:

$$\sigma_{\omega_x} = \left(\frac{\sigma_{U_z}^2}{4Y_g^2} + \frac{\sigma_{U_y}^2}{4Z_g^2} \right)^{\frac{1}{2}} \tag{A.5}$$

Then the uncertainty can be obtained σ_{ω_x}=1.0042$\frac{mm}{s}$. The uncertainty in Γ cab be determine from:

$$\Gamma_x = \omega_x \Delta y \Delta z \tag{A.6}$$

And therefore:

$$\sigma_{\Gamma_x} = \sigma_{\omega_x} \Delta y \Delta z \tag{A.7}$$

Then the uncertainty can be obtained σ_{Γ_x}=1.8845$\frac{mm^2}{s}$. Therefore, in the case of the transverse planes, we looked at the transverse ellipsoid's left tip and base vortices to do the uncertainty analysis. The very weak left tip vortex yielded uncertainties in the Γ_x and ω_x to be 3.12% and 16.83%, respectively while the left base vortex had relative uncertainty values of 0.13% and 1.67% for Γ_x and ω_x, respectively. We then approximated the overall uncertainties in Γ_x, $\sigma_{\Gamma_x}/\Gamma_x$, and ω_x, $\sigma_{\omega_x}/\omega_x$, to be 1.5% and 8%, respectively.

In summary for transverse planes, uncertainties in velocity and vorticity were estimated to be 3% and 8%. The resulting measurement uncertainty in streamwise vortex circulation (2%) does not include errors due to asymmetry in the wake or ambiguity in the boundary of the vortex. More representative uncertainties in circulation based on the data are given in Sec. 4.1.3.

A.2 Symmetry Plane

In the streamwise direction, the boundary layer experiments yielded an approximate particle shift of 9 pixels which resulted in an uncertainty of 1% for the x- and z-component of the velocity. As far as the streamwise direction is concerned, the transverse ellipsoid was used again which resulted in an approximate uncertainty of Γ_x and ω_y of 0.0066% and 0.315%, respectively.

APPENDIX B
UNCERTAINTY ANALYSIS-THERMAL ANEMOMETRY

B.1 Strouhal Number

To determine the uncertainty in the Strouhal number, the potential sources of errors were added in quadrature as demonstrated below. The Strouhal number definition is:

$$f_s = \frac{f_s d}{U_\infty} \tag{B.1}$$

The uncertainty in the diameter is assumed to be negligible.

$$\sigma_{St} = \left[\left(\frac{\partial St}{\partial f}\sigma_f\right)^2 + \left(\frac{\partial St}{\partial\, U_\infty}\sigma_{U_\infty}\right)^2\right]^{\frac{1}{2}} \tag{B.2}$$

The uncertainty on frequency can be calculated from the sample standard deviation, SD, and the degrees of freedom, N as:

$$f_s = t\frac{SD}{\sqrt{N}} \tag{B.3}$$

For sample of N=10 and t=2.179 within a 95% confidence interval, SD was measured 0.14 which yields the σ_{f_s}=0.096. For diameter of 75 mm and U_∞=0.35 m/s, the uncertainty in the Strouhal number was measured σ_{St}=2.5 %.

REFERENCES

M. M. AbuOmar and R. J. Martinuzzi. Vortical structures around a surface-mounted pyramid in a thin boundary layer. 96:769–778, 2008.

E. Achenbach. Experiments on the flow past spheres at very high reynolds numbers. *J. Fluid Mech.*, 62:565–575, 1972.

E. Achenbach. Vortex shedding from spheres. *J. Fluid Mech.*, 62:209–221, 1974.

M. S. Adaramola, O. G. Akinlade, D. Sumner, D. J. Bergstrom, and A. J. Schenstead. Turbulent wake of a finite circular cylinder of small aspect ratio. *J. Fluid. Struct.*, 22:919–928, 2006.

R. J. Adrian. Twenty years of particle image velocimetry. *Exp. Fluids*, 39:159–169, 2005.

C. J. Baker. The laminar horseshoe vortex. *J. Fluid Mech.*, 95(2):347–367, 1979.

C. J. Baker. The turbulent horseshoe vortex. *J. Wind Eng. Ind. Aerodyn.*, 6:9–23, 1980.

F. Ballio, C. Bettoni, and S. Franzetti. A survey of time-averaged characteristics of laminar and turbulent horseshoe vortices. *ASME J. Fluids Eng.*, 120:233–242, 1998.

P. W. Bearman and T. Morel. Effect of free stream turbulence on the flow around bluff bodies. *Prog. Aerospace Sci.*, 20:97–123, 1983.

S. Becker, H. Lienhart, and F. Durst. Flow around three-dimensional obstacles in boundary layers. 90:265–279, 2002.

P. M. Biron, C. Robson, M. Lapointe, and S. Gaskin. Comparing different methods of bed shear stress estimates in simple and complex flow fields. *Earth Surf. Process. Land.*, 29(11):1403–1415, 2004.

J. Bourgeois. *Three-dimensional topology and dynamical modelling of vortex shedding from finite surface-mounted bluff bodies*. PhD thesis, University of Alberta, Canada, 2012.

J. Bourgeois, Z. Hosseini, and R. Martinuzzi. Half-loop and full-loop shedding in the wake of wall-mounted square cylinders due to boundary layer-wake interaction. *Abstract Submitted for the DFD11 Meeting of The American Physical Society*, 2011a. Abstract ID: BAPS.2011.DFD.R11.10.

J. A. Bourgeois, P. Sattari, and R. J. Martinuzzi. Alternating half-loop shedding in the turbulent wake of a finite surface-mounted square cylinder with a thin boundary layer. *Phys. Fluids*, 23, 095101:1–14, 2011b.

G. Byun and R. L. Simpson. Structure of three-dimensional separated flow on an axisymmetric bump. *AIAA J*, 44(5):999–1008, 2006.

I. P. Castro and P. Rogers. Vortex shedding from tapered plates. *Exp Fluids*, 33: 66–74, 2002.

I. P. Castro and L. Watson. Vortex shedding from tapered, triangular plates: taper and aspect ration effects. *Exp Fluids*, 37:159–167, 2004.

I. P. Castro, S. Vosper, M. Paisley, and P. Hayden. Vortex shedding behind tapered obstacles in neutral and stratified flow. *Dyn Atmos Oceans*, 34:145–163, 2001.

M. Chyu and V. Natarajan. Heat transfer on the base of threedimensional protruding elements. *Int J Heat Mass Transfer*, 39:2925–2935, 1996.

G. S. Constantinescu and K. D. Squires. Les and des investigations of turbulent flow over a sphere at re = 10000. *Flow, Turbulence and Combustion*, 70:267–298, 2003.

G. S. Constantinescu and K. D. Squires. Numerical investigations of flow over a sphere in the subcritical and supercritical regimes. *Phys Fluids*, 16:1449–1466, 2004.

B. Dargahi. The turbulent flow field around a circular cylinder. *Exp. Fluids*, 8:1–12, 1989.

W. J. Devenport and R. L. Simpson. Some time-dependent features of turbulent appendage-body junction flows. In *The 16th Symposium on Naval Hydrodynamics*, pages 312–335, Berkeley, CA, 1987a.

W. J. Devenport and R. L. Simpson. Turbulent structure near the nose of a wing-body junction. AIAA Paper 87-1310, 1987b.

W. J. Devenport and R. L. Simpson. Time-dependent and time-averaged turbulence structure near the nose of a wing-body junction. *J. Fluid Mech.*, 210:23–55, 1990.

S. Dey, S. Sarkar, S. Bose, S. Tait, and O. Castro-Orgaz. Wall-wake flows downstream of a sphere placed on a plane rough-wall. *J. Hydraul. Eng.*, 137:1173–1189, 2011.

F. Etzold and H. Fiedler. The near-wake structure of a cantilevered cylinder in a cross flow. *J. Z., Flugwiss*, 24:77–82, 1976.

C. Farell, S. Carrasquel, O. Guven, and V. Patel. Effect of windtunnel walls on the flow past circular cylinders and cooling tower models. *ASME J Fluid Eng*, 99: 470–479, 1977.

T. A. Fox and G. S. West. Fluid-induced loading of cantilevered circular cylinder in a low turbulence uniform flow. part 1. mean loading with aspect ratios in the range 4 to 30. *J. Fluid. Struct.*, 7:15–28, 1993a.

T. A. Fox and G. S. West. Fluid-induced loading of cantilevered circular cylinder in a low turbulence uniform flow. *J. Fluid. Struct.*, 7:1–14, 1993b.

O. Frederich, E. Wassen, and F. Thiele. Prediction of the flow around a short wall-mounted cylinder using les and des. *J. Num. Ana. Ind. App. Math.*, 3:231–247, 2008.

H. Fu and D. Rockwell. Shallow flow past a cylinder: Transition phenomena at low reynolds number. *J. Fluid Mech.*, 540:75–97, 2005.

R. Hain, C. J. Kahler, and D. Michaelis. Tomographic and time resolved piv measurements on a finite cylinder mounted on a flat plate. *Exp. Fluids*, 45:715–724, 2008.

S. M. Hajimirzaie, C. J. Wojcik, and J. H. J. Buchholz. The role of shape and relative submergence on the structure of wakes of low-aspect-ratio wall-mounted bodies. *Exp. Fluids*, 53:1943–1962, 2012.

H. Huang, D. Dabiri, and M. Gharib. On errors of digital particle image velocimetry. *Meas. Sci. Tech.*, 8:1427–1440, 1997.

J. C. R. Hunt, C. J. Abell, J. A. Peterka, and H. Woo. Kinematical studies of the flows around free or surface-mounted obstacles. *J. Fluid Mech*, 86:179–200, 1978.

H. J. Hussein and R. J. Martinuzzi. Energy balance of turbulent flow around a surface mounted cube placed in a channel. *Phys. Fluids*, 8:764–780, 1996.

Y. Jang and S. Lee. Piv analysis of near-wake behind a sphere at a subcritical reynolds number. *Exp. Fluids.*, 44:905–914, 2008.

T. Kawamura, M. Hiwada, T. Hibino, I. Mabuchi, and M. Kumuda. Flow around a finite circular cylinder on a flat plate. *Bull. JSME*, 27(232):2142–2151, 1984.

H. Kim and P. Durbin. Observations of the frequencies in a sphere wake and of drag increase by acoustic excitation. *Phys. Fluids*, 31:3260–3265, 1988.

S. Krajnović. Large eddy simulation of the flow over a three-dimensional hill. 81: 189–204, 2008.

S. Krajnović. Flow around a tall finite cylinder explored by large eddy simulation. *J. Fluid Mech.*, 676:294–317, 2011.

R. W. J. Lacey and C. D. Rennie. Laboratory investigation of turbulent flow structure around a bed-mounted cube at multiple flow stages. *J. Hydraulic Eng.*, 138:71–84, 2012.

A. Larousse, R. Martinuzzi, and C. Tropea. Flow around surface-mounted, three-dimensional obstacles. In *Turbulent Shear Flows 8; Eighth Int. Symp. on Turbulent Shear Flows*, Munich, Germany, 1991. Springer-Verlag.

A. Leder. 3d-flow structures behind truncated circular cylinders. In *Proceedings of the 4th ASME/JSME Joint Fluids Engineering Conference, FEDSM2003-45083*, Honolulu, Hawaii, 2003.

B. E. Lee. The effect of turbulence on the surface pressure field of a square prism. *J. Fluid Mech.*, 69:263–282, 1975.

R. Martinuzzi. Dual vortex structure shedding from low aspect ratio, surface-mounted pyramids. *J. Turbulence.*, 9:1–16, 2008.

R. Martinuzzi and C. Tropea. The flow around surface-mounted, prismatic obstacles placed in a fuly-developed channel flow. *ASME J. Fluids Eng.*, 115:85–92, 1993.

R. J. Martinuzzi and M. AbuOmar. Study of the flow around surface-mounted pyramids. *Exp. Fluids*, 34:379–389, 2003.

P. J. Mason and B. R. Morton. Trailing vortices in the wakes of surface-mounted obstacles. *J. Fluid Mech.*, 175:247–293, 1987.

R. Mittal and F. M. Najjar. Flow around a sphere in a plane turbulent boundary layer. 1999.

M. Morrison, R. Martinuzzi, E. Savory, and G. Kopp. Vortex shedding from slender surface mounted pyramids. *Canadian Society of Mechanical Engineering Forum*, Kananaskis, Canada:21–24 May, 2006.

N. Nakamura. Bluff body aerodynamics and turbulence. *J. Wind Eng. Ind. Aerodyn.*, 49:65–78, 1993.

T. Nakato, J. Christensen, and B. Schonhoff. Freshwater mussel survey in pool 16, the mississippi river, near fairport, iowa: R.m. 463.5 - r.m. 464.1, approximately. IIHR Technical Report 464, The University of Iowa, IIHR - Hydroscience & Engineering, 2007.

R. Narasimha and S. N. Prasad. Leading edge shape for flat plate boundary layer studies. *Exp. Fluids*, 17:358–360, 1994.

NCEA. *Biofuels and the Environment: First Triennial Report to Congress*. Environmental Protection Agency (US), epa/600/r-10/183a edition, 2011.

M. Ochi. *Ocean Waves: The Stochastic Approach*. Cambridge University Press, 2005.

A. Okajima. Strouhal numbers of rectangular cylinders. *J Fluid Mech*, 123:379–398, 1982.

S. Okamoto. Turbulent shear flow behind hemisphere-cylinder placed on ground plane. In L. J. S. Bradbury, F. Durst, B. E. Launder, F. W. Schmidt, and J. H. Whitelaw, editors, *Turbulent Shear Flows 2*, pages 171–185. Springer, 1980.

S. Okamoto and Y. Sunabashiri. Vortex shedding from a circular cylinder of finite length placed on a ground plane. *ASME J. Fluids Eng.*, 112:512–521, 1992.

S. Okamoto and N. Uemura. Effect of rounding side-corners on aerodynamic forces and turbulent wake of a cube placed on a ground plane. *Exp. Fluids*, 11:58–64, 1991.

T. Okamoto, M. Yagita, and S. Kataoka. Flow past cone placed on flat plate. *Bull. JSME*, 20:329–336, 1977.

O. Olçmen and R. L. Simpson. Some features of a turbulent wing-body junction vortical flow. AIAA Paper 97-0651, 1997.

P. L. ONeill, D. Nicolaides, D. Honnery, and J. Soria. Autocorrelation functions and the determination of integral length with reference to experimental and numerical data. In *Proc. 15th Australasian Fluid Mechanics Conference*, pages 573–581, 2004.

M. Ozgoren, A. Okbaz, S. Dogan, B. Sahin, and H. Akilli. Turbulent shear flow downstream of a sphere with and without an o-ring located over a plane boundary. *EPJ Web of Conferences*, 25 (01066), 2012.

M. Ozgoren, A. Okbaz, S. Dogan, B. Sahin, and H. Akilli. Investigation of flow characteristics around a sphere placed in a boundary layer over a flat plate. *Experimental Thermal and Fluid Science,*, 44:62–74, 2013.

N. Ozturk, A. Akkoca, and B. Sahin. Piv measurements of flow past a confined cylinder. *Exp. Fluids*, 44:1001–1014, 2008.

J. Paik, C. Escauriaza, and F. Sotiropoulos. On the bimodal dynamics of the turbulent horseshoe vortex system in a wing-body junction. *Phys. Fluids*, 19, 2007. Art. 045107.

G. Palau-Salvador, T. Stoesser, J. Fröhlich, M. Kappler, and W. Rodi. Large eddy simulations and experiments of flow around finite-height cylinders. *Flow Turbulence Combust.*, 84(2):239–275, 2009.

A. Papangelou. Vortex shedding from slender cones at low reynolds numbers. *J Fluid Mech*, 242:299–321, 1992.

A. N. Papanicolaou and C. Kramer. The role of relative submergence on cluster microtopography and bedload predictions in mountain streams. In *Proc. Int. Symp. River, Coastal, and Estuarine Morphodynamics*, London, 2005. Taylor and Francis.

A. N. Papanicolaou, D. Dermisis, and M. Elhakeem. Investigating the role of clasts on the movement of sand in gravel bed rivers. *J. Hydraulic Eng.*, 137(9):871–883, 2011.

A. N. Papanicolaou, C. Kramer, A. Tsakiris, T. Stoesser, S. Bomminayuni, and Z. Chen. Effects of a fully submerged boulder within a boulder array on the mean and turbulent flow fields: Implications to bedload transport. *Acta Geophysica: 10.2478/s11600-012-0044-6*, pages 1–45, 2012a.

A. N. Papanicolaou, C. Kramer, A. Tsakiris, T. Stoesser, S. Bomminayuni, and Z. Chen. Effects of a fully submerged boulder within a boulder array on the mean and turbulent flow fields: Implications to bedload transport. *Acta Geophysica: 10.2478/s11600-012-0044-6*, pages 1–45, 2012b.

C. Park and S. Lee. Effects of free-end corner shape on flow structure around a finite cylinder. *J. Fluid. Struct.*, 19:141–158, 2004.

R. J. Pattenden, S. R. Turnock, and N. W. Bressloff. An experimental and computational study of 3-d unsteady flow features found behind a cylinder. *Third Fluids Engineering Summer Meeting, Japan.*, 2002.

R. J. Pattenden, S. R. Turnock, and Z. Zhang. Measurements of the flow over a low-aspect-ratio cylinder mounted on a ground plane. *Exp. Fluids*, 39:10–21, 2005.

M. Raffel, C. Willert, S. T. Wereley, and J. Kompenhans. *Particle Image Velocimetry: A Practical Guide*. Springer, 2007.

D. Rockwell. Vortex formation in shallow flows. *Phys. Fluids*, 20, 2008. Art. 031303.

S. C. Roh and S. O. Park. Vortical flow over the free end surface of a finite circular cylinder mounted on a flat plate. *Exp. Fluids*, 34:63–67, 2003.

P. Rowinski, J. Aberle, and A. Mazurczyk. Shear velocity estimation in hydraulic research. *Acta Geophys*, 53:567–583, 2005.

M. A. F. Sadeque, N. Rajaratnam, and M. R. Loewen. Flow around cylinders in open channels. *J. Eng. Mech.*, 134(1):60–71, 2008.

M. A. F. Sadeque, N. Rajaratnam, and M. R. Loewen. Effects of bed roughness on flow around bed-mounted cylinders in open channels. *J. Eng. Mech.*, 135(2): 100–110, 2009.

H. Sakamoto and M. Arie. Vortex shedding from a rectangular prism and a circular cylinder placed vertically in a turbulent boundary layer. *J. Fluid Mech.*, 126: 147–165, 1983.

H. Sakamoto and H. Haniu. A study on vortex shedding from sphere in uniform flow. *Trans. ASME. J. Fluid Eng.*, 112:386–392, 1990.

P. Sattari, J. A. Bourgeois, and R. J. Martinuzzi. Turbulent wake of surface-mounted finite aspect ratio bluff bodies. *ASME Conference Proceedings*, (30811), 2010.

E. Savory and N. Toy. Hemispheres and hemisphere-cylinders in turbulent boundary layers. *J. Wind Eng. Ind. Aerodyn.*, 23:345–364, 1986.

E. Savory and N. Toy. The separated shear layers associated with hemispherical bodies in turbulent boundary layers. *J. Wind Eng. Ind. Aerodyn.*, 28:291–300, 1988.

C. V. Seal, C. R. Smit, O. Akin, and D. Rockwell. Quantitative characteristics of a laminar, unsteady necklace vortex system at a rectangular block - flat plate juncture. *J. Fluid Mech.*, 286:117–135, 1995.

H. Shamloo, N. Rajaratman, and C. Katopodis. Hydraulics of simple habitat structures. *J. Hydraulic Res.*, 39(4):351–366, 2001.

R. L. Simpson. Junction flow. *Annu. Rev. Fluid Mech.*, 33:415–443, 2001.

R. L. Simpson, C. Long, and G. Byun. Study of vortical separation from an axisymmetric hill. *Int. J. Heat Fluid Flow.*, 23:582–591, 2002.

R. B. Smith and V. Grubišić. Aerial observations of hawaii's wake. *J. Atmos. Sci.*, 50 (22):3728–3750, 1993.

J. M. M. Sousa and J. C. F. Pereira. DPIV study of the effect of a gable roof on teh flow structure around a surface-mounted cubic obstacle. *Exp. Fluids*, 37:409–418, 2004.

D. Strayer, J. Downing, and T. Newton. Changing perspectives on pearly mussels, north americas most imperiled animals. *Biosciences*, 54(5):429–439, 2004.

K. Strom and A. Papanicolaou. ADV measurements around a cluster microform in a shallow mountain stream. *J. Hydraulic Eng.*, 133(12):1379–1389, 2007.

K. Strom, A. Papanicolaou, and G. Constantinescu. Flow heterogeneity over 3d cluster microform: Laboratory and numerical investigation. *J. Hydraulic Eng.*, 133(3):273–287, 2007.

D. Sumner and J. L. Heseltine. Tip vortex structure for a circular cylinder. *J. Wind Eng. Ind. Aerodyn.*, 96:1185–1196, 2008.

D. Sumner, J. L. Heseltine, and O. J. P. Dansereau. Wake structure of a finite circular cylinder of small aspect ratio. *Exp. Fluids*, 37:720–730, 2004.

S. Tanaka and S. Murata. An investigation of the wake structure and aerodynamic characteristics of a finite circular cylinder. *Bull. JSME*, 42:178–187, 1999.

S. Taneda. Visual observations of the flow past a sphere at reynolds numbers between 10^4 and 10^6. *J. Fluid Mech.*, 85(1):187–192, 1978.

H. M. Tritico and R. H. Hotchkiss. Unobstructed and obstructed turbulent flow in gravel bed rivers. *J. Hydraulic Eng.*, 131:635645, 2005.

T. Tsutsui. Flow around a sphere in a plane turbulent boundary layer. *J Wind Eng Ind Aerodyn*, 96:779792, 2008.

R. Turner, N. Rabalis, and D. Justic. Gulf of mexico hypoxia: Alternate states and a legacy. *Environ. Sci. Technol.*, 42:23232327, 2008.

Y. Uematsu, M. Yamada, and K. Ishii. Some effects of free-stream turbulence on the flow past a cantilevered circular cylinder. *J. Wind Eng. Ind. Aerodyn.*, 33:43–52, 1990.

P. P. Vlachos and M. R. Hajj. A time-resolved DPIV study of the unsteady character of the flow over a surface-mounted prism. *J. Wind Eng. Ind. Aerodyn.*, 90:543–553, 2002.

S. B. Vosper. Three-dimensional numerical simulations of strongly stratified flows past conical orography. *J. Atmos. Sci.*, 57:3716–3739, 2000.

S. B. Vosper, I. Castro, W. Snyder, and S. Mobbs. Experimental studies of strongly stratified flow past three-dimensional orography. *J. Fluid Mech.*, 390:223–249, 1999.

H. F. Wang and Y. Zhou. The finite-length square cylinder near wake. *J. Fluid Mech.*, 638:453–490, 2009.

H. F. Wang, Y. Zhou, C. K. Chan, and K. S. Lam. Effect of initial conditions on interaction between a boundary layer and a wall-mounted finite-length-cylinder wake. *Phys. Fluids*, 18:453–490, 2006.

G. West and C. Apelt. The effects of tunnel blockage and aspect ratio on the mean flow past a circular cylinder. *J Fluid Mech.*, 114:361–377, 1982.

M. M. Zdravkovich. *Flow around circular cylinders, vol 1: Fundamentals*. Oxford University Press, 1997.